Azimuthal angular correlations between D^{*+} mesons and charged hadrons in proton-proton collisions at 13 TeV with the ALICE experiment at the LHC

Fatiha Lehas

A catalogue recored is available from the Utrecht University Library
ISBN: 978-94-6423-416-9
DOI: https://doi.org/10.33540/603

Typset using LaTeX

Azimuthal angular correlations between D^{*+} mesons and charged hadrons in proton-proton collisions at 13 TeV with the ALICE experiment at the LHC

Azimutale hoekcorrelaties tussen D^{*+} mesonen en geladen hadronen in proton-proton botsingen bij 13 TeV met het ALICE-experiment bij de LHC

(met een samenvatting in het Nederlands)

Proefschrift

ter verkrijging van de graad van doctor aan de Universiteit Utrecht op gezag van de rector magnificus, prof.dr. H.R.B.M. Kummeling, ingevolge het besluit van het college voor promoties in het openbaar te verdedigen op woensdag 8 september 2021 des middag te 12.15 uur

door

Fatiha Lehas

geboren op 27 oktober 1989 te Chelghoum Laid, Algerije

Promotoren:

Prof. dr. R.J.M. Snellings

Prof. dr. J. Aichelin

Copromotoren:

Dr. A. Mischke

Dr. A. Grelli

The degree is awarded as part of a Joint Doctorate with IMT Atlantique University, Nantes - France

... that the heavens and the earth were a joined entity, and We separated them and made from water every living thing ? ...

If there is no enemy inside, the enemy outside can do us no harm.

Stand up for the teacher and show him your respect, he could have been a messenger.

Abstract

The Large Hadron Collider at CERN-LHC [1] allows for the acceleration of protons and heavy-ions to unprecedented energies. Heavy-ion collisions provide the ideal conditions (high temperature and energy density) for ordinary matter to undergo a phase transition to the so-called Quark-Gluon-Plasma (QGP), a state of matter that is assumed to have existed in our universe a few micro-seconds after the Big Bang. Collisions in smaller systems, like proton-proton and proton-nucleus, allow for the study of Quantum ChromoDynamics (QCD) and cold nuclear matter effects, and, in addition, to set a solid reference for heavy-ion studies.

Due to its short lifetime, the study of the QGP proceeds by means of probes. For this, heavy quarks are ideally suited due to the fact that they are produced early in the collision, at the time of the hard scattering, and they can witness the full evolution of the system while keeping their identity. In addition, heavy-quarks production in smaller systems, such as pp, p-Pb, allow for testing perturbative QCD calculations and Cold Nuclear Matter effect, respectively. The main focus of this manuscript will be the study of charm production mechanisms via correlation measurements. Indeed, correlations are a powerful tool to investigate several physics questions. In pp collision via D-h (and especially D-D) correlation studies it is possible to investigate the charm production mechanisms (pair creation, gluon splitting and flavour excitation) and therefore set strong constraints on QCD calculations. At the same time, a solid pp reference is vital for Pb-Pb studies, where correlations among heavy-quarks can be used to investigate in-medium energy loss of partons. Indeed, several theoretical models [2] [3] predict that the mechanisms of collisional and radiative energy loss will have a different footprint on the final charm correlation shape, allowing us to evaluate their relative contribution.

This thesis will be organised as follows. Chapter 1 will include an introduction to heavy flavour physics with specific focus on correlations. Some key measurements will be discussed. In Chapter 2, the Large Hadron Collider is briefly described. In addition, the ALICE detector is introduced with attention on the sub-detectors used for correlation studies. In Chapter 3, the quality assurance of the ALICE proton-proton data, exploited for the analyses presented in this thesis, is discussed. In Chapter 4, the analysis strategy is described and the obtained results are presented. In Chapter 5, the PYTHIA event generator is exploited to study heavy-flavour correlations at different energy scales. Chapter 6 includes an overview of the physics implemented in the EPOS/EPOSHQ event generator as well as the presentation of the results and the comparison between the experimental measurements and the theoretical simulations. Finally, the conclusions and perspectives are given in Chapter 7.

Contents

Abstract **iv**

1 From the Big Bang to Correlations **1**
1.1 The standard model . . . 1
1.1.1 Quantum ChromoDynamics (QCD) . . . 4
1.1.2 Colour confinement . . . 5
1.1.3 Asymptotic freedom . . . 5
1.2 Quark-Gluon-Plasma (QGP) . . . 7
1.2.1 QCD Phase diagram . . . 8
1.2.2 Signatures of the QGP . . . 10
1.3 Heavy-ion collisions . . . 12
1.3.1 Global properties . . . 13
1.3.2 Evolution of the collision . . . 16
1.4 Heavy flavour production . . . 18
1.4.1 Heavy flavour production in proton-proton collisions . . . 20
1.4.2 Heavy flavour production in proton-Nucleus collisions . . . 26
1.4.3 Heavy flavour production in heavy-ion collisions . . . 31
1.5 Heavy Flavour Correlations . . . 38
1.6 Chapter Conclusion . . . 48

2 ALICE Experiment **49**
2.1 The Large Hadron Collider . . . 49
2.1.1 Operating mode . . . 49
2.2 ALICE Detector . . . 52
2.2.1 Inner Tracking System . . . 54
2.2.2 Time Projection Chamber . . . 56
2.2.3 Time-Of-Flight . . . 57
2.3 Chapter conclusion . . . 58

3 Data sample and quality assurance **59**
3.1 Data sample . . . 59
3.2 Quality assurance . . . 59
3.2.1 Event selection . . . 60
3.2.2 Tracks . . . 62
3.2.3 Particle Identification (PID) . . . 66

PID-TPC . . . 66
PID TOF . . . 68
3.3 Chapter conclusion . . . 69

4 Correlation analysis and Results **71**
4.1 Analysis strategy . . . 71
4.2 Analysis results in pp collisions at 13 TeV . . . 73
4.2.1 D^{*+} mesons reconstruction . . . 73
4.2.2 Tracks reconstruction . . . 78
4.2.3 Single events and mixed events distributions . . . 79
4.2.4 Corrected single events . . . 81
4.2.5 Projection on $\Delta\phi$ . . . 83
4.2.6 Background subtraction . . . 85
4.2.7 Correction for the Purity . . . 88
4.2.8 B feed-down subtraction . . . 89
4.2.9 Final corrected D^{*+}-charged particles correlations in p-p collisions at 13 TeV . . . 92
4.3 D^{*+}-charged particles angular-correlations in pp collisions at 8 TeV . . . 103
4.4 Chapter conclusion . . . 115

5 PYTHIA event generator **117**
5.1 Introduction . . . 117
5.2 Basics and physics features . . . 118
5.2.1 Parton showers (ISR/FSR) . . . 119
5.2.2 Multi-Parton Interactions (MPI) . . . 121
5.2.3 Color Reconnection (CR) . . . 122
5.2.4 Beam Remnants (BR) . . . 122
5.2.5 Hadronisation . . . 123
5.3 Heavy flavours in PYTHIA . . . 123
5.4 Results and discussions . . . 125
5.4.1 $D-\bar{D}/B-\bar{B}$ correlations obtained with different configurations . 126
5.4.2 $B-\bar{B}/D-\bar{D}$ correlations in pp collisions at 7 TeV and 200 GeV . . 130
5.4.3 $c-\bar{c}$ vs $D-\bar{D}$ correlations and $b-\bar{b}$ vs $B-\bar{B}$ correlations 136
5.4.4 $D-\bar{D}/B-\bar{B}$ correlations with/without Initial State Radiation and Final State Radiation (ISR/FSR) . . . 140
5.4.5 $D-\bar{D}/B-\bar{B}$ correlations with/without Multiple Parton Interaction (MPI) . . . 145
5.4.6 $D-\bar{D}/B-\bar{B}$ correlations with/without Colour Reconnection (CR) 150
5.4.7 $D-\bar{D}/B-\bar{B}$ correlations Monash2013 versus 4C Tune . . . 155
5.5 Chapter Conclusion . . . 160

6 EPOSHQ Event generator **163**
6.1 Theoretical basics . . . 163

6.1.1 Initial conditions . . . 168
6.1.2 Parton ladders . . . 168
6.1.3 Core-Corona approach . . . 170
6.1.4 Hydrodynamic evolution . . . 172
6.1.5 Hadronisation . . . 174
6.2 MC@sHQ approach . . . 177
6.3 EPOSHQ event generator . . . 178
6.4 Correlation analysis and Results for p-p and p-Pb collisions . . . 178
6.4.1 D-h correlations in p-p collisions at $\sqrt{s}$ = 7 TeV . . . 179
6.4.2 D-h correlations in pp collisions at $\sqrt{s} = 13$ TeV . . . 183
6.4.3 $D - \bar{D}$ correlations in pp collisions at $\sqrt{s}$= 7 TeV . . . 185
6.4.4 D-h and $D - \bar{D}$ correlations in pp collisions at 500 GeV . . . 187
6.4.5 D-h correlations in $p - \bar{p}$ collisions at $\sqrt{s}$= 1.96 TeV . . . 189
6.4.6 D-h correlations in p-Pb collisions at $\sqrt{s} = 5.02$ TeV . . . 190
6.5 Chapter conclusion . . . 195

7 Conclusions and Perspectives **197**

A Run list for p-p collisions at 13 TeV **199**

B Topological cuts **203**

C The partonic profile function **207**

D Hadronization and pomerons **209**

Bibliography **213**

Samenvatting in het Nederlands **223**

Acknowledgements **225**

Chapter 1

From the Big Bang to Correlations

In this introductory chapter, an overview is given on the main aspects concerning the connection between the Quark-Gluon-Plasma (QGP) and the early Universe and on the role of the ultra-relativistic collisions of heavy-ions. The essential features of Quantum Chromodynamics are presented. Finally, heavy-flavours and the associated correlation physics are discussed.

1.1 The standard model

The standard model is considered among the triumphs of modern physics. This triumph lies in the success of this model to describe the observed phenomena by the mathematical equations for a determined energy scale.

Quantum ElectroDynamics (QED) presents the low-energy theory that describes the electrostatic interaction between opposite charges within the atom through the exchange of photons (γ). The Atom is composed of negatively charged electrons orbiting around a positively charged nucleus. The nucleus consists of bound states of protons and neutrons which are positively and neutrally charged, respectively.

The nucleons (protons and neutrons) themselves consist of bound states of quarks, for instance, 2 "up" quarks and one "down" quark for the proton [4]. Another example, the Deuterium (Hydrogen isotope) as presented in figure.1.1, is an atom composed of an electron orbiting around a nucleus. The nucleus consists of one proton (2 "up"+1"d") and one neutron (1"u"+2"d"). The quarks within each nucleon are bounded through the gluons.

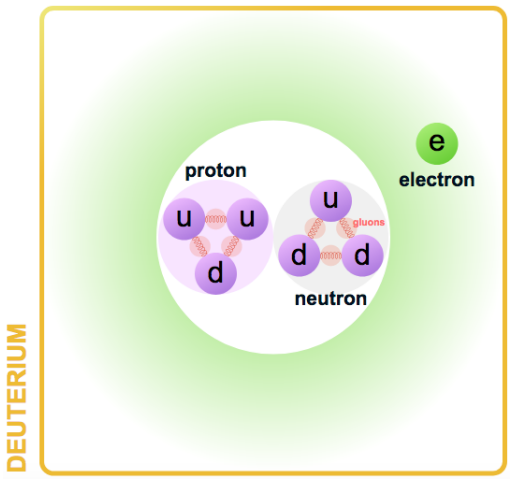

FIGURE 1.1: Example of the elementary constituents particles of Deuterium in the Standard Model.

A schematic presentation of the components of the matter with their correspondent dimensions is displayed in figure.1.2.

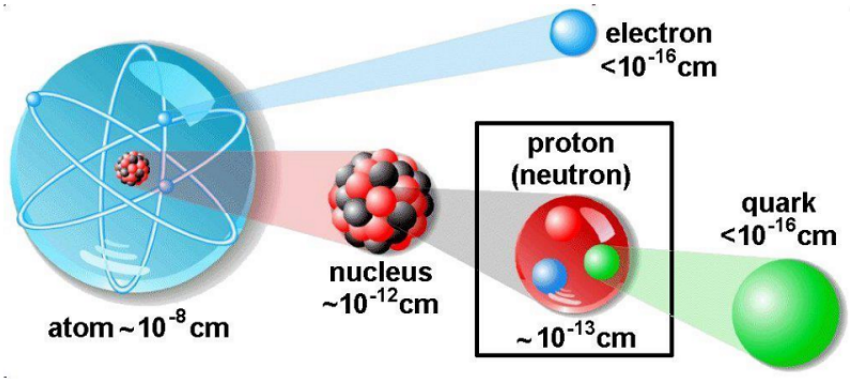

FIGURE 1.2: The components of the matter at different scales.

Quantum ChromoDynamics (QCD) presents the high-energy theory that describes the strong interactions between the components of the nucleons (partons) via the exchange of gluons.

Among the fundamental interactions, there is also the weak force which contributes significantly, for instance, in the radioactive interactions (β-decays) and nuclear fusion where the almost massless particles, the famous neutrinos (ν), are produced. Finally, the gravitational force but it is not included in the Standard Model [4].

In the common physics phenomena, the main contributing particles (undergo specific interactions) are the protons (strong/electromagnetic interactions), neutrons (strong interactions), electrons (electromagnetic/weak interactions) and neutrinos (weak interactions). For each energy scale, a different particle structure arises as displayed in figure.1.3.

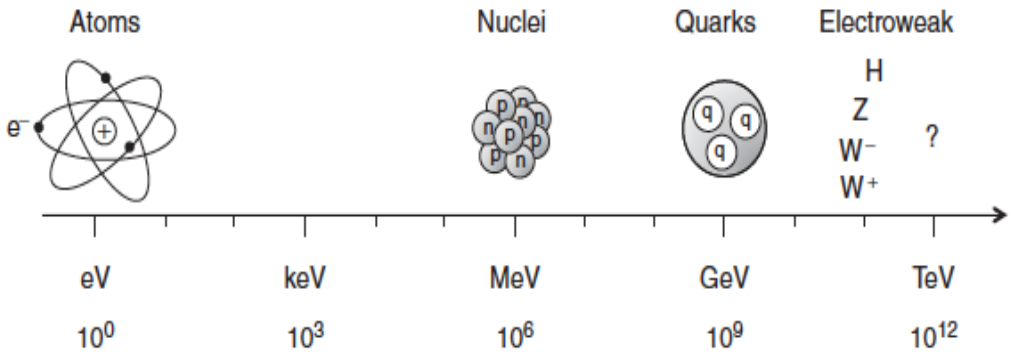

FIGURE 1.3: The components of the matter at different energy scales [4].

The elementary particles in the Standard Model include 12 fermions and 5 bosons. Among the fermions, there are 6 *leptons* that undergo the weak interaction and the electromagnetic interaction, except for the neutrinos that undergo only the weak interaction. As for the strong interaction, only *quarks* are concerned. The Standard Model of elementary particles is presented in figure.1.4.

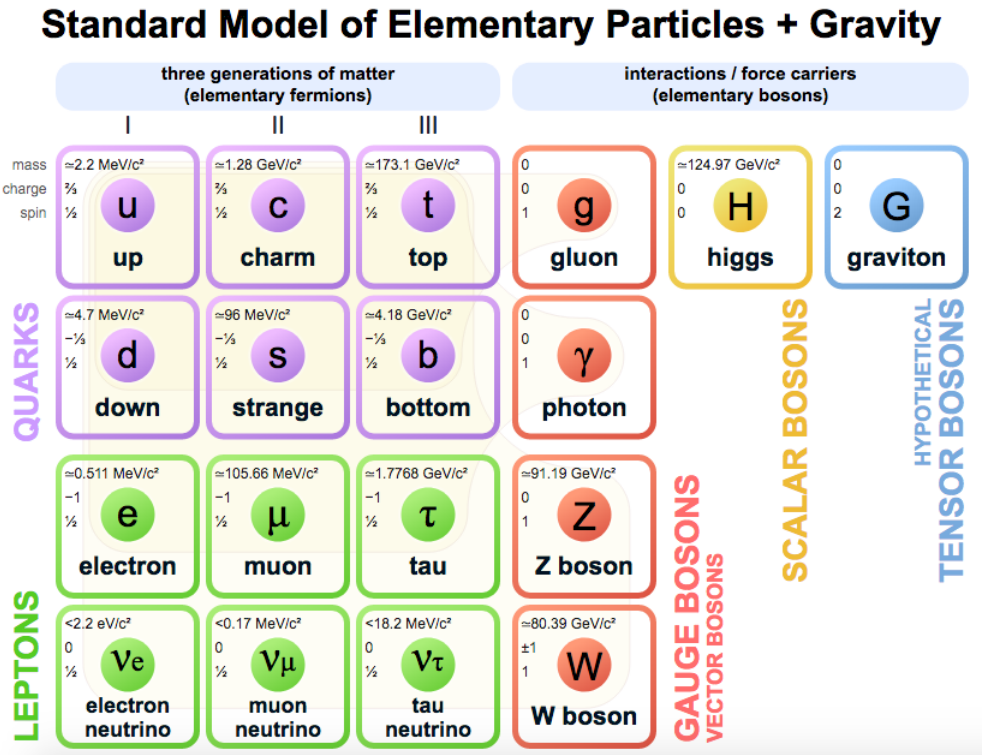

FIGURE 1.4: The Standard Model of elementary particles + Gravity

The elementary particles are classified into generations. The *first generation* includes the electron and its associated neutrino, *up* and *down* quarks, in another word, the building blocks of the matter at the low-energy Universe.

However, higher energy scales can be reached at colliders which gives rise to two other generations: the *second generation* and *third generation*. Both are copies of the first

one and the correspondent elementary particles have similar charges and they undergo the same fundamental interactions but they have different masses. For instance, the copies of electrons, the muon (μ) and tau (τ) are 200 and 3500 times heavier than the electron, respectively.

For each elementary particle, an anti-particle is associated which has the same mass but opposite quantum numbers. This notion is the consequence of the Dirac equation in relativistic quantum mechanics that describes the dynamics of the fermions [4].

The interactions between particles take place through the exchange of force carrier with spin 1 or what is called $gauge\ boson$ and each force is described by Quantum Field Theory (QFT). The exchanged gauge boson in electromagnetic interaction is the photon. For strong interaction, the gluon is the representative gauge boson or force carrier. As for the weak interaction, the gauge bosons can be the $W^{\pm}$ or the Z^0 where both have a mass unlike the photon and the gluon. A very important boson in the standard model is the Higgs which was discovered in 2012 by the CMS and ATLAS Collaborations at the Large Hadron Collider (LHC). The Higgs boson is an elementary particle with a spin-0 with no colour charge and no electric charge and a mass of approximately 125 GeV. It is characterised by a quantum field and those particles interacting with it can gain a mass [4].

1.1.1 Quantum ChromoDynamics (QCD)

QCD is the basic theory that describes strong interactions due to the exchange of the gluon which is the force carrier in this case. Due to the nature of the strong interaction, quarks have never been observed as free elementary particles. Instead, they are always bound to form hadrons. Until now, the common studied and discovered hadrons can consist of either 2 quarks (quark + anti-quark) to form the $meson$ ($anti-meson$) or 3 quarks (or 3 anti-quarks) to form the $baryon$ ($anti-baryon$).

The interaction dynamics between the quarks and the gluons is presented by the QCD Lagrangian equation [6],

$$\mathcal{L} = \bar{q}\Big(i\gamma^{\mu}\partial_{\mu} - m\Big)q - g\Big(\bar{q}\gamma^{\mu}T_a q\Big)G^a_{\mu} - \frac{1}{4}G^a_{\mu\nu}G^{\mu\nu}_a \tag{1.1}$$

T_a are 3x3 traceless matrices and linearly independent (with $a = 1, .., 8$), q refers to the coloured quarks that interact with the vector gluons G_{μ} with a coupling g. G^a_{μ} (with $a = 1, ..., 8$) presents 8 vector gluon fields. $G^a_{\mu\nu}$ is the field strength tensor defined by:

$$G^a_{\mu\nu} = \partial_{\mu}G^a_{\nu} - \partial_{\nu}G^a_{\mu} - g f_{abc}G^b_{\mu}G^c_{\nu} \tag{1.2}$$

f_{abc} presents the structure constants of the group which are real numbers and they are defined by the commutation relation:

$$[T_a, T_b] = i f_{abc}T_c \tag{1.3}$$

where the labels a, b, c refer to the 3 colour charges. The 8 SU(3) generators represent the 8 colour charged gluons of QCD. The colour charge can be either red (r), green (g), blue (b) which is just a notion to distinguish the 3 orthogonal states of the SU(3) colour space.

The QCD Lagrangian defined in eq.1.1 is Gauge invariant provided that the Gauge fields G^a_μ transform as

$$G^a_\mu \rightarrow G^a_\mu - \frac{1}{g}\partial_\mu \alpha_a - f_{abc}\alpha_b G^c_\mu \tag{1.4}$$

The non-Abelian nature of this Gauge group leads to the gluon self-interactions via a vertex of three or four gluons, unlike QED where photons do not interact with themselves.

1.1.2 Colour confinement

Several experiments have provided evidence for the existence of quarks [4]. However, no free quark was observed directly till now. This is due to the $colour\ confinement$ hypothesis which suggests that the quarks should remain confined into colourless objects. In addition to that, an object with a non-zero colour charge can not propagate freely. This is believed to be the consequence of the fact that gluons and quarks are colour charged particles. One can understand the origin of this hypothesis by considering the interaction between 2 quarks. This interaction takes place by the exchange of virtual gluons which form a squeezed colour field (tube) and become a constant at large distances. As a consequence, the larger the distance, the higher the energy stored in this tube for which the associated potential can be expressed by,

$$V(r) \approx kr \tag{1.5}$$

where $k \approx 1$ GeV/fm and it is determined experimentally and corresponds to an extremely large force of the order of 10^5 N. Hence, the energy needed to separate 2 quarks at larger distances would be huge. Due to these facts, it would be more suitable for the coloured quarks to remain in bounded states without a colour field between them within the hadrons which is believed to be the reason for the existence of quarks bounded and confined in colourless objects.

1.1.3 Asymptotic freedom

The strong coupling constant α_S is not a constant but it depends on the interaction energy scale. Based on the order of magnitude of α_S, QCD includes 2 regimes. The first one is the perturbative regime at the high-energy scale where α_S becomes small enough which allows for perturbative calculations to be applied. In this case, the partons don't interact strongly and can be considered as $quasi - free$ particles which led to the concept of $asymptotic freedom$. The second regime is the non-perturbative at the low-energy scale where α_S has a value of the order of 1.

This characteristic of the running coupling constant α_S originally comes from renormalisation calculations. In QCD, the interaction between the gluon and the quark has the effective strength α_S obtained by summing over all appropriate high-order correction diagrams of QCD. These summed corrected diagrams lead to divergences. Thanks to some properties, for instance, the divergence absorption by the quark charge, the infinities in the gluon propagators and incoming/outgoing currents can be renormalised. This gives rise to the strong interaction coupling constant that depends on the energy scale and which is defined by the expression,

$$\alpha_s(Q^2) = \frac{4\pi}{\beta_0 ln(Q^2/\Lambda^2)} \tag{1.6}$$

where β_0 is defined by,

$$\beta_0 = 11 - \frac{2}{3}n_f \tag{1.7}$$

n_f is the number of active quark flavours in the concerned loop for the scale Q^2, Q is the momentum transfer and Λ is the QCD scale that gives the limit for which α_s is considered small (large) consequently, perturbative (non-perturbative) QCD calculations are applicable (not applicable). More details concerning α_S can be found in [4] [5] [6] [7].

The evolution of α_S was verified experimentally through measurements for different momentum transfer as can be seen in figure.1.5. At larger values of Q i.e. of the order of 100 GeV which is a common momentum transfer at high-energy particle colliders, α_S gets smaller ($\approx$ 0.1). For momentum transfer of the order of 1 GeV, α_S is of the order of 1. The performed measurements in different experiments show also that $\Lambda \approx$ 200 MeV.

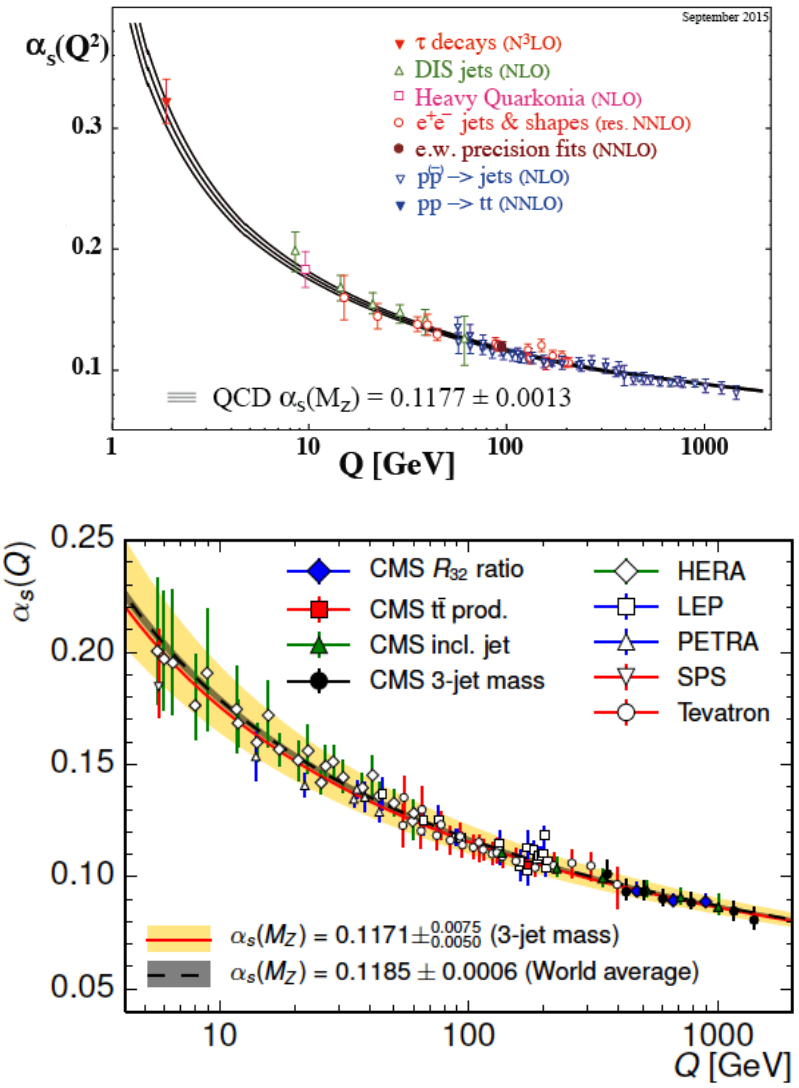

FIGURE 1.5: The running coupling constant α_S of QCD. Top: predictions from QCD versus measurements from different experiments in different energy scale. Bottom: Recent measurements of α_S performed at CMS in jet analysis and compared to the estimation of α_S in electron-positron, electron-proton, proton-antiproton collisions [8].

1.2 Quark-Gluon-Plasma (QGP)

The astronomical observations of galaxies show that the universe is expanding. At the same time, temperature and radiation are decreasing which means that the early universe was hotter and denser than nowadays and it is argued that it consisted of a soup of elementary particles.

Within hadrons and at normal energies, these elementary particles (quarks and gluons) exist in bounded states and none of them has been observed in a free state until now (see the part of *colour confinement* in section.1.1.2). However, when the universe was created, the baryo-chemical potential was zero while both the temperature and the energy density

were extremely high so that these quarks and gluons were not confined in the hadrons (see $asymptotic\ freedom$ in section.1.1.3) but were in a state called "Quark-Gluon-Plasma". As the universe expanded, it cooled down. After reaching the critical temperature T_C, the hadronisation occurred and hadrons were formed. This is called the Quantum ChromoDynamics phase transition.

To mimic the early universe, a QGP droplet can be recreated in laboratories on earth (colliders) in small bangs through the collisions of accelerated heavy nuclei at relativistic energies where extreme energy densities and temperature can be reached. These collisions provide the extreme conditions suitable for the study of the properties of the strong interaction in this state of matter [9] [10]. It is crucial to point out the fact that the QGP produced in colliders is a very small droplet that differs in some properties from the QGP produced in the early Universe. More details concerning the differences and similarities between the QGP created in the Big Bang and Micro-Bang can be found in [11].

The first evidence of the creation/production of quark-gluon plasma was found at the SPS (CERN) at the energy $\sqrt{s_{NN}} = 17.3$ GeV in Pb-Pb collisions with fixed target and at the RHIC (BNL) in Au-Au collisions at $\sqrt{s_{NN}} = 200$ GeV where some quantitative properties of this matter were determined for the first time [12].

1.2.1 QCD Phase diagram

The progress on the understanding of the QCD phase transition diagram is the result of theoretical and experimental research at different energy scales. The investigations are shared between several facilities in the world and the understanding of this phase diagram is not only crucial in the field of particle physics but also in astrophysics as will be discussed in the next part. The QCD phase diagram is presented in figure.1.6 and one can observe that the created deconfined matter at both LHC and RHIC highest energies, is categorised by high temperatures and nearly zero net-baryon density.

Lattice QCD (lQCD) calculations suggest that the phase transition is of a "cross-over" type at zero net baryon density μ_B (or zero baryo-chemical potential) at a critical temperature of about 160 MeV and for an energy density near 0.7 GeV/fm^3. At this point, it is expected that the mass of the quarks decreases from the effective mass to the small bare one and the phase transition takes place from the nuclear matter to a state where quarks and gluons are deconfined. This is similar to what is observed in a liquid when atoms/molecules will be evaporated as the temperature increases. Likewise, if energy is provided to a nucleus in a normal state, the temperature will rise and nucleons/nuclei will be emitted and if the matter is confined, the constituents (internal degrees of freedom) will get excited [12] [13] [14].

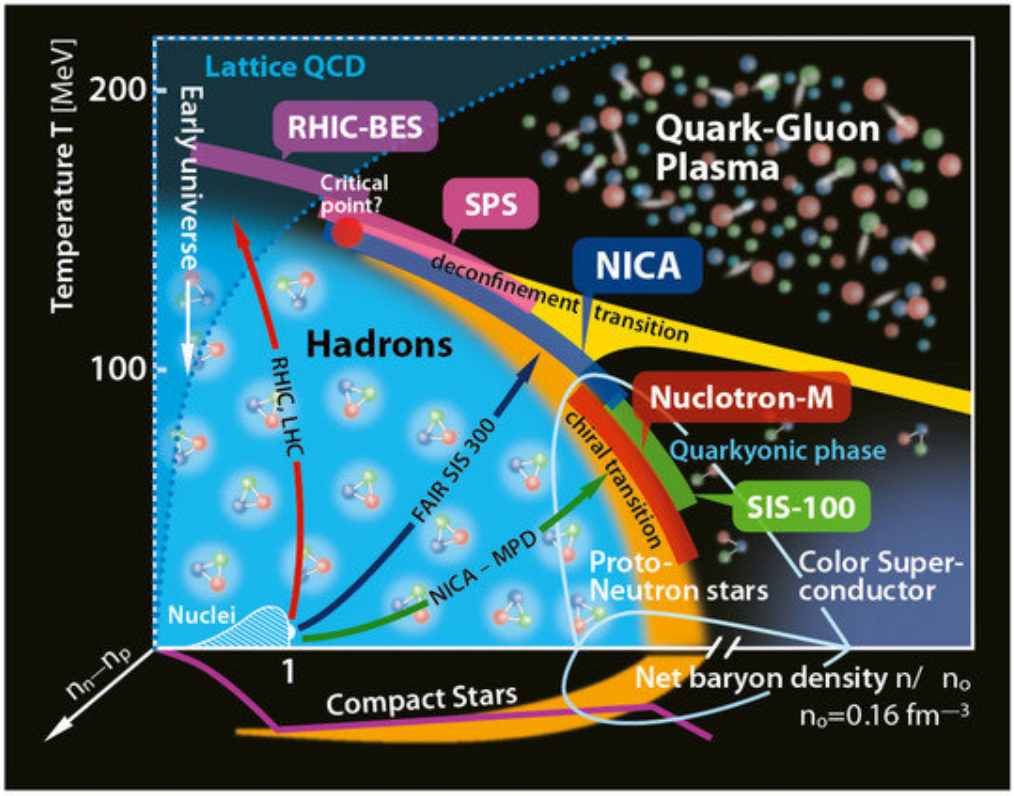

FIGURE 1.6: The QCD phase diagram.

It is proposed that within the core of neutron stars, created in supernova explosions, the conditions are ideal for the existence of the quark-gluon plasma or at least matter whose properties match those of high-density matter. The pressure, in these astronomical objects, increases significantly inward. The core temperature is 1000 times cooler (compared to the expected temperature of the QGP created in accelerators). The density ρ_N within the core is assumed to be larger than that of nuclei so that a state called "condensate" can be formed. Under these circumstances (low temperature and high pressure/baryon density), it is plausible that the quark-gluon plasma can be present. For low temperatures and higher net-baryon density μ_B, the existence of strongly interacting exotic matter is expected like superconducting matter.

In summary, at extreme conditions of temperature and energy density, the hadronic matter undergoes a phase transition to become a soup of quarks and gluons or QGP. At low temperature and high net baryon density, it is expected that exotic matter will be formed like the one in neutron stars or superconducting matter. To investigate this matter (at low temperatures and high net-baryon densities), some dedicated facilities are in construction such as FAIR and NICA. At high temperature and low energy density, we are close enough to the created matter in current particle accelerators where the QGP can be created at moderate density and temperature [9].

1.2.2 Signatures of the QGP

There is no straightforward method to deduce firmly whether a QGP is formed in a specific collision or not. This is due to the small size of QGP (radius of the order of femtometer) in addition to the absence of equipment that can endure the ultimate conditions for which the QGP can be created. The signatures described briefly in the following are therefore based on theoretical principles or experimental observations [15] [16].

Among the possible observables of the QGP creation, one can mention the yield of bound states (charmonium and bottomonium). The charm quarks, for instance, should be created in pairs of $c\bar{c}$ to conserve flavour and colour number. From one side, the interaction between such pairs is decreased because of the presence of other particles. From the other side, the charm and anti-charm will be prohibited to bind because of the colour charge screening in a deconfined medium like the QGP. For these reasons, it is more likely that these pairs will propagate separately and thermalise in the medium instead of forming a bound state. In addition to that, the high temperature reached within such created medium gives rise to more repulsion between the pairs. Suppression of the J/ψ yield was observed in central Pb-Pb collisions at SPS. The production cross-section of J/ψ was also found to be lower in nucleus-nucleus collisions compared to p-p collisions. However, this is not conclusive yet because in such a deconfined medium, not only dissociation of a bound state of heavy flavour can take place but also regeneration, if the number of created pairs is large enough. At SPS, less than one pair of heavy flavour is created so the regeneration process does not have any contribution. Otherwise, in Au-Au collisions at RHIC where more than 10 heavy flavour pairs are created and at the LHC in Pb-Pb collisions with more than 100 created pairs, regeneration contributes significantly [12] [15].

Another possible signature of the QGP creation is the modification of strangeness production in the A-A collision. If sufficient energy is available, heavier quarks, such as strange (s) and charm (c), can be formed in pairs (quark+anti-quark) to conserve the flavour quantum number. The modification of strange hadron production is verified through the measurement of the ratio between strange to non-strange particles, i.e. the particles with s,$\bar{s}$ quarks to those with u,$\bar{u}$,d,$\bar{d}$ quarks as a function of the centre-of-mass energy. In Pb-Pb collisions, an increase in the number of strange (anti-)particle was observed compared to the one measured in p-Pb collisions at the same energy per nucleon. In some other analysis, the ratio is a λ parameter defined by $u\bar{u} : d\bar{d} : s\bar{s} = 1 : 1 : \lambda$. In p-p collisions at $\sqrt{s} \sim 5$ GeV, λ is approximately 0.1 and at $\sqrt{s} = 50$ GeV, it increased to 0.2. In silicon-silicon and sulfur-sulfur collisions, λ was found to be larger by a factor of 2, and at 5 GeV it was 0.3 and it became 0.4 at 50 GeV. Other observations showed also that in nucleus-nucleus collisions at 200 GeV, the ratio $(K^+ + K^-)/(\pi^+ + \pi^-)$ was twice larger in comparison to the case of p-p collisions at the same energy [10][15].

Electromagnetic or thermal radiation is another tool to exploit in order to investigate the existence of the QGP state. It is expected in such medium that photons (real and virtual) will be produced in tremendous number via:

- Quark-gluon scattering $g + q \rightarrow \gamma + q$ or/and $g + \bar{q} \rightarrow \gamma + \bar{q}$ (see diagram(a)/figure.1.7)
- Quark-anti-quark annihilation $q + \bar{q} \rightarrow \gamma + g$ (see diagram(b)/figure.1.7)

and with a small probability the electromagnetic interaction $g + \bar{q} \rightarrow \gamma + \gamma$.

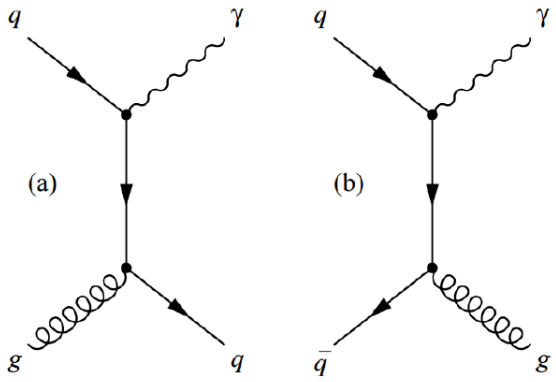

FIGURE 1.7: Feynman presentation for possible schemes of photon production via (anti)quark-gluon scattering (a) or quark-antiquark annihilation (b) [17]

Photons are weakly coupled with the strongly interacting matter but its magnitude is twice larger than the coupling magnitude with quarks. Therefore, in heavy-ion collisions where the creation of QGP is supposed to take place, the electromagnetic radiations will be most likely produced and come out from the interaction region without experiencing collisions and they won't fade away as the system expands. The measured photons in heavy-ion collisions are more associated with the QGP, unlike hadrons which have shorter free paths due to their interactions with the medium constituents before they leave the interaction zone. The interesting signal of QGP photons is obtained over some "background" since photons have many other sources such as those coming from the decay of neutral mesons π^0 and η [14][15].

The production of dilepton is also considered as observable for similar reasons as the photons because of the weak interaction undergone with the QGP. Therefore, modifications of leptons due to in-medium effects can provide information on the QGP properties. The main process through which lepton pairs (l^+l^-) are created is the quark-antiquark annihilation via the exchange of a virtual photon: $q + \bar{q} \rightarrow$ virtual photon $\rightarrow l^+ + l^-$ where the quark and the antiquark are both free constituents coming from the QGP. The production cross-section of lepton pairs from the QGP was suggested to increase with the temperature. No information can be concluded when the temperature is below 300 MeV due to the dominance of the Drell-Yann process. Above 300 MeV, the separation of QGP leptons from Drell-Yann ones would be feasible [15]. A good example of analysis to investigate the QGP involving photons and leptons as probes can be found in [18].

1.3 Heavy-ion collisions

As it was already mentioned, colliding heavy nuclei at ultra-relativistic energies aims to create high energy density and temperature in a small volume to provide the suitable conditions to produce a new form of matter, the Quark-Gluon Plasma or QGP (section.1.2). After the achieved success in the world laboratories following several indications ($QGP\ signatures$ section.1.2.2) for its effective creation, the next challenge was to determine the characteristics of this deconfined strongly interacting matter. Among the most prominent observations accompanied with theoretical predictions are those measurements performed at RHIC where Au-Au collisions at $\sqrt{s_{NN}} = 200$ GeV took place and the analyses showed that a partonic matter was created with a ratio η/S (shear viscosity to entropy) value near the predicted theoretical limits. This result led to conclude that the QGP behaves as an almost perfect liquid [19] [20]. Several analyses are ongoing to extract and understand more properties regarding the initial conditions, equation of state, transport properties, QCD phase diagram which involve several observables such as the volume, temperature, lifetime, pressure evolution, energy, viscosity and many others. At the LHC where the energies are of the order of TeV, more suitable conditions are available (higher temperature and larger density) to create a QGP with a longer lifetime, in comparison to RHIC. In fact, at the LHC in Pb-Pb collisions at $\sqrt{s_{NN}}$ =2.76 TeV, the volume and lifetime of the created fireballs were deduced based on Bose-Einstein correlations and found to be larger (twice in volume) compared to those created at RHIC in Au-Au collisions. From RHIC to the LHC, there are hints of an increase in the initial energy density. In some other analysis, a comparison was performed between the elliptic flow v_2 measured at RHIC and LHC. A similarity was observed which lead to the fact that the properties of the created medium in heavy-ion collisions are similar between RHIC and LHC even if the initial energy density is not the same [12].

Some of the properties of the created deconfined matter (fireball) in a wide range of energies were estimated from comparisons between models and experimental data. The correspondent intervals for each observable are listed in the following:
- Temperature 100-500 MeV, which is a million times larger than the center temperature of the sun (1 MeV or 10^{10} K), according to some other hydrodynamical models, the initial temperature of the fireball can be in the interval 300-600 MeV.
- Volume of 1-5 $\times$ 10^3 fm^3
- Lifetime 10-20 fm/c which is about 3-6 $\times$ 10^{-23} s
- Pressure 100-300 MeV/fm^3 where 1 MeV/fm^3 $\approx$ 10^{33} Pa
- Density 1-10 $\times$ ρ_0 where ρ_0 refers to the normal density of nuclear matter
with $\rho_0 = 0.17$ fm^{-3} = 2.7 $\times$ 10^{14} g/cm^3
- Thermalisation time $\tau_0 \approx$ 0.6-0.15 fm/c [13] [12].

1.3.1 Global properties

The analysis of heavy-ion collisions requires the frequent use of some control parameters. One can mention $\sqrt{s_{NN}}$, the energy of collision per nucleon pair that is beam-energy dependent. The overlap region, where the collision of the two nuclei takes place, is another control parameter that results from the structure or the geometry of the collisions that is not the same between all events occurring in accelerators/colliders. The $centrality$ is another control parameter that presents the fraction of a geometrical cross-section in percentage (%) and the centrality, in turn, is associated with the $impact\ parameter$ through the Glauber Model. Within the same model, two control parameters arise, N_{coll} the number of nucleon-nucleon collisions and N_{part} the number of nucleons participating in the collisions and which contribute to the formation of the fireball.

The different initial collision geometry results in two main types of collisions. When the nucleons from both accelerated beams do not participate in their totality, the collisions are called "peripheral". The nucleons that do not participate are referred to as $spectators$ and those that collide with each other to form the fireball, are called $participants$. A schematic presentation of a peripheral collision is displayed in the top panel of figure.1.8.

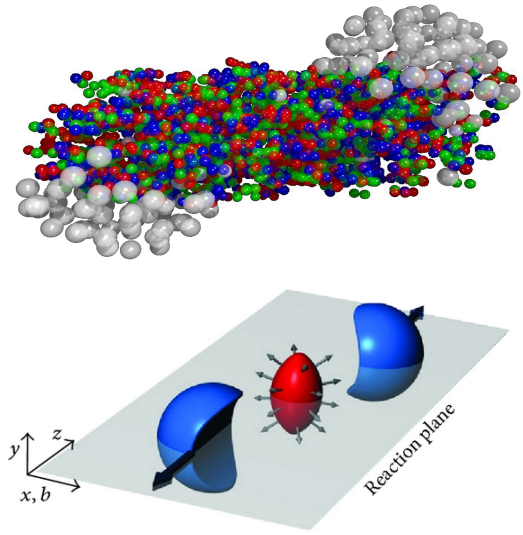

FIGURE 1.8: Top: Schematic presentation of the peripheral collisions of two heavy nuclei beams. The spectator nucleons are presented in white and the participants in colours. Bottom: Presentation of the reaction plane in peripheral heavy-ion collisions where the red almond shape presents the interaction zone.

This can be visualised in a different perspective in terms of the impact parameter b which is the distance, in the reaction plane, between the centers of the 2 colliding nuclei. When b is different than zero, it results in an overlap region presented by the red area (almond shape) in the bottom panel of figure.1.8. When the collisions are head-on between the nuclei (an impact parameter close to zero), the collisions are called "central". Figure.1.9 presents

a central collision between two heavy-ion beams and its evolution with time from left to right [13].

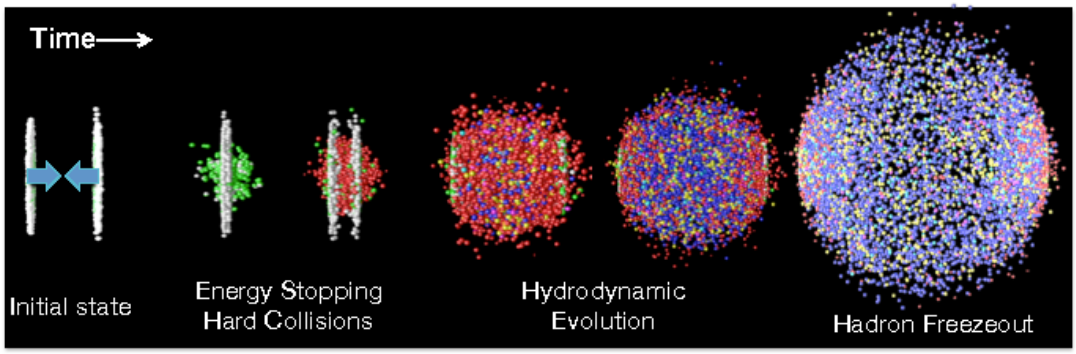

FIGURE 1.9: Spacial-temporal evolution of a central heavy-ion collision.

The control parameters can be considered, in theoretical models, and some in experiments, as input parameters. In addition to that and to determine the properties of the events or the created medium, there are also the extracted parameters or observables [13] [21]. Among these observables, one can mention the $Multiplicity\,of\,charged\,hadrons$ which is defined by the number of charged particles produced in events in a determined rapidity (pseudo-rapidity) range. The multiplicity was among the first distributions obtained in heavy-ion runs at the LHC. Its importance comes from its connection to the initial energy density and the centrality of the collision. For example, in the most 0-5% central Pb-Pb collisions at $\sqrt{s_{NN}} = 2.76$ TeV, the multiplicity was estimated to be around 1600 in a pseudo-rapidity range $|\eta| < 0.5$. A good summary is given in figure.1.10 where the pseudo-rapidity density of the charged particles is presented as a function of collision energy in different systems (pp, p-A, A-A). The multiplicity, in this case, evolves by following a power law, as a function of the collision energy S_{NN}^{α} where $\alpha = 0.1$ for the case of pp and p-A (elementary systems) and α =0.16 in the case of A-A. The fast increase in A-A compared to the pp and p-A is probably because A-A can not be just a simple independent superposition of nucleon-nucleon interactions.

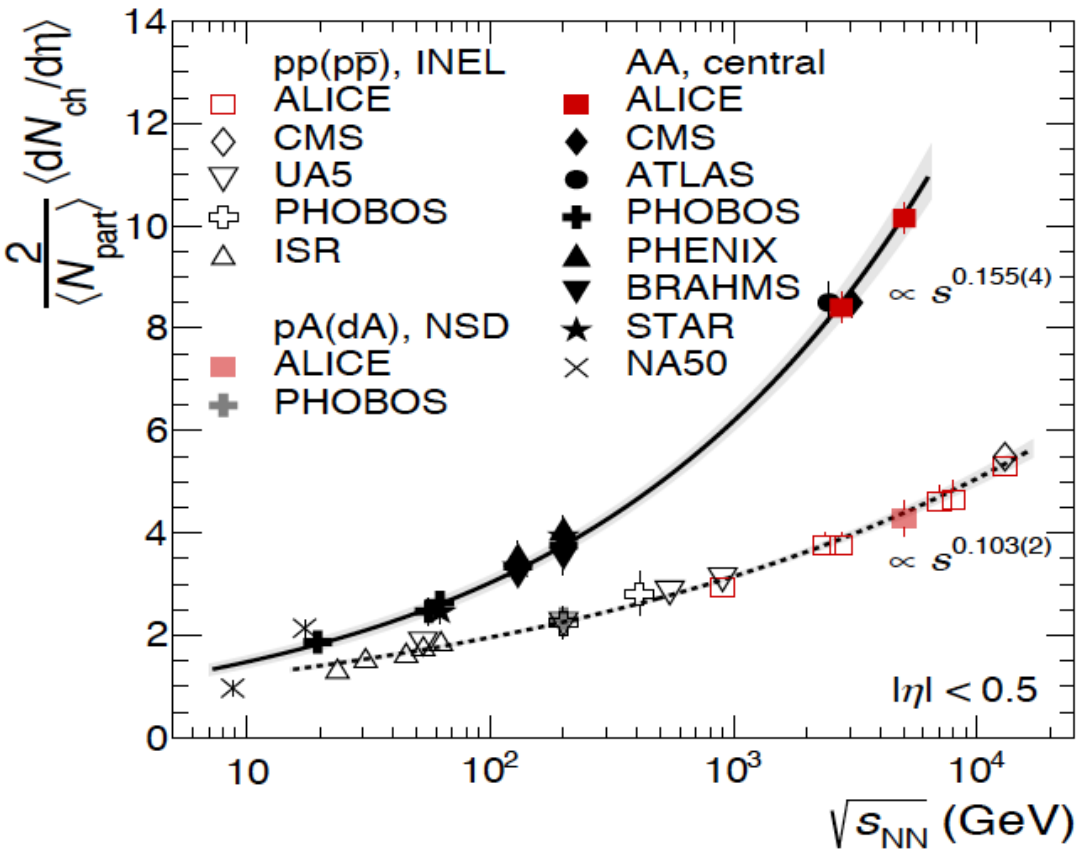

FIGURE 1.10: Pseudorapidity density of charged particles per participant pair as a function of the collision energy for different systems (pp,$p\bar{p}$, p-A, d-A, Pb-Pb, Au-Au) [13].

The $Transverse\ energy$ is another important observable exploited to determine the energy density using the "Bjorken hydrodynamic model" that is based on geometrical considerations. The transverse energy is associated to the energy density via the equation $\epsilon = (dE_T/d\eta)|_{\eta=0}/(A \times \tau_0)$ where A is the area of the overlap region where the collision of the 2 nuclei took place. τ_0 is the formation time of the partons. The energy density was estimated to be 12-14 GeV/fm^3 in Pb-Pb collisions at $\sqrt{s_{NN}}$ =2.76 TeV at the LHC which is 2-3 times larger than the reported value at RHIC.

$Initial\ temperature$ is estimated when the QGP is in equilibrium through the electromagnetic probes (for instance photons). Due to their weak interactions with the created medium in heavy-ion collisions, photons can provide information on the early stage of the collisions. The interesting photon spectrum is obtained after subtracting the background. After that, a fit is performed by taking advantage of the NLO pQCD calculations. In Pb-Pb collisions at $\sqrt{s_{NN}}$ =2.76 TeV, an effective initial temperature was estimated to be around 297 MeV which is above the critical temperature 160 MeV. While in other calculations where more restrictions and consideration were taken into account, the initial temperature was estimated to be in the interval 350-700 MeV [13].

$Size\ of\ the\ QGP$, very important observable for which information can be extracted through the space-time evolution of the created fireball using the technique called "identical pion interferometry" or "Hanbury-Brown Twiss (HBT) correlations". In the 5% most central Pb-Pb collisions at $\sqrt{s_{NN}}$ =2.76 TeV, the volume at kinetic freezeout is approximately 5000 fm^3 which is twice larger than the evaluated volume at RHIC. It was noticed that the volume of the fireball increases as a function of multiplicity.

1.3.2 Evolution of the collision

The different stages of the collisions have similar aspects in comparison to the evolution of the universe from the big bang until the formation of galaxies, except that in colliders the evolution is much faster and the resulting product are much smaller, however, the beginning was with a similar matter, created in each case due to a different cause.

Due to the principle of the length contraction from special relativity and at relativistic velocities, the two incoming colliding nuclei are considered as two Lorentz contracted disks. The typical value of the diameter of nuclei like Pb or Au is about 14 fm while the thickness is near 14/γ, with γ (Lorentz relativistic factor) about 100 and 2500 at RHIC and the LHC, respectively [22]. Each of the two incoming disks, includes within it coloured quarks, antiquarks and gluons, or in other words, partons, distributed in the nucleons according to some structure functions.

When the collision occurs between the two disks (see figure.1.9), the partons undergo a partial energy loss. Consequently, a transverse momentum transfer, as well as colour charge exchange, take place at the parton level. This gives rise to longitudinal colour fields between the two disks as they recede which leads to an energy reduction of the disks and a small fraction of partons undergo hard interactions.

Due to the length contraction in ultra-relativistic collisions, a dense gluon field is generated which leads in turn to the production of a strongly interacting medium in a small volume and high energy density. The energy density as estimated by the LHC at the very beginning, after the collision, is about 12 GeV/fm^3 that is 20 times larger than hadrons density. In such density, quarks and gluons are strongly coupled with the medium (QGP) and they are not attributed to a specific hadron. In small systems like p-p collisions, the creation of such deconfined medium is not supposed to happen and if it does, it is expected to be smaller in volume.

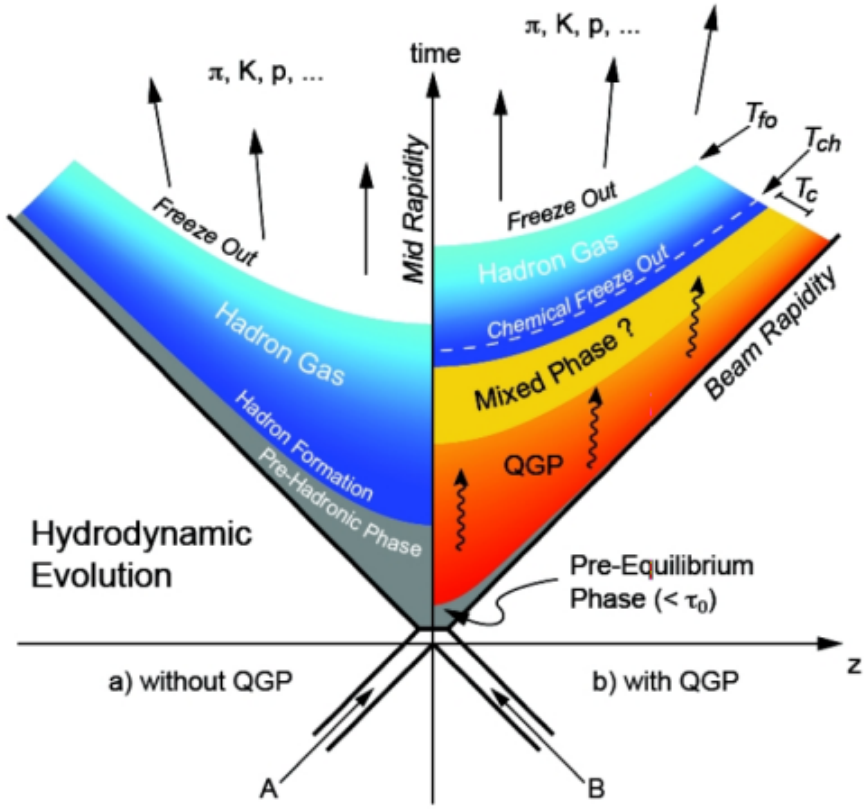

FIGURE 1.11: Space-time evolution of heavy-ion collisions with QGP (right) and without QGP (left).

This strongly interacting matter or the QGP (see figure.1.11), expands and thermalises rapidly which causes a decrease in temperature till reaching the critical point (160 MeV) where hadronisation takes place. At this level, the hadron constitution is fixed which is referred to as the $chemical\ \ freezeout$ with an associated temperature (T_{ch}) near the critical one. The comparison between statistical models and data in Pb-Pb collisions at $\sqrt{s_{NN}}$ =2.76 TeV are in good agreement at baryochamical potential $\mu_B \approx 1$ MeV and at $T_{ch} \approx 156$ MeV.

After that, particles keep on interacting where their momentum exhibit a change several times till this interaction stops at a specific temperature T_{kin} where the kinematical properties are fixed for each produced particle which presents a stage called $kinetic\ \ freeze-out$ [13]. The predictions from the hydrodynamics-inspired blast-wave models compared to the experimental data led to the extraction of the associated temperature T_{kin}= 96 MeV similar to the one extracted at RHIC. A more complete theoretical treatment of hydrodynamical evolution of heavy-ion collisions can be found in [23] where medium properties were reported by emphasising on the elliptic flow v_2, the viscosity, the ratio η/s.

1.4 Heavy flavour production

The $charm$ quarks were discovered first through the charmonium which is a bound state of charm and anti-charm quarks and it is also referred to as heavy quarkonia. The discovery of the particle J/Ψ (charmonium) took place in p-Be collisions at the Brookhaven AGS and in e^+e^- collisions at the Storage ring SPEAR in Stanford at the same time during the "November revolution" [6]. Similarly, the $bottom$ quarks were discovered via the bound state bottomonium in the proton-nucleus at FNAL. The findings on open charm and open bottom hadrons came later. The neutral and charged open-charm, for instance, were observed in their hadronic decay channel in the SLAC SPEAR storage ring. As for open-bottom hadrons, they were observed through their semi-leptonic decay channel with the detectors CLEO and CUSB at the Cornell Electron Storage (CESR). The RHIC and LHC era has marked the role of open-charm and open-bottom as hard probes where higher energies of nucleus-nucleus collisions were reached. Before that, they were studied mainly in e^+e^- collisions via photoproduction and restricted by elementary particle physics only unlike heavy quarkonia which were studied and exploited extensively at the CERN SPS in fixed-target heavy-ion collisions.

The term heavy flavour was attributed to the quarks $charm$ and $bottom$ to distinguish them from the other quarks: up, down and strange. This is due to their heavier bare mass, m(charm)$\approx$ 1.28 GeV and m(bottom)$\approx$ 4.18 GeV not only in comparison to the lighter quarks but also in comparison to the QCD scale Λ_{QCD} ($\approx$ 0.2 GeV). This difference results in a production of heavy flavour pairs initially through a strong partonic scattering in ultra-relativistic proton-proton collisions which allows for a perturbative treatment in theoretical QCD calculations. Therefore, an important test of pQCD calculations can be obtained by taking advantage of such characteristics of heavy-flavours in p-p collisions. Moreover, the understanding of these baseline calculations, either from the theoretical side or the experimental one, is decisive before exploiting these heavy flavours as probes in heavy-ion collisions to investigate the properties of the created medium.

In short, the objective of the open heavy-flavour measurements, within experiments in both LHC and RHIC, incorporates the understanding and the exploitation of their properties in different collisional systems. In p-p collisions, the reference measurements to nucleus-nucleus collisions can be provided. They are of great importance since they can help to investigate the effects due to the presence of the dense and hot matter created in heavy-ion collisions. In addition to that and thanks to the properties of heavy-flavours, perturbative QCD calculations can be applied which symbolises a testing ground for QCD theoretical calculations. In p-nucleus collisions, effects due to cold nuclear matter (CNM) can be distinguished by using measurements in p-p collisions, not to mention that theoretical models parameterising CNM can be tested too. Other collisional systems can be exploited such as Cu-Cu which may help to investigate the system sizes of course by taking advantage of the p-p collisions measurements of open heavy-flavour as a reference.

In this part, the main interest is the production of heavy flavour hadrons, which can be resolved into three parts according to the pQCD approach.

- **initial conditions (non-perturbative).** are a reflection of Parton Distribution Function (PDF) that determines the momentum fraction x acquired by a parton from the original nucleon. The fraction x depends on Q^2 with Q the energy-momentum transferred when the interaction between two partons takes place. There is not only one PDF but several ones studied for different partons.
- **Partonic scattering cross-section (perturbative).** Perturbative QCD calculations are applicable at this stage. Heavy flavours can be created through the pair creation process (quark-antiquark annihilation and gluon fusion) at the Leading Order (LO) and gluon splitting and flavour excitation at the Next-to-Leading Order (NLO). Thestate-of-the-art calculations are performed at the fixed order with next-to-next-to-leading-logarithm resummation (FONNLL).
- **Fragmentation of heavy quarks into heavy-flavour hadrons (non-perturbative).** where two situations are distinguished:
    1. A heavy flavour is bound with a light quark and fragment to form an open heavy flavour hadron whose energy is determined based on the energy of the initial heavy-quark through the $fragmentation\ function$. These functions are supposed to be universal whatever the production mechanism and they are measured in $e^+ - e^-$ reactions.
    2. A heavy quark is bound with its anti-quark and fragmentation takes place to form a quarkonium where 1-2% of the created heavy flavour pairs form quarkonium rather than the production of 2 separate hadrons [12].

The production of heavy flavours takes place via the processes of Flavour Creation (FCR), Flavour Excitation (FEX) and Gluon Splitting (GSP). The Leading Order (LO) is symbolised by flavour creation which can be either through the quark-antiquark annihilation $q\bar{q} \rightarrow Q\bar{Q}$ or gluon fusion $gg \rightarrow Q\bar{Q}$, where $q/\bar{q}$ are generic quarks and $Q/\bar{Q}$ is the produced heavy-quark pair. As for the Next-to-Leading Order (NLO), flavour excitation takes place when a gluon from an incoming nucleon splits into a heavy flavour pair $Q\bar{Q}$ and one of this pair undergoes a hard scattering with a generic parton $qQ \rightarrow qQ$. Gluon splitting takes place in the final state after a normal hard scattering of 2 partons. The example diagrams of these processes are presented in figure.1.12. These production channels of heavy flavours can be separated using a Monte Carlo event generator based on parton shower in order to distinguish the contribution of each process as a function of p_T. An example study, performed with Herwig at RHIC and LHC energies, can be found in [24].

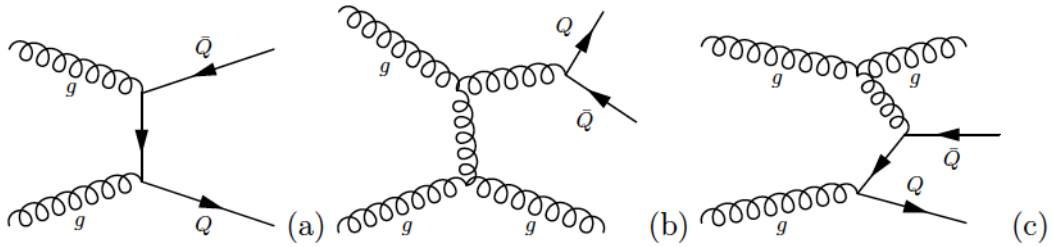

FIGURE 1.12: Example of 3 hard scattering processes of heavy flavour production (a) Pair Production (b) Gluon Splitting (c) Flavour Excitation [25].

Heavy flavours were studied in different collaborations at different energies and collisional systems. Interesting theoretical studies on charm and bottom quarks production at the LHC were held [26] where approaches like MC@NLO [27] and POWHEG [28] coupled with either PYTHIA [29] or HERWIG [30] were used to obtain the theoretical predictions and they were compared to the first measurements of heavy flavours in pp collisions at 7 TeV at the LHC.

Apart from the heavy-flavour production mechanisms, several other studies aimed to compute the fragmentation fractions of heavy quarks i.e. the probability for a charm (or bottom) to fragment into charmed hadrons. For example, one can mention the study that was driven at LEP [31] [32] and the one within ZEUS collaboration at HERA [33] where fragmentation fractions of charm quarks into the mesons D^0, D^+, D_s, D^{*+} and the baryon Λ_c were determined as well as the fraction of b quarks that fragment into charmed hadrons. A general study concerning this topic in more details and inputs from different collaborations and energies can be found in [34] where several heavy meson species were included. In a different perspective, the heavy flavour can also be studied through CP violation and rare decays of heavy mesons as it was done in [35] where the obtained experimental results with LHCb, ATLAS and CMS detectors were consistent with the predictions from the Standard Model.

An example of interesting analyses performed at the Tevatron can be checked in [36] where the first data in Run 1 and 2 were collected and analysed by CDF and DO collaborations. Both charmed and bottom hadrons (open and hidden heavy flavours) were reconstructed and several experimental observables were compared to those predicted by the theoretical calculations. Among the observables, one can mention the differential cross-section, lifetime decay, fragmentation fractions and so on. More insights on heavy flavour can be found in the generalised proceedings/papers [37] [38] [39] [40] [41] or workshop discussion [42]. The next parts will be dedicated to the presentation and discussion for some of the interesting analysis results performed on heavy-flavour production in different experiments and collisional systems.

1.4.1 Heavy flavour production in proton-proton collisions

At LHCb Collaboration, the production cross-section of B mesons was obtained as a function of the transverse momentum in a kinematical range down to 0 GeV/c and up to 40

GeV/c in a rapidity range $2 < y < 5$ as represented in black solid line in the left panel of figure.1.13. The experimental cross-section was compared to the predictions from FONLL and more precisely the upper and the lower uncertainty limits represented by the 2 dashed red lines. An agreement is established between the predictions and measurements. For a better visualisation of the agreement, the p_T range was narrowed to [0-12] GeV/c as presented in the right panel of figure.1.13.

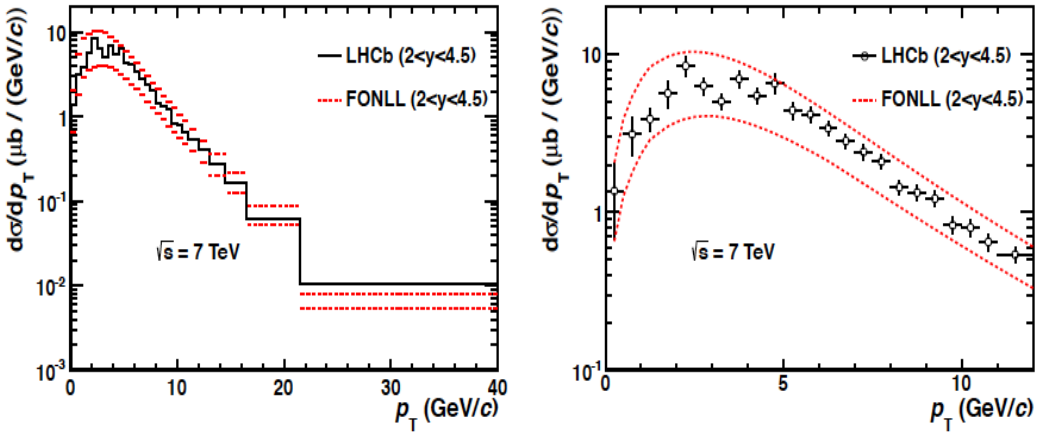

FIGURE 1.13: Left : $B^{\pm}$ differential production cross section in p-p collisions at 7 TeV with LHCb experiment (black solid line) versus the theoretical prediction from FONLL (red dashed line). Right : Same as the left plot but for a p_T range up to 12 GeV/c [43].

Prompt charm was studied in p-p collisions with the LHCb detector at $\sqrt{s} = 5$ TeV [44], 7 TeV [45] and 13 TeV [46] through the measurement of the differential cross-section of open heavy flavours represented by the D meson species $D^0/\bar{D}^0$, $D^{\pm}$, $D^{*\pm}$ in different p_T ranges and for the rapidity range $2 < y < 4.5$. The comparison to the theoretical predictions from the NLO QCD calculations were performed and they were found to be in agreement within uncertainties despite the fact that the central values lie below the data generally. Hidden heavy flavours, such as J/Ψ, were also reconstructed within LHCb Collaboration [47] where the differential cross section was obtained for prompt J/Ψ ($c \rightarrow J/\Psi$) and non-prompt J/Ψ ($b \rightarrow J/\Psi$) and have been compared to models. An agreement was observed especially for the differential cross-section of non-prompt J/Ψ between the measurements and FONLL predictions.

B mesons are studied also via their semi-leptonic decay [48] within ALICE collaboration in p-p collisions at 2.76 TeV where the cross-section of electrons coming from the decay of B mesons was computed and compared to the theoretical predictions from FONLL, GM-VFNS and k_T factorisation. An agreement is established between theory and data within uncertainties as presented in the figure.1.14.

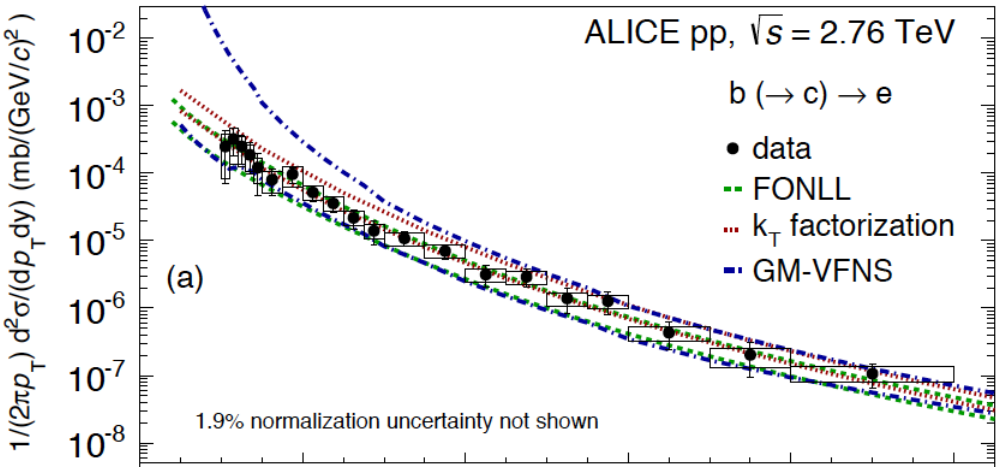

FIGURE 1.14: p_T-differential cross-section of electrons coming from the decay of B mesons in pp collisions at 2.76 TeV with ALICE detector (black closed dots) versus theoretical predictions from FONLL (dashed green lines), GM-VFNS (blue dot-dashed lines) and k_T factorisation (red dotted lines) [48].

ALICE Collaboration has studied charmed mesons in p-p collisions at 2.76 TeV [49] through the measurement of the p_T-differential production cross-section of prompt D^0, D^+ and D^{*+} in the kinematical range $1 < p_T < 12$ GeV/c and the rapidity range $|y| < 0.5$. The pQCD calculations describe qualitatively well the data (figure.1.15). However, the Fixed-Order Next-to-Leading Logarithm FONLL [50] (GM-VFNS [51]) underestimates (overestimates) the data. GM-VFNS refers to the General Mass Variable Flavour Number Scheme which is a parton model based on NLO calculations with finite-mass effects in order to improve the theoretical descriptions at low p_T. While FONLL refers to the Fixed-Order Next-to-Leading Logarithm and it is based on the QCD calculations at the NLO matched with the resummation of all orders from the Next-to-Leading Logarithm NLL.

Within ALICE collaboration also, the D^{*+}, D^0, D^+ mesons differential cross-sections were deduced in p-p collisions at 7 TeV [52] in the p_T range $1 < p_T < 24$ GeV/c and $|y| < 0.5$ where the data is reasonably described by the theoretical predictions from FONLL and GM-VFNS within uncertainties. More detail can be checked in [53] concerning the performed comparison between the calculated production cross-section of D^0, D^{*+} and D^+ with ALICE experiment [52] and the theoretical predictions from NLO GM-VFNS.

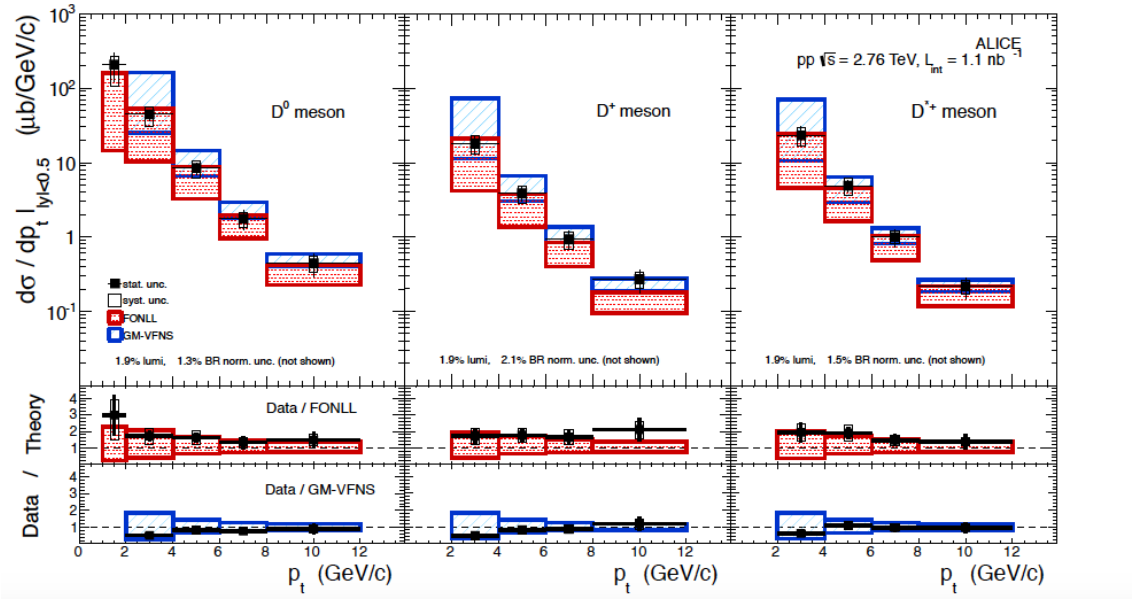

FIGURE 1.15: p_T-differential production cross-section of the prompt mesons : D^0, D^+ and D^{*+} in p-p collisions at 2.76 TeV with ALICE detector (black squares) versus the theoretical calculations from FONLL (red squares) and GM-VFNS (blue squares) [49].

The performed analyses in [52] were repeated in [54] in order to improve some aspects. The meson D_s^+ is included in the analysis in addition to the previous 3 non-strange D mesons. The p_T range was extended, the uncertainties were reduced and one more calculation from theoretical predictions was added (LO k_T fact). D^0 mesons were reconstructed in the kinematical p_T range $0 < p_T < 36$ GeV/c, D^+ and D^{*+} in $1 < p_T < 24$ GeV/c and D_s^+ in $2 < p_T < 12$ GeV/c. An example of the computed p_T differential production cross-section compared to the theoretical models is displayed in figure.1.16 for D_s^+ in the left panel and D^{*+} in the right panel. The data are well described by the FONLL and GM-VFNS models. However, the LO k_T describes the data only qualitatively.

In a recent study within ALICE collaboration [55], analyses were performed in pp collisions at 5.02 TeV. The same D meson species were considered as in [54]. Among the interesting conclusions, one can state the compatibility of the cross-section of D mesons computed in pp collisions at 5.02 TeV compared to those in pp collisions at 7 TeV within uncertainties.

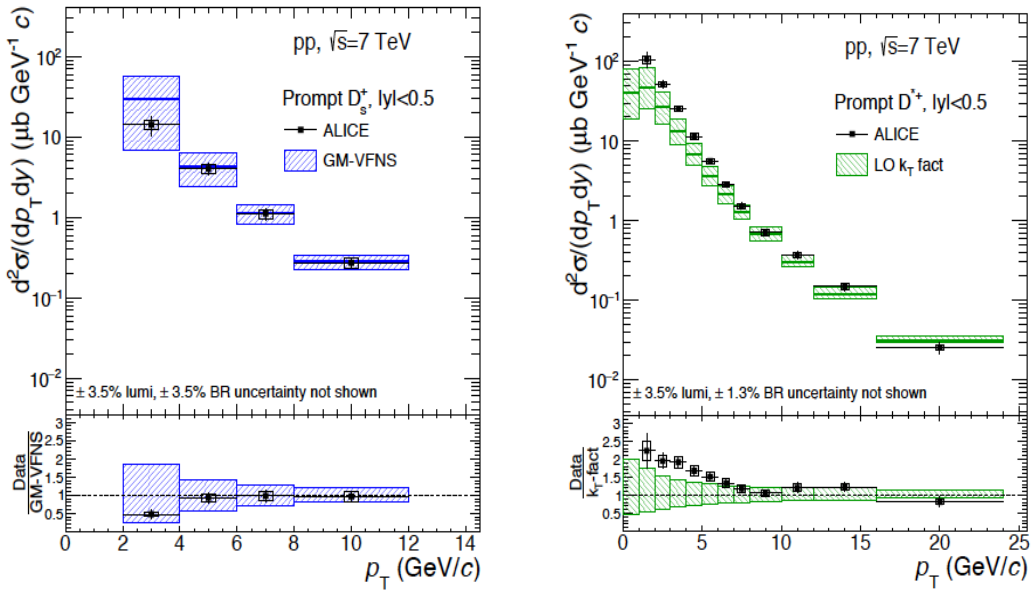

FIGURE 1.16: p_T-differential production cross-section of the prompt mesons : D_s^+ (left panel) and D^{*+} (right panel) in p-p collisions at 7 TeV with ALICE detector (black squares) versus the theoretical predictions from GM-VFNS (blue dashed squares) and LO k_T fact (green dashed squares) [54].

Within the ATLAS collaboration, heavy flavours were studied too. An example can be found in [56] where D mesons ($D^{*\pm}$, $D^{\pm}$, $D_s^{\pm}$) were reconstructed in p-p collisions at 7 TeV in the p_T range $3.5 < p_T < 20$ GeV/c and the pseudo-rapidity range $|\eta| < 2.1$. Within these kinematical intervals, the differential production cross-section for both $D^{*\pm}$ and $D^{\pm}$ was calculated as presented in figure.1.17. The top panel shows the cross-section for $D^{*\pm}$ and the bottom one for $D^{\pm}$. From these distributions, the theoretical predictions seem to reproduce qualitatively well the data but it lies below them, unlike FONLL and POWHEG which reproduce the data within large theoretical uncertainties. POWHEG is a framework dedicated for the implementation of the Next-to-Leading-Order (NLO) with Parton showers (PS).

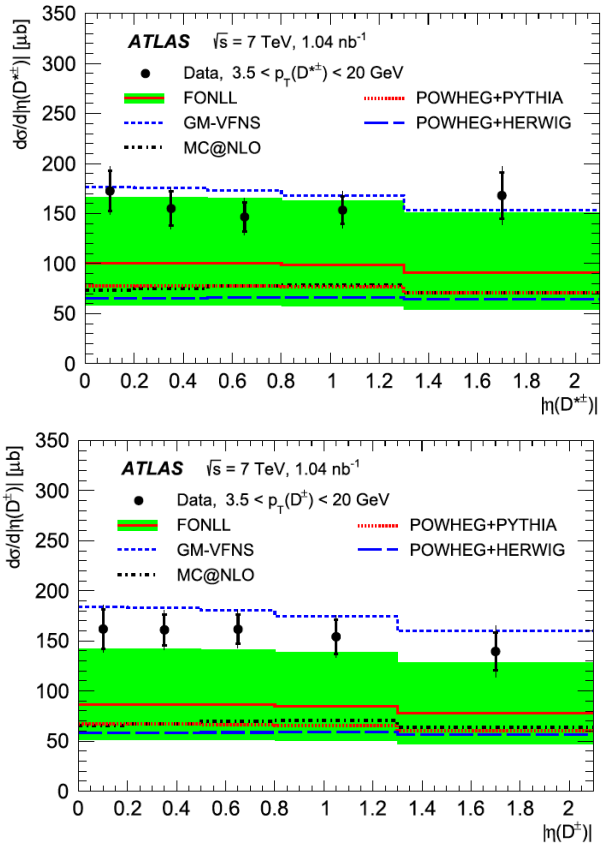

FIGURE 1.17: Differential production cross-section of $D^{*\pm}$ (top) and $D^{\pm}$ (bottom) as a function of $|\eta|$ computed in p-p collisions at 7 TeV with ATLAS detector (black points) versus calculations from different theoretical calculations [56].

In the PHENIX Collaboration [57], heavy flavour mesons (D and B) were studied through their semi-electronic decay channel where the production cross-section of heavy flavour electrons was calculated in p-p collisions at $\sqrt{s}$ =200 GeV and compared to the theoretical predictions from FONLL. Although the data is a bit higher than the theoretical prediction, the two agree qualitatively well, as can be seen in figure.1.18.

An example of $c\bar{c}$ production cross-section obtained from the measurements of D^*, D^0 mesons within STAR collaboration can be found in [58]. The cross-section from the experiment was found to match the upper bound of FONLL calculations and a better agreement was established with PYTHIA down to 2 GeV/c as shown in figure.1.19.

At the Tevatron within CDF Collaboration, heavy flavours were also analysed, precisely the heavy mesons D^{*+}, D^+ and D^0 produced in $p\bar{p}$ collisions at 1960 GeV. The performed comparison of the inclusive cross-section obtained from the data versus the theoretical predictions shows a general agreement within the theoretical uncertainties band [59] [60].

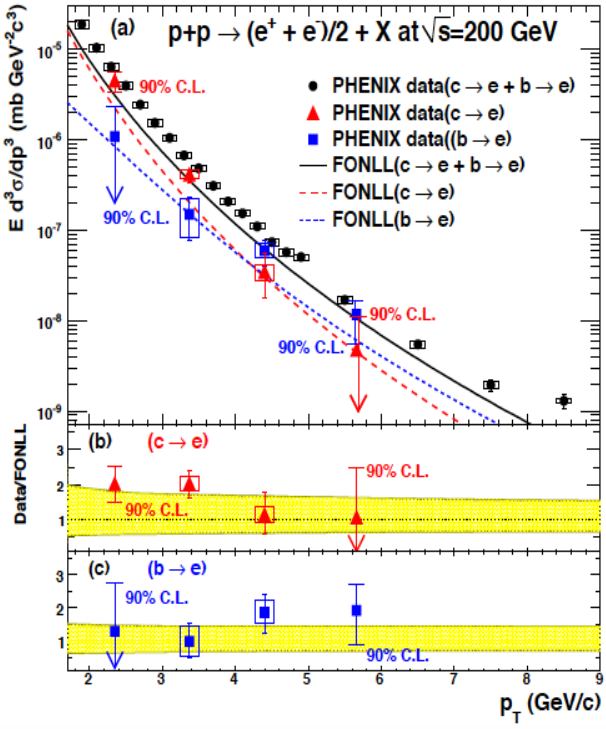

FIGURE 1.18: Top panel: The invariant cross-section of electrons from charm mesons and bottom mesons reconstructed within PHENIX collaboration (black points) versus FONLL predictions (dashed line). Middle panel: Ratio of data to FONLL for charm. Bottom panel: Ratio of data to FONLL for bottom [57].

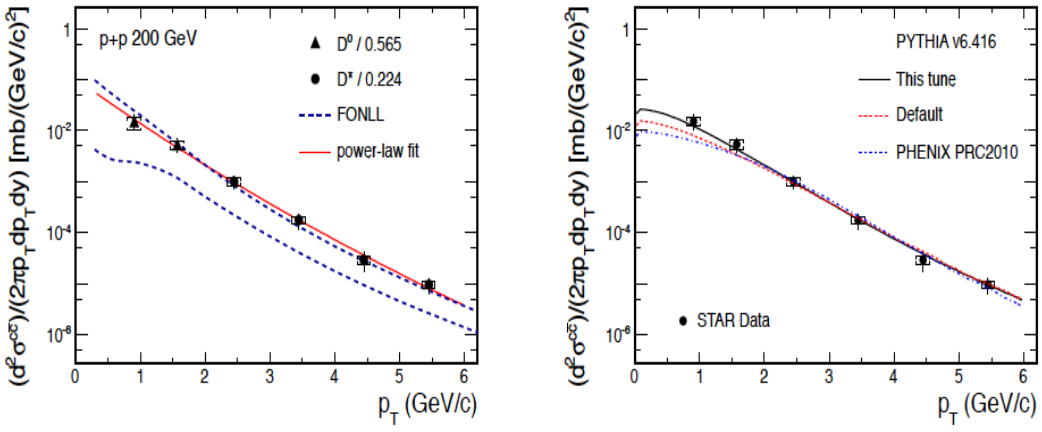

FIGURE 1.19: Left: The production cross-section of $c\bar{c}$ deduced from D^0, D^* production in p-p collisions at 200 GeV with STAR detector (points) versus FONLL predictions (lines). Right: same as the left panel but versus PYTHIA predictions [58].

1.4.2 Heavy flavour production in proton-Nucleus collisions

Concerning heavy flavour in p-nucleus collisions, several studies were performed in different collaborations. With ALICE detector, heavy flavour mesons were studied and the

cross-section was computed in p-Pb collisions at 5.02 TeV at mid-rapidity in the p_T range 1 $< p_T <$ 24 GeV/c for the mesons D^0, D^+, D^{*+} and in the p_T range 2 $< p_T <$ 12 GeV/c for the meson D_s^+ [61].

The obtained distributions for the cross-section are presented in figure.1.20 for the mesons D^{*+} (top left), D^+ (top right), D^0 (bottom left), D_s^+ (bottom right) presented in red filled diamonds and compared to the scaled cross-section obtained in p-p collisions at 7 TeV (blue filled squares).

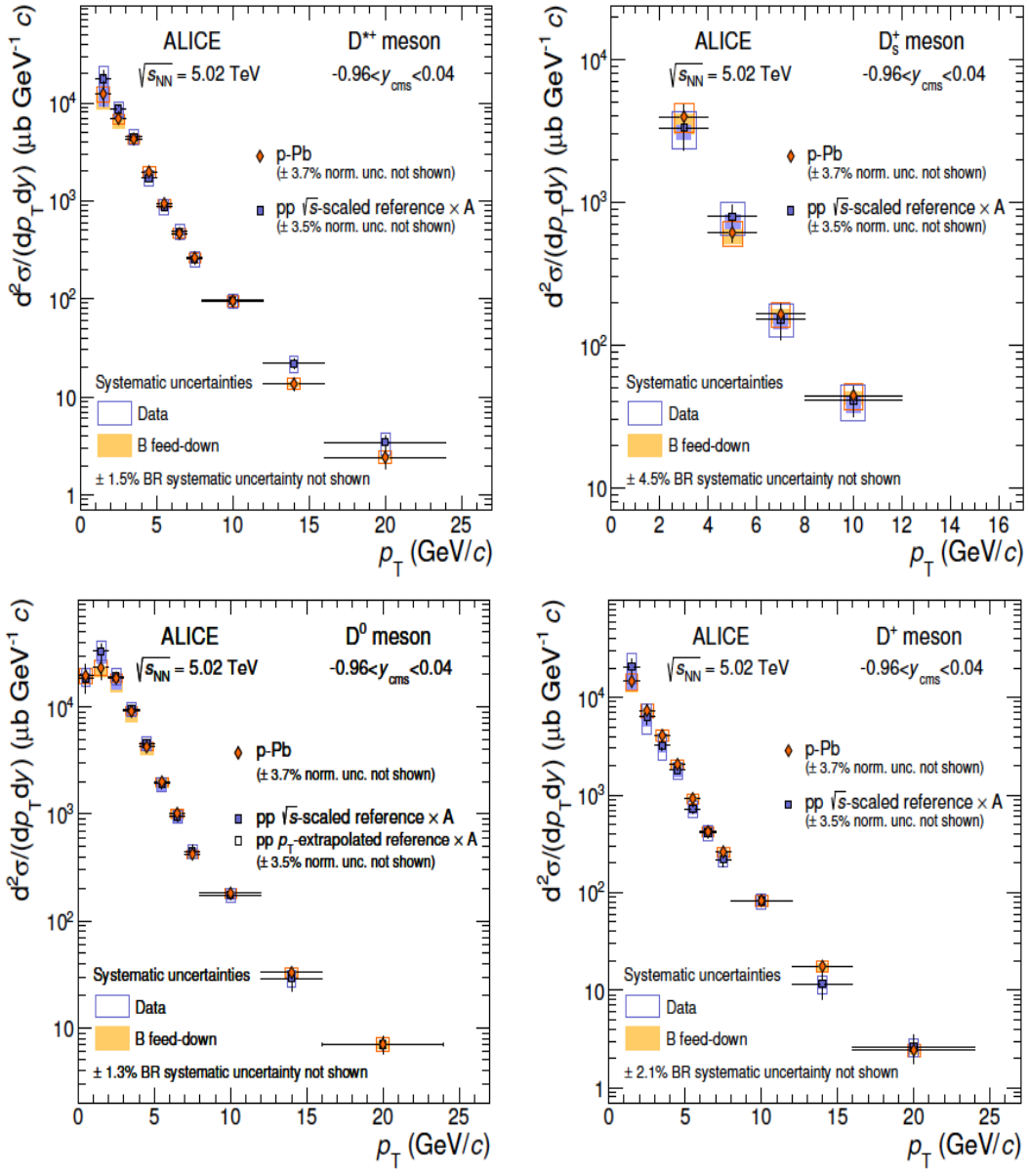

FIGURE 1.20: p_T-differential production cross-section of D^{*+} (top left), D^+ (top right), D^0 (bottom left), D_s^+ (bottom right) in the rapidity range - 0.96 $< y_{cm} <$ 0.04 in p-Pb collisions at 5.02 TeV (red filled diamond) versus the scaled p_T-differential cross-section in p-p collisions at 7 TeV with ALICE detector [61].

From this comparison, one can see clearly that the behaviour of the mesons between the

two colliding systems is similar as a function of the transverse momentum. However, no quantitative agreement is established which is expected theoretically. This is probably due to the Shadowing effect which refers to the central nucleons being shadowed by the surface ones in the nucleus and that results in a smaller cross section. This phenomenon is expected to take place for the low x-region ($x < 0.1$) for example in p-Pb collisions which modifies the production of particles at low momentum at LHC energies [62].

The nuclear modification factor is an important observable to be exploited in proton-nucleus collisions and it is defined by the equation,

$$R_{pA} = \frac{1}{< N_{coll} >} \frac{dN_{pA}/dp_T}{dN_{pp}/dp_T} \tag{1.8}$$

where $< N_{coll} >$ is the number of binary collisions for a determined centrality class while dN_{pA}/dp_T and dN_{pp}/dp_T are the p_T-dependent differential yield of the considered particle species in p-A and p-p collisions, respectively. The importance of this observable comes from the definition itself because if this fraction is equal to one, this means that there is no modification in the production of D mesons in p-Pb compared to p-p collisions and if it is different than one, then D meson production is modified probably due to in-medium effects.

The nuclear modification factor R_{pPb} of D mesons was extracted in p-Pb collisions at 5.02 TeV as presented in figure.1.21. One can see that the nuclear modification factor is compatible with unity within statistical and systematic uncertainties. This is a hint that cold nuclear matter may not have an important impact on the production of D mesons in p-Pb collisions in comparison to their production in p-p collisions.

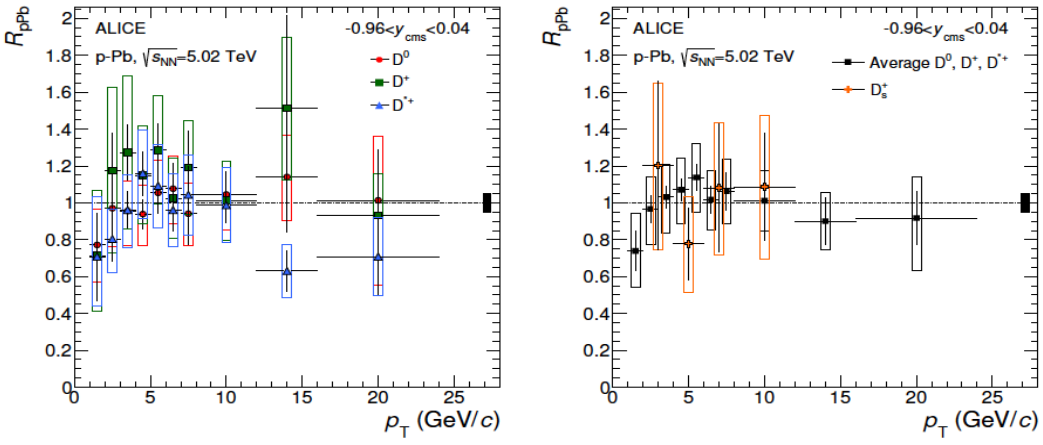

FIGURE 1.21: Left : Nuclear modification factor R_{pPb} of D^0 (red circles), D^+ (green squares) and D^{*+} (blue triangles) as a function of p_T in the rapidity range -0.96 $< y_{cms} <$ 0.04. Right : Nuclear modification factor R_{pPb} of the average D^0, D^+, D^{*+} (black squares) and of D_s^+ (orange crosses) [61].

Concerning the comparison of the computed nuclear modification factor versus models,

several approaches were considered as presented in figure.1.22 where the theoretical predictions provide an acceptable qualitative description to the data especially at some specific p_T range for some models. However, no firm conclusion can be deduced until the consideration of calculations and measurements with better precision.

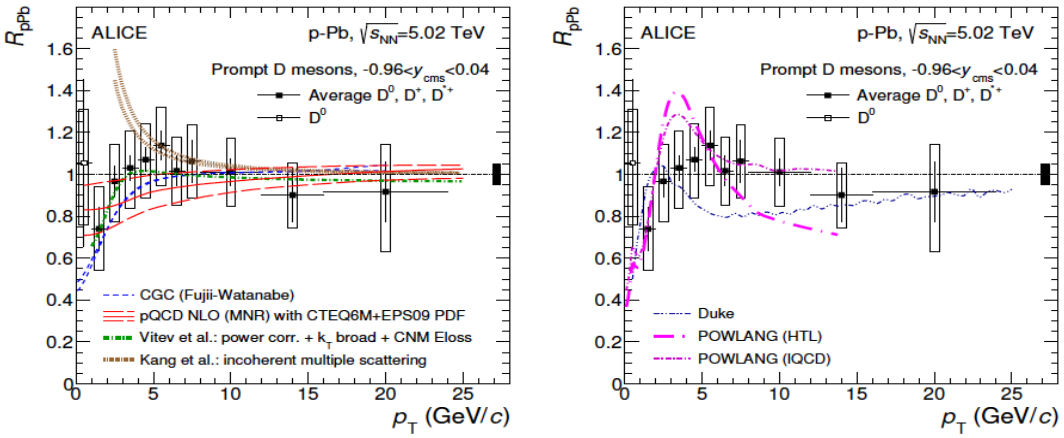

FIGURE 1.22: Nuclear modification factor R_{pPb} as a function of p_T in p-Pb collisions at 5.02 TeV with ALICE detector for the average D^0, D^+, D^{*+} (filled black squares) and D^0 (empty squares) versus predictions from different theoretical approaches : CGC (dashed blue line), pQCD NLO (triple red lines), Vitev et al (dashed green line), Kang et al (maroon thick line), Duke (dot-dashed blue thin line), POWLANG-HTL (dot-dashed pink line) and POWLANG-lQCD (dot-dashed thin line) [61].

An example of analysis involving quarkonium in p-Pb collisions can be found in [63]. The production of the J/ψ was studied in p-Pb collisions at the centre of mass energy $\sqrt{s_{NN}} = 5$ TeV with LHCb detector. These analyses were performed in a transverse momentum range up to 14 GeV/c. The production cross-section of J/ψ is calculated for the prompt J/ψ and non-prompt J/ψ as a function of the transverse momentum p_T in the forward and backward rapidity ranges $1.5 < y < 4.0$ and $-5.0 < y < -2.5$ as presented in the left and right panels of figure.1.23, respectively. The p_T-differential production cross-section of prompt J/ψ is presented in black circles and the one of non-prompt J/ψ in red squares. The cross-section of prompt J/ψ is larger than the cross-section of non-prompt J/ψ.

Figure.1.24 presents the calculated nuclear modification factor R_{pPb} of both prompt J/ψ (left) and non-prompt J/ψ (right) with LHCb detector in p-Pb collisions at $\sqrt{s_{NN}} = 5$ TeV as a function of the rapidity y compared to different theoretical predictions including cold nuclear matter effects where the agreement is established within uncertainties. One can see that the suppression is not different between the non-prompt J/ψ and prompt J/ψ. Indeed, at backward rapidity, they are almost equal while at forward rapidity the observed difference can be just a 1-2 sigma statistical fluctuations.

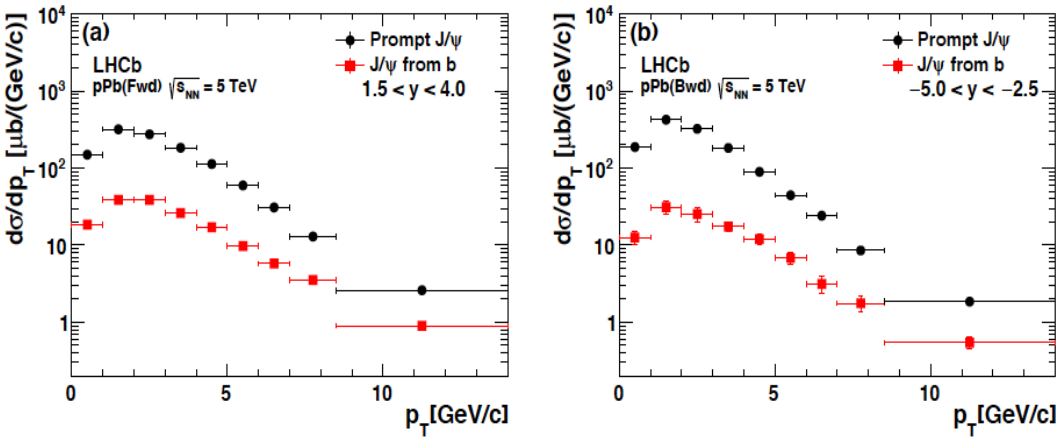

FIGURE 1.23: p_T-differential production cross-section in forward rapidity (left plot) and backward rapidity (right plot) for prompt J/ψ (black squares) and non-prompt J/ψ (red squares) in p-Pb collisions at $\sqrt{s_{NN}} = 5$ TeV with LHCb detector [63].

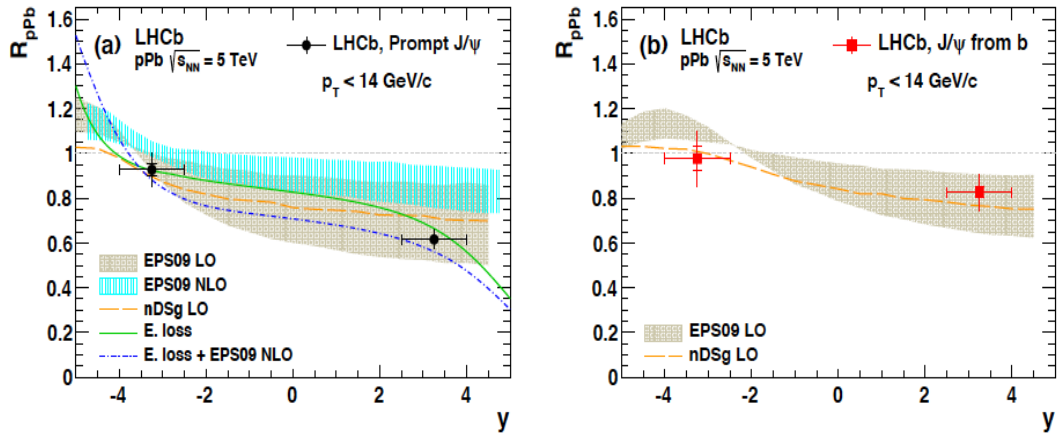

FIGURE 1.24: Nuclear modification factor R_{pPb} as a function of the rapidity in the range $p_T < 14$ GeV/c for prompt J/ψ (left) and non-prompt J/ψ (right) in p-Pb collisions at $\sqrt{s_{NN}} = 5$ TeV with LHCb detector versus the theoretical predictions : EPS09 LO (maroon band), EPS09 NLO (cyan band), nDSg LO (dashed orange line), E. loss (solid green line), E. loss + EPS09 NLO (dot-dashed purple line) [63].

The CMS Collaboration also has deduced the p_T-differential production cross-section of B mesons and the associated nuclear modification factor in p-Pb collisions at $\sqrt{s_{NN}} = 5.02$ TeV [64] in a transverse momentum range $10 < p_T < 60$ GeV/c and rapidity $|y_{lab}| < 2.4$ as presented in figure.1.25 and figure.1.26, respectively. For what concerns the cross-section, the data were compared to the theoretical predictions from FONLL where the latter seems to agree well with the data within uncertainties. As for the nuclear modification factor of B mesons, an agreement is established between the experimental measurements and the predictions from FONLL within systematic and statistical uncertainties of the measurements.

No suppression was observed concerning the production of B mesons since the nuclear modification factor of these B mesons is consistent with unity within the large systematic/statistical uncertainties. Consequently, no cold nuclear matter effect was observed.

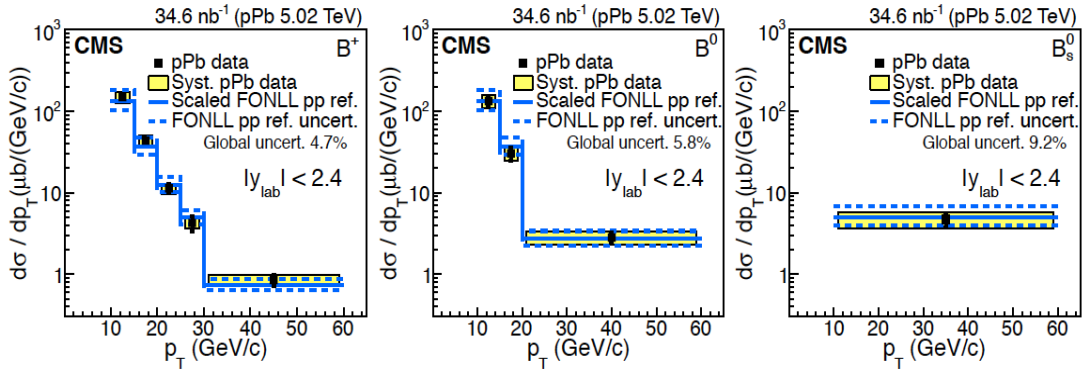

FIGURE 1.25: p_T differential production cross-section (black squares) of B^+ mesons (left), B^0 mesons (middle), B_s^0 (right) in the rapidity range $|y| < 2.4$ versus the theoretical predictions from FONLL (solid blue line) in p-Pb collisions at $\sqrt{s_{NN}} = 5.02$ TeV with CMS detector [64].

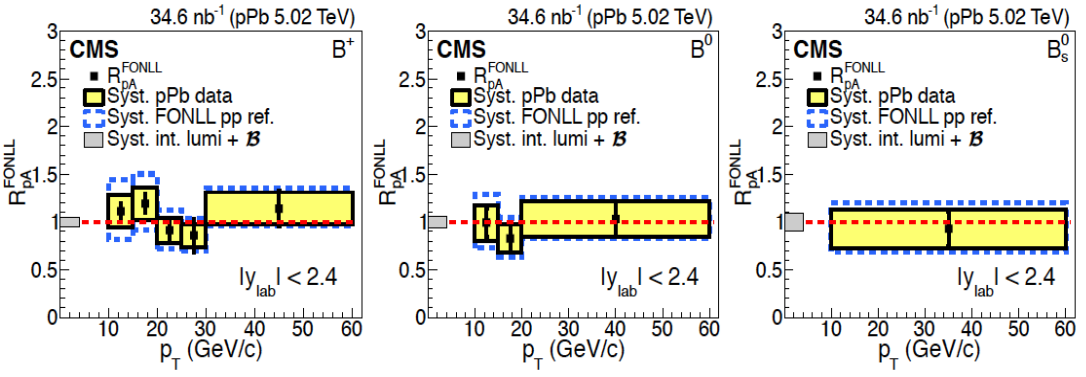

FIGURE 1.26: Nuclear modification factor R_{pPb} of B^+ (left), B^0 (middle), B_s^0 (right) as a function of the transverse momentum versus predictions from FONLL (black squares) [64].

1.4.3 Heavy flavour production in heavy-ion collisions

As in p-A collisions, the nuclear modification factor also can be exploited in heavy-ion collisions to study the differences that could take place compared to p-p collisions or even p-nucleus collisions. It is defined by the expression,

$$R_{AA} = \frac{dN_{AA}/dp_T}{< N_{coll} > \times dN_{pp}/dp_T} = \frac{dN_{AA}/dp_T}{< T_{AA} > \times d\sigma_{pp}/dp_T} \tag{1.9}$$

where dN_{AA}/dp_T is the differential yield of particles in A-A collisions. dN_{pp}/dp_T ($d\sigma_{pp}/dp_T$) is the differential yield (cross-section) of particles in p-p collisions. $< N_{coll} >$ is the number of binary collisions for a specific centrality class. $< T_{AA} >$ is the nuclear thickness (overlap) function.

As an example of measurements of the nuclear modification factor in heavy-ion collisions, one can cite the analysis performed at CMS collaboration [65] where both the cross-section and the R_{AA} of the prompt, non-prompt J/ψ and Υ(1S) were studied via their semi-leptonic decay channel ($\mu^+\mu^-$) in Pb-Pb collisions at the center-of-mass energy $\sqrt{s_{NN}} = 2.76$ TeV in the mid-rapidity range $|y| < 2.4$. Figure.1.27 presents the calculated cross-section (left column) and the nuclear modification factor (right column) of prompt and inclusive J/ψ (top and middle rows) as a function of the rapidity $|y|$ and N_{part} and non-prompt J/ψ (bottom row) as a function of N_{part}. Figure.1.28 presents the production cross-section (left column) and nuclear modification factor (right column) of Υ(1S) particles as a function of the transverse momentum p_T, the rapidity $|y|$ and N_{part}.

According to figure.1.27 and figure.1.28 for what concerns the prompt J/ψ, the cross-section is smaller at forward/backward rapidities compared to mid-rapidities and it also gets smaller with N_{part}. As for the nuclear modification factor, there is a clear large suppression at central collisions compared to peripheral ones. Concerning the non-prompt J/ψ, a suppression is also observed but it is not centrality-dependent. For the Υ(1S) as observed in figure.1.28, the cross-section decreases with p_T and the correspondent nuclear modification factor shows that the suppression in comparison to p-p collisions, is more pronounced at low p_T. Concerning the other observables, the suppression is important closer to mid-rapidity and more pronounced at the most central collisions (0-10%).

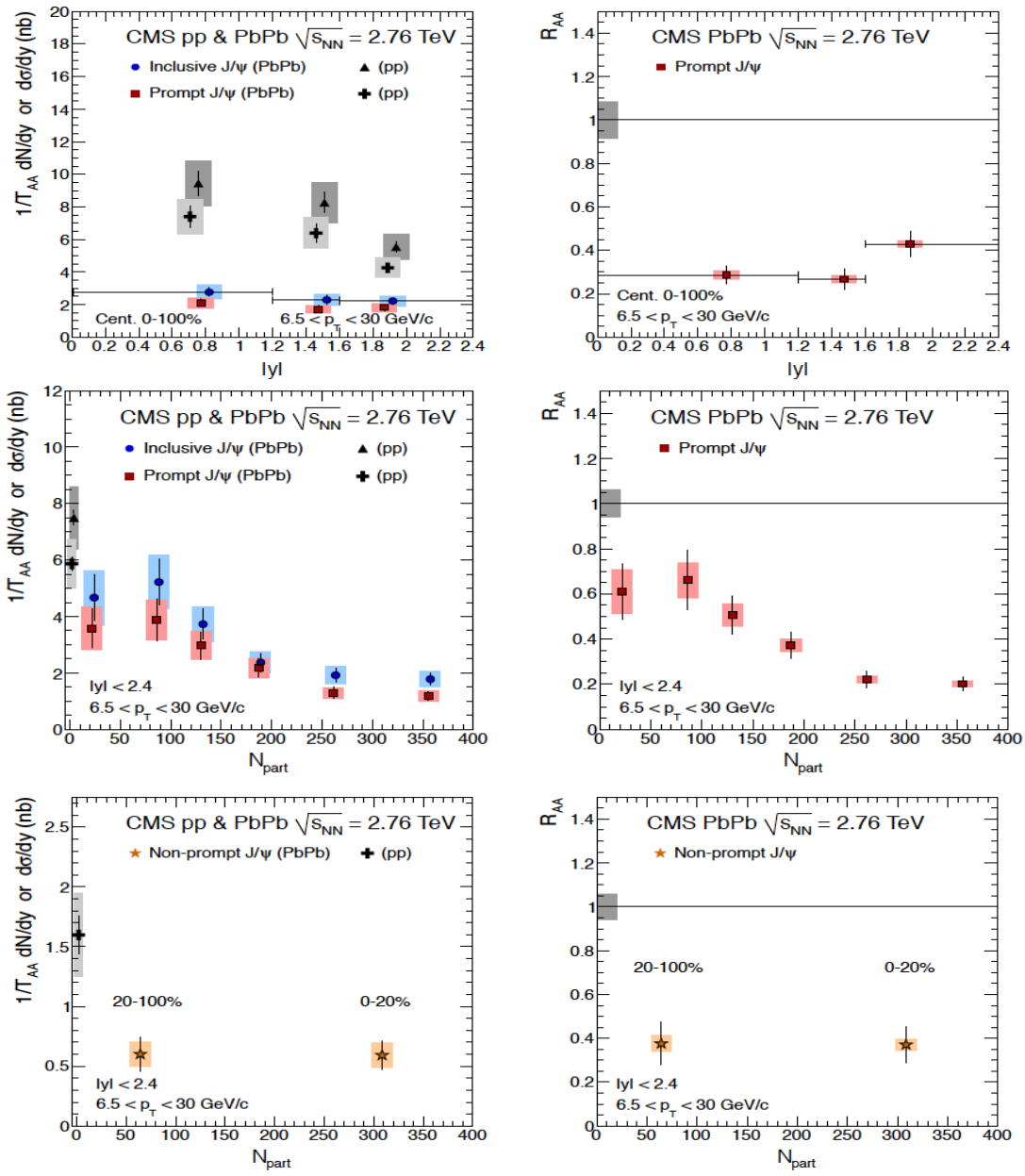

FIGURE 1.27: Top row : y-differential production cross-section of inclusive J/ψ and prompt J/ψ (left column) and R_{AA} (right column) of prompt J/ψ as a function of the rapidity y in Pb-Pb and p-p collisions at 2.76 TeV. Middle row : differential production cross-section (left column) and R_{AA} (right column) as a function of N_{part}. Bottom row : Differential production cross-section (left column) and nuclear modification factor R_{AA} (right column) of non-prompt J/ψ as a function of N_{part} [65].

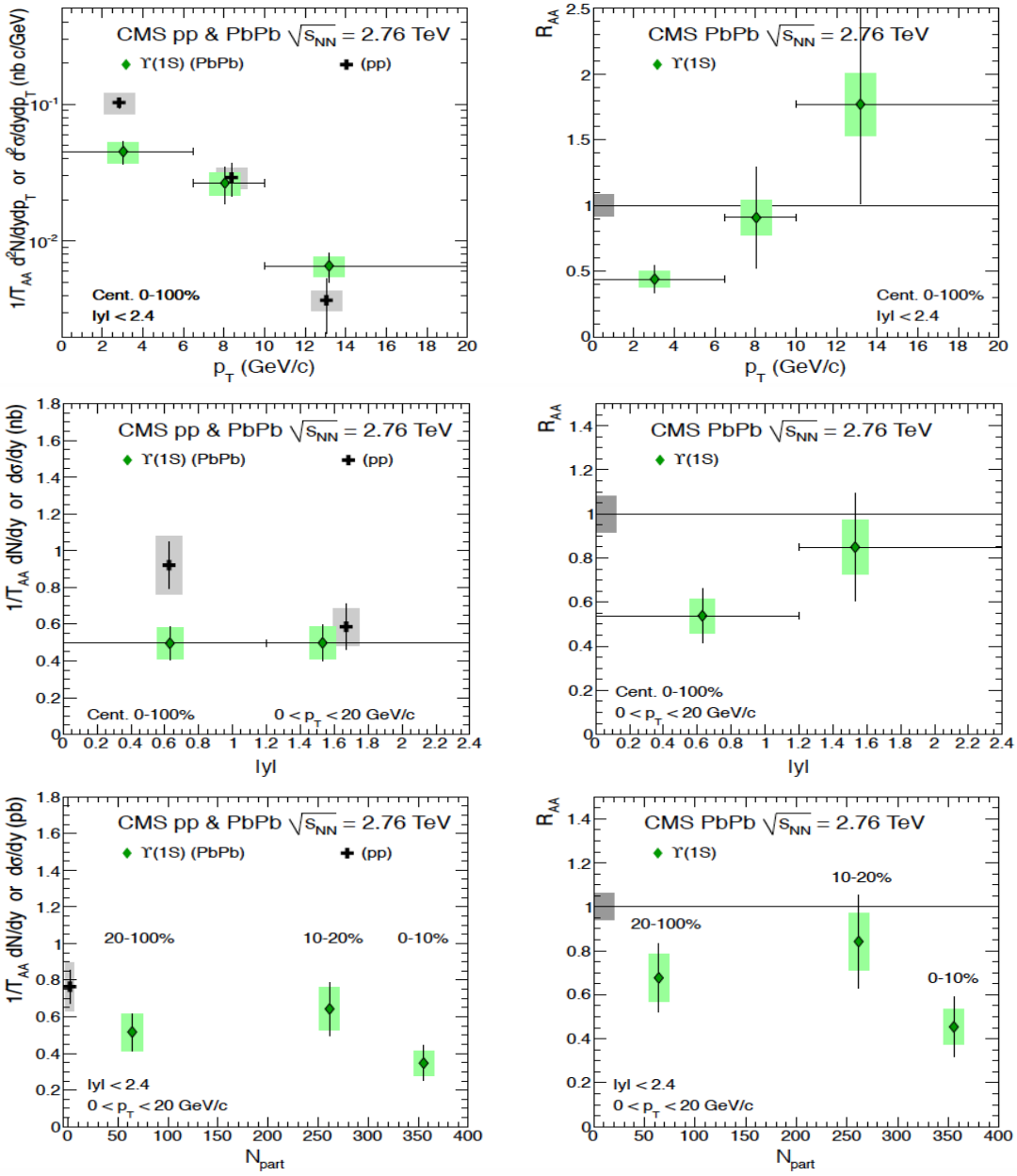

FIGURE 1.28: Left column : Differential production cross-section of Υ(1S) in Pb-Pb and p-p collisions at 2.76 TeV as a function of the transverse momentum p_T (top row), as a function of the rapidity y (middle row) and the Number of participating nucleons N_{part} (bottom row). Right column : Nuclear modification factor R_{AA} as a function of p_T (top row), y (middle row) and N_{part} (bottom row) [65].

Within CMS Collaboration, the nuclear modification factor of D^0 mesons was calculated [66] in Pb-Pb collisions at $\sqrt{s_{NN}} = 5.02$ TeV. D^0 mesons were reconstructed in the rapidity range $|y| < 1$ and the transverse momentum range $2 < p_T < 100$ GeV/c. It was found that the computed p_T-differential production cross-section of D^0 in p-p collisions at 5.02 TeV is in agreement within uncertainties with the predictions from FONLL and GM-VFNS as presented in the left panel of figure.1.29.

A comparison was performed between the p_T-differential production cross-section of D^0 mesons in pp collisions at 5.02 TeV and the one obtained in Pb-Pb collisions at the same energy for the centrality classes 0-100% and 0-10% as displayed in the right panel of figure.1.29. In both pp and Pb-Pb collisions (for both centrality classes), similar qualitative behaviour is observed.

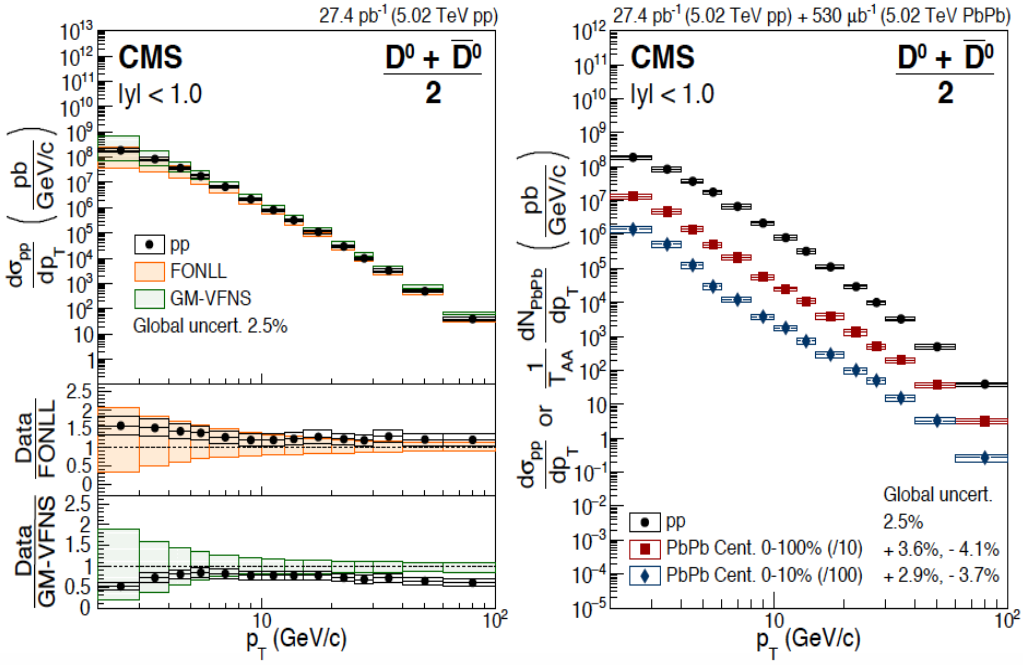

FIGURE 1.29: Left panel: p_T-differential production cross-section of D^0 mesons in pp collisions at 5.02 TeV (black filled circles) versus theoretical predictions from FONLL calculations (orange) and GM-VFNS (green). Right panel: p_T-differential production cross-section of D^0 mesons in pp collisions at 5.02 TeV (black circles) versus the scaled number of particles measured in minimum bias (0-100%) (red squares) versus the one scaled and measured in 0-10% most central collisions (blue diamonds) [66].

The extracted nuclear modification factor R_{AA} is presented in figure.1.30 for the centrality classes 0-100% in the left panel and 0-10% in the right panel. A comparison with respect to several models was performed. It is clear that the theoretical predictions reproduce the behaviour of the R_{AA} from CMS within uncertainties for intermediate p_T (10-40 GeV/c) for both centrality classes. For $p_T < 10$ GeV/c, PHSD predictions, that integrate shadowing and only collisional energy loss and adapt Boltzmann approach as a transport model, describe reasonably the data. As for the model based on Langevin calculations, it predicts more suppression compared to data. For $p_T > 40$ GeV/c, perturbative QCD-base models (labeled as M. Djordjevic, CUJET 3.0, I. Vitev) reproduce the data behaviour within uncertainties.

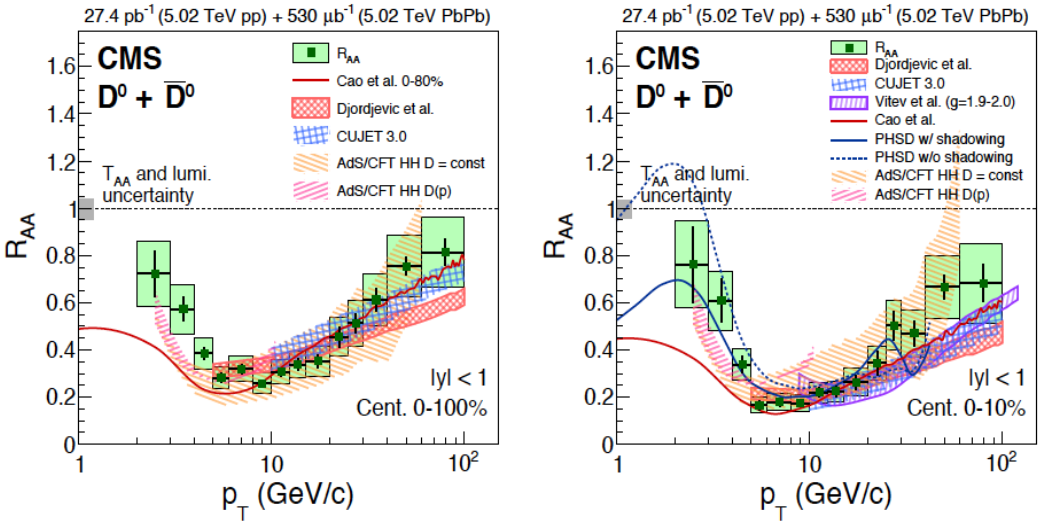

FIGURE 1.30: Nuclear modification factor R_{AA} of D^0 mesons as a function of p_T in Pb-Pb collisions at $\sqrt{s_{NN}} = 5.02$ TeV (green squares) in minimum bias 0-100% central collisions (left panel) and 0-10% most central collisions (right panel) versus different theoretical predictions [66].

ALICE collaboration has studied D_s^+ mesons through the extraction of the associated nuclear modification factor [67] in Pb-Pb collisions at $\sqrt{s_{NN}} = 2.76$ TeV as displayed in the left panel of figure.1.31 where the R_{AA} was obtained for two centrality classes 0-10% (orange crosses) and 20-50% (green diamonds). One can notice that the suppression of D_s^+ is more prominent at central collisions than at peripheral ones and it gets more important at larger p_T. This can be interpreted by the importance of in-medium effects in central collisions.

In the right panel of figure.1.31, a comparison was performed between the average D^0, D^+, D^{*+} (black circles), D_s^+ mesons (orange crosses) and the theoretical predictions from TAMU for non-strange D mesons and D_s^+ presented in black and orange solid lines, respectively. The predictions reproduce qualitatively the data and agree quantitatively only in some specific p_T ranges within uncertainties. For non-strange D mesons, the agreement is established up to 5 GeV/c otherwise the data are underestimated for $p_T > 5$ GeV/c. For D_s^+, there is an agreement up to 10 GeV/c.

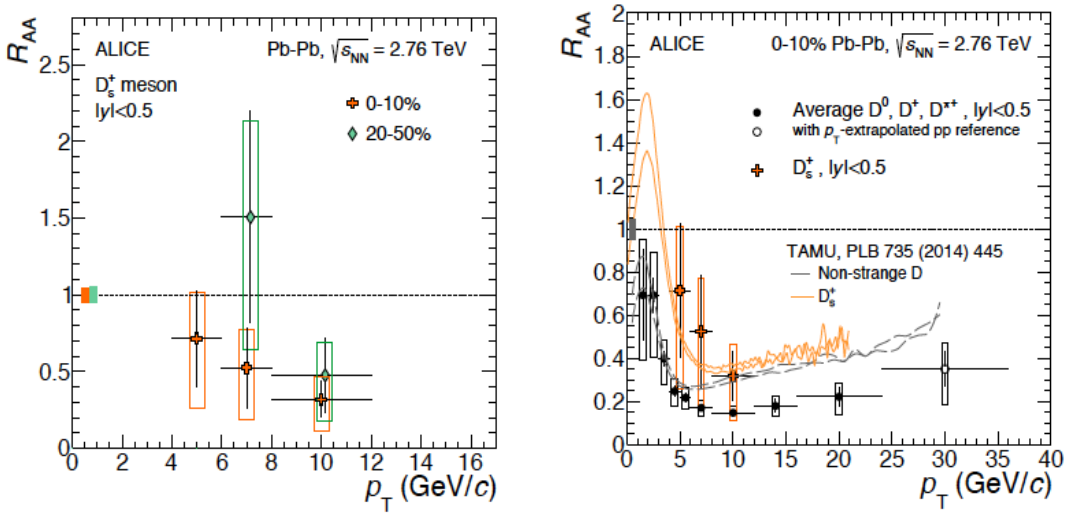

FIGURE 1.31: Left : Nuclear modification factor R_{AA} of D_s^+ mesons as a function of p_T in Pb-Pb collisions at $\sqrt{s_{NN}} = 2.76$ TeV with ALICE detector for 0-10% most central collisions (red filled crosses) and semi-peripheral collisions with 20-50% centrality (green filled diamonds). Right : Nuclear modification factor R_{AA} of D mesons : Average D^0, D^+, D^{*+} (closed black circles) and D_s^+ (red filled crosses) in the 0-10% most central Pb-Pb collisions at $\sqrt{s_{NN}} = 2.76$ TeV versus theoretical prediction from TAMU for Non-strange D mesons (black solid line) and D_s^+ (solid orange line) [67].

More results and discussions on some of the previous studies on heavy flavour productions at the LHC can be found in [68] where an interesting comparison was presented concerning the production cross-section of heavy quark pairs ($c\bar{c}$ and $b\bar{b}$) as displayed in figure.1.32. The interesting conclusion is the total production cross-section of $c\bar{c}/b\bar{b}$ pairs which was measured in different energies and experiments and it increases with increasing energy $\sqrt{s}$ at the center-of-mass frame. This trend is in agreement with the predictions from NLO (MNR) up to the upper bound.

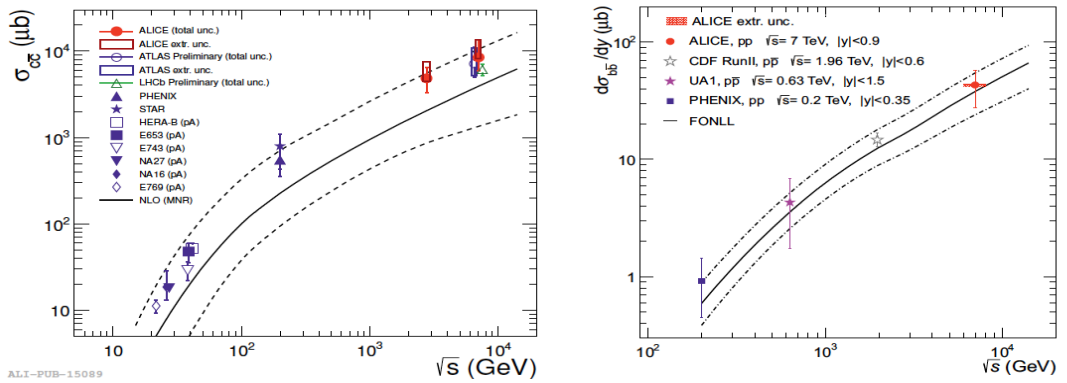

FIGURE 1.32: Left: Total production cross-section of $c\bar{c}$ pairs as a function of the energy $\sqrt{s}$. Right: Mid-rapidity production cross-section of $b\bar{b}$ pairs as a function of the energy $\sqrt{s}$ [68].

Among the theoretical analyses and models, one can mention the Parton-Hadron-String Dynamics (PHSD) exploited in [69] to study charm production in heavy-ion collisions. In this approach, the PYTHIA event generator is used to generate the initial charm p_T and rapidity spectrums to match those from FONLL. The Dynamical Quasi-Particle Model (DQPM) was exploited to compute the masses of the off-shell QGP partons as well as for the calculation of the cross-section. The nuclear modification factor and the elliptic flow extracted from this approach were compared to those obtained from STAR and ALICE collaborations in Au-Au/Pb-Pb collisions at $\sqrt{s_{NN}} = 200$ GeV and 2.76 TeV, respectively. The data are reproduced by the PHSD without considering the radiative energy loss since it was observed that the collisional energy loss is dominant up to 6 GeV/c and 15 GeV/c at RHIC and LHC, respectively.

Heavy mesons like $D^{*\pm}$ were studied for example in [70] within a theoretical framework where the inclusive production cross-section was computed as a function of the transverse momentum and the rapidity at the next-to-leading order by exploiting the massive and the massless charm quarks approaches and the realistic non-perturbative Fragmentation Functions. Although the experimental cross-section lies in the upper bound of the theoretical cross-section, a qualitative agreement is established between the theoretical and the experimental cross-section. The latter was calculated within CDF collaboration in $p\bar{p}$ collisions at 1.96 TeV.

Heavy flavours were also studied within other theoretical frameworks [71] for example the POWLANG package used as a transport setup of heavy flavours in the QGP plus simulating their hadronisation via string fragmentation by taking advantage of PYTHIA. The predictions of this improved model concerning the R_{AA}, v_2 and correlations (D-h, HFe-hadron) were compared to the experimental data from RHIC (STAR) in Au-Au collisions at $\sqrt{s_{NN}} =$ 200 GeV and LHC (ALICE) in Pb-Pb collisions at $\sqrt{s_{NN}} = 2.76$ TeV and they were found to be in a qualitative agreement. More details on the advancement in the sector of heavy flavours in heavy-ion collisions can be found in [72].

1.5 Heavy Flavour Correlations

Several studies in both experiment and theory were performed on correlations. This proves the crucial role of this observable in our understanding not only for what concerns the production mechanism of heavy flavours but also the thermalisation of heavy flavours within the created medium in heavy-ion collisions.

Among the studies held in this topic, one can mention what was done in [73] where the correlations of $D\bar{D}$ were studied as a function of $\Delta\phi$ for different initial transverse momentum values and different values of the drag coefficient. The correspondent distributions obtained in Au-Au collisions for $\sqrt{s}_{NN} = 200$ GeV are displayed in figure.1.33. The left and right columns present the distributions for the initial temperatures 300 MeV and 700 MeV, respectively. While the top and bottom rows present the distributions for different initial

transverse momentum and different drag coefficients, respectively. For different p_T values, one can see clearly that the distributions are more peaked toward $\Delta\phi = \pi$ when p_T gets larger. At low p_T, no correlation behaviour is observed. In the case of different drag coefficient values, the distributions are more peaked around $\Delta\phi = \pi$ for small drag coefficient values and the correlations are washed out when this coefficient gets larger. These observations can be explained by the fact that the absence of correlations might be a sign of the interaction of heavy flavour with the QGP created in Au-Au collisions which is a feature favoured at low p_T and large drag coefficient.

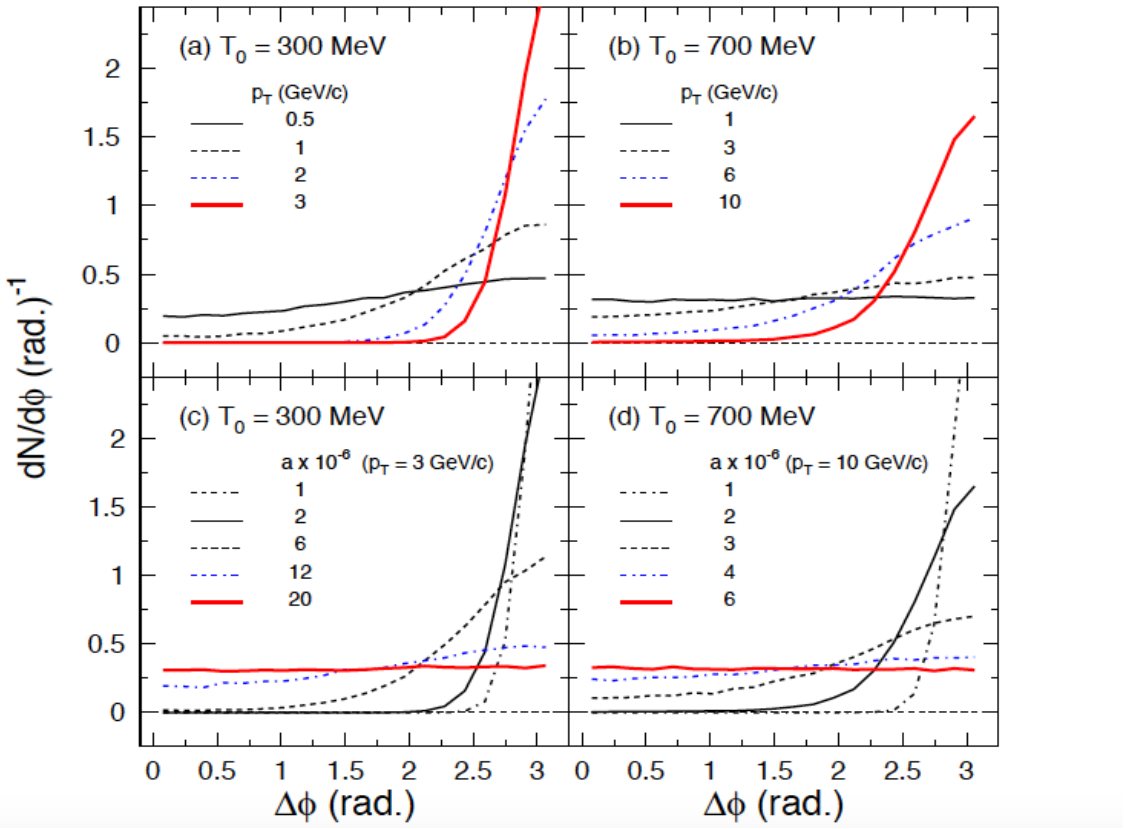

FIGURE 1.33: $D\bar{D}$ correlation distribution as a function of $\Delta\phi$ for the temperature $T_0 = 300$ MeV (a, c) and $T_0 = 700$ MeV (b, d) for different initial transverse momentum (top row) and drag coefficients (bottom row) [73].

In a different perspective [74], the effect of partonic wind - which is a consequence of the QGP formation - was studied via $D\bar{D}$ correlations obtained at RHIC energies in Au-Au collisions at $\sqrt{s_{NN}} = 200$ GeV and LHC energies in Pb-Pb collisions at $\sqrt{s_{NN}} = 5500$ GeV as presented in figure.1.34. These distributions were obtained for different drag coefficients a with the unit $[10^{-6}\ (\text{fm/c})^{-1}\text{MeV}^{-2}]$. At RHIC, 340 MeV and 0.6 fm/c were taken as initial temperature T_0 and thermalization time τ_0 while at LHC, the values 610 MeV and 0.3 fm/c were considered, respectively. According to the figure.1.34, correlations at RHIC energies are washed out when the drag coefficient is large enough. The large value of the drag coefficient here reflects the strong interaction with the created medium. The opposite is observed at LHC energies i.e. for large drag coefficients, correlations are getting more

important specifically on the near side. These observations can be interpreted by the quick thermalization of heavy flavour within the QGP and their movement in the same direction as the partonic wind.

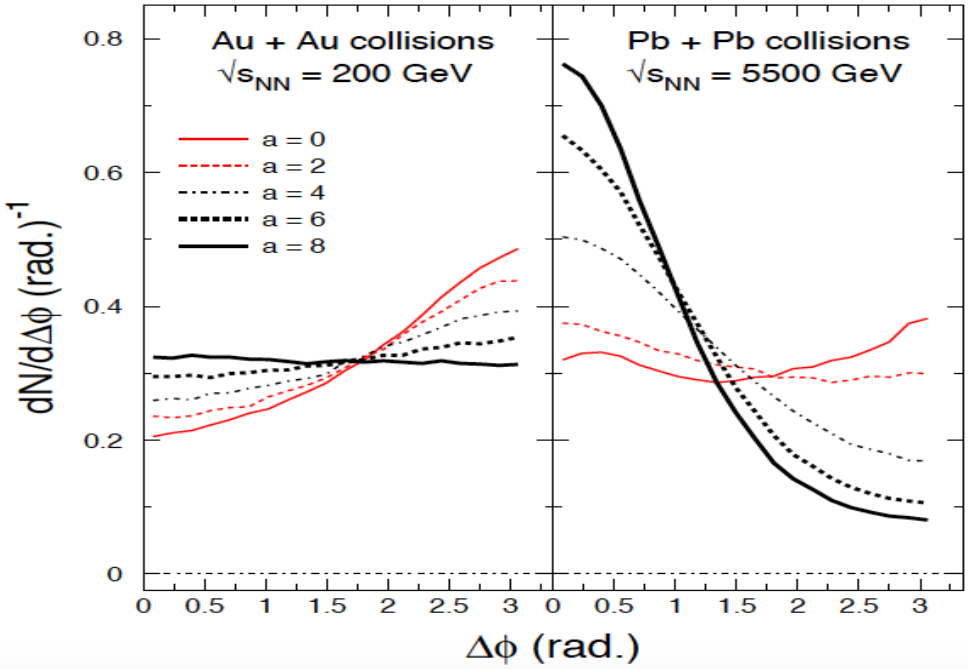

FIGURE 1.34: $D\bar{D}$ correlations as a function of $\Delta\phi$ in Au-Au collisions at $\sqrt{s}_{NN} = 200$ GeV/c (left) and Pb-Pb collisions at $\sqrt{s}_{NN} = 5500$ GeV/c (right) for different drag coefficient values [74].

Important conclusions were extracted from another theoretical study [75] and the concerned distributions are displayed in figure.1.35. The left plot presents the angular correlations between $c - \bar{c}$ pairs simulated using the LO pQCD in the 0-10% most central Au-Au collisions at 200 GeV. The red solid line presents the distribution for collisional and radiative energy loss. The dotted blue curve presents the collisional case only, the dashed purple line presents the collisional energy loss only where the longitudinal and transverse transport coefficients (k_L and k_T) are velocity dependent, the yellow dotted-dashed line presents the collisional case only but without flow, while the green dashed line presents the distribution for radiative energy loss only. These distributions are obtained for different values of the diffusion coefficient adjusted according to the considered energy loss mechanism.

For the purely collisional energy loss, correlation distribution shows a near side peak ($\Delta\phi = 0$) due to the partonic wind effect. When this effect is disabled, it gives the distribution in yellow dotted-dashed line where the enhancement in the near side disappeared and one can deduce that the partonic wind is indeed responsible for the collinear motion of $c - \bar{c}$ pairs in the created medium in heavy-ion collisions. For the purely radiative energy loss, correlation distribution shows an away side peak ($\Delta\phi = \pi$) with a large magnitude that gets smaller once the collisional energy loss is taken into account with the radiative one.

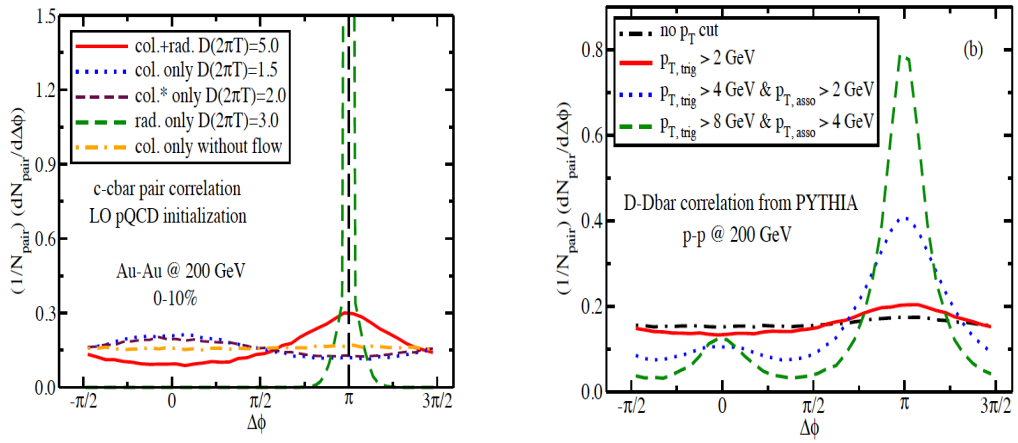

FIGURE 1.35: Left: $c - \bar{c}$ angular correlations in Au-Au collisions at 200 GeV in the centrality class 0-10% as a function of $\Delta\phi$ for different energy loss mechanisms. Right: $D - \bar{D}$ angular correlations obtained from PYTHIA in p-p collisions at 200 GeV as a function of $\Delta\phi$ for different p_T thresholds on the triggers and the associated particles [75].

The right plot of figure.1.35 presents the $D\bar{D}$ angular correlations obtained in p-p collisions at 200 GeV in the cases : no p_T cut (dotted-dashed black line), $p_{T,trig} > 2$ GeV/c (red solid line), $p_{T,trig} > 4$ GeV/c, $p_{T,asso} > 2$ GeV/c (dotted blue lines) and $p_{T,trig} > 8$ GeV/c, $p_{T,asso} > 4$ GeV/c (dashed green line). These distributions were obtained using the same parameter settings used to obtain the p_T spectrum in agreement with the one measured by STAR collaboration. Correlation distribution with no cut shows a flat behaviour and once a p_T cut is applied, one starts to see an enhancement around $\Delta\phi = \pi$. The peak is getting clearer once the cut is higher until correlations around $\Delta\phi = 0$ appear as well.

According to [75] [76], the angular correlations of $D\bar{D}$ in Au-Au collisions at 200 GeV for different energy loss mechanisms do not show a difference when sufficiently higher p_T cuts are applied. While at low p_T cuts, one can see that correlations in the case of the collisional energy loss show a near side peak while for radiative energy loss, the distribution shows an away side peak. When both energy loss mechanisms are considered, the obtained distribution shows a near side peak (small in magnitude) but no away side peak. This is due to the average number of pairs which is large at low p_T and to the large number of uncorrelated pairs as well. This number gets smaller once we deal with higher p_T.

D-hadron correlations were simulated in p-p collisions and Au-Au collisions [77] using the Linear Boltzmann Transport (LBT) model for which the theoretical predictions concerning the nuclear modification factor (R_{AA}) and the elliptic/triangular flow (v_2,v_3) were found to agree with the experimental data from RHIC and LHC. Correlation distributions for the number of correlated pairs and their energy were obtained as presented in figure.1.36. The red solid line presents the distribution in Au-Au collisions while the dashed blue line presents the distribution in p-p collisions. The left plot shows the distributions for the correlated pair numbers as a function of $\Delta\phi$. The near side and the away side peaks are both visible but the distributions in Au-Au collisions are larger in magnitude which is reasonable

due to the large multiplicity and underlying events expected in heavy-ion collisions. The right plot is similar to the left one except that the energy is shown instead. The distribution obtained in p-p collisions shows 2 peaks in the near side and the away side although not similar in magnitude but both are narrow which is not the case in Au-Au collisions where the difference lies in the broadened away side peak, a feature that reflects probably the interaction of the jet of particles with the created medium (QGP) in heavy-ion collisions.

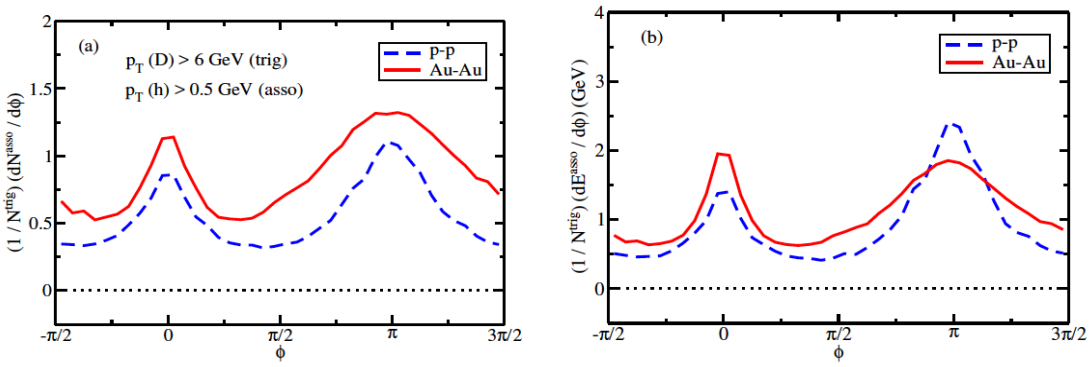

FIGURE 1.36: Normalised D-h azimuthal correlations as a function of $\Delta\phi$ of the correlated pairs number (a) and correlated pairs energy (b) [77].

A particularly interesting study on the production processes of heavy flavours was performed [78] by exploiting the correlation of b-jets and PYTHIA simulations. The weighted $\Delta\phi$ distributions obtained for b-tagged jets are presented in figure.1.37. The histograms in green, orange and blue present the correspondent PYTHIA simulations respectively for Flavour Creation (FCR), Flavour Excitation (FEX) and Gluon Splitting (GSP). The solid black points present the experimental data. The lower panel in this figure shows the difference Data - MC. There is a reasonable agreement between the data and simulations. The 3 processes predict similarly the experimental data at larger angles, unlike the smaller ones where the 3 processes describe differently the data. The GSP becomes the dominant mechanism at smaller angles followed by FEX.

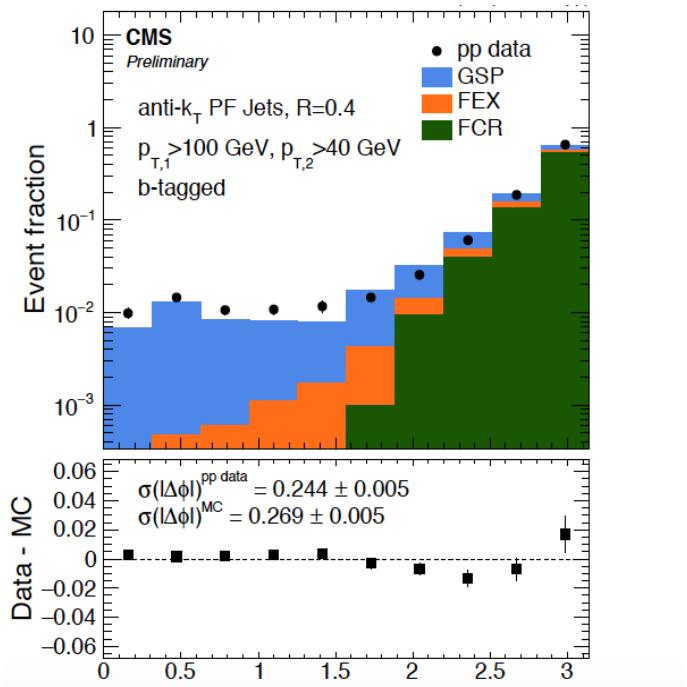

FIGURE 1.37: $\Delta\phi$ distributions of b-tagged jets in p-p collisions from CMS experiment (solid points) and from PYTHIA 6 simulations (histograms) of the 3 production processes of heavy flavour [78].

Within LHCb Collaboration, an interesting correlation analysis was performed [79] where charmed hadrons were selected in the rapidity range $2 < y_C < 4$ and transverse momentum range $3 < p_C^T < 12$ GeV/c. These charmed hadrons were considered in different combinations. As a result, several cases of correlations distributions are obtained as presented in figure.1.38.

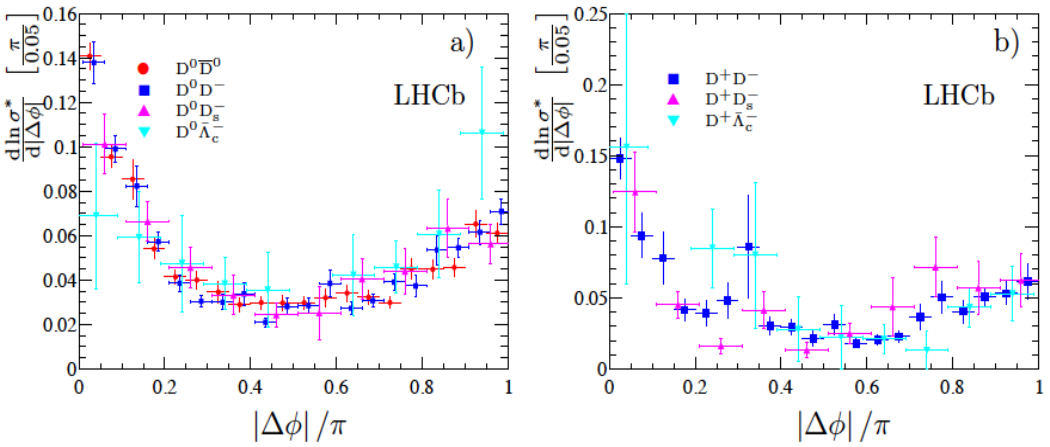

FIGURE 1.38: Azimuthal correlation distributions for $C\bar{C}$ events in proton-proton collisions at 7 TeV with LHCb experiment. Left: $D^0\bar{D}^0$ (red circles), D^0D^- (blue squares), $D^0D_s^0$ (pink triangles), $D^0\Lambda_c^-$ (cyan triangles). Right : D^+D^- (blue squares), $D^+D_s^-$ (pink triangles), $D^+\Lambda_c^-$ (cyan triangles) [79].

One can see clearly that the enhancement at smaller angles ($\Delta\phi = 0$) is more important

than those at larger angles ($\Delta\phi = \pi$). This means that gluon splitting is the dominant process which is expected at high energies of the order of TeV at the LHC.

An example of correlation between b and $\bar{b}$ is shown in figure.1.39 which was obtained with LHCb detector. The performed comparison shows an agreement between the experimental data (black points) and the predictions from POWHEG (yellow cross-hatched area) and PYTHIA (green area) [80].

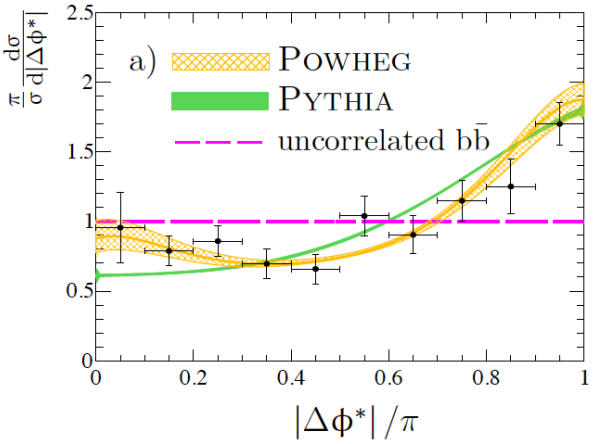

FIGURE 1.39: Normalized differential production cross section of $b\bar{b}$ correlations in p-p collisions at 7 TeV as a function of $|\Delta\Phi^*|$ with LHCb detector (black points) versus predictions from POWHEG (cross-hatched yellow area) and PYTHIA (green area) in addition to the production of uncorrelated $b\bar{b}$ (dashed magneta line) and statistical uncertainties are presented by error bars [80].

At CMS collaboration, heavy flavour correlations were studied differently. Instead of considering just the B mesons, the whole jet tagged by the presence of the B meson is considered in the analysis performed on the data collected in p-p collisions at 7 TeV [81]. Figure.1.40 shows the obtained $B\bar{B}$ correlation differential production cross-section as a function of the opening angle $\Delta\phi$ for three different p_T thresholds on the jet. The distributions show similar behaviour for the 3 thresholds. The produced jets with smaller opening angles are a bit larger in magnitude in comparison to jets produced at larger opening angles which indicates that gluon splitting is important production mechanism at this energy scale at the LHC. PYTHIA simulations reproduce the shape of the experimental distributions but underestimate them at smaller angles.

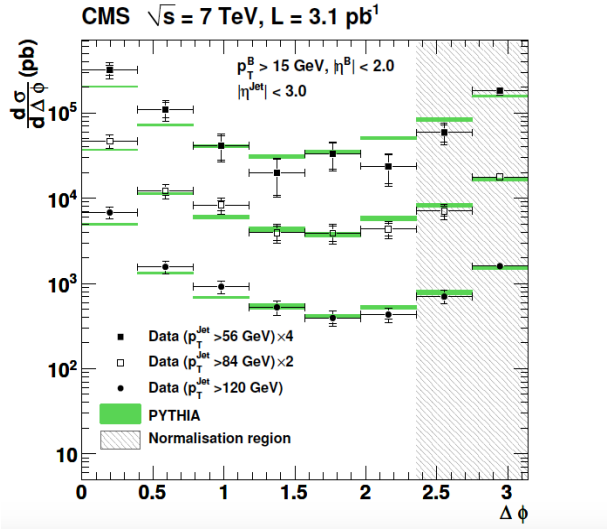

FIGURE 1.40: $B\bar{B}$ differential production cross-section as a function of the opening angle $\Delta\phi$ in p-p collisions at 7 TeV with CMS detector (black filled/empty squares/ black circles) versus PYTHIA simulations (green area) [81].

At CDF collaboration, different combinations were considered to study correlations. Figure.1.41 presents in the left panel the cross-section of D^0-D^{*-} correlations and in the right panel the cross-section of D^+-D^{*-} correlations and both were computed in $p-\bar{p}$ collisions at 1.96 TeV. The data are presented in black points while the black solid lines refer to the cross-section of correlations from PYTHIA simulations where the contribution of flavour creation, flavour excitation and gluon splitting are displayed in red, green and blue dashed lines, respectively. The D mesons were considered in the rapidity range $|y| < 1$ and in the transverse momentum ranges $5.5 < p_T(D^0) < 20$ GeV/c, $5.5 < p_T(D^{*-}) < 20$ GeV/c, $7 < p_T(D^+) < 20$ GeV/c. There is no agreement between the predictions from PYTHIA and the experimental data from CDF.

The predictions underestimate the data at smaller angles ($\Delta\phi = 0$) and overestimate them at larger angles ($\Delta\phi = \pi$). It is possible to say that a qualitative agreement is established although the quantitative difference at smaller/larger angles. From the experimental data, both near-side and away-side peaks have an almost similar magnitude so the contribution from flavour creation is closer to gluon splitting. From the predictions, it is clear that flavour creation is the dominant production process at larger angles around $\Delta\phi = \pi$ while at smaller angles $\Delta\phi = 0$, gluon splitting is the dominant one. Flavour excitation contributes significantly only at larger angles [82].

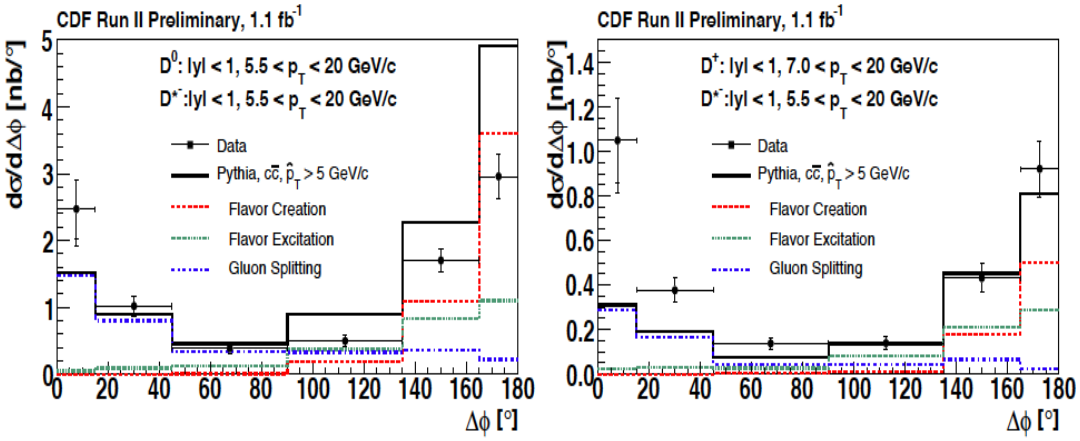

FIGURE 1.41: The cross-section of D^0D^{*-} correlations (left) and D^+D^{*-} correlations (right) in $p-\bar{p}$ collisions at 1.96 TeV with CDF experiment at the Tevatron (black points) versus the theoretical predictions from PYTHIA (black solid line) with the contribution of the production mechanisms : flavour creation (red dashed line), flavour excitation (green dashed line) and gluon splitting (blue dashed line) [82].

Correlations were also studied in STAR collaboration by considering the combinations D^{*+}-D^{*-} within the transverse momentum range $2.5 < p_T(D^*) < 20$ GeV/c, as well as the combinations hadron-hadron and D*-hadron within the transverse momentum intervals $8 < p_T^{Trig}(D/h) < 20$ GeV/c and $p_T^{assoc}(h) > 0.5$ GeV/c. The considered pseudo-rapidity range was $|\eta| < 1$.

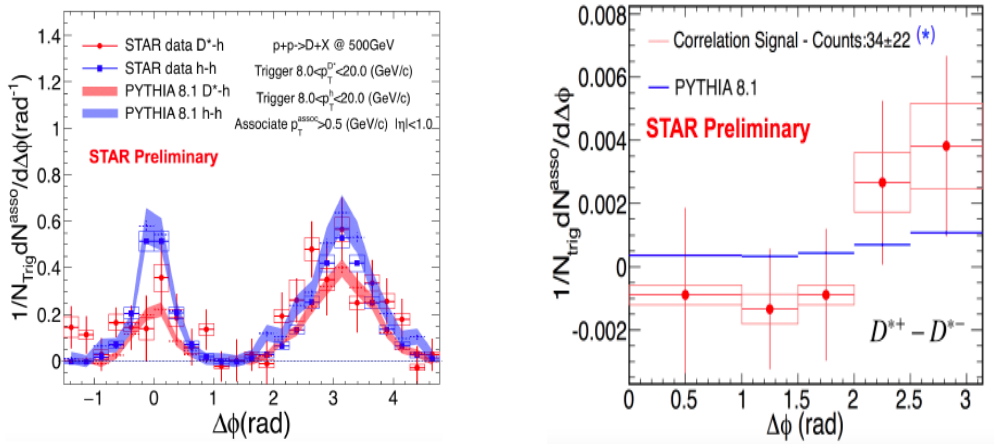

FIGURE 1.42: Left : D*-hadron correlations (red points) and hadron-hadron correlations (blue points) in p-p collisions at 500 GeV versus predictions from PYTHIA 8.1 of D*-h (red shaded area) and h-h (blue shaded area). Right : D^{*+}-D^{*-} correlations in pp collisions at 500 GeV (red points) [83].

Figure.1.42 presents the preliminary results from the STAR experiment where the left panel shows correlations of D*-h (red points) and h-h correlations (blue squares) compared to the predictions from PYTHIA 8.1 tuned to STAR: D*-h (red shaded area) and h-h correlations (blue shaded area). The away-side peak from D*-h matches the one from h-h, unlike the near-side peak. Otherwise, an agreement is established between PYTHIA8.1 and the

experimental data from STAR within uncertainties. In the right panel of figure.1.42, the correlations of D^{*+}-D^{*-} (red points) compared to the predictions from PYTHIA 8.1 (blue solid lines) are presented [83].

Within ALICE collaboration, some correlation analyses were held by considering a different perspective such as correlations between charged particles and their dependence on the multiplicity [84]. It was found that both the near-side and the away side yields grow with the multiplicity. As for the combinatorial background, the growth is linear with charged-particle multiplicity. The trigger particle number increases faster than linear. For a fixed multiplicity, the near-side yield increases with $\sqrt{s}$ while the away-side yield decreases with $\sqrt{s}$. As for the combinatorial background, no dependence was observed. An example of the correlations between charged particles can be found in [85]. The correspondent famous ridge feature is shown in figure.1.43.

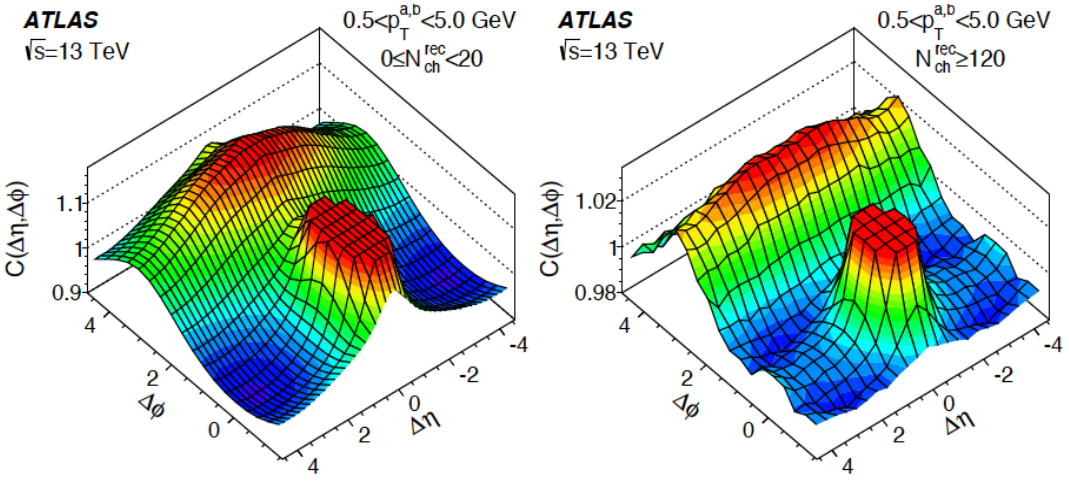

FIGURE 1.43: Two particle correlations in p-p collisions at 13 TeV with ATLAS detector for $0 < N_{ch}^{rec} < 20$ (left) and $N_{ch}^{rec} > 120$ (right) [85].

This two-particle correlations distribution is clearly showing a $\Delta\phi$ $\Delta\eta$-dependence where the peak around $(\Delta\phi, \Delta\eta) = (0, 0)$ is a feature suggesting a strong correlation between charged particles which proves the production of a jet of particles in the same direction as the trigger particles. On the other side, around $\Delta\phi = \pi$, the distribution seems peaked but broadened in $\Delta\eta$ which can be interpreted by the production of di-jets. It is also clear that the correlation peak is stronger for larger multiplicity. Among the interesting conclusions, one can mention that the ridge phenomenon in p-p collisions or p-Pb collisions is most likely based on similar physics aspects from which one can infer that there is probably no dependence on $\sqrt{s}$.

Two-particle correlations were studied in Pb-Pb collisions at 2.76 TeV with ALICE detector [86] where the obtained $\Delta\phi - \Delta\eta$ distributions also show the ridge feature. It was deduced that the peak widths increase from peripheral to central collisions and those in peripheral collisions are larger than those obtained in p-p collisions. Concerning p_T dependence, the

peak width gets narrower at larger p_T. The distributions are broadened for central collisions in the $\Delta\eta$ direction. A depletion is observed in $\Delta\eta$ too which was interpreted by the interaction between the fragmenting partons and the radial/longitudinal flows of the created medium in Pb-Pb collisions.

The yield of charged particles per trigger is another alternative observable for correlation studies [87]. In such analyses, the yield is obtained in di-hadron correlations in Pb-Pb and pp collisions at 2.76 TeV with the ALICE detector. The ratio between the Y_{Pb-Pb} and Y_{p-p} is noted as I_{AA}. An enhancement (suppression) is observed in the near-side (away-side) which indicates an energy loss in the created medium in central collisions. As for peripheral collisions, no energy loss can be concluded since the I_{AA} was found to be closer to 1 for both near-side and away-side. Concerning the comparison between the output from the LHC and RHIC, the suppression in the latter was found to be larger than the former.

1.6 Chapter Conclusion

In this chapter, the Quark-Gluon-Plasma and its connection with the early Universe was discussed. Laboratories on Earth re-created a small droplet of this state of matter via heavy-ion collisions, and several experiments shared the study of its properties and evolution as a function of the temperature and the baryonic density to constitute the phase diagram. In accelerators, signatures of the creation of the Quark-Gluon-Plasma were inferred and exploited, such as quarkonium suppression, thermal radiation and strangeness enhancement. Heavy-ion collisions were then treated where the global properties and input parameters were presented and then the main stages and the evolution of heavy nuclei collisions were presented. After that, the basic features of the Standard Model were presented and explained with focus on elementary particle classification and on the forces responsible for their interaction. The theory of the Strong interactions, Quantum Chromodynamics, was discussed briefly with attention on colour confinement and asymptotic freedom. Some highlights on the results of heavy flavours production in the different collisional systems and energies were presented and discussed mainly through the presentation of the differential production cross-sections in p-p collisions and a focus on the nuclear modification factor results in p-nucleus and nucleus-nucleus collisions. Finally, correlation analyses were presented and discussed from the experimental and the theoretical point of view involving the contributions of the production processes of Flavour Creation, Flavour Excitation and Gluon Splitting as well as the importance of partonic wind with the presence of a medium and how it does impact the correlation pattern.

Chapter 2

ALICE Experiment

In this chapter, an overview of the Large Hadron Collider (LHC) is given. After that, the ALICE experiment is presented briefly, and more details are provided on the relevant detectors for the correlation analysis.

2.1 The Large Hadron Collider

The LHC is the biggest machine ever built. It was designed to accelerate beams of particles, mainly protons and lead nuclei. Between 2010 and 2013 (Run I), the LHC reached a center of mass energy of 8 TeV in proton-proton collisions, 5.02 TeV in p-Pb collisions, and 2.76 TeV per nucleon-nucleon pair in Pb-Pb collisions. From 2015 (Run II), the achieved energy per nucleon-nucleon pair was 13 TeV in pp collisions and 5 TeV in Pb-Pb collisions. In this thesis, the correlation analyses are performed by exploiting the data collected in the central barrel of the ALICE detector at the LHC in pp collisions at 13 TeV.

The LHC project was approved by CERN Council in 1994. The initial plan was to build the accelerator in two steps so that it would have reached energy at the center of mass system of 10 TeV and 14 TeV in the first step and second one, respectively. But in December 1996, the Council approved the construction of the LHC at CERN in one stage instead of two with the aim to reach immediately 14 TeV. The hardware of the machine was built by both members and non-members states of CERN. The LHC was redesigned several times for matter of cost and performance purposes. These activities had been published in October 1995 in the "Yellow Book" (the LHC Conceptual Design Report [88]). The redesign touched the superconducting magnet system, precisely, the main dipoles, the beam collimation systems, the Radiofrequency (RF), and Beam Feedback. The design of the vacuum system was not changed. More details can be found in [89].

2.1.1 Operating mode

The accelerated beams of protons at the LHC are supplied from the injector chain LINAC2, while ions (Pb in ALICE) are supplied from the injector chain LINAC3. To reach an energy

of 13 TeV in the centre of mass system, the beam of protons is injected in a chain of accelerators where the beam energy increases in steps. The LHC accelerator complex is shown in figure.2.1.

The acceleration of proton beams at the LHC starts with a bottle of compressed hydrogen gas. Hydrogen atoms (lead atoms) from this gas cylinder are fed with a controlled rate into a linear accelerator chamber CERN's LINAC2 (LINAC3), where their electrons are stripped off to leave hydrogen nuclei with a positive charge (protons) which enable them to be accelerated by an electric field. After that, this packet of protons will leave LINAC2, and it will be traveling at one-third of the speed of light. Then, it will enter the booster stage. To maximise the intensity of the beam, the packet is split into four, one for each of the boosters' rings. The booster is circular with a circumference of 157 meters. To accelerate the packets in it, they are circulated repeatedly by a pulsed electric field. Powerful electromagnets are exploited to bend the beam of protons by applying a force at the right angles compared to the direction of their motion. The booster accelerates the protons up to 91.6 % of the speed of light and squeezes them closer together. The packets are recombined from the four rings and injected into the proton synchrotron (PS). The PS is 628 meters in circumference, and protons need to circulate for 1.2 seconds to reach over 99.9% of the velocity of light. At this stage, the energy added to the protons by the pulsating electric field cannot be converted into velocity as they are already approaching the limit of the speed of light. The added energy manifests itself as an increasing mass of the protons instead. In short, the protons cannot go faster; consequently, they get heavier. The microscopic kinetic energy of each proton is measured in units called electron volts (eV). So far, the energy of each proton has increased to 25 Giga electron volts (GeV), i.e. the protons are 25 times heavier than they are at rest. Next, the packets of protons are channeled into the Super Proton Synchrotron (SPS), a huge ring of 7 kilometers in circumference designed specifically to accept protons at this energy and increase it to 450 GeV.

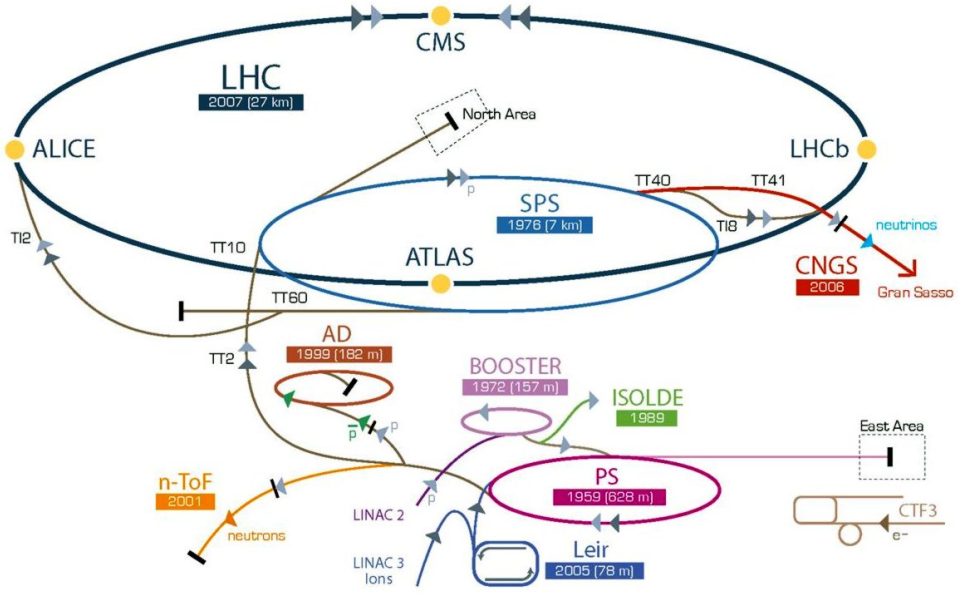

FIGURE 2.1: Layout of the Large Hadron Collider facility at CERN [92]. See text for details.

Soon, the packets of protons will be energised sufficiently to be launched into the orbit of the gigantic Large Hadron Collider (LHC), which is a 27 km circumference underground tunnel of depth 50-175 m on the border between France and Switzerland. It consists of two adjacent beam pipes parallel to each other where two proton beams can travel in opposite directions (one clockwise and the other one anti-clockwise). Ultra sophisticated kickers are used to synchronise the incoming packets with those circulating already. The SPS injects protons for half an hour. During this time, the LHC adds extra energy to each proton whose velocity is so near to the speed of light that it goes around the 27 kilometers ring over 11.000 times each second.

In the end, each proton has an energy of seven Tera electron volts (TeV), and they are 7000 times heavier than at rest.

The circular path of the beam is maintained by the superconducting dipole magnets, while the quadrupole magnets keep the beams focused for more interactions.

At this stage, the rotating beams cross over in the four detector caverns where they are ready to collide with the double of the individual energy of the opposing protons, and it can reach 14 TeV at the LHC. A stirring magnet brings them onto a collision point.

The debris, or in other words particle tracks from these collisions, will be analysed by computers connected to the detectors with the hope that these tracks will give insights into the beginning of our universe, how it was evolved, what governs its behaviour today, and where it's going in the future.

Briefly, the two accelerated beams of particles intersect in four points where the interaction between the beams of particles takes place. At each intersection point, a detector of an experiment is installed. Each experiment was designed and dedicated to studying a couple of fundamental questions.

The LHCb experiment is designed to study rare decays of beauty mesons and to search for new ones to explain the asymmetry between matter and antimatter in the universe. A Toroidal LHC Apparatus (ATLAS) is dedicated to the study of the Higgs boson, the origin of mass, and to search for physics beyond the standard model. The Compact Muon Solenoid (CMS) is designed to search for the nature of the dark matter in addition to the studies on the Higgs boson as in ATLAS. A Large Ion Collider Experiment (ALICE) is the only experiment that was designed and built to study heavy-ion collisions where the Quark-Gluon-Plasma (QGP) is created. In this thesis, the data exploited in the correlation analysis were collected with the ALICE experiment.

Three other small experiments were added. TOTal Elastic and diffractive cross section Measurement (TOTEM), installed near CMS at point 5, is an experiment devoted to measuring the total cross-section, small-angle elastic scattering, and diffraction dissociation. The Large Hadron Collider forward (LHCf) detector where physicists aim to study cosmic rays and the experiment will be sharing the interaction point 1 near ATLAS. Monopole and Exotics Detector at the LHC (MoEDal) searches for the magnetic monopole or any other highly ionising stable/pseudo stable massive particles. The cavern is shared with LHCb at point 8 [1] [90] [91].

2.2 ALICE Detector

The ALICE detector was built by a collaboration that consists of more than 1,500 physicists and engineers from 37 countries. The total weight of the detector is about 10.000 tons, and it keeps the dimensions 16 x 16 x 26 m^3. ALICE main purpose is the study of matter at extreme conditions and more precisely the investigation of the properties of the Quark-Gluon-Plasma (QGP) created in heavy-ion collisions [93].

The ALICE detector consists of two parts: the muon spectrometer and the central barrel as displayed in figure.2.2. In ALICE, particles are reconstructed in their hadronic and semi-leptonic decay channels in the central barrel and only in their leptonic decay channels in the Muon Spectrometer.

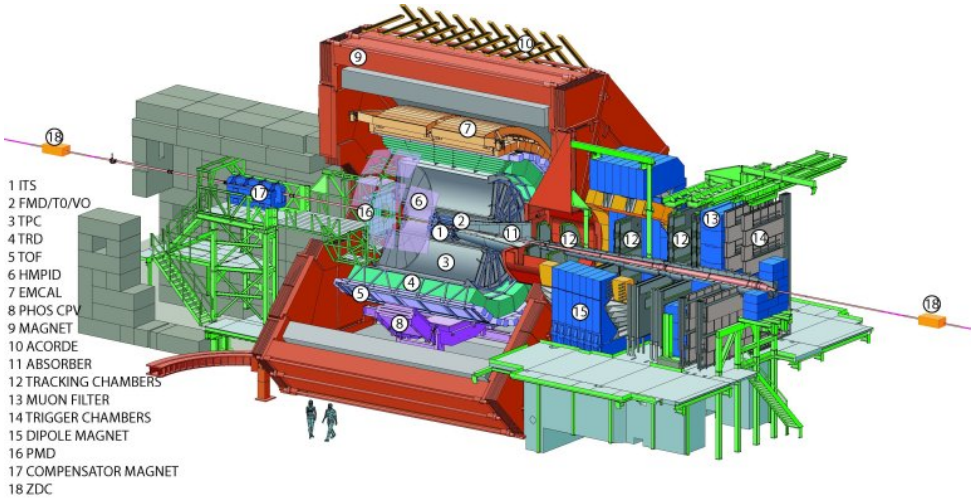

FIGURE 2.2: Layout of the ALICE detector [94].

The Muon spectrometer is designed to reconstruct hadrons (quarkonia and open heavy flavour) in their muonic or semi-muonic channels. It covers a range of pseudo-rapidity $-4.0 < \eta <$ -2.5, which is equivalent to an angular acceptance from 171° up to 178°. It consists of the following sub-detectors, the front absorber, a passive sub-detector installed between the interaction point, and the beginning of the muon spectrometer to absorb hadrons from the interaction point. After the front absorber, we can find the tracking system composed of 5 stations where each station consists of 2 chamber planes of high granularity. The third station is embedded in a magnetic field induced by a large dipole magnet. After the last station of the tracking chamber, a 1.2 m thick passive muon-filter wall is installed to protect the trigger chambers installed behind them. Another sub-detector, considered as an absorber, the inner beam shield, is installed to protect the chambers from the background (primary and secondary particles produced from the interaction with the detector at large rapidities).

The other main part of the ALICE detector is the central barrel. The central barrel is embedded in a magnetic field of 0.5 Tesla created by the large solenoid L3 magnet inherited from the LEP experiment. The central barrel covers a polar angle from 45° up to 135°. Most sub-detectors from the central barrel cover the full azimuth (except HMPID, PHOS, and EMCal). From inside to outside, the build-up detectors in the central barrel are as follows. The Inner Tracking System (ITS) is composed of 6 layers of silicon: two layers of Silicon Pixel Detectors (SPD), two layers of Silicon Drift Detectors (SDD), and two layers of Silicon Strip Detectors (SSD). The principal role of the ITS, in a standalone status, is to identify particles by measuring $\mathrm{d}E/\mathrm{d}x$ at low p_T in addition to tracking and vertexing. The Time Projection Chamber (TPC) is a cylindrical-shaped detector exploited for Particle Identification by measuring the energy loss $\mathrm{d}E/\mathrm{d}x$. The Time Of Flight (TOF) and a High Momentum Particle Identification Detector (HMPID) are used for particle identification at high p_T, the Transition Radiation Detector (TRD) is exploited for electron identification.

There are two calorimeters: the Electromagnetic Calorimeter (EMCal) and the PHOtons Spectrometer (PHOS) used both for the identification of photons and neutral pions.

Smaller detectors are installed at small angles to characterise the global event properties. In this set, one finds the Zero Degree Calorimeter (ZDC) used to determine the spectators' energy, the Forward Multiplicity Detectors (FMD) used to measure charged particles at small angles, T0 and V0 are both exploited to determine the luminosity and the multiplicity. A COsmic Rays DEtector (ACORDE), an array of scintillators, is installed on the top of the L3 magnet to detect cosmic rays.

Among this collection of sub-detectors in the central barrel, three detectors are essential for the data exploited for the correlation analysis of the current work. Those detectors are the ITS, TPC, and TOF. The properties of each detector are going to be presented in more detail in the upcoming sections.

2.2.1 Inner Tracking System

The ITS consists of 6 cylindrical layers of Silicon Detectors, 2 Pixels (SPD), 2 Strips (SSD) and, 2 Drifts (SDD), as displayed in figure.2.3. All layers cover a pseudo-rapidity $|\eta| < 0.9$ but not the first two where the range is extended to $|\eta| < 1.98$ to have continuous coverage of charged particles measurement in combination with the Forward Multiplicity Detector (FMD).

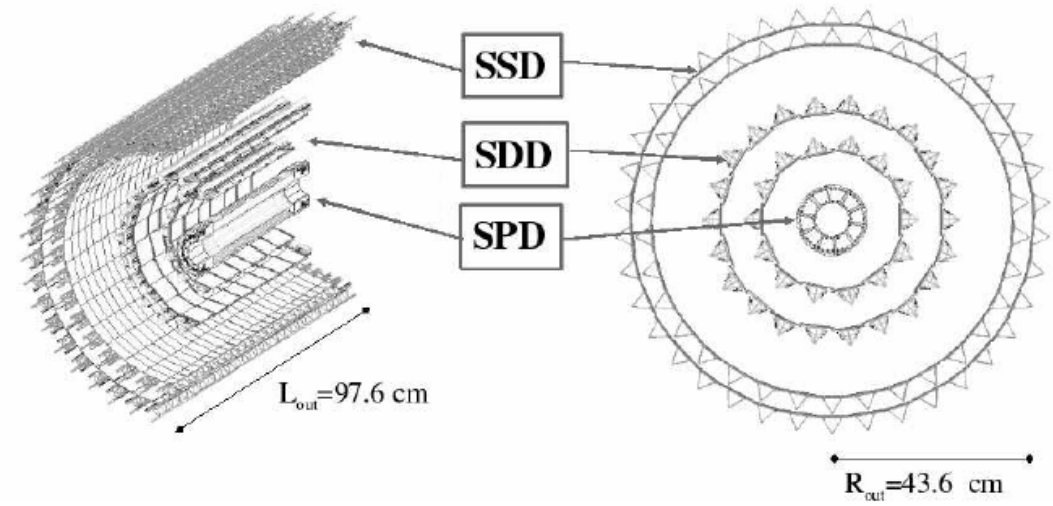

FIGURE 2.3: Layout of the ALICE Inner Tracking System.

- **Silicon Pixel Detector (SPD)** presents the two innermost layers of the ITS and the closest to the interaction point (IP). The SPD is used to determine the primary vertex position and the impact parameter of secondary tracks. The capability of track density can reach 50 tracks/cm^2. The inner layer of the SPD is located at 3.9 cm from the beam axis and the outer at 7.6 cm on average. To protect the SDD layers from radiation and

heat, the SPD is surrounded by an external shield made of aluminum-coated carbon fiber.

- **Silicon Drift Detector (SDD)** presents the middle layers of the ITS (the third and the fourth layers). The expected density of charged particles is around 7 / cm^2. The multitrack capability enables the SDD and the ITS, in general, to identify particles through their energy loss dE/dx.
- **Silicon Strip Detector (SSD)** presents the outer layers in the ITS (the fifth and the sixth). They are of great importance to match the tracks passing by the ITS to the TPC. As the SDD, the SSD also contributes to the PID through the dE/dx for low momentum particle identification.

The ITS is the principal detector in ALICE used for vertexing and Particle Identification (PID) at low p_T. Precisely, the ITS main role is to find the primary vertex where the collisions take place (or Interaction Point), as well as the secondary vertices where short-lived particles coming from the Interaction Point (IP) will decay. The ITS has a standalone capability to participate in Particle Identification at low transverse momentum. The analogy between the four outer layers readout could provide a measurement of the deposited charge; consequently, Particle Identification is possible through the measure of the ionisation energy loss dE/dx in the non-relativistic region at very low p_T.

The ionisation energy loss is determined by computing the path length from the parameters of the reconstructed track while the energy is measured from the cluster charge and then normalised to the path length.

Figure.2.4 presents an example of the ionisation energy loss in Pb-Pb collisions at 2.76 TeV as a function of the momentum in the ITS (standalone case).

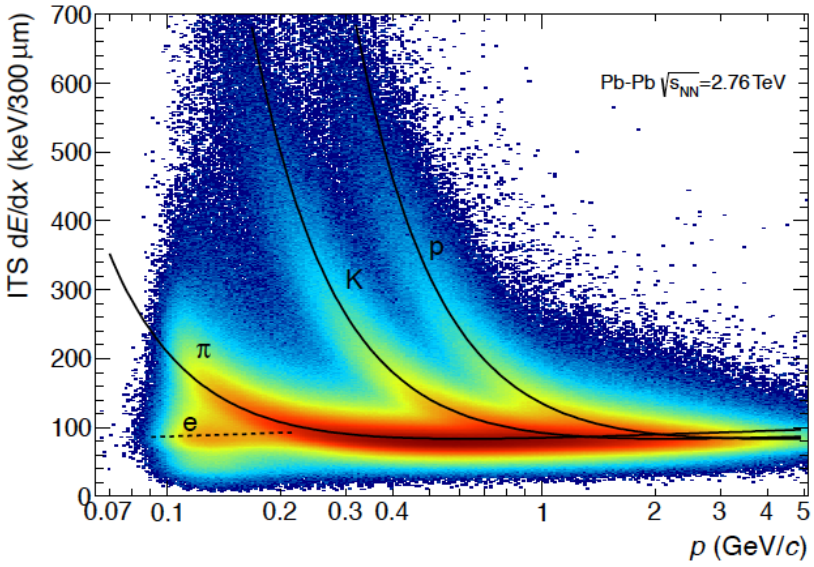

FIGURE 2.4: Specific ionisation energy loss measured by the ALICE Inner Tracking System in Pb-Pb collisions at $\sqrt{s_{NN}}$ =2.76 TeV.

2.2.2 Time Projection Chamber

The Time Projection Chamber (TPC) is the principal detector dedicated to particle identification and tracking in ALICE. It is a cylindrical detector with a length of 500 cm along the beam direction filled with a mixture of gases Ne(90%)/CO_2(10%) and included in an active volume of around 90 cm^3 with the inner (outer) radius of 85 cm (250 cm). The layout of the TPC is displayed in figure.2.5.

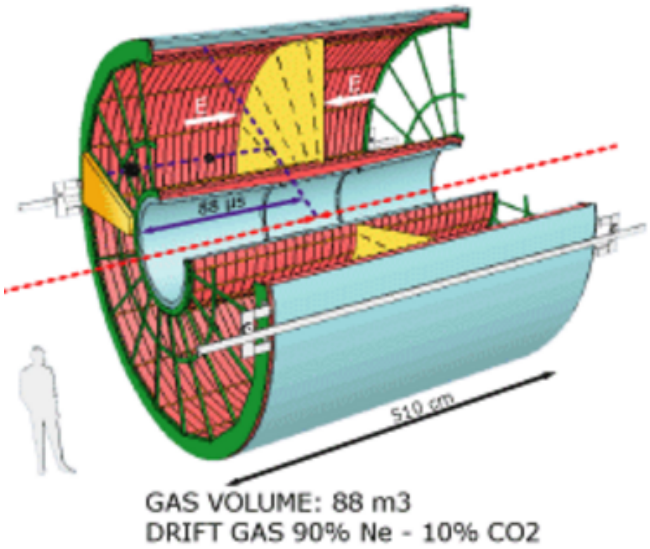

FIGURE 2.5: Layout of the ALICE Time Projection Chamber.

The TPC covers the full azimuth and the pseudo-rapidity range $|\eta| < 0.9$ for the full length of the tracks matched between the ITS, TPC and TOF. The pseudo-rapidity can reach $|\eta| = 1.5$ when the length of the tracks is reduced. The covered transverse momentum range can vary from 0.1 up to 100 GeV/c. For each particle passing through the gas of the detector, the energy loss (dE/dx), the charge and the momentum are measured. According to the Bethe-Bloch formula, the energy loss can be parametrised by

$$f(\beta\gamma) = \frac{P_1}{\beta^{P_4}} \left(P_2 - \beta^{P_4} - ln \left(P_3 + \frac{1}{(\beta\gamma)^{P_5}} \right) \right), \tag{2.1}$$

where β and γ correspond to the particle velocity and the Lorentz factor, respectively. P_{1-5} are the fit parameters. Figure.2.6 shows an example of the specific energy loss dE/dx as a function of the particle momentum in the TPC in Pb-Pb collisions at 2.76 TeV. There is a clear separation between the different particle species.

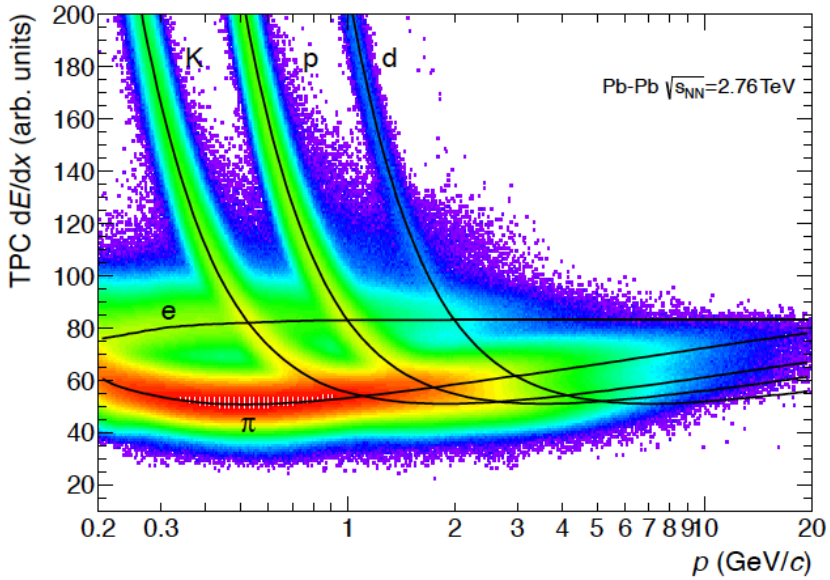

FIGURE 2.6: Specific ionisation energy loss measured by the ALICE Time Projection Chamber in Pb-Pb collisions at $\sqrt{s_{NN}} = 2.76$ TeV.

2.2.3 Time-Of-Flight

The Time-Of-Flight (TOF) is a large array of Multigap Resistive Plate Chambers (MRPC) that covers a pseudo-rapidity range $|\eta| < 0.9$ which is equivalent to a cylindrical surface with a polar acceptance $|\theta - 90°| < 45°$. It consists of 18 sectors in azimuthal coordinates and five segments in the beam direction (or z). The internal (external) radius is about 370 cm (399 cm). The layout of the TOF is displayed in Figure.2.7.

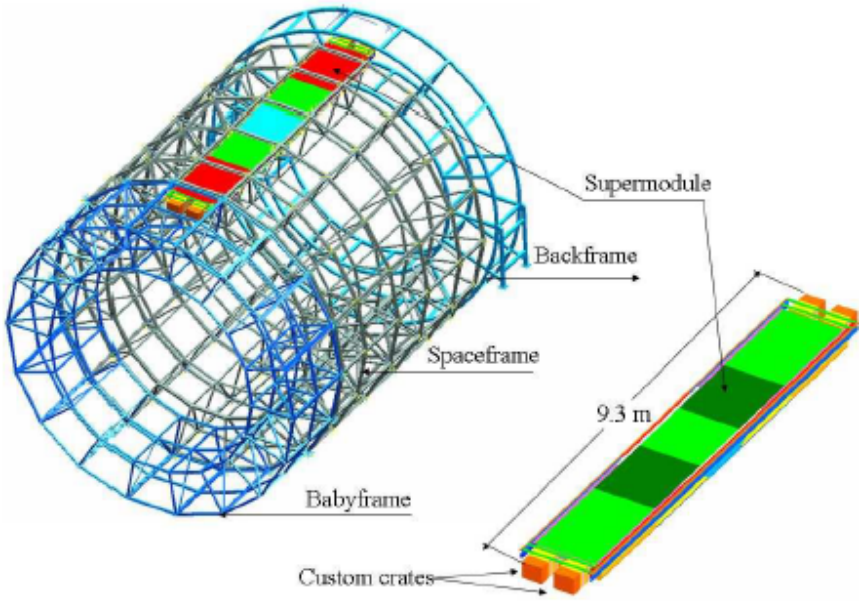

FIGURE 2.7: Layout of the ALICE Time-Of-flight Detector

The TOF is another cylindrical detector used for Particle Identification in ALICE at intermediate p_T, up to 2.5 and 4 GeV/c for π, K, and p, respectively. A separation of better than 3 σ is achieved for π/K and K/p. The tracks in the TOF are matched with those in the ITS and the TPC in order to reconstruct tracks, vertices and to perform the Particle Identification (PID). Figure.2.8 shows an example of the particle identification with the TOF in Pb-Pb collisions at 2.76 TeV. This figure presents the measured velocity of particles β as a function of the momentum where the separation between the particles (p, K, π, d, and electrons) is possible.

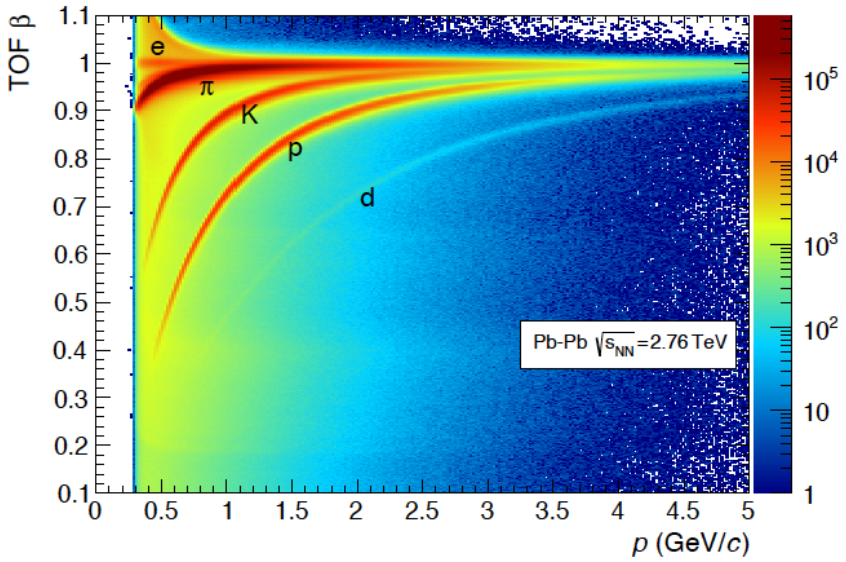

FIGURE 2.8: Velocity of particles as a function of the momentum measured with the ALICE Time-Of-Flight detector in Pb-Pb collisions at $\sqrt{s_{NN}}$= 2.76 TeV .

2.3 Chapter conclusion

In this chapter, an overview was given on the large hadron collider, its operating mode, the main experiments, and their detectors, and physics goals. After that, ALICE detectors were described briefly. Then, a detailed description was given on the relevant detectors for D-hadron correlations analyses: ITS, TPC, TOF. Thanks to the ITS, the primary vertices can be reconstructed. The TPC is the principal detector in ALICE used for tracking and particle identification. The TOF is also exploited to identify particles.

Chapter 3

Data sample and quality assurance

In this Chapter, the quality assurance of the data sample used for correlation analysis is presented.

3.1 Data sample

The data sample exploited for correlation analysis was collected during 2016 and it consists of the periods: $LHC16d\_pass1$, $LHC16e\_pass1$, $LHC16g\_pass1$, $LHC16h\_pass1$, $LHC16j\_pass1$, $LHC16k\_pass1$, $LHC16l\_pass1$, $LHC16o\_pass1$, $LHC16p\_pass1$. The total number of selected events considered in the analysis was 433 Million Minimum Bias events in proton-proton collisions at 13 TeV. In pp collisions, an event is classified in the minimum bias category when each of the particles produced within it, has at least one hit either in the SPD or in the VZero. The concerned trigger, in this case, is called the INT7. Other triggers detectors are also considered but none of them will be taken into account in the analysis of this work. The associated run number to each period from pass1 and the number of selected events are shown in table.A.1 in Appendix.A.

3.2 Quality assurance

The Quality Assurance (QA) of the data sample is a crucial step before passing to the analysis since it helps to make sure that we are using the convenient data sample with good performances of all detectors included in the data-taking procedure. For the current correlation analyses, the QA distributions are obtained based on the regular distributions of particles .i.e spectrums of associated tracks and D mesons as a function of different observables (p_{T}, η, ϕ). For the QA of events, the global properties of the events are verified (statistics, vertex, multiplicities, ...). Concerning the QA of tracks, the distributions obtained with the ITS and TPC are presented to study the possible effects of the detector. With the QA of PID, the shape of the energy loss dE/dx in the TPC and TOF are inspected. The QA figures are obtained for all periods, but only distributions from LHC16k_pass1 are presented since it is the period with the largest statistics.

3.2.1 Event selection

The left panel of figure.3.1 shows the selected number of events after applying the selection criteria on the total number of events for all triggers. The right panel of figure.3.1 is similar to the left one, but it represents the fraction of the selected number of events. The main observation concerns the trigger INT7 which shows the fraction of selected events 0.92 from the total number of events. This means that 8% of the statistics were lost after passing the selection criteria, and it does not seem that it is a large number.

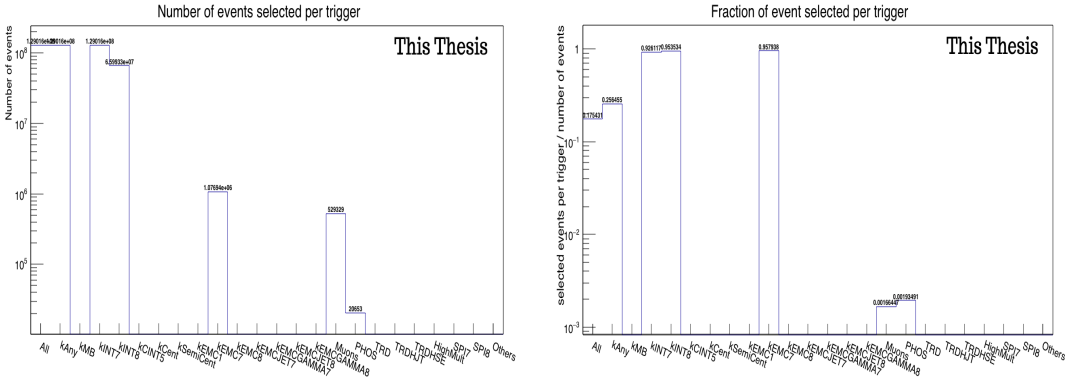

FIGURE 3.1: Number of selected events (left) and fraction of selected events (right) per trigger.

The left panel of figure.3.2 presents the number of events as a function of the vertex type. The type can be either: not found, track, SPD-3D, or SPD-z. For the selected events, the only vertex left should be of the type $track$ which is the case according to the right plot of figure.3.2.

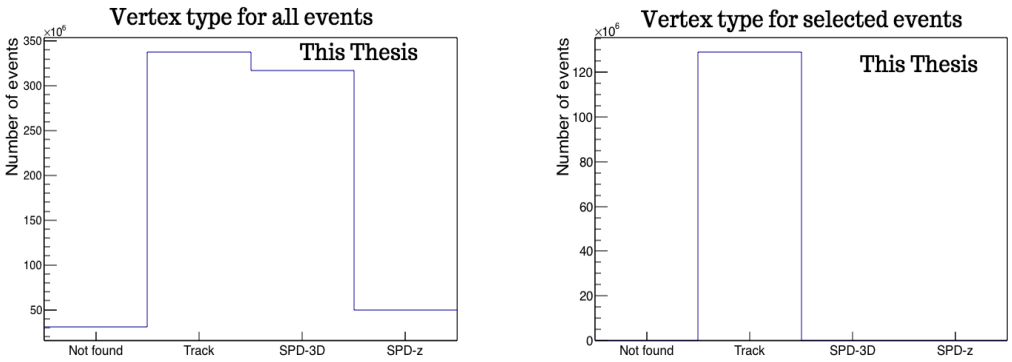

FIGURE 3.2: Number of all events (left) and selected events (right) as a function of the vertex type.

The distributions of the x-vertex, y-vertex, and z-vertex are presented in figure.3.3, figure.3.4 and figure.3.5, respectively. In each figure, the left panel corresponds to the distribution for all events, and the right panel corresponds to the distribution after applying the selection criteria. The right plot is the most relevant because it provides information on how the selection criteria impact the initial distribution of the vertex and the abundance of events

for the different directions. The vertices distributions in the x and y directions are fine. The z-axis distribution is also fine, although it goes beyond 10 cm which is one of the selection criteria since it was not included in the cut file then the distribution is fine.

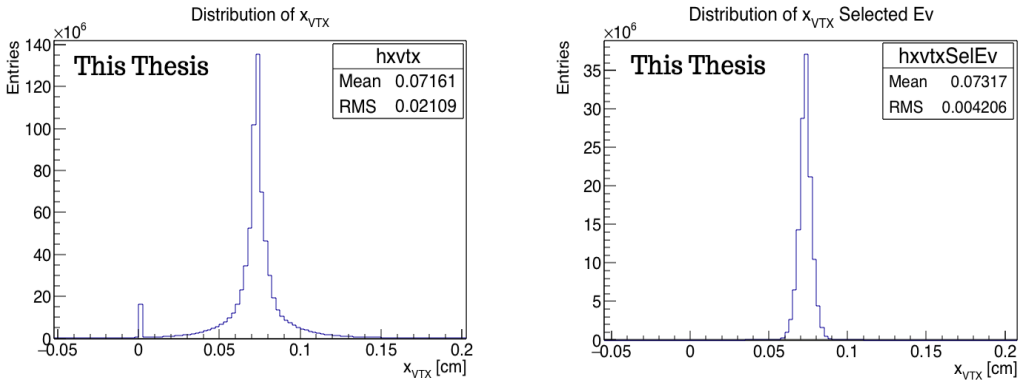

FIGURE 3.3: x-vertex distributions in the period LHC16k_pass1

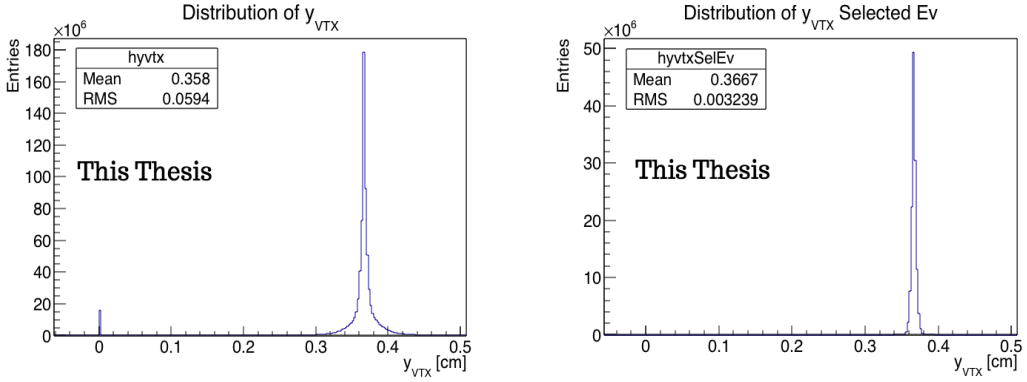

FIGURE 3.4: y-vertex distributions in the period LHC16k_pass1

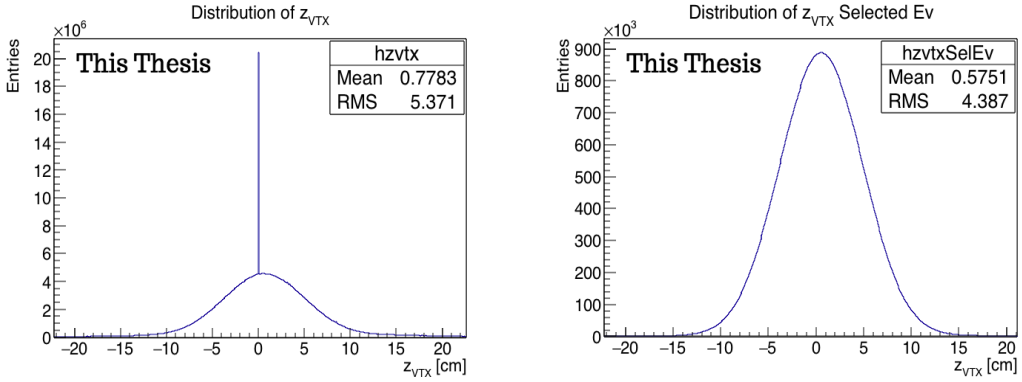

FIGURE 3.5: z-vertex distributions in the period LHC16k_pass1

Among the common distributions that characterise an event, one can mention the multiplicity. It presents the number of events with a determined number of particles in the event as displayed in figure.3.6. It was obtained for events produced in p-p collisions at 13 TeV. The distribution shows a normal behaviour where the number of produced particles is low for most events. The number of events gets smaller when a larger number of particles is

produced. This leads to the known fact that lower multiplicities are dominant compared to larger multiplicities.

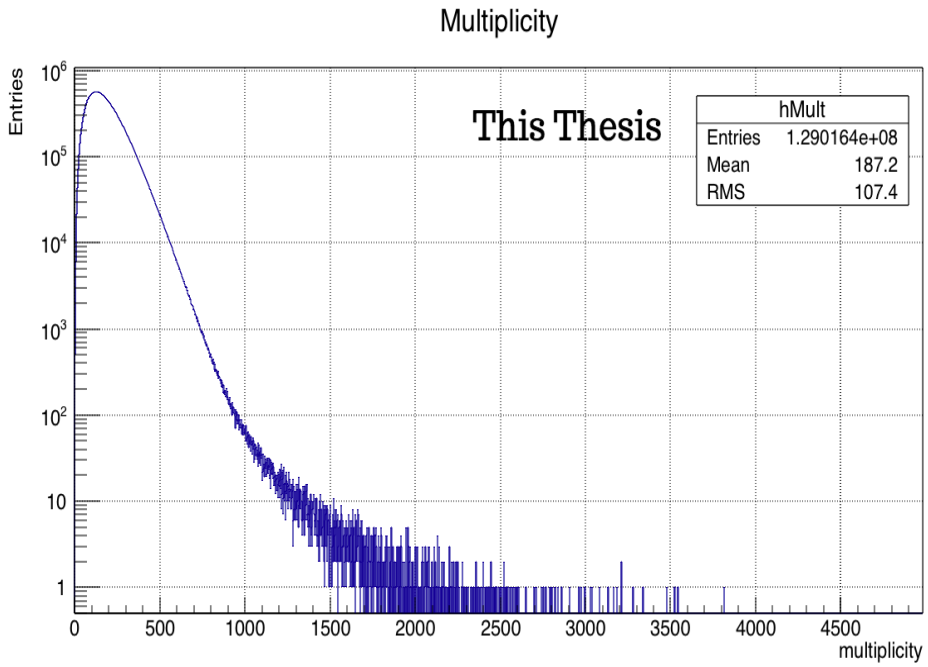

FIGURE 3.6: Multiplicity distribution of the period LHC16k_pass1

3.2.2 Tracks

To determine the impact parameter position in $r\phi$ direction, four different configurations were considered:
- Refit the trajectory points of the tracks in the ITS layers and requiring one hit in the inner SPD
- Refit by requiring one hit in one of the SPD layers (ITS),
- Fit the trajectory points in the TPC and requiring one hit in any SPD layers (ITS)
- The Filter Bit 4.

The distribution of the impact parameter obtained for these configurations in the period LHC16k_pass1 is presented in figure.3.7.

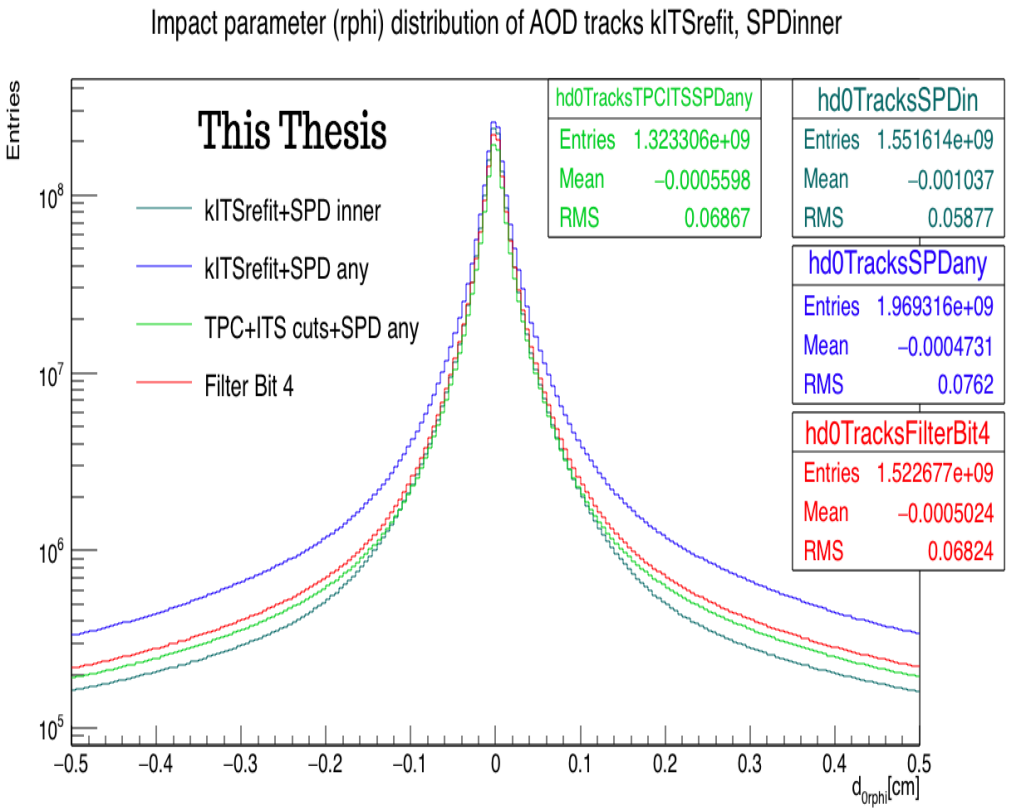

FIGURE 3.7: Impact parameter distributions of AOD tracks for different configurations : kITSrefit + SPD inner (dark green), kITSrefit + SPD any (blue), TPC+ITS cuts + SPD any (light green), Filter Bit 4 (red).

The distributions are in agreement qualitatively. Otherwise, it is reasonable to have a quantitative difference between the four distributions since the considered configurations include different (part of) detectors. Consequently, the number of tracks will be modified each time, and so does the impact parameter. However, the interpretation remains similar because of the narrow peak and the symmetric behaviour around rϕ =0 exhibited for the 4 cases. The best quality of tracks corresponds to the dark green distribution which is the narrowest.

Tracks distributions at the level of the ITS can be inspected. For instance, the number of AOD tracks with N SPD point in the left panel of figure.3.8 and the selected events distributions with N SPD point in the right panel of figure.3.8. One can see that there are AOD tracks with no point in the SPD that disappears in the distribution of selected tracks. This is probably due to the selection criteria where the selected tracks are required to have at least one hit point in one of the SPD layers which is the case according to the resulting distribution of the selected tracks in the right panel of figure.3.8.

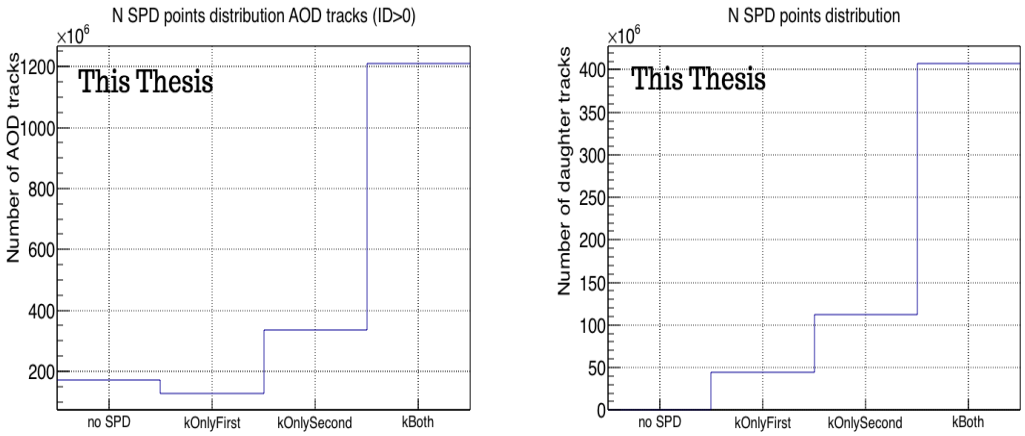

FIGURE 3.8: Distribution of tracks with N SPD points for AOD tracks (left) and selected tracks (right)

More globally, other characteristic distributions can be obtained as well concerning the ITS layers. For example, the distribution of AOD tracks with a point in one of the layers of the ITS is presented in the left panel of figure.3.9. The correspondent distribution for selected tracks with a point in the ITS layers is displayed in the right panel of figure.3.9. All six layers of the ITS can detect tracks passing by. Otherwise, the number of tracks with n point for some layers is reduced considerably compared to the others. This is probably due to the selection criteria or even the detection capability of the concerned layer.

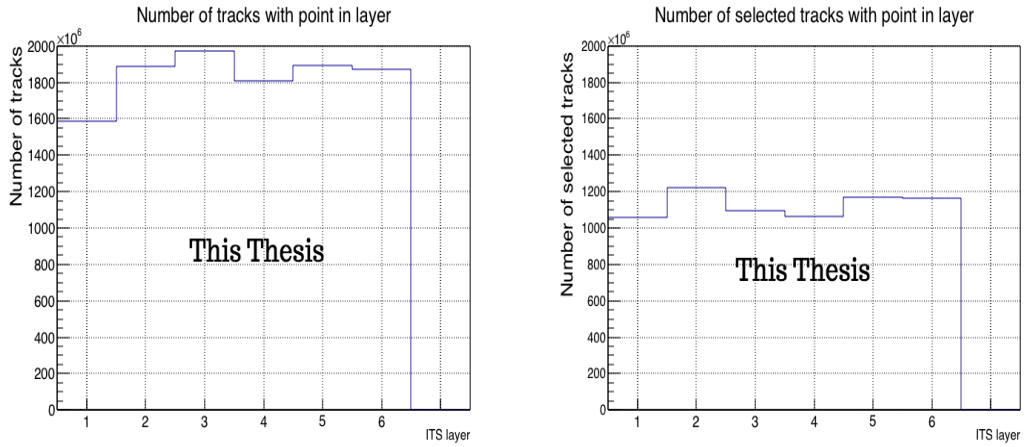

FIGURE 3.9: Number of tracks with N point in ITS layers (left) and number of selected tracks with N point in ITS layers (right)

The transverse momentum distributions are also obtained in the period LHC16k_pass1 for all tracks and daughter tracks as presented in figure.3.10 in the left and right panels, respectively. Both distributions show the ordinary behaviour of a p_{T}-spectrum where the number of produced particles is large at low p_{T}, and it gets smaller with increasing p_{T}.

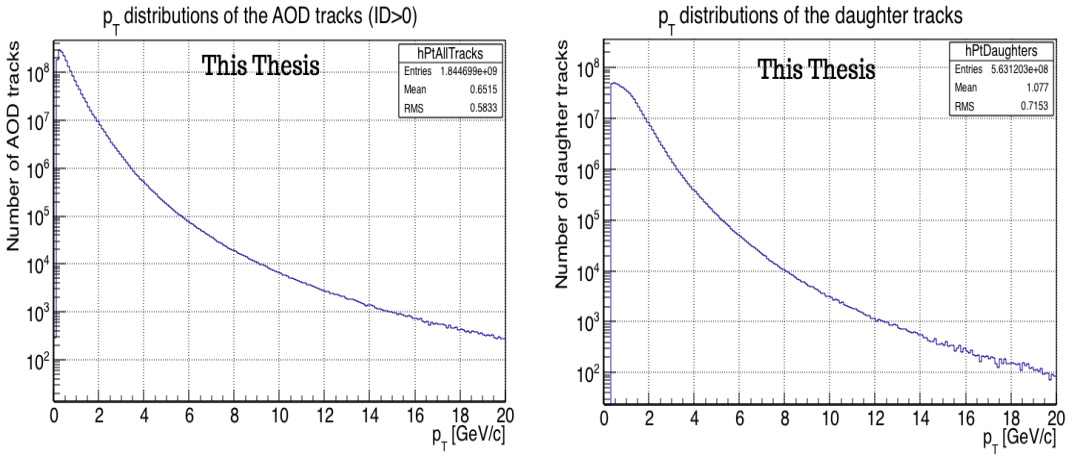

FIGURE 3.10: Transverse momentum distributions in the period LHC16k_pass1 for all tracks (left) and for daughter tracks (right).

The ϕ and η distributions of the tracks are presented in figure.3.11. The left panel shows the distribution for all tracks and the right one for the daughter tracks. The left distribution is limited in statistics (up to $\eta = 1$). This is the consequence of the selection cut applied on the pseudo-rapidity ($|\eta| < 0.9$) for the tracks. Concerning the ϕ direction, no cut was applied besides the TPC detector covers the full azimuth. The daughter distribution is limited to $\eta = \pm 0.8$ due to the selection criteria on the kaons and the pions. The low statistics around 2.2-2.3, 4, and 5 rad is due to the SPD dead pixels in this ϕ range.

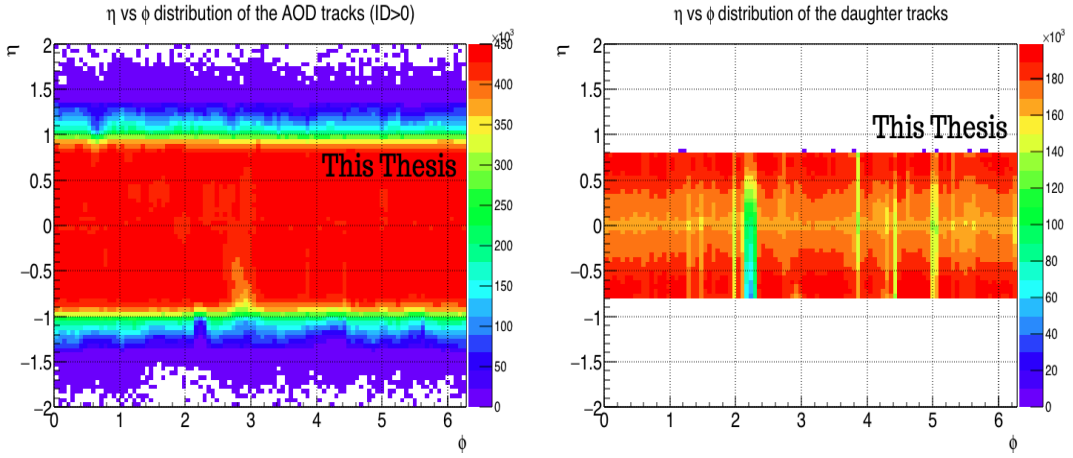

FIGURE 3.11: Distributions of all tracks (left) and daughters (right) as a function of ϕ and η.

The one-dimensional distributions for all tracks and daughter tracks as a function of ϕ and η are presented in figure.3.12 and figure.3.13, respectively.

For the case of "all tracks" (left panel of figure.3.12), the full acceptance along ϕ is visible, but the statistics are low in some ϕ regions, for example around $\phi = 3$, which is clearer in the 2-dimensional distribution in the left panel of figure.3.11. The inhomogeneities are more prominent in the daughter tracks distribution (right panel of figure.3.12) and reflecting the low statistics around $\phi \approx 2$ in the 2-dimensional distribution.

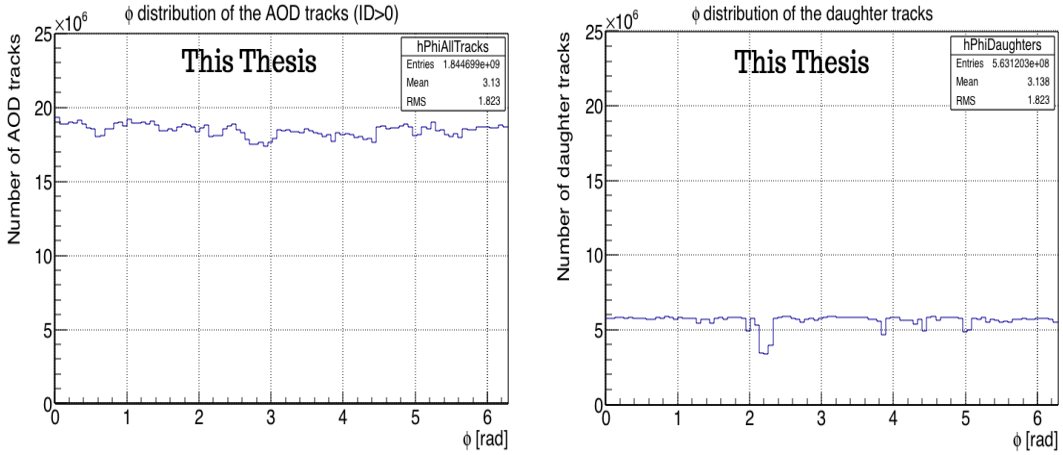

FIGURE 3.12: Distributions of AOD tracks (left) and daughters (right) as a function of ϕ.

For η distributions (figure.3.13), the limited acceptance is due to the acceptance of ALICE detector in the case of all tracks. Whereas, for the daughters tracks, the limited statistics are due to the selection cuts applied to K, π to be in the range $|\eta| < 0.8$.

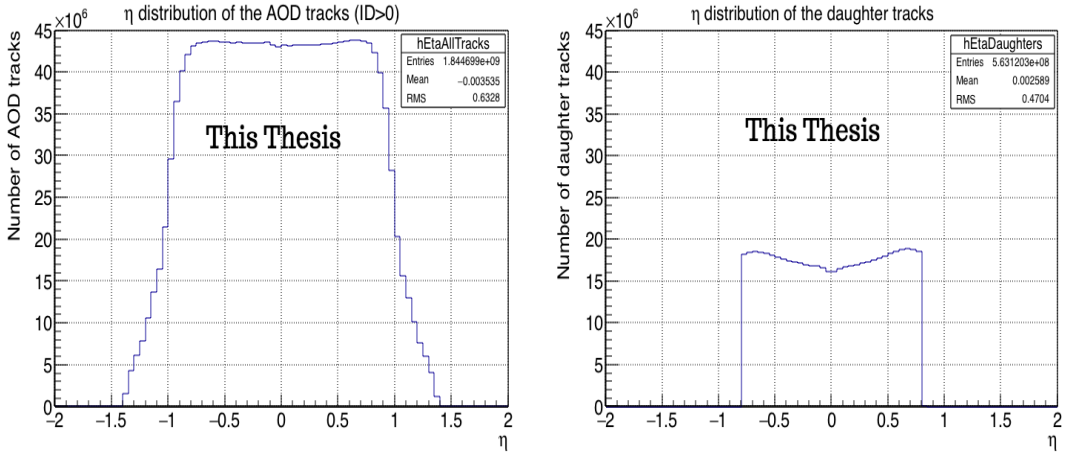

FIGURE 3.13: Distributions of AOD tracks (left) and daughters (right) as a function of η.

3.2.3 Particle Identification (PID)

PID-TPC

Although the QA figures for particle identification were obtained by considering only one period (LHC16k_pass1), the large statistics of the latter allowed for the extraction of clear distributions.

Figure.3.14 shows the signal obtained from the TPC which presents the specific energy loss dE/dx of particles as a function of their momentum. The identification of the particles is performed based on the specific energy loss that is proportional to the particle mass.

This correspondence is included in the Bethe-Bloch formula which is already introduced in chapter.2 (section 2.2.2).

Particle identification can be understood in a different perspective by obtaining the distributions of sigma as a function of momentum. The exploited sigma, in this case, is the one extracted from the fit of the specific energy loss with the Bethe-Bloche formula. The associated sigma distributions as a function of particle momentum p are presented in figure.3.15 for protons, pions and kaons.

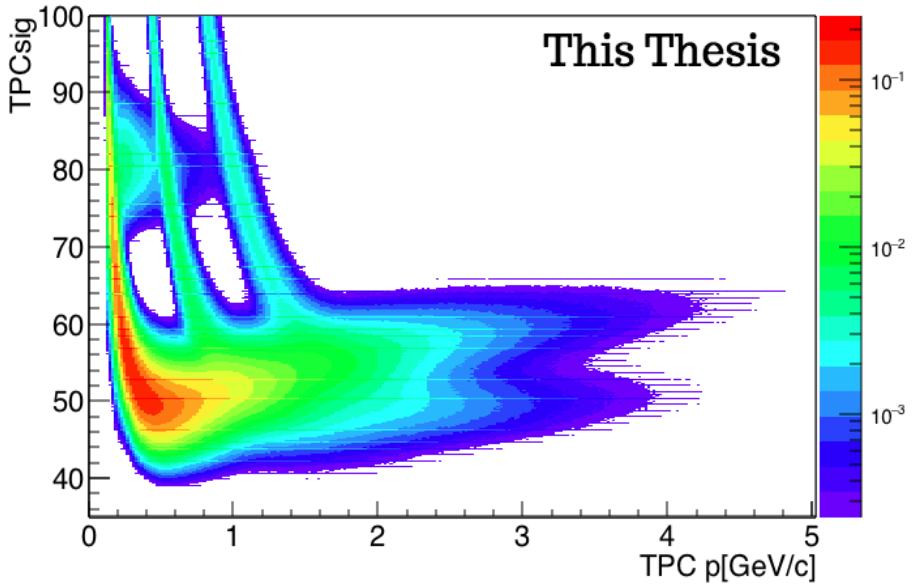

FIGURE 3.14: TPC signal as a function of the particle momentum for the period LHC16k_pass1 in p-p collisions at 13 TeV.

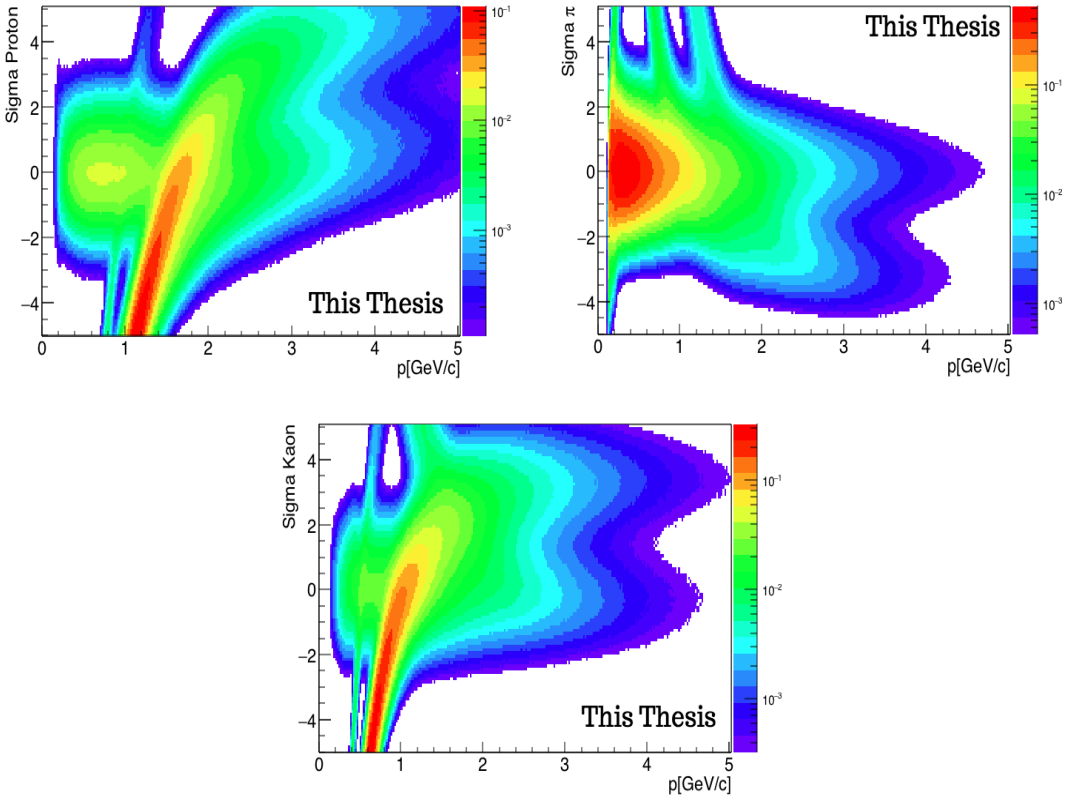

FIGURE 3.15: TPC sigma of the protons (top left), pions (top right) and kaons (bottom) as a function of the momentum for the period LHC16k_pass1 in p-p collisions at 13 TeV.

PID TOF

Figure.3.16 presents the measured time of flight of particles subtracted from the hypothesis time and normalised to sigma as a function of the momentum for the considered particles: protons, pions, kaons, respectively. From these PID figures, one can conclude that the main particles, important in the correlation analysis, can be identified.

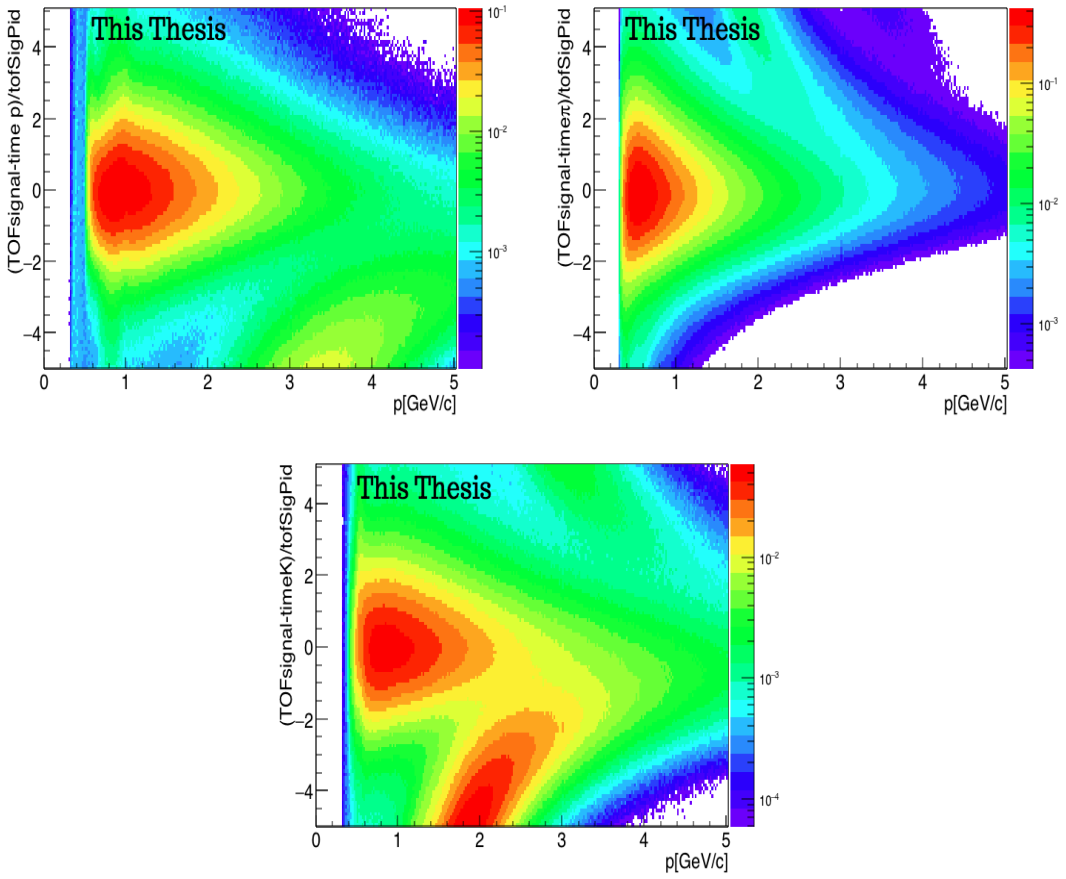

FIGURE 3.16: Measured Time of Flight - hypothesis time normalised by sigma for protons (top left), pions(top right), kaons (bottom) for the period LHC16k_pass1 in p-p collisions at 13 TeV.

3.3 Chapter conclusion

With ALICE and thanks to the characteristics of the TPC, TOF, and ITS detectors, it is possible to reconstruct D mesons and other particles, in addition to the ability to detect and identify them. This is feasible in the full range of ϕ and pseudo-rapidity range $|\eta| < 0.8$. The representative sample of data shown in this chapter is suitable and can be generalised for the other periods.

Chapter 4

Correlation analysis and Results

In this chapter, the analysis strategy applied to obtain the D^{*+}-hadron azimuthal correlation distributions in minimum bias proton-proton collisions at 13 TeV with the ALICE detector at the LHC is described.

4.1 Analysis strategy

The applied analysis strategy includes the reconstruction of D^{*+} mesons and charged particles, the efficiency corrections for both D^{*+} and associated tracks, background subtraction, correction for the purity due to secondary tracks contamination and finally subtraction of the B feed-down contribution to get the distributions of azimuthal correlations between prompt D^{*+}- primary charged particles.

1. **Reconstruction of D mesons** In this work, D^{*+} mesons are correlated with charged particles. Consequently, the first step is to reconstruct the D^{*+} candidates. This can be done via the hadronic decay channel: $\mathrm{D}^{*+} \rightarrow \mathrm{D}^0\pi$ (BR $\sim$ 67.7 %) $\rightarrow (K\pi)\pi$ (BR $\sim$ 2.62 %) i.e. a pion (soft pion) is combined with the D^0 candidate, which in turn is reconstructed by combining two tracks with opposite charges (supposed to be a pion and a kaon). The pions and kaons are identified with the TPC and TOF (plus the ITS for kaons). This step results in the invariant mass of the D^{*+} mesons reconstructed in the transverse momentum range $3 < p_{\mathrm{T}} < 16$ GeV/c. The mass difference M($K\pi\pi$)-M($K\pi$) is exploited instead of the ordinary spectrum M($K\pi\pi$) because of the resolution effects of the D^0 that cancels partially resulting in a narrower peak. Moreover, the D^{*+} signal, in the mass difference, sits close to the end phase space for the combinatorial background. Therefore, it ensures a high value of the signal-over-background (S/B).

2. **Reconstruction of associated tracks** After reconstructing D^{*+} mesons, which we refer to as the trigger particles, each of them is correlated with charged particles (associated tracks). The second step then in this analysis strategy is the reconstruction of associated tracks. The contribution from the daughters of the trigger particles is removed. Those charged particles are reconstructed in the pseudo-rapidity range $|\eta| < 0.8$ with a transverse momentum range p_{T}(assoc) $>$ 0.3 GeV/c.

3. **Single and mixing events** is the following step where correlation between the reconstructed D^{*+} and the associated tracks is performed. For each correlated pair D meson - charged particle, the difference in azimuthal angle (ϕ) and pseudo-rapidity (η) is calculated,

$$\Delta\phi = \phi^{assoc} - \phi^{trigg} \tag{4.1}$$

$$\Delta\eta = \eta^{assoc} - \eta^{trigg} \tag{4.2}$$

   If the correlated pairs are in the same event, the obtained distribution is called "single event". If those pairs are from two different events, the obtained distribution is called "mixing event". Both single and mixing events distributions are obtained in the signal region and the sideband region (background) of the D^{*+} candidates. The mixing event distribution is exploited in the correlation analysis to correct for the limited acceptance of the detectors and for the possible inhomogeneities that could exist in these detectors.

4. **Efficiency correction for D^{*+} and associated tracks.** The efficiency distribution corresponds to the fraction of the reconstructed number of particles to the generated one as a function of the transverse momentum and the multiplicity for D mesons. For the associated tracks, the vertex in the z-direction and the rapidity y are considered in addition to the transverse momentum p_{T}. At this step of the analysis, the invariant mass spectra are weighted by the inverse of the D^{*+} efficiency distribution. For the single events and mixing events, on the other side, they are weighted by the inverse of the product of D^{*+} and associated tracks efficiencies.

5. **Projection on $\Delta\phi$.** The single event distributions are scaled by the mixing event distributions in the considered transverse momentum ranges and for both signal and sideband regions. The signal region lies within $\pm 2\sigma$ from the peak position (or the mean) while the sideband region is considered in the range [4-8]σ on the right side from the peak position. The distributions obtained in the sideband region are scaled to those in the signal region. The scaling exploits a factor extracted from the fit of the D^{*+} invariant mass spectra. Once the corrected single event distributions (signal and sideband) are obtained, the projection is performed along $\Delta\phi$.

6. **Background subtraction.** The previous step resulted in two $\Delta\phi$ distributions, D(signal)-hadron and D(sideband)-hadron correlation distributions. Background subtraction is done with the scaled correlation distribution obtained in the sideband region from the one obtained in the signal region. After that, normalisation to the number of triggers (number of D^{*+} in the peak region) is done.

7. **Correction for the secondary tracks contamination.** In these analyses, we are interested in the correlations of D^{*+} with charged tracks only coming from the primary vertex. To reject the secondary charged tracks, we take advantage of a Monte Carlo sample to get the purity (to be used as a scale factor) that corresponds to the

fraction of primary particles. In this way, the primary charged tracks only are correlated with the D^{*+} mesons.

8. **Subtraction of the B feed-down contribution.** At this step, we are interested in prompt D^{*+} mesons only .i.e those coming directly from the fragmentation of charm quarks. It is not always the case since a fraction of D mesons can be produced from B-meson decays. To correct for this effect, we use a Monte Carlo template to obtain the correlation distribution of B $\rightarrow$ D-hadrons that will be subtracted from the distribution D(inclusive)-hadrons. In the end, the obtained distribution is the azimuthal angular correlations between prompt D^{*+} and primary charged particles.

4.2 Analysis results in pp collisions at 13 TeV

In this section, the results obtained using the analysis strategy described briefly above are presented. More details are provided on those steps later.

4.2.1 D^{*+} mesons reconstruction

- **Topological cuts** The reconstruction of D^{*+} decay topology is not possible via three charged tracks because the decay is strong .i.e too fast. Therefore, D^{*+} mesons are reconstructed by the combination of soft pion and a D^0. In turn, D^0 is reconstructed by combining two charged tracks with opposite charges (K and π) to get the displaced primary and secondary vertices to rebuild the topology decay of D^0, as displayed in the figure.4.1.

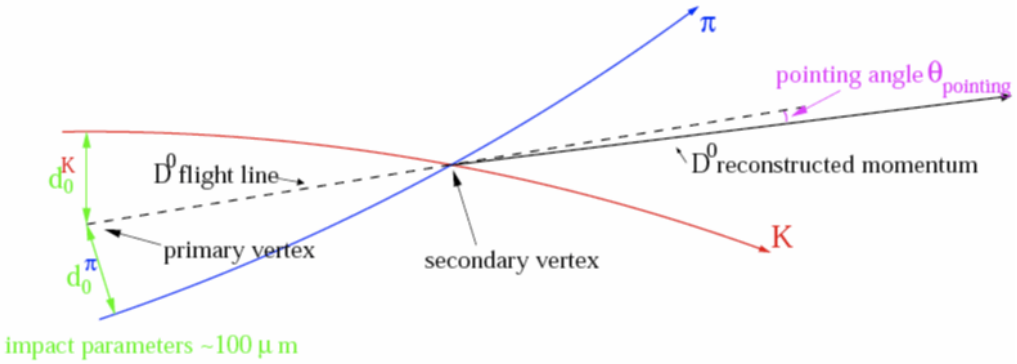

FIGURE 4.1: D^0 decay topology

On this principle, one can have up to 16 parameters or what is called topological cuts that are p_T dependent. Those parameters are explained in the following:

1. D^0 **invariant mass M($K\pi$)**, is an upper cut applied on the mass range of D^0 in order to have the combined mass of K and π within the expected range of D^0 mass.

2. **dca** is an upper cut applied on the distance of the closest approach between the daughters of the D^0 (Kaons and pions).
3. **cos**θ^* is an upper cut on θ^* where θ^* is the angle between the D^0 and the Kaon in the rest frame of the D^0.
4. $p_{\mathrm{T}}(K)$ lower cut to be applied on the transverse momentum of the Kaon.
5. $p_{\mathrm{T}}(\pi)$ lower cut to be applied on the transverse momentum of the pion.
6. $d_0(K)$ The impact parameter of the kaon is the distance of the closest approach between the primary vertex and the decay path of the kaon in the transverse plane (upper cut).
7. $d_0(\pi)$ The impact parameter of the pion is the distance of the closest approach between the primary vertex and the decay path of the pion in the transverse plane (upper cut).
8. $d_0(K)\mathbf{x}d_0(\pi)$ vectorial product of the impact parameters of the kaon and the pion (upper cut).
9. **cos**θ_{point} is a lower cut to be applied on θ_{point}, where θ_{point} is the angle between the reconstructed D^0 momentum and the flight line relating between the primary and the secondary vertices (lower cut).
10. **Half width of D^{*+} invariant mass** an upper cut applied on the window of the peak in the D^{*+} invariant mass.
11. **Half width of M($K\pi\pi$)-M($K\pi$)** an upper cut applied on the window of the peak in the M($K\pi\pi$)-M($K\pi$) invariant mass spectra.
12. $p_{\mathrm{T}}^{min}(\pi_{soft})$ minimum transverse momentum of the soft pion.
13. $p_{\mathrm{T}}^{max}(\pi_{soft})$ maximum transverse momentum of the soft pion.
14. Θ angle between the π_{soft} and decay plane of the D^0 (lower cut).
15. $|cosThetaPointXY|$ is the cosine of the angle θ_{point} in the XY plane. This cut is more sensitive in Pb-Pb collisions.
16. **NormDecayLenghtXY** represents the decay length in the XY plane, and it is also more sensitive in Pb-Pb collisions.

The values of the topological cuts - exploited to reconstruct D* mesons in the considered kinematical range in pp collisions at 13 TeV - are summarised in Table.B.2 in the Appendix.B. In addition to the 16 parameters, some additional selection criteria are applied on the D^{*+} candidates (the daughters of D^{*+}) and they are summarised in Table.B.1 in the Appendix.B.

- **Efficiency correction for D^{*+}** : The detectors are not perfect. Consequently, the number of measured (detected) D^{*+} is not the number of the produced D^{*+}. A

Monte Carlo (MC) sample (LHC17c3a1 and LHC17c3a2) is exploited to obtain the efficiency distribution to correct for this effect. The efficiency is nothing but the ratio $Reco(MC)/Gen(MC)$ where $Reco(MC)$ symbolizes the reconstructed D^{*+} mesons hypothetically with similar kinematics as in data while $Gen(MC)$ stands for the generated D^{*+} mesons within a determined acceptance.

An example of a D^{*+} efficiency distribution is presented in Figure.4.2. The top left plot presents the efficiency distribution of prompt D^{*+} as a function of p_T and multiplicity while the top right plot shows the efficiency as a function of p_T only. The bottom left plot presents the efficiency of D^* from B feed-down as a function of p_T and multiplicity, and the bottom right plot is the efficiency distribution as a function of p_T only. For both distributions (prompt and B feed-down), one can notice that the efficiency $\times$ Acc is getting larger with increasing transverse momentum and the increase gets slow at high p_T bins. The efficiency does not show an important dependence as a function of the multiplicity.

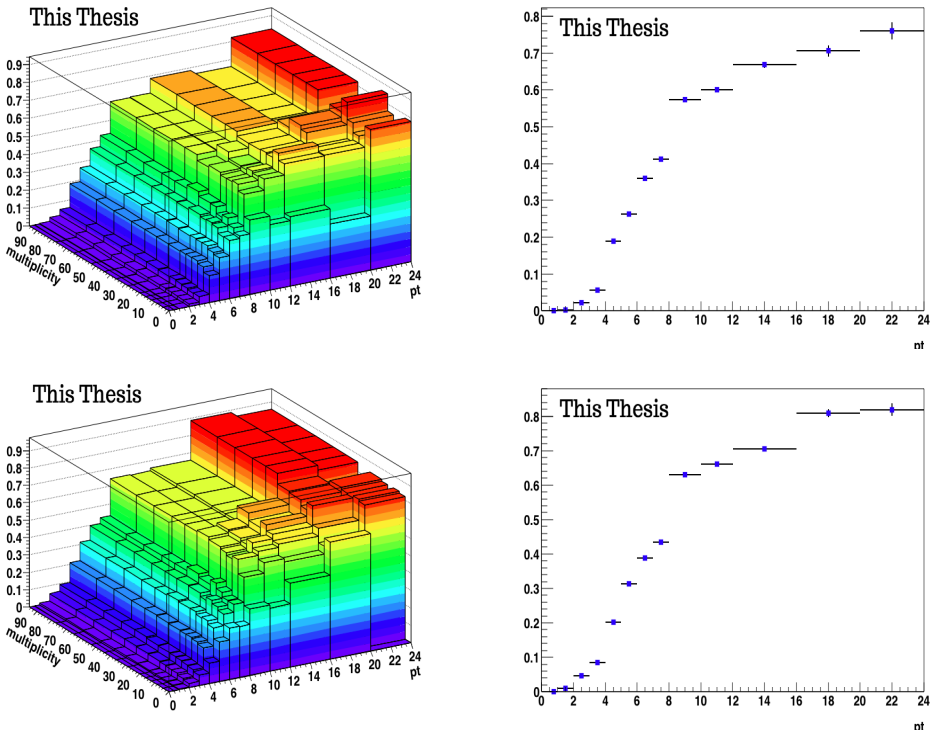

FIGURE 4.2: Efficiency x acceptance distributions versus the transverse momentum and the multiplicity obtained in minimum bias p-p collisions at 13 TeV for c $\rightarrow$ D^{*+} (top left), c $\rightarrow$ D^{*+} as a function of p_T only (top right), b $\rightarrow$ D^{*+} (bottom left) and b $\rightarrow$ D^{*+} as a function of p_T only (bottom right).

The correction at this step is performed by weighting the invariant mass spectra, single and mixed events distributions by the inverse of the efficiency. Within the next sections, only the obtained distributions with efficiency correction are presented.

- **Invariant mass spectra**: D^{*+} mesons are reconstructed by combining three tracks

to obtain the invariant mass spectra M(K$\pi\pi$)-M(Kπ). The signal or the peak representing the D^{*+} is expected to be at 145.42 MeV/c^2. 3 up to 16 GeV/c is the considered kinematical range to reconstruct the D^{*+}. The obtained invariant mass spectra at low $p_{\mathrm{T}}(3 < p_{\mathrm{T}} < 5$ GeV/$c)$, intermediate $p_{\mathrm{T}}(5 < p_{\mathrm{T}} < 8$ GeV/$c)$ and high $p_{\mathrm{T}}(8 < p_{\mathrm{T}} < 16$ GeV/$c)$, are presented in figure.4.3, figure.4.4, figure.4.5, respectively. To obtain the number of triggers (D^{*+}) in the peak region for the considered p_{T} ranges, the invariant mass spectra of the D^{*+} is supposed to be a sum of two spectra, the first is the signal represented by the peak and the second is the background represented by the threshold function convoluted with an exponential. The signal and background distributions are expressed by the equations.4.3 and 4.4, respectively.

$$Y_D \frac{1}{\sqrt{2\pi}\sigma} e^{\frac{(\Delta M-\mu)^2}{2\sigma^2}} \tag{4.3}$$

$$a\sqrt{\Delta M - M_\pi} \times e^{b(\Delta M - M_\pi)} \tag{4.4}$$

ΔM and M$_\pi$ refer to the invariant mass spectra and the pion mass, respectively. The invariant mass spectra are fitted using the sum of the signal and background functions. From the fit and for each p_{T} range, the values of the constants Y_D, μ, σ, a and b are obtained, and they symbolize respectively the number of triggers, the peak position (mean), the width of the peak and the background parametrisation. In this procedure, the parameters a and b are determined first by fitting the background only (presented by the red line in the invariant mass spectra figure.4.3, figure.4.4, figure.4.5). After that, the constants a and b are fixed and a fit is performed for the whole mass spectra (presented in blue line in the invariant mass spectra figure.4.3, figure.4.4, figure.4.5). The values of the fit parameters are of great importance, specifically, the number of triggers and the scale factor that will be used at later steps for the normalisation and for scaling the background to the signal, respectively.

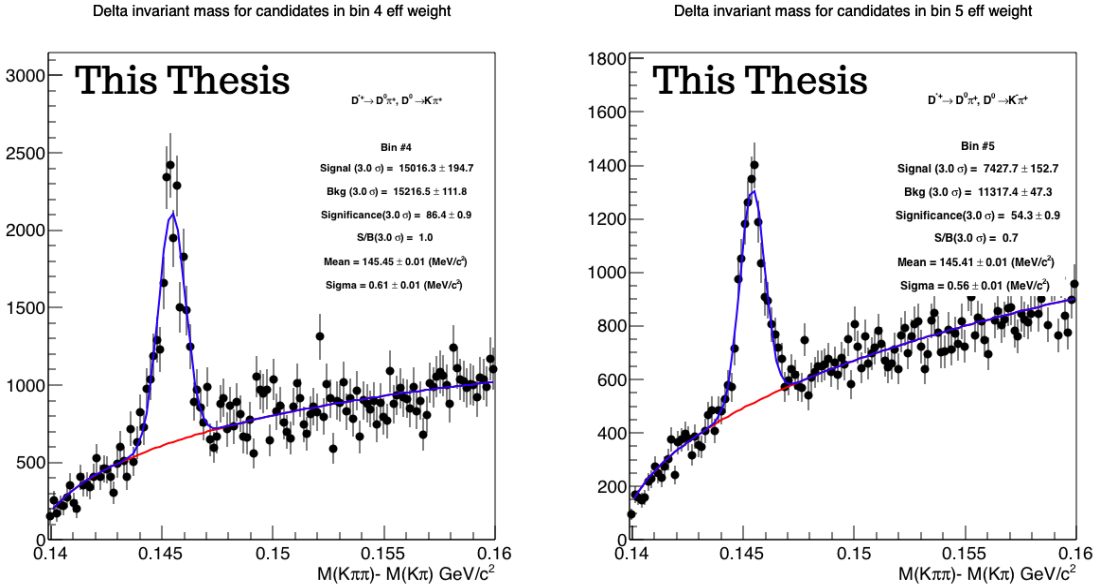

FIGURE 4.3: Invariant mass spectra ΔM = M($K\pi\pi$)-M($K\pi$) in the ranges $3 < p_{\rm T} < 4$ GeV/c (left) $4 < p_{\rm T} < 5$ GeV/c (right) in minimum bias p-p collisions at $\sqrt{s}$ =13 TeV.

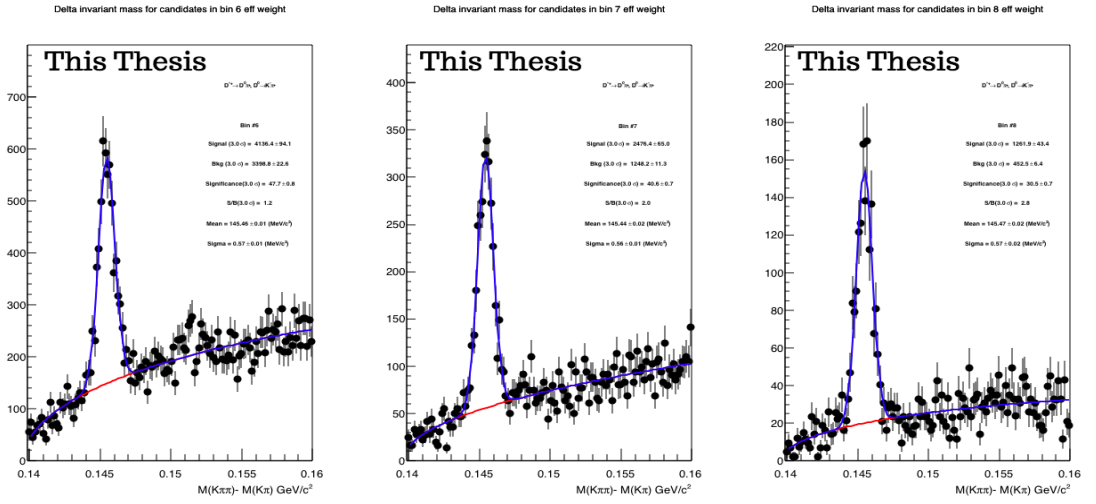

FIGURE 4.4: Invariant mass spectra ΔM = M($K\pi\pi$)-M($K\pi$) in the ranges $5 < p_{\rm T} < 6$ GeV/c (left), $6 < p_{\rm T} < 7$ GeV/c (middle), $7 < p_{\rm T} < 8$ GeV/c (right) in minimum bias p-p collisions at $\sqrt{s}$ =13 TeV.

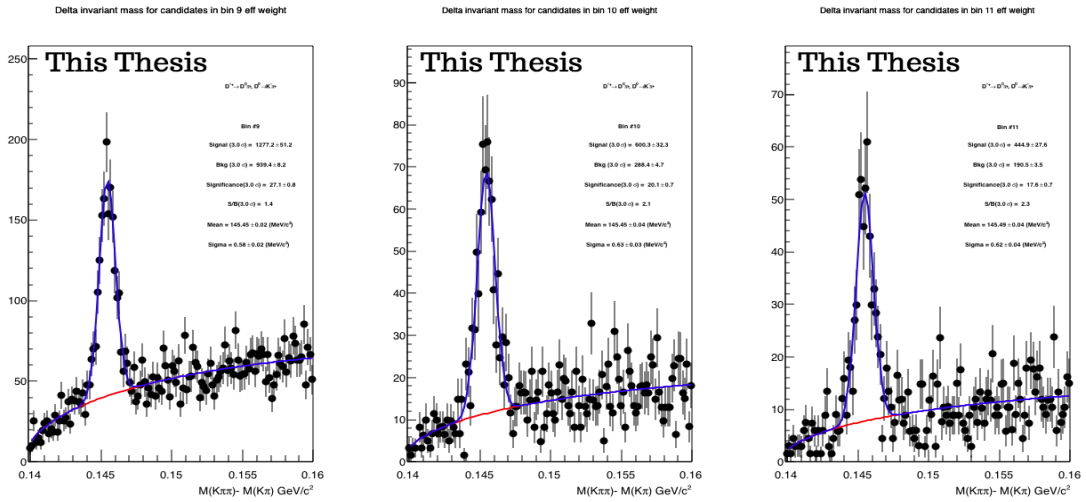

FIGURE 4.5: Invariant mass spectra ΔM = M($K\pi\pi$)-M($K\pi$) in the ranges $8 < p_{\mathrm{T}} < 10$ GeV/c (left), $10 < p_{\mathrm{T}} < 12$ GeV/c (middle), $12 < p_{\mathrm{T}} < 16$ GeV/c (right) in minimum bias p-p collisions at $\sqrt{s}$ =13 TeV.

4.2.2 Tracks reconstruction

The associated tracks (charged particles) in these analyses include mostly protons, kaons, pions, and electrons. Some selection criteria are also required, and they are summarised in Table.B.3 in the Appendix.B. The daughters of the D^{*+} (kaons and pions) are not considered.

- **Efficiency correction for tracks** : The correction for the efficiency of the tracks is needed for the same reason mentioned earlier for the D^{*+} mesons. A Monte Carlo sample (LHC17d20a1_extra and LHC17d20a2_extra) is also exploited. In this sample, there is no enhancement concerning the production of any particle species which is convenient to correct for associated tracks efficiency. An example distribution is presented in Figure.4.6.

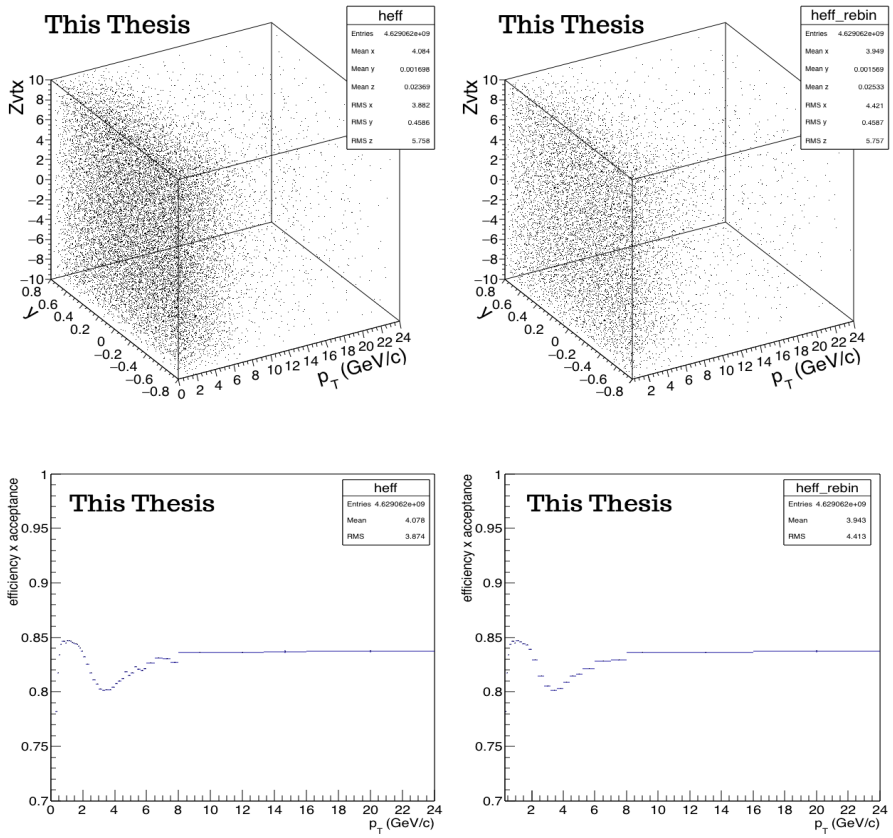

FIGURE 4.6: Efficiency x Acceptance distribution of the associated tracks, versus p_{T}, rapidity (y) and Z_{vertex} (top left), vs p_T only (bottom left). Rebinned distribution vs p_{T}, rapidity (y) and Z_{vertex} (top right) and the rebinned distribution vs p_T only (bottom right).

The associated tracks efficiency is dependent on the transverse momentum (p_{T}), the rapidity (y), and the vertex position of the tracks in Z direction (Z_{vtx}). The top left plot of figure.4.6 presents the efficiency distribution as a function of p_T, y, Z_{vtx}. The bottom left plot is the efficiency distribution projected on p_T. The right column (top and bottom plots) are similar to those on the left but they have been rebinned.

The efficiency shows a p_T dependence at low and intermediate p_T. At high p_T, the distribution is stable where a plateau is formed, down to 8 GeV/c.

4.2.3 Single events and mixed events distributions

The goal of this step is to obtain the single events and mixing events distributions. Mixing events is a technique used in correlation analysis to correct for the existing inhomogeneities and the limited acceptance in the detector. Single events distribution is obtained by combining, in the same event, a D^{*+} candidate with a charged track. For each D-hadron pair, the differences of the azimuthal angle and pseudo-rapidity are calculated ($\Delta\eta = \eta_D - \eta_h$ and $\Delta\phi = \phi_D - \phi_h$) and this results in a 2-dimensional distribution (as a function of $\Delta\eta$ and $\Delta\phi$). Two cases are distinguished, the D^{*+} candidates are considered either in the signal

region or the sideband region. This way, two distributions are obtained for single events, one in the signal region and the other one in the sideband region. Mixing events distributions are also obtained in the signal region and sideband region. We end up with four distributions: single events and mixing events; for each of them, there is a correspondent distribution in the signal and sideband regions. Furthermore, those four distributions are obtained for the three considered p_{T} ranges [3-5], [5-8], and [8-16] GeV/c as presented in figure.4.7, figure.4.8 and figure.4.9, respectively where the efficiency is already taken into account.

In each figure, the top row corresponds to the distributions in the signal region and the bottom one to those in the sideband region. The left column presents the single event distribution, the middle column presents the mixing events, and the right column displays the corrected single event distribution.

The mixing event distribution is flat in $\Delta\phi$. It reflects the full acceptance of the detectors (ITS, TPC, and TOF) in azimuth. Concerning the triangular shape in $\Delta\eta$, it is the consequence of the pseudo-rapidity acceptance of ALICE detector which is $|\eta| < 0.8$. The mixing event distributions are already normalised to the central bin ($\Delta\phi$,$\Delta\eta$)=(0,0). The central bin is exploited because the D^{*+} mesons and the charged hadrons undergo the same effects.

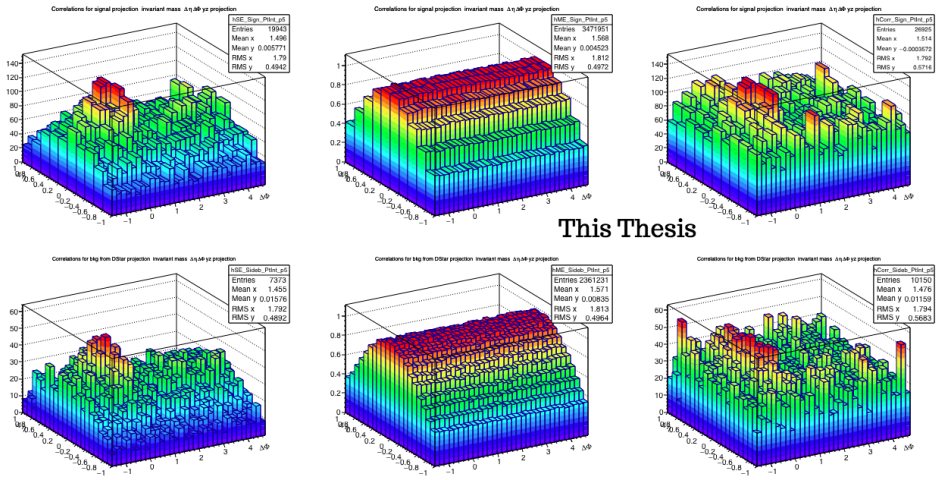

FIGURE 4.7: Top row: Single events distribution (left), mixing event distribution (middle), corrected single event distribution (right) in the signal region. Bottom row: Single events distribution (left), mixing event distribution (middle), corrected single event distribution (right) in the sideband region. The distributions are obtained for pool number 5 in the range $3 < p_{\mathrm{T}} < 5$ GeV/c.

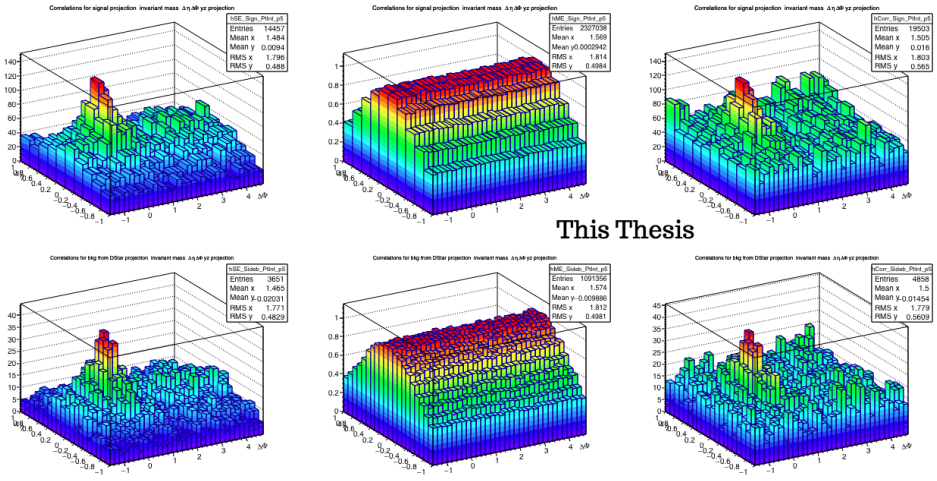

FIGURE 4.8: Same as figure 4.7 for the range $5 < p_{\mathrm{T}} < 8$ GeV/c.

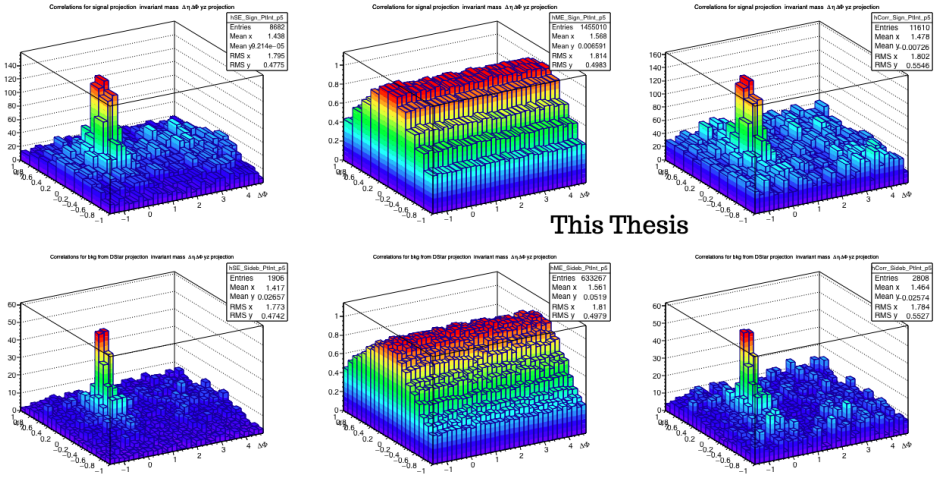

FIGURE 4.9: Same as figure 4.7 for the range $8 < p_{\mathrm{T}} < 16$ GeV/c.

4.2.4 Corrected single events

At this step, the obtained single events $C(\Delta\phi, \Delta\eta)$ in the signal region and sideband region are corrected using the normalised mixing event distributions $ME(\Delta\phi, \Delta\eta)$ in each p_T range. This correction can be expressed by,

$$C^{corr}_{peak}(\Delta\phi, \Delta\eta) = \frac{C(\Delta\phi, \Delta\eta)}{< ME(\Delta\phi, \Delta\eta) >}\Bigg|_{peak}, \tag{4.5}$$

$$C^{corr}_{sideband}(\Delta\phi, \Delta\eta) = \frac{C(\Delta\phi, \Delta\eta)}{< ME(\Delta\phi, \Delta\eta) >}\Bigg|_{sideband} \tag{4.6}$$

$< ME(\Delta\phi, \Delta\eta) >$ is defined by,

$$< ME(\Delta\phi, \Delta\eta) >= \left(\frac{ME(\Delta\phi, \Delta\eta)}{ME(0,0)} \right)_{Mixed \quad Events} \tag{4.7}$$

In the old analysis procedure [95] [96] [97] [98], this step is performed in the integrated pool of events. A pool is a concept referring to the number of events as a function of multiplicity and Z_{vtx}. In the recent procedure applied in this thesis, the integrated pool is divided into 9 pools by considering the $multiplicity$ limits 0, 20, 35, 200 and Z_{vtx} limits -10, -2.5, 2.5, 10. Both single events and mixed events are obtained in each pool as well as the corrected single events distributions (correction pool-by-pool). An example distribution is presented for pool number 5 obtained in p-p collisions at 13 TeV for the ranges [3,5] GeV/c, [5,8] GeV/c, [8,16] GeV/c in the right columns of figure.4.7, figure.4.8, figure.4.9, respectively. The top ones correspond to the distributions obtained in the signal region and those in the bottom present the distributions in the sideband region.

The corrected single events distributions obtained in the integrated pool of event are presented in figure.4.10, figure.4.11 and figure.4.12 for the 3 D^{*+} p_{T} and the 3 p_T associated tracks ranges are presented in both signal region and sideband region.

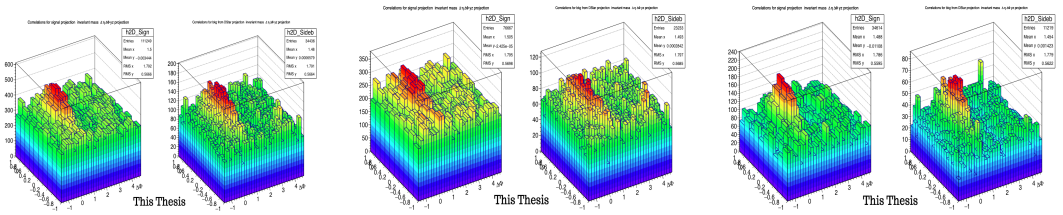

FIGURE 4.10: Corrected single events distributions obtained in the integrated pool for the associated tracks range $p_{\mathrm{T}} > 0.3$ GeV/c (two leftmost plots: in the signal region (left) and in the sideband region (right)), $0.3 < p_{\mathrm{T}} < 1$ GeV/c (two middle plots : in the signal region (left) and in the sideband region (right)), $p_{\mathrm{T}} > 1$ GeV/c (two rightmost plots : in the signal region (left) and in the sideband region (right)) in the range $3 < p_{\mathrm{T}} < 5$ GeV/c.

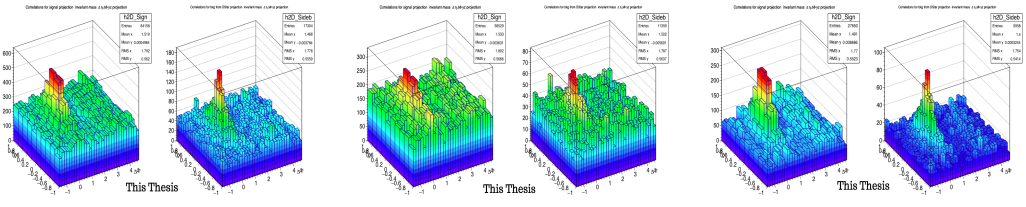

FIGURE 4.11: Same as figure.4.10 in the range $5 < p_{\mathrm{T}} < 8$ GeV/c.

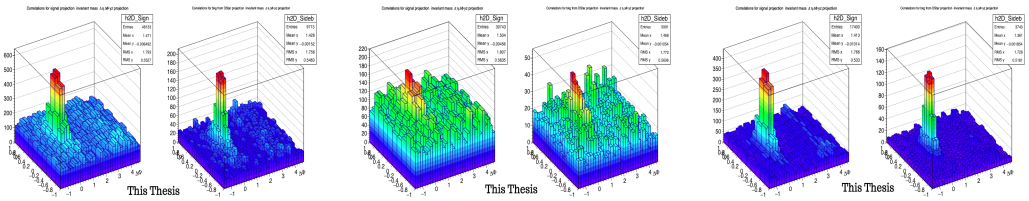

FIGURE 4.12: Same as figure.4.10 in the range $8 < p_{\mathrm{T}} < 16$ GeV/c.

4.2.5 Projection on $\Delta\phi$

The lack of statistics does not allow for a 2-dimensional study of correlations because of that this step is not optional. The distributions obtained in the previous step (corrected single event) are projected along $\Delta\phi$. For each p_T range, the $\Delta\phi$ correlation distribution in the sideband region is scaled to the one obtained in the signal region using the scale factor defined by:

$$\frac{\int_{peak} Background(\Delta M)}{\int_{Sideband} Background(\Delta M)} = \frac{B_{peak}}{B_{sideband}} \tag{4.8}$$

where B_{peak} and $B_{sideband}$ are the number of background D^{*+} candidates in the peak region and sideband region, respectively.

The one-dimensional distributions of the correlated pairs (D-hadron) projected on $\Delta\phi$ are displayed in figure.4.13 for the 3 considered $p_{\mathrm{T}}(D^{*+})$ ranges : $3 < p_{\mathrm{T}}(D^{*+}) < 5$ GeV/c, $5 < p_{\mathrm{T}}(D^{*+}) < 8$ GeV/c and $8 < p_{\mathrm{T}}(D^{*+}) < 16$ GeV/c in the top, middle and bottom rows, respectively. For each p_T range, the corresponding distributions in the integrated p_{T} of associated tracks $p_T(h) > 0.3$ GeV/c are shown as well as the subranges : $0.3 < p_{\mathrm{T}}(h) < 1$ GeV/c and $p_{\mathrm{T}}(h) > 1$ GeV/c.

The distributions in the sideband region are presented in red points and those in the signal region in blue points. Each distribution is normalised to the number of D^{*+} candidates in the sideband region and the signal region, respectively. The black points present the distribution of correlation after background subtraction which will be discussed in detail in the next step.

According to these curves, one can notice that the distribution of correlations with D^{*+} candidates in the sideband region (red points) is higher in comparison to the one with D^{*+} in the signal region (blue points). This is reasonable since the number of correlated pairs in the sideband region is larger than the number of pairs in the signal region. In addition, the distribution in the sideband region is not yet scaled to the one in the signal region. After scaling, it is possible to perform the background subtraction to get the final correlations (black points).

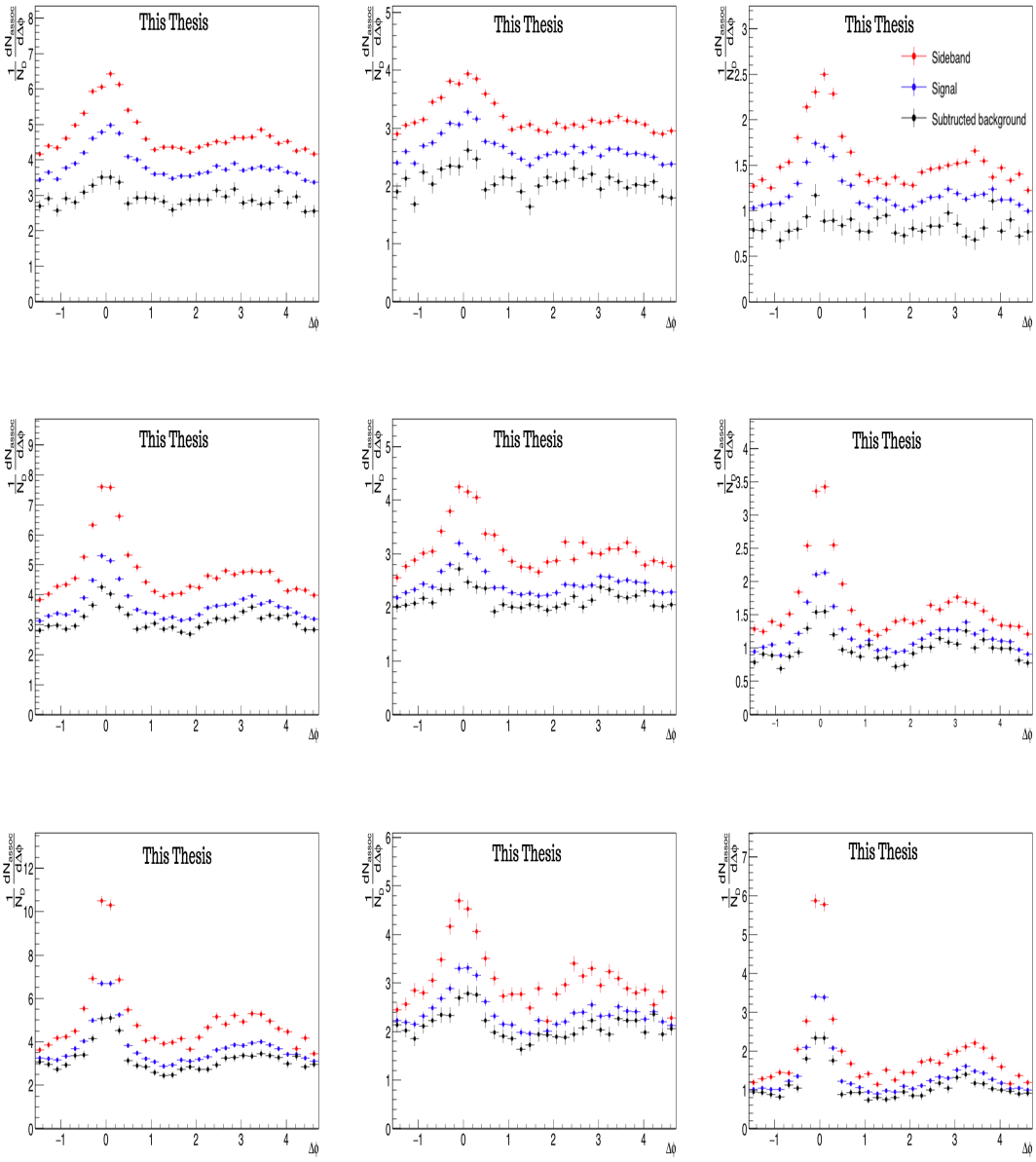

FIGURE 4.13: Normalised D^{*+}-hadron correlation distributions in the ranges $3 < p_{\mathrm{T}}(D^{*+}) < 5$ GeV/c (top row), $5 < p_{\mathrm{T}}(D^{*+}) < 8$ GeV/c (middle row) and $8 < p_{\mathrm{T}}(D^{*+}) < 16$ GeV/c (bottom row) with the associated tracks ranges : $\mathrm{p}_T > 0.3$ GeV/c (left column), $0.3 < p_{\mathrm{T}} < 1$ GeV/c (middle column) and $\mathrm{p}_T > 1$ GeV/c (right column) for D^{*+} mesons considered in the sideband region (red points), in the signal region (blue) and the corrected ones after background subraction (black points).

4.2.6 Background subtraction

After the background is scaled to the signal, the subtraction can be performed to obtain the normalised angular correlation distribution $C_{Norm}(\Delta\phi, \Delta\eta)$. This is expressed by,

$$C_{Norm}(\Delta\phi, \Delta\eta) = \frac{1}{S_{peak}} \left(\frac{C(\Delta\phi, \Delta\eta)}{< ME(\Delta\phi, \Delta\eta) >} \Bigg|_{peak} - \frac{B_{peak}}{B_{sideband}} \frac{C(\Delta\phi, \Delta\eta)}{< ME(\Delta\phi, \Delta\eta) >} \Bigg|_{sideband} \right) \tag{4.9}$$

It is interesting to have a look at correlation distributions in 2 dimensions (as a function of $\Delta\phi$ and $\Delta\eta$) before the projection on $\Delta\phi$ and without normalisation to the number of triggers. The corresponding distributions of correlations are shown in figure.4.14. The top, middle and bottom rows correspond to the $p_T(D^{*+})$ ranges [3-5] GeV/c, [5-8] GeV/c and [8-16] GeV/c respectively while the left, middle and right columns present respectively the distributions in the p_T(associated tracks) ranges $p_T > 0.3$ GeV/c, $0.3 < p_T < 1$ GeV/c and $p_T > 1$ GeV/c.

Although the statistics are not enough, one can see clearly in the 2-dimensional distributions that the near side peak ($\Delta\phi = 0$) is visible, and it is getting narrower at higher p_T while the away side peak ($\Delta\phi = \pi$) is not clear where the distributions are dominated by fluctuations especially at low p_T. The baseline, representing the underlying events, decreases with increasing p_T and it is larger for the associated tracks range $0.3 < p_T < 1$ GeV/c than the range $p_T > 1$ GeV/c since more background is expected at low p_T.

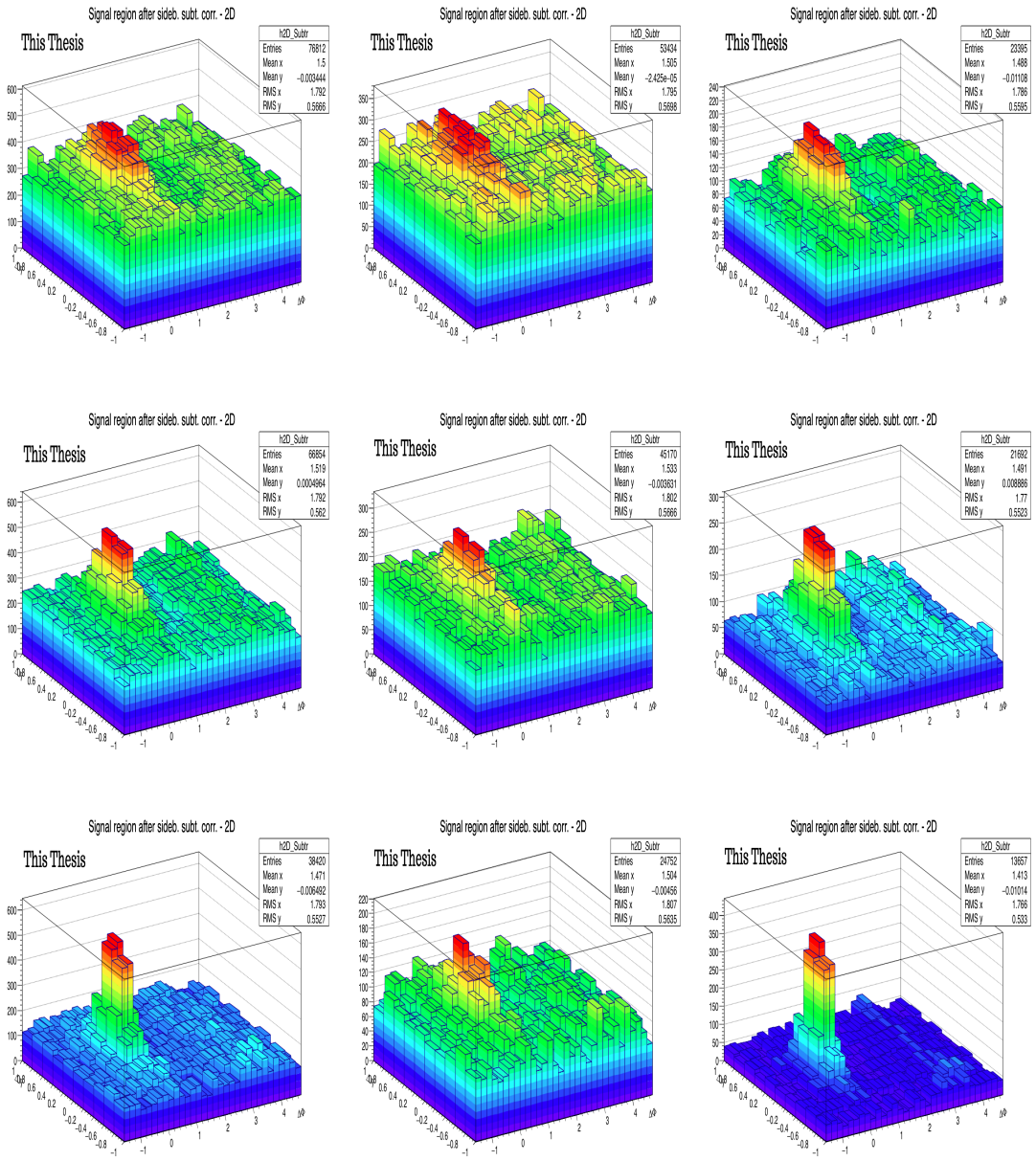

FIGURE 4.14: Non-normalized D^{*+}-charged particles correlation distributions as a function of $\Delta\phi$ and $\Delta\eta$ in the $p_T(D^{*+})$ ranges $3 < p_T < 5$ GeV/c (top row), $5 < p_T < 8$ GeV/c (middle row) and $8 < p_T < 16$ GeV/c (bottom row) and p_T associated tracks ranges : $p_T > 0.3$ GeV/c (left column), $0.3 < p_T < 1$ GeV/c (middle column) and $p_T > 1$ GeV/c (left column).

Concerning the distributions in one dimension (only as function of $\Delta\phi$), the obtained correlations are normalised to the number of triggers S_{peak} (see eq.4.9) which was extracted from the fit of the invariant mass spectra of the D^{*+} in each p_T range. The normalised D^{*+}-hadron correlations are presented for low, intermediate and high $p_T(D^{*+})$ in figure.4.15 and it corresponds to the top, middle and bottom rows, respectively. The distributions for the associated tracks intervals $p_T > 0.3$ GeV/c, $0.3 < p_T < 1$ GeV/c, $p_T > 1$ GeV/c correspond respectively to the left, middle and right columns.

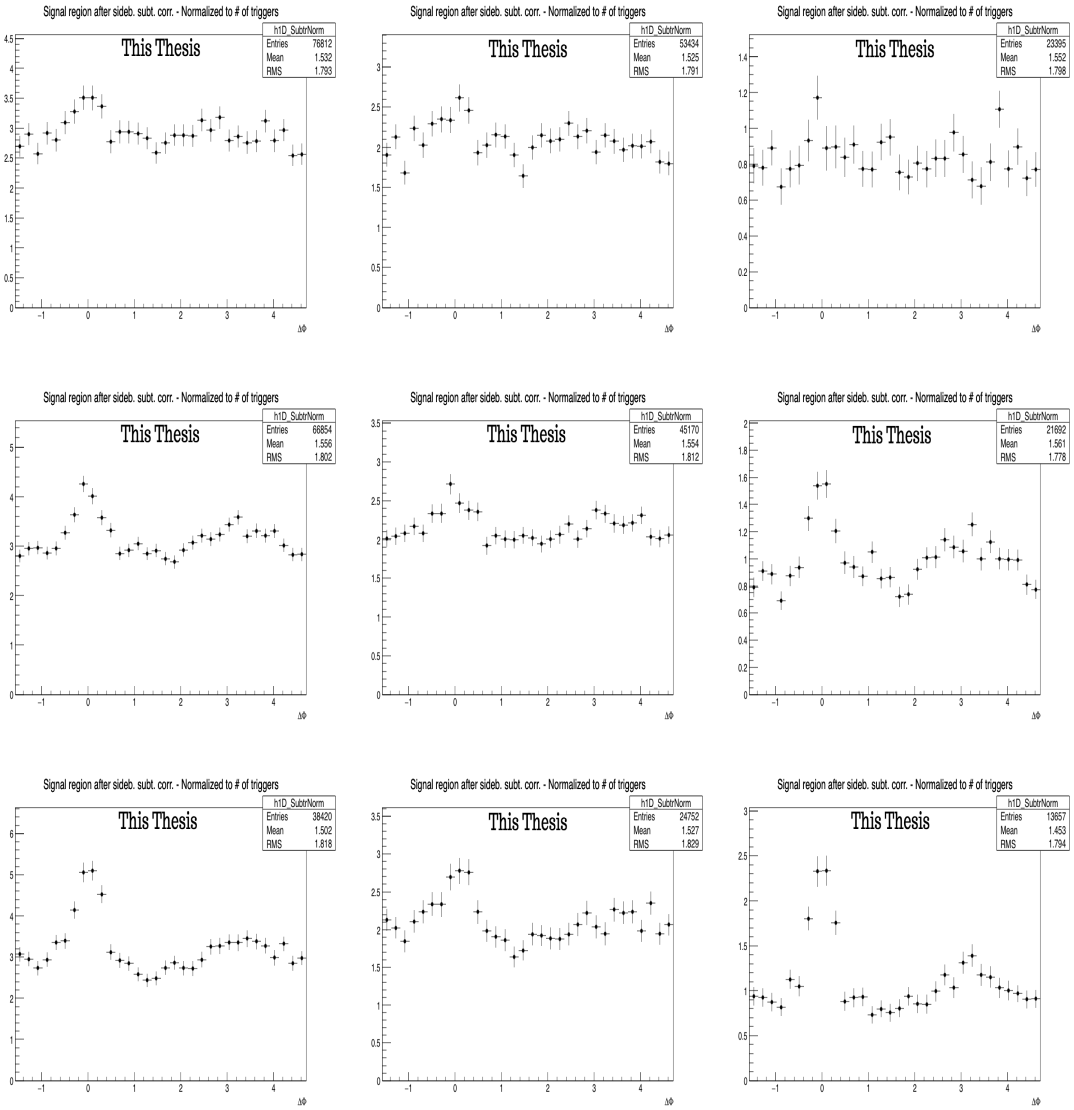

FIGURE 4.15: Normalised D^{*+}-charged particles correlation distributions as a function of $\Delta\phi$ in the p_T(D^{*+}) ranges $3 < p_{\mathrm{T}} < 5$ GeV/c (top row), $5 < p_{\mathrm{T}} < 8$ GeV/c (middle row) and $8 < p_{\mathrm{T}} < 16$ GeV/c (bottom row) and p_T associated tracks ranges : $p_T > 0.3$ GeV/c (left column), $0.3 < p_{\mathrm{T}} < 1$ GeV/c (middle column) and $p_T > 1$ GeV/c (left column).

One can consider that each normalised distribution presents the number of charged particles associated with one trigger as a function of the difference in azimuthal angle between that trigger and the associated particles. The baseline (that represents the underlying events) is lower in the range $p_{\mathrm{T}}(h) > 1$ GeV/c (around 1) with respect to the range $0.3 < p_{\mathrm{T}}(h) < 1$ GeV/c (around 2). By taking both subranges into account .i.e the integrated range $p_T(h) >$ 0.3 GeV/c, it is reasonable to have a distribution with a baseline around 3. This feature is observed for the three p_T ranges of D^{*+}, and it depends only on the transverse momentum of associated charged tracks.

At low p_T ([3-5] GeV/c) in the top row of figure.4.15, the near-side peak is visible though not large in magnitude whereas the away-side peak is not visible. Otherwise, one can see only

fluctuations in the two p_T subranges of associated tracks. At intermediate p_T ([5-8] GeV/c), both peaks are visible and their magnitude gets smaller in the range $0.3 < p_{\mathrm{T}}(h) < 1$ GeV/c but they become clearer in the range $p_T > 1$ GeV/c . The same can be deduced at high p_T ([8-16] GeV/c).

4.2.7 Correction for the Purity

So far, the angular-correlation distributions are contaminated with the secondary tracks .i.e D^{*+} mesons are correlated with charged tracks whether they are primary or secondary. The primary particles come directly from the primary vertex. While secondary particles are coming from the decay of primaries (secondary vertices). We are interested in the correlations of D^{*+} with primary tracks only. Consequently, the secondary track contamination has to be removed by weighting the distribution of correlations with the purity,

$$\tilde{C}_{inclusive}(\Delta\phi, \Delta\eta) = \textbf{Purity} \times C_{Norm}(\Delta\phi, \Delta\eta) \tag{4.10}$$

The purity is defined by :

$$Purity = \frac{\int_0^{DCA_{XY}^{cut}} f_{prim}(DCA_{XY}) dDCA_{XY}}{\int_0^{DCA_{XY}^{cut}} [f_{prim}(DCA_{XY}) + f_{sec}(DCA_{XY})] dDCA_{XY}} \tag{4.11}$$

DCA_{XY}^{cut} is the distance of the closest approach in the XY plane. It is a lower cut with the value 0.25 cm that is applied on the associated tracks. $f_{prim}(DCA_{XY})$ and $f_{sec}(DCA_{XY})$ present the distributions of primary and secondary charged particles extracted using Monte Carlo simulations as a function of DCA_{XY}.

In the old analysis strategy adopted for the data collected in p-p collisions at 7 TeV, only one value of the purity was extracted for each p_T range of D meson to scale the distributions. In the new analysis strategy, the purity does not depend on the transverse momentum range of D mesons only but on the p_T of associated tracks as well. The purity values are computed by applying the equation.4.11 for the distributions of primary and secondary tracks obtained both with a determined Monte Carlo sample. The simulations resulted in the figure.4.16 and according to the different combinations of p_T ranges of D^{*+} mesons and associated tracks, nine values of the purity are extracted and summarised in table.4.1.

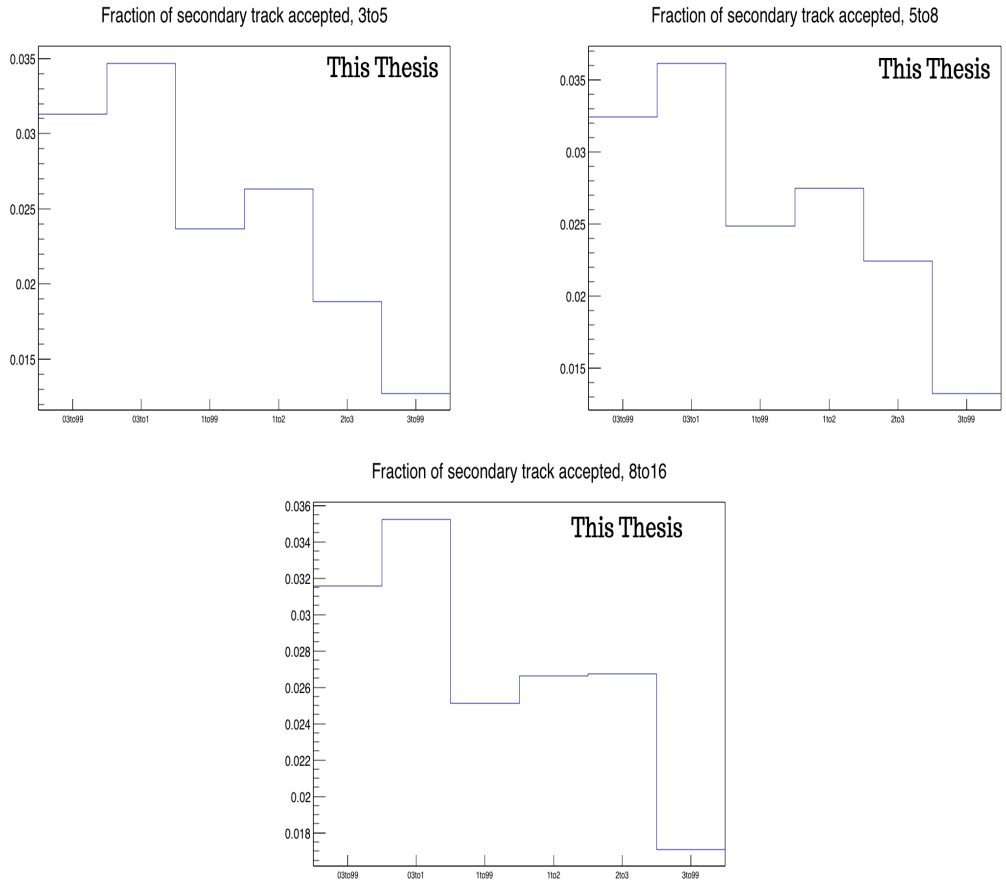

FIGURE 4.16: Fraction of secondary tracks accepted by DCA_{XY} cut in the range $3 < p_T(D) < 5$ GeV/c (top left), $5 < p_T(D) < 8$ GeV/c (top right) and $8 < p_T(D) < 16$ GeV/c (bottom) in the associated charged tracks intervals $0.3 < p_T < 99$ GeV/c (bin0), $0.3 < p_T < 1$ GeV/c (bin1), $1 < p_T < 99$ GeV/c (bin2), $1 < p_T < 2$ GeV/c (bin3), $2 < p_T < 3$ GeV/c (bin4), $3 < p_T < 99$ GeV/c (bin5).

Purity	$3<p_T(D)<5$ GeV/c	$5< p_T(D)<8$ GeV/c	$8<p_T(D)<16$ GeV/c
$0.3<p_T(h)<99$ GeV/c	0.968	0.967	0.968
$0.3<p_T(h)<1$ GeV/c	0.965	0.963	0.964
$1<p_T(h)<99$ GeV/c	0.976	0.975	0.975

TABLE 4.1: The extracted purity values in pp collisions at 13 TeV.

4.2.8 B feed-down subtraction

The last step in this analysis strategy is the correction for the beauty feed-down. Charged tracks are correlated with D^{*+} whether they are prompt (c $\rightarrow$ D) or non-prompt (b $\rightarrow$ B $\rightarrow$ D). The latter is equivalent to the so-called B feed-down. In the current study, only the correlations of prompt D^{*+} mesons with primary charged tracks are considered. For that purpose, Monte Carlo simulations are exploited to obtain a template representing B $\rightarrow$ D^{*+} - hardons correlations which will be subtracted from the latest corrected distribution of

correlation, as expressed by,

$$\widetilde{C}_{promptD}(\Delta\phi) = \frac{1}{f_{prompt}}\left(\tilde{C}_{inclusive}(\Delta\phi) - (1 - f_{prompt})\tilde{C}^{MCtempl}_{feed-down}(\Delta\phi)\right), \quad (4.12)$$

$\tilde{C}_{inclusive}(\Delta\phi)$ is the D^{*+}-h correlation distribution obtained in the previous step.
$\tilde{C}^{MCtempl}_{feed-down}(\Delta\phi)$ is the Monte Carlo template (B $\rightarrow$ D^{*+}-hadron correlations).
f_{prompt} is the fraction of D^{*+} coming from the fragmentation of charm quarks only and it is defined by :

$$f_{prompt} = \left(1 + \frac{(Acc \times \epsilon)_{feeddownD^{*+}}}{(Acc \times \epsilon)_{promptD^{*+}}} \frac{\frac{d\sigma}{dp_{\mathrm{T}}}^{feeddownD^{*+}} \mid |y| < 0.5}{\frac{d\sigma}{dp_{\mathrm{T}}}^{promptD^{*+}} \mid |y| < 0.5}\right), \quad (4.13)$$

$(Acc \times \epsilon)_{feeddownD^{*+}}$ and $(Acc \times \epsilon)_{promptD^{*+}}$ are the acceptance times the efficiency of the non-prompt D^{*+} (from B feed-down) and the prompt D^{*+}, respectively. The efficiency distributions were already presented in figure.4.2. $\frac{d\sigma}{dp_{\mathrm{T}}}$ is the production cross-section either of non-prompt D^{*+} (from B feed-down) or prompt D^{*+} obtained from Monte Carlo simulations based on Fixed Order Next-to-Leading-Logarithm (FONLL) calculations [50].

An example of the Monte Carlo templates is displayed in figure.4.17 for B feed-down and figure.4.18 for prompt D^{*+}. The top row shows the templates in 2-dimensions and the bottom row shows the 1-dimensional templates. The left column presents the distributions in the range $3 < p_{\mathrm{T}}(D^{*+}) < 5$ GeV/c, the middle column in $5 < p_{\mathrm{T}}(D^{*+}) < 8$ GeV/c and the right column in $8 < p_{\mathrm{T}}(D^{*+}) < 16$ GeV/c. The templates are shown only for the integrated p_T of associated tracks ($0.3 < p_{\mathrm{T}} < 99$ GeV/c).

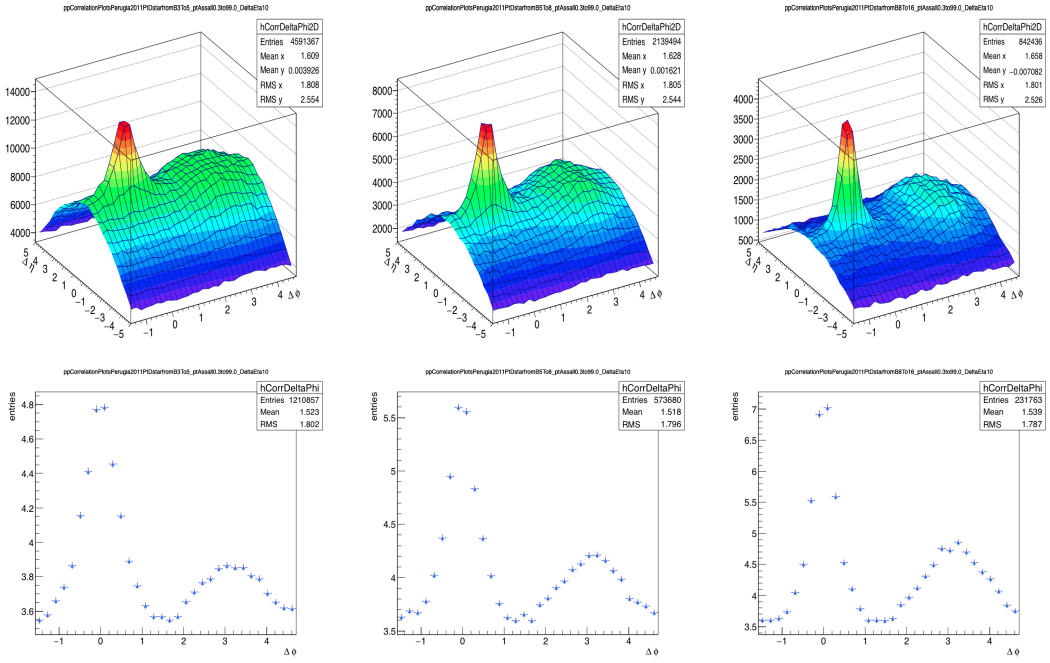

FIGURE 4.17: Example of B feed-down templates obtained using PYTHIA6 with the tune Perugia 2011 in 2 dimensions ($\Delta\phi$ and $\Delta\eta$) in the integrated p_T range of associated tracks and in the D^{*+} p_T range [3-5] GeV/c (top left), [5-8] GeV/c (top middle) and [8-16] GeV/c (top right) and in one dimension ($\Delta\phi$) [3-5] GeV/c (bottom left), [5-8] GeV/c (bottom middle), [8-16] GeV/c (bottom right).

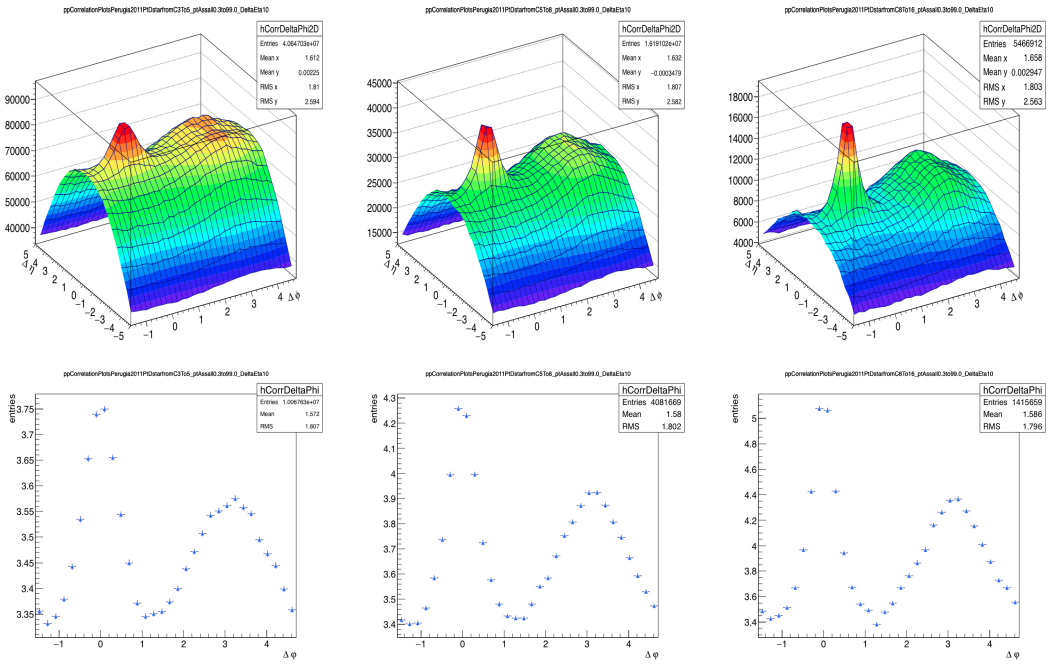

FIGURE 4.18: Example of prompt D^{*+} templates obtained using PYTHIA6 with the tune Perugia 2011 in 2 dimensions ($\Delta\phi$ and $\Delta\eta$) in the integrated p_T range of associated tracks and in the D^{*+} p_T range [3-5] GeV/c (top left), [5-8] GeV/c (top middle) and [8-16] GeV/c (top right) and in one dimension ($\Delta\phi$) [3-5] GeV/c (bottom left), [5-8] GeV/c (bottom middle), [8-16] GeV/c (bottom right).

4.2.9 Final corrected D^{*+}-charged particles correlations in p-p collisions at 13 TeV

After Applying all the steps of the analysis strategy as explained in the previous sections, the final corrected angular-correlation between prompt D^{*+} mesons and primary charged particles is obtained in proton-proton collisions at $\sqrt{s} = 13$ TeV. These distributions are presented in figure.4.19. The left, middle and right columns correspond to the p_T ranges of D^{*+} : $3 < p_T(D) < 5$ GeV/c, $5 < p_T(D) < 8$ GeV/c, $8 < p_T(D) < 16$ GeV/c, respectively. While the top, middle and bottom rows correspond to the p_T ranges of associated tracks : $p_T(h) > 0.3$ GeV/c, $0.3 < p_T(h) < 1$ GeV/c and $p_T(h) > 1$ GeV/c, respectively.

For a considered row where the p_T range of associated tracks is determined, one can see that the baseline level is similar for the three p_T ranges of D mesons. So, the baseline is not dependent on the p_T of D mesons since the distributions are normalized to the correspondent number of triggers in each D^{*+} p_T range. Instead, it is dependent on the number of charged tracks associated with one D meson, and since in each row the p_T range of associated tracks is the same then the baseline is supposed to be the same as well. This deduction can be generalised for the 3 p_T ranges of associated tracks and the difference between them lies in the value of the baseline which is around 3 for the integrated range $p_T(h) > 0.3$ GeV/c and smaller for $0.3 < p_T(h) < 1$ GeV/c and even smaller for $p_T(h) > 1$ GeV/c. Concerning the near side and the away side peaks around $\Delta\phi = 0$ rad and $\Delta\phi = \pi$ rad, both of them are visible and most prominent at larger p_T of the D mesons and associated tracks, especially the near side peak.

Concerning physics, the baseline is a graphical feature that symbolizes the underlying events. It depends on the considered p_T range of the associated tracks. According to the distributions, one can observe clearly that the larger the p_T of the associated tracks, the lower the level of the baseline. It is probably due to the low background at high p_T. The peaks represent the jet-like events assumed to come from $c\bar{c}$ fragmentation. The near-side peak is the manifestation of the particles, within a jet, created collinearly with the trigger particles ($\Delta\phi = 0$). On the same basis, we can infer that the away-side peak represents the jet of particles created in the opposite direction in comparison to the direction of the produced trigger particle. The difference in the amplitude between the two peaks reflects the difference in the number of charged particles associated with one D^{*+} meson collinearly or back-to-back..

Based on these observations, one can deduce that charm quarks are produced mainly via the process called $gluon\ splitting$ where the charm quarks are created initially in the same direction, and that should lead to a small angle difference between the created pairs and the accompanied produced jets of particles. This is the case according to the previous observations on the obtained azimuthal correlation distributions. This process is expected to be important at energies of the order of TeV (at the centre of mass system) at the LHC.

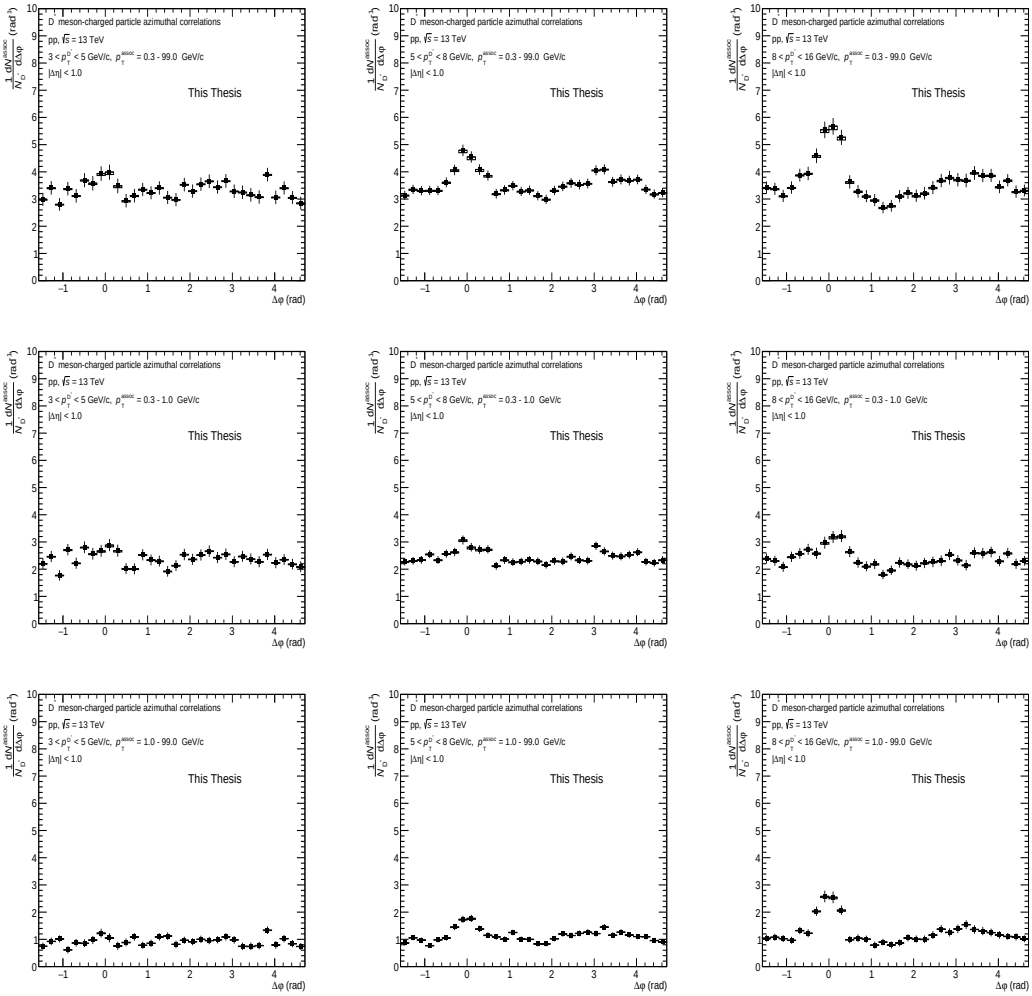

FIGURE 4.19: Final D^{*+}-charged particles correlation distributions as a function of $\Delta\phi$ in the $p_T(D^{*+})$ ranges $3 < p_T(D) < 5$ GeV/c (left column), $5 < p_T(D) < 8$ GeV/c (middle column) and $8 < p_T(D) < 16$ GeV/c (right column) and p_T associated tracks ranges : $p_T(h) > 0.3$ GeV/c (top row), $0.3 < p_T(h) < 1$ GeV/c (middle row) and $p_T(h) > 1$ GeV/c (bottom row).

So far, the performed correlation analysis considered D^{*+} mesons only. Within the physics working group HFCJ, both D^0 and D^{*+} were included to deal with the average correlation distributions. For one side, more statistics were considered, therefore less fluctuations. On the other side, the study can be generalised on several mesons.

The average correlation distribution was extracted by applying the analysis strategy described previously on each D meson separately. The final angular correlation of each D meson was weighted by the correspondent systematic uncertainties. After that, the two distributions were summed. The results of average D-h correlations include the uncertainties from both D^{*+} and D^0 mesons where they were estimated independently.

Systematic uncertainties

The statistical uncertainties are presented usually by error bars in the figures whereas systematic uncertainties are visualised via bands or squares/rectangles around the data points. Systematic uncertainties are accumulated with every performed step of the analysis. In the following, only D^{*+} mesons are discussed. The sources of the systematic uncertainties are listed according to what was done within the Physics Working Group - Heavy Flavour, Correlations and Jets (PWG-HFCJ) [99]. The estimated uncertainties are provided later.

- **Extraction of S and B.** where S (signal) and B (background) are extracted from the fit parameters. The uncertainties are estimated by following new approaches - different than those applied in the analysis strategy. The new approaches involve the use of a different background fit function, a different range (smaller or larger) to extract the signal, the rebinning of the mass spectra before the fit, and the estimation of S and B either by performing an integral or bin counting. The analyses are repeated to obtain the distributions with these new approaches, and the ratios between the new obtained correlations distributions and the standard one, are computed.

- **Background correlation shape.** The D^{*+} candidates in the sideband region are considered within a range of 4 to 8 σ from the peak position. To estimate the correspondent uncertainty, different ranges are suggested: 8 to 15 σ and 5 to 15 σ. The ratios between the distributions with the new ranges and the standard one are evaluated.

- **D meson cuts.** The three topological cuts, cosθ_{point}, DCA and $d_0(K) \times d_0(\pi)$ were varied by 15%, 20% and 30% with respect to their original values in order to have 3 looser and 3 tighter cuts. The analysis strategy is repeated to get the fully corrected D-h correlations with these 6 sets of cuts. The ratios between the new distributions and those obtained with the standard cuts are computed.

- **Efficiency of tracks.** To determine the uncertainty, a variation was made on; the minimum number of the ITS clusters, the requirement on the ITS refit, the minimum number of crossed rows in the TPC, and the minimum ratio crossed rows over the findable TPC clusters.

- **Contamination of secondary particles.** It is also the uncertainty on the purity. It is affected by the choice of the DCA$_{xy}$ (1 cm in the current analysis). The analysis strategy is repeated by considering different values of DCA$_{xy}$: 0.1 cm, 0.25 cm, 0.5 cm, 2.4 cm, 999 cm (no DCA cut).

- **B feed-down subtraction** The correction exploited the central value of f$_{prompt}$ and a generated template with PYTHIA6 tune Perugia2011. To estimate the correspondent uncertainty, other templates were generated with PYTHIA6 tune 2010 and PYTHIA8. For f$_{prompt}$, the minimum/maximum values are considered.

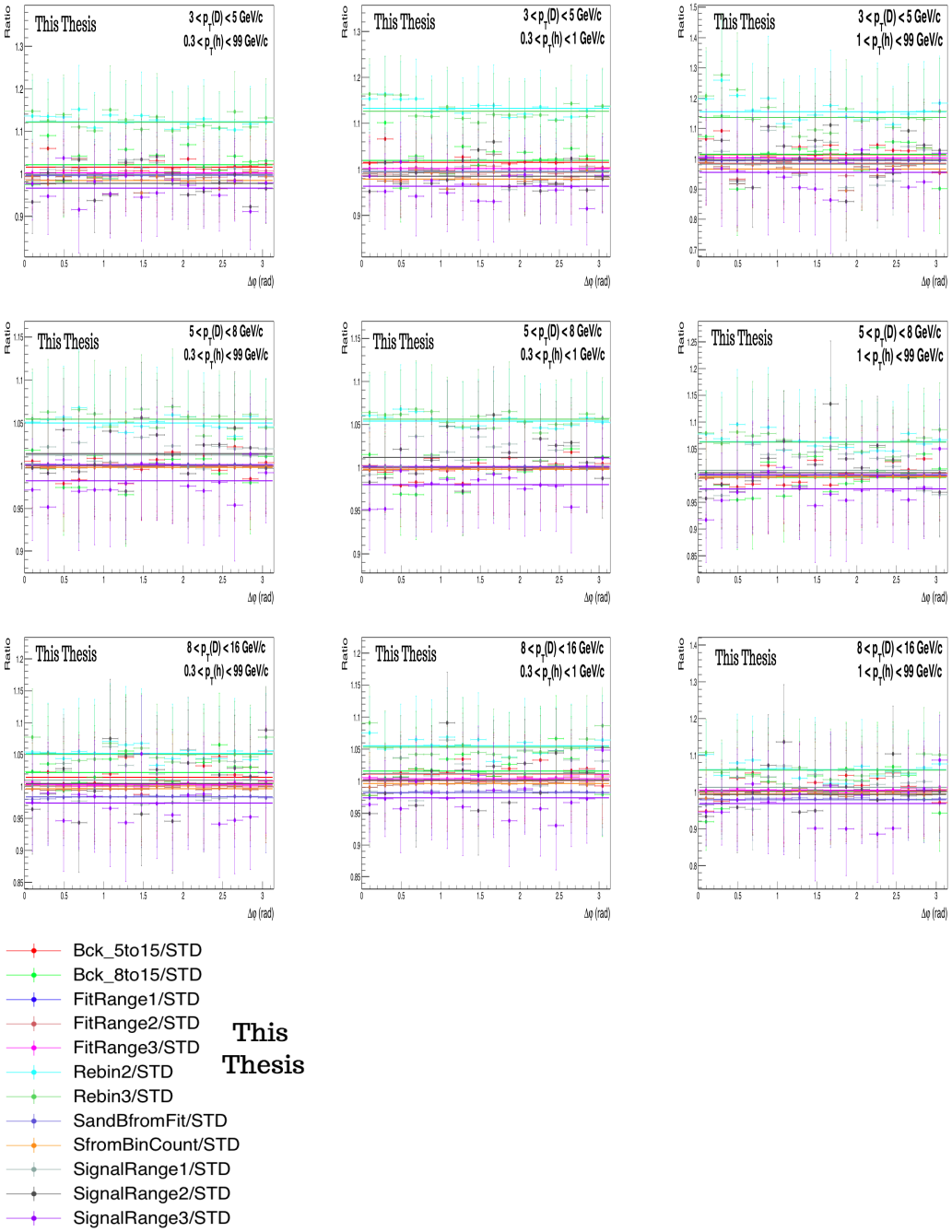

FIGURE 4.20: Computed ratios of the final correlation distributions obtained with modified parameters to those with the standard ones.

The computed ratios and their fit are presented in figure.4.20 for the 3 p_{T} intervals of D mesons [3,5] GeV/c, [5,8] GeV/c, [8,16] GeV/c and displayed in the top, middle and bottom rows, respectively and for the $\mathrm{p_T}$ ranges of associated tracks $p_{\mathrm{T}} > 0.3$ GeV/c, $0.3 < p_{\mathrm{T}} < 1$ GeV/c, $p_{\mathrm{T}} > 1$ GeV/c presented in the left, middle and right columns, respectively. Only some specific sources were considered for the matter of performance and accessibility to some required tools. The estimated uncertainties are summarised in table.4.2. The values are presented in percent, and they are in similar order to the estimated uncertainties within

the PWG-HFCJ for the average correlation distributions.

$p_T(D)$ [GeV/c]	[3,5]			[5,8]			[8,16]		
$p_T(h)$ [GeV/c]	[0.3-99]	[0.3-1]	[1,99]	[0.3-99]	[0.3-1]	[1,99]	[0.3-99]	[0.3-1]	[1,99]
Background [5,15] σ	1.53	1.52	1.42	0.07	0.046	0.01	1.5	1.15	0.52
Background [8,15] σ	2.1	1.97	1.45	0.19	0.21	0.4	2.2	1.6	0.22
Fit range [0.142, 0.16]	1.57	2.1	3.34	0.2	0.21	0.23	0.33	0.40	0.55
Fit range [0.142, 0.164]	0.29	0.626	1.54	0.02	0.01	0.01	0.1	0.1	0.1
Fit range [0.14, 0.164]	0.13	0.15	0.21	0.1	0.11	0.14	0.34	0.4	0.5
Rebin 2	12.26	13.25	15.6	4.98	5.4	6.4	5.2	5.5	6.1
Rebin 3	12.14	12.7	13.7	5.4	5.6	6.2	5	5.33	5.9
SandBfromFit	0.44	0.47	0.5	0.1	0.1	0.11	1.6	1.8	2.1
SfromBinCount	1.57	2.1	3.3	0.2	0.2	0.23	0.33	0.4	0.55
Signal range 1.5 σ	0.16	0.5	1.8	1.3	1.8	0.95	1.	1.15	1.25
Signal range 1 σ	2.25	1.5	0.33	1.4	1.2	0.5	0.48	0.1	0.6
Signal range 3 σ	3.45	3.6	4.4	1.8	1.2	2.5	2.5	2.6	3.2

TABLE 4.2: The estimated systematic uncertainties (in %) in pp collisions at 13 TeV.

In the following, some of the results of the average correlations (from PWG-HFCJ) are presented and discussed.

Figure.4.21 displays the distributions of the average D^{*+}, D^0 - charged particles correlations with a subtracted baseline from ALICE in proton-proton collisions at 13 TeV presented in the black points. Simulations, with different models/event generators, were presented: PYTHIA6 with 3 different tunes, Perugia0 (red solid line), Perugia2010 (cyan solid line), and

Perugia2011 (green solid line), and also PYTHIA8 (pink solid line), and POWHEG+PYTHIA6 (blue solid line).

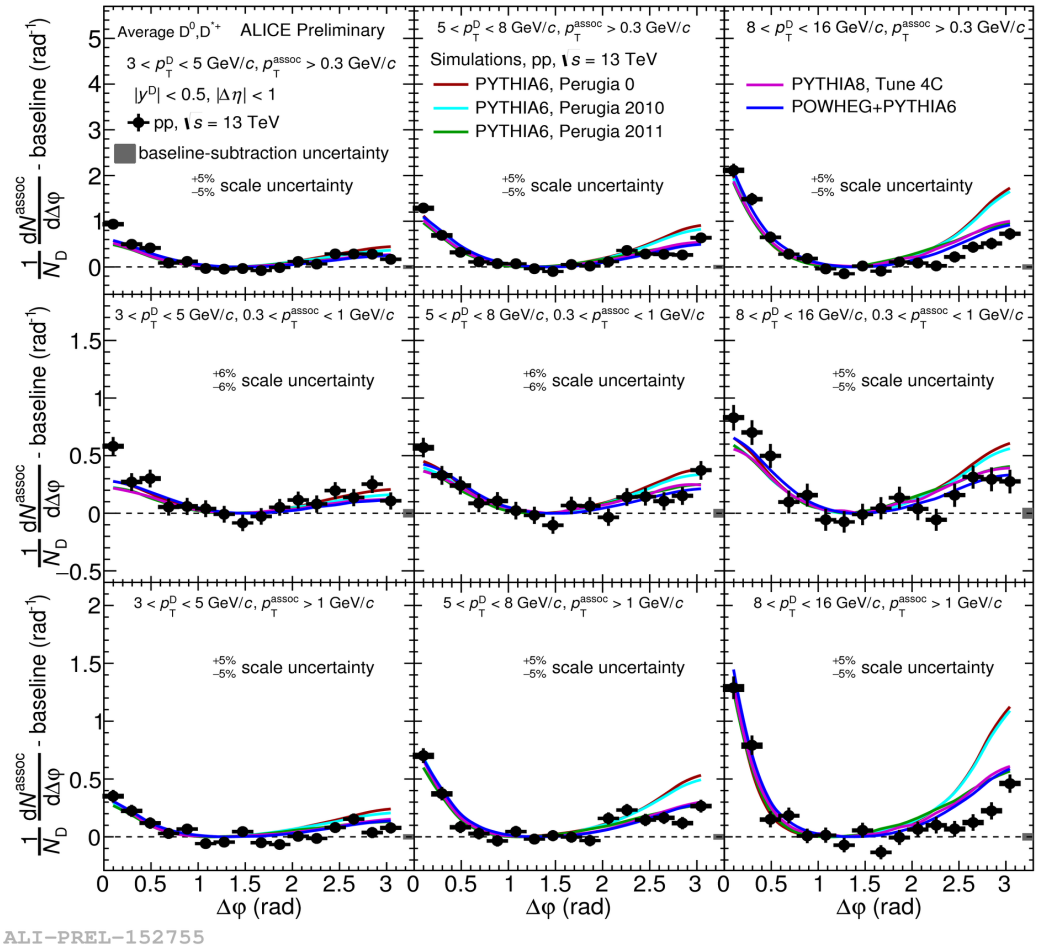

FIGURE 4.21: Average D meson - charged particles correlation in pp collisions at 13 TeV versus different Monte Carlo models : PYTHIA6 Perugia0 (red), PYTHIA6 Perugia2010 (cyan), PYTHIA6 Perugia2011 (green), PYTHIA8 Tune 4C (pink), POWHEG+PYTHIA6 (blue).

PYTHIA6 simulations are based on the LO-pQCD calculations using matrix elements for $2\rightarrow2$ interactions with parton showers based on the leading-logarithmic p_{T}-ordering. Hadronisation is treated based on the Lund string model while underlying events are simulated by integrating the Multiple-Parton Interaction (MPI). Perugia Tunes are different for what concerns initial-state radiation, final-state radiation, and parton showers. These features are treated based on the p_{T}-ordering instead of virtuality ordering in addition to some other introduced modification in the colour reconnection, Multiple Parton Interaction, and underlying events. The tune Perugia-2010 is different from Perugia0 in the generated quantity of initial-state radiation and the high z fragmentation. While for the tune Perugia-2011, the correspondent measurements of multiplicity and underlying events were considered with the first LHC collected data. The event generator POWHEG, based on the NLO-pQCD

calculations, was coupled with Parton showers simulated with PYTHIA. Such a combination of POWHEG+PYTHIA simulations gave compatible cross-section results compared to those obtained with FONLL [50]. As for PYTHIA8 simulations, several improvements were implemented concerning the multiparton interactions and colour reconnection treatment [96]. PYTHIA8 will be discussed in more detail in Chapter.5.

There is a good agreement between the experimental distributions and the models within uncertainties. A disagreement appears at small angles, and it is clear at larger angles around $\Delta\phi = \pi$ where PYTHIA6 (Perugia0 and 2010) underestimates the experimental distributions in the three p_T ranges of D mesons and for the associated tracks p_T range $p_T > 1$ GeV/c. Less discrepancy is observed for the range $0.3 < p_{\rm T} < 1$ GeV/c. The MC simulations reproduce the data qualitatively which is promising despite the discrepancies at small/large angles. So, event generators like PYTHIA (or combined with POWHEG) have succeeded so far to reproduce the general behaviour of data but several points need to be understood from the theory side to include new aspects properly in the event generators. In PYTHIA, for example, a real event can not be generated due to the lack of the full treatment of particle production in the NLO. This is why a combination with another package such as POWHEG is necessary. The integration of such aspects has a decisive impact on the predictions of correlations at small angles where physics is expected to be important at LHC energies.

Another example concerning EPOS, when it is combined with MC@sHQ, the NLO is taken into account whereas particles at the excitation state like D^{*+} are not implemented. The main physics aspects of PYTHIA will be presented in general in Chapter.5 and those related to EPOS in Chapter.6.

From the distributions of correlations, several observables can be extracted by fitting the distributions using the function,

$$f(\Delta\phi) = b + \frac{A_{NS}}{\sqrt{2\pi}\sigma_{fit,NS}} e^{-\frac{(\Delta\phi)^2}{2\sigma^2_{fit,NS}}} + \frac{A_{AS}}{\sqrt{2\pi}\sigma_{fit,AS}} e^{-\frac{(\Delta\phi-\pi)^2}{2\sigma^2_{fit,AS}}} \tag{4.14}$$

where b is a fixed term, and it presents the baseline that is extracted first and then fixed for the rest of the procedure. The 2 peaks are fitted using 2 Gaussians with the means 0 and π indicating the positions of the near-side and the away-side peaks, respectively. For each Gaussian, the width of the peak $\sigma_{fit,NS/AS}$ is extracted. Finally, a factor multiplied by each gaussian (A_{NS} and A_{AS}) corresponds to the associated yield. These observables are displayed in figure.4.22. The associated yield is shown in the top row, the width of the near-side peak in the middle row, and the baseline in the bottom row. In each row, the 3 p_T ranges of associated tracks are shown : $p_T > 0.3$ GeV/c (left column), $0.3 < p_{\rm T} < 1$ GeV/c (middle column) and $p_T > 1$ GeV/c (right column). The observables are presented for the three p_T ranges of D mesons as well [3-5] GeV/c, [5-8] GeV/c, and [8-16] GeV/c.

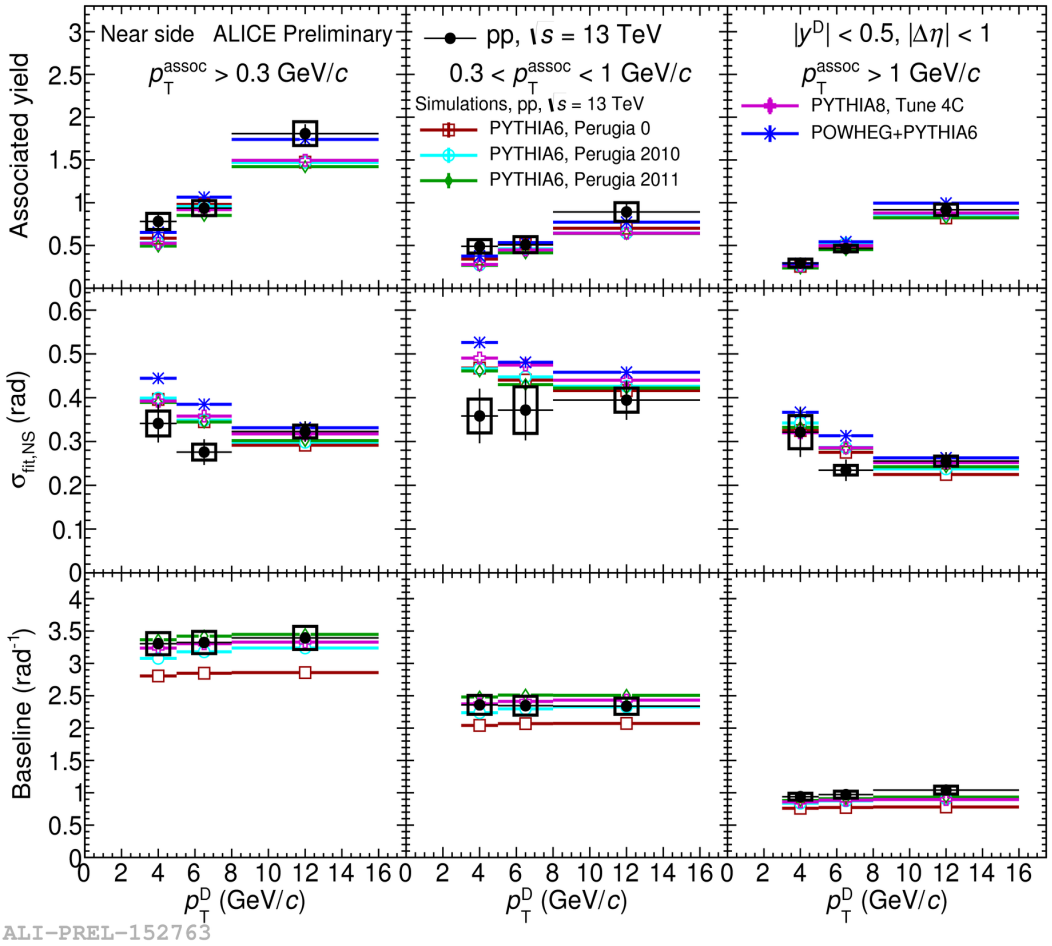

FIGURE 4.22: Associated yield (top row), Width of the near side peak (middle row) and the baseline (bottom row) extracted from correlations in pp at 13 TeV versus those extracted using different MC model : PYTHIA6 Perugia0 (red), PYTHIA6 Perugia2010 (cyan), PYTHIA6 Perugia2011 (green), PYTHIA8 Tune 4C (pink), POWHEG+PYTHIA6 (blue).

Concerning the associated yield displayed in the top row, one can observe a qualitative and quantitative agreement between experiment and simulations within uncertainties except for the range [8-16] GeV/c where all simulations except PYTHIA6 + POWHEG underestimate the data. Otherwise, the behaviour in both data and simulation is similar: the associated yield increases with the transverse momentum of D mesons.

Concerning the baseline presented in the bottom row, data and simulations agree within uncertainties except for PYTHIA6 (Perugia0) which underestimates the data. As discussed previously, the baseline for the three p_T ranges of D mesons is constant for each p_T range of associated tracks, and the larger the p_T of the associated tracks, the lower the baseline.

For the width of the near-side peak, both data and simulation do not show an explicit agreement, particularly in the p_T range of associated tracks $0.3 < p_T < 1$ GeV/c. While for the other ranges, the trend is not clear in the data. For simulations, one can notice that the width of the near-side peak is getting narrower at larger p_T(D) which seems to be the trend

if only low and intermediate p_T of D mesons are considered in the data. More comparisons data versus simulations will be presented in Chapter.6.

The other interesting comparison is the one involving the correlations obtained in pp collisions at 7 TeV. Figure.4.23 shows the correlation distribution obtained in p-p collisions at 13 TeV (blue squares) versus those obtained in p-p collisions at 7 TeV (black squares). The distributions obtained in p-p collisions at 13 TeV are smoother than those obtained in p-p collisions at 7 TeV. It is probably related to the large statistics in the data collected in p-p collisions at 13 TeV compared to the 7 TeV. In addition to that, correlations at 13 TeV look a little bit higher than those obtained at 7 TeV. This is directly related to the baseline that depends on the number of associated tracks due to the larger statistics in the 13 TeV where more important underlying events can take place.

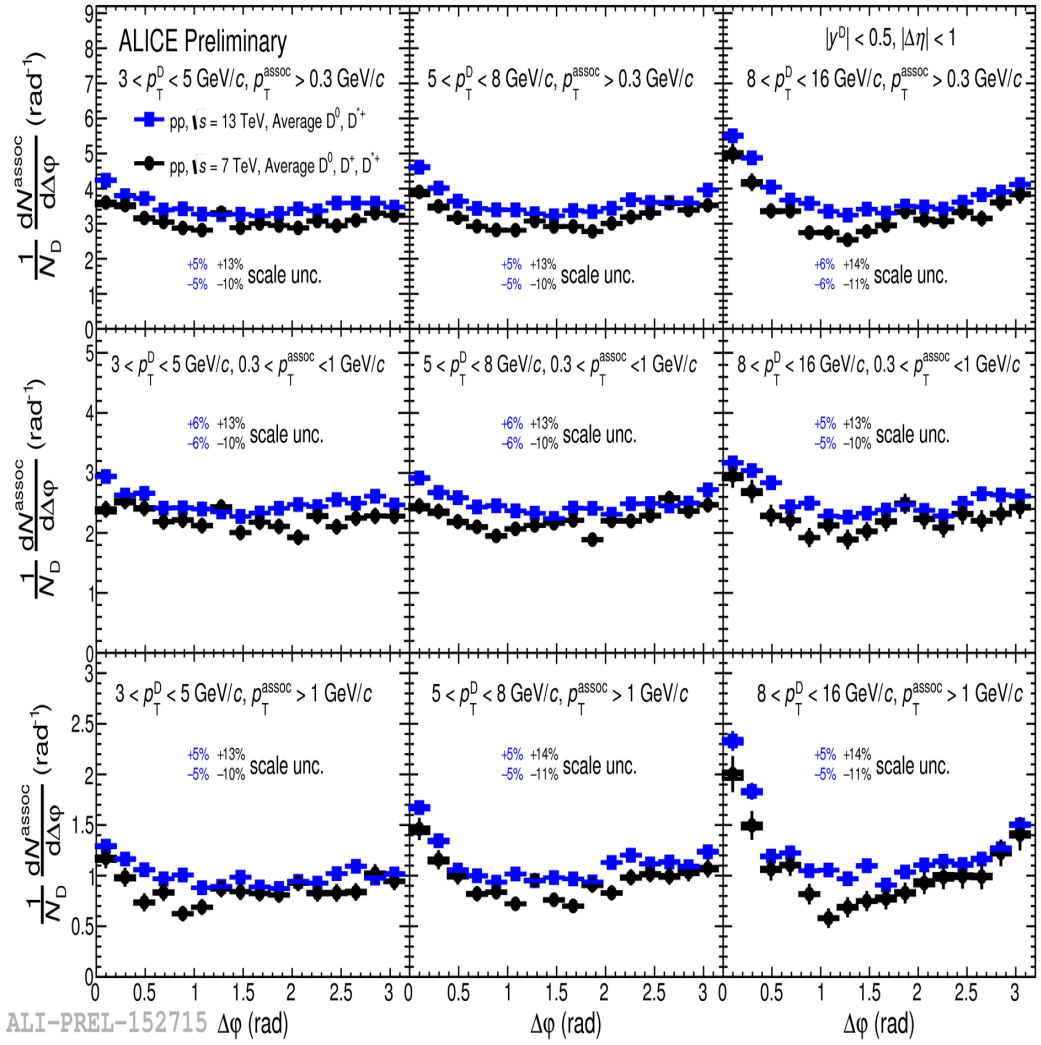

FIGURE 4.23: Average D meson - charged particles correlations in pp collisions at 13 TeV (blue squares) versus those in pp at 7 TeV (black squares). Left column : 3< $p_{\mathrm{T}}(D)$ <5 GeV/c, middle column : 5< $p_{\mathrm{T}}(D)$ <8 GeV/c, left column : 8< $p_{\mathrm{T}}(D)$ <16 GeV/c. Top row : $p_T^{assoc} > 0.3$ GeV/c, middle row : $0.3 < p_T^{assoc} < 1$ GeV/c, bottom row : $p_T^{assoc} > 1$ GeV/c.

The correlations in p-p collisions at 5 TeV were added to the comparison of distributions at 7 TeV and 13 TeV. The correspondent distributions for the 3 energies, where the baseline was subtracted, are presented in figure.4.24. One can see that there is a good agreement between the 3 distributions within statistical uncertainties despite the fluctuations observed for 7 TeV which have larger statistical error bars particularly at larger p_T.

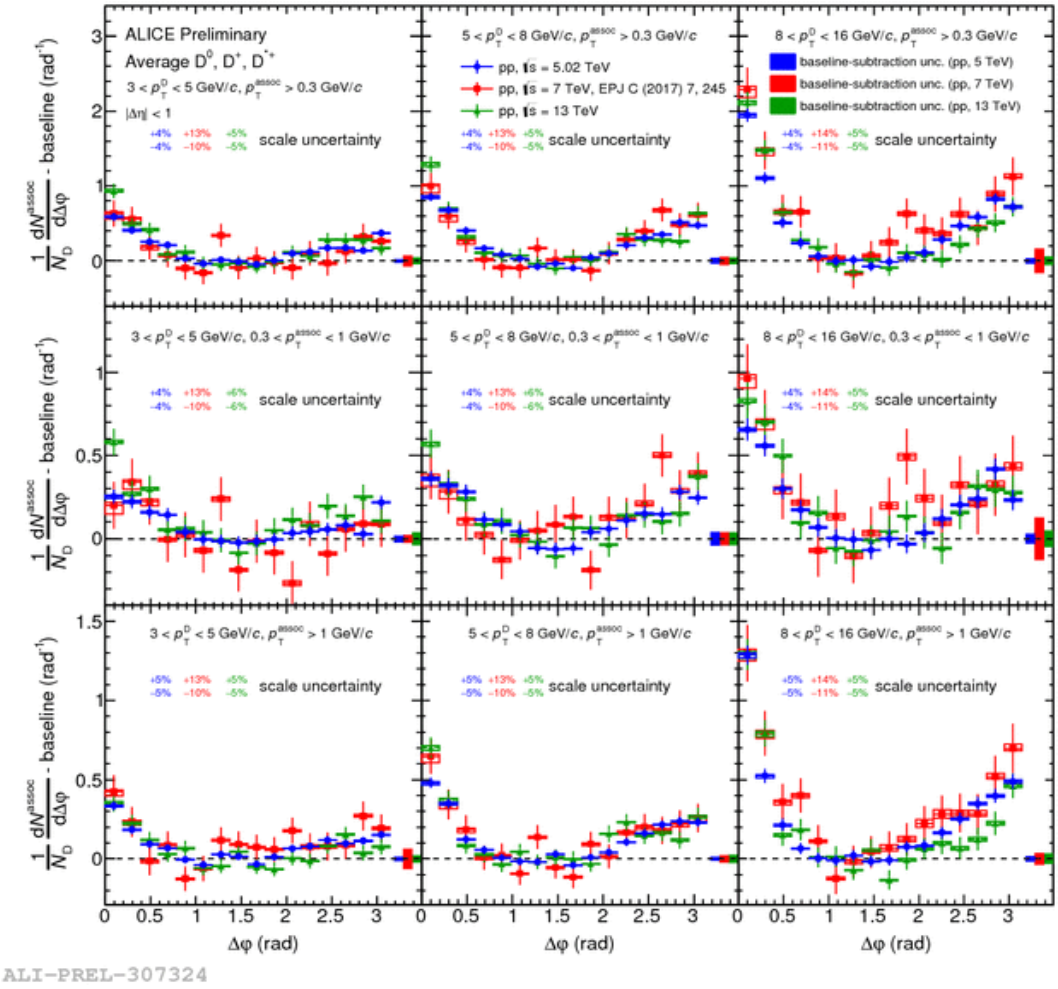

FIGURE 4.24: Average D meson - charged particles correlations with subtracted baseline in p-p collisions at 5 TeV (blue points) vs 7 TeV (red points) and versus 13 TeV (green points) . Left column : 3< $p_{\mathrm{T}}(D)$ <5 GeV/c, middle column : 5< $p_{\mathrm{T}}(D)$ <8 GeV/c, left column : 8< $p_{\mathrm{T}}(D)$ <16 GeV/c. Top row : p_T^{assoc} > 0.3 GeV/c, middle row : 0.3 < p_T^{assoc} < 1 GeV/c, bottom row : p_T^{assoc} > 1 GeV/c.

Figure.4.25 shows the subtracted baseline distribution of correlations in p-p collisions at 13 TeV (blue points) and 7 TeV (black points) and in p-Pb collisions at 5.02 TeV (red points). Although the statistical error bars are large, the agreement is established in general between the three curves.

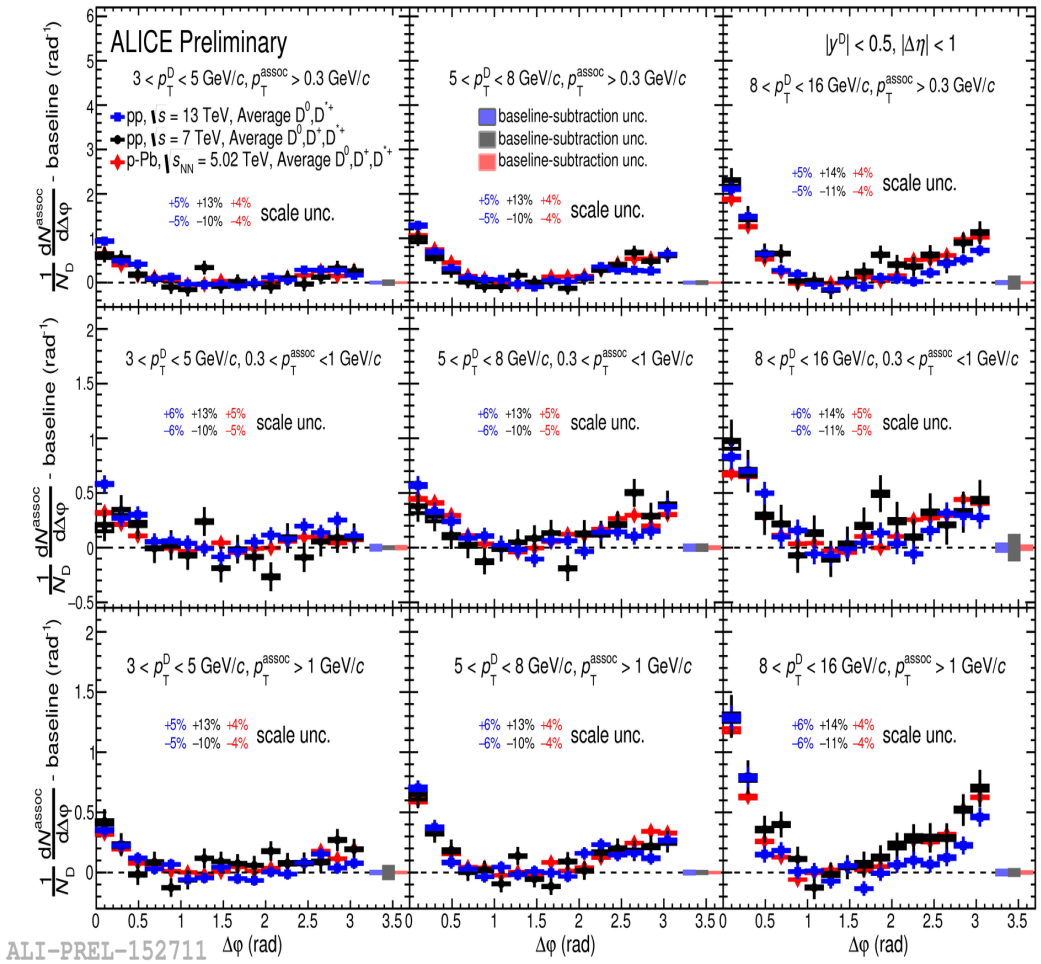

FIGURE 4.25: Average D meson - charged particles correlations with subtracted baseline in p-p collisions at 13 TeV (blue points) vs p-p at 7 TeV (black points) versus p-Pb collisions at 5.02 TeV (red points). Left column : 3< $p_T(D)$ <5 GeV/c, middle column : 5< $p_T(D)$ <8 GeV/c, right column : 8< $p_T(D)$ <16 GeV/c. Top row : p_T^{assoc} > 0.3 GeV/c, middle row : 0.3 < p_T^{assoc} < 1 GeV/c, bottom row : p_T^{assoc} > 1 GeV/c.

From the previous correlation distributions, the associated yield and the width of the near-side peak are extracted and presented in figure.4.26 in the top and bottom rows, respectively. The same trend in associated yield is observed for pp and p-Pb. The yield in both cases increases with the transverse momentum of D mesons. As for the width, the trend evolution is not clear and more statistics are probably needed to get a firm conclusion.

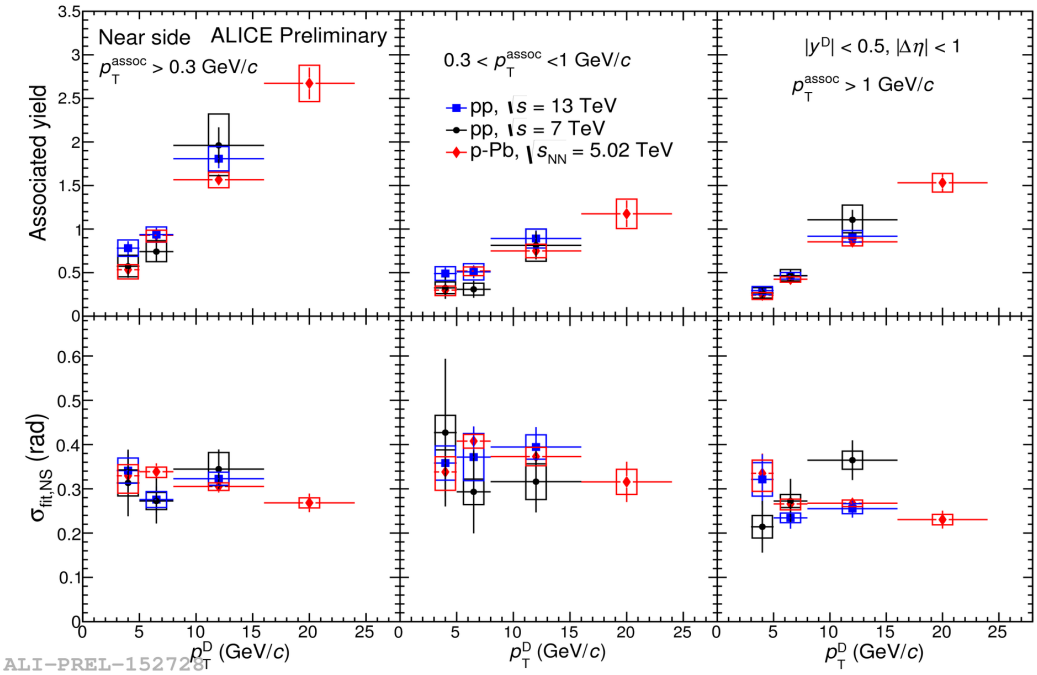

FIGURE 4.26: Associated yield (top row), Width of the near side peak (bottom row) extracted from correlations in pp collisions at 13 TeV (blue points) versus pp at 7 TeV (black points) versus p-Pb at 5.02 TeV (red points).

4.3 D^{*+}-charged particles angular-correlations in pp collisions at 8 TeV

Before the 13 TeV data was available, some time was devoted to analyse the data collected in the pp collisions at 8 TeV where the EMCal trigger was part of the functional detectors during this period. The analyses presented in this part, adopted the strategy used at that time (2015) which is similar to the one applied for the 7 TeV data.

The procedure includes the steps from the reconstruction of D^{*+} mesons and tracks to the final correlations without any correction for the efficiency, purity, and B feed-down. This is due to the fact that these analyses were not anymore a focus or a priority by the *Physics Working Group – Heavy Flavour* (PWG-HF) after the availability of the 13 TeV data. In addition, the trigger bias .i.e the effects caused by the EMCal (for example, on the mixed events) were not clear and needed some dedicated studies. Finally, the statistics collected with the EMCal trigger were not enough to carry on with these analyses.

Starting from the invariant mass spectra, the D^{*+} mesons were reconstructed in the channel $D^{*+} \rightarrow D^0\pi^+ \rightarrow K^-\pi^+\pi^+$ as it was done for the 5, 7 and 13 TeV. The spectra were obtained for a transverse momentum up to 36 GeV/c. That was an attempt to extend the p_T range beyond 16 GeV/c with respect to the considered one at that time in pp at 7 TeV. This interval was divided into the following p_T bins : [3,4], [4,5], [5,6], [6,7], [7,8], [8,10], [10,12], [12,16], [16,24], [24,36] GeV/c, as presented in figure.4.27.

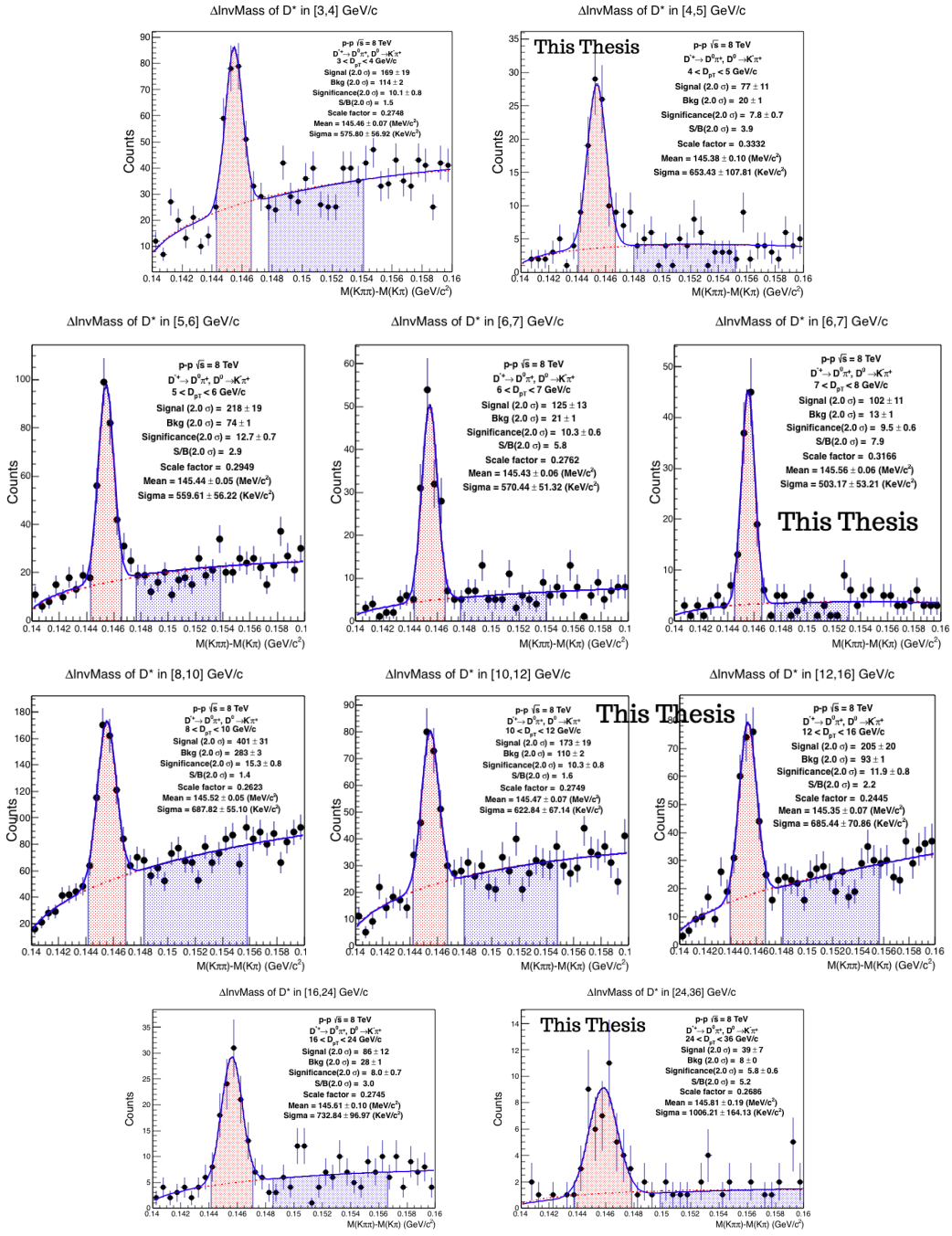

FIGURE 4.27: D^{*+} invariant mass spectra $(M(K\pi\pi) - (K\pi))$ for 10 p_T bins in p-p collisions at 8 TeV.

By merging the 10 p_T bins, the invariant mass spectra can be reorganised into the 4 transverse momentum ranges : low [3,5] GeV/c, intermediate [5,8] GeV/c and high p_T [8,16] GeV/c, [16,36] GeV/c as presented in figure.4.28. In fact, from these distributions, it is clear that the D^{*+} mesons can be reconstructed in a p_T range going from 3 up to 36 GeV/c.

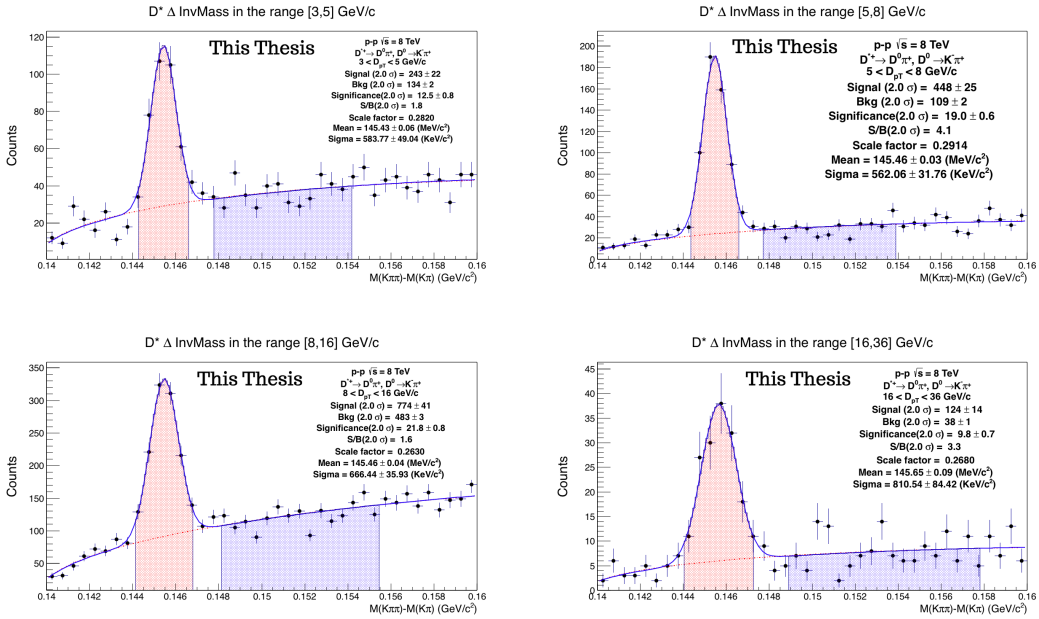

FIGURE 4.28: ΔMD^{*+} invariant mass spectra in pp collisions at 8 TeV: [3,5] GeV/c (top left), [5,8] GeV/c (top right), [8,16] GeV/c (bottom left), [16,36] GeV/c (bottom right).

The following step consists to correlate the D^{*+} mesons and the associated charged tracks after passing some selection criteria. This results in distributions where the correlated pairs can be in the same event (Single Events) or from different events (Mixed Events) for both signal region and sideband region of the D^{*+} invariant mass spectra and for each p_T range. The accomplishment of these steps leads to the 4 distributions presented in figure.4.29, figure.4.30, figure.4.31 and figure.4.32 for the p_T ranges [3,5] GeV/c, [5,8] GeV/c, [8,16] GeV/c, [16,36] GeV/c, respectively.

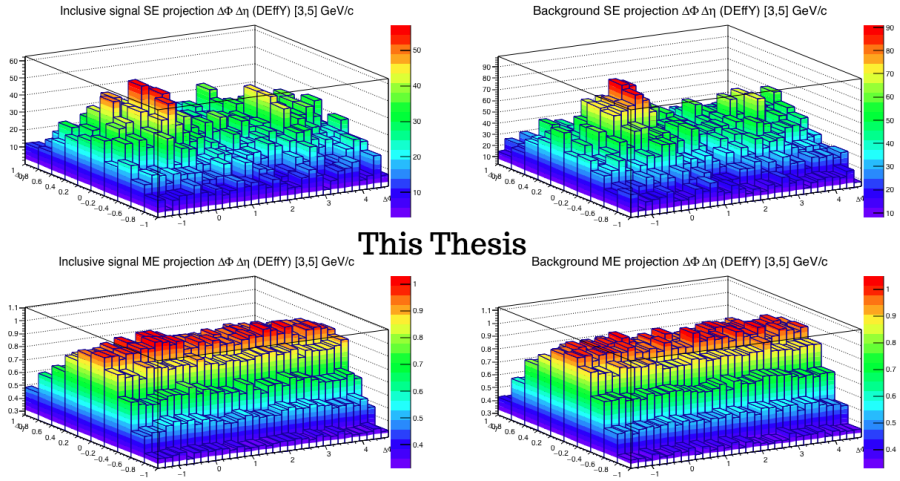

FIGURE 4.29: Top row: Single event distribution in the signal region (left) and sideband region (right). Bottom row: Mixed Event distribution in the signal region (left) and sideband region (right) in the p_T range [3,5] GeV/c.

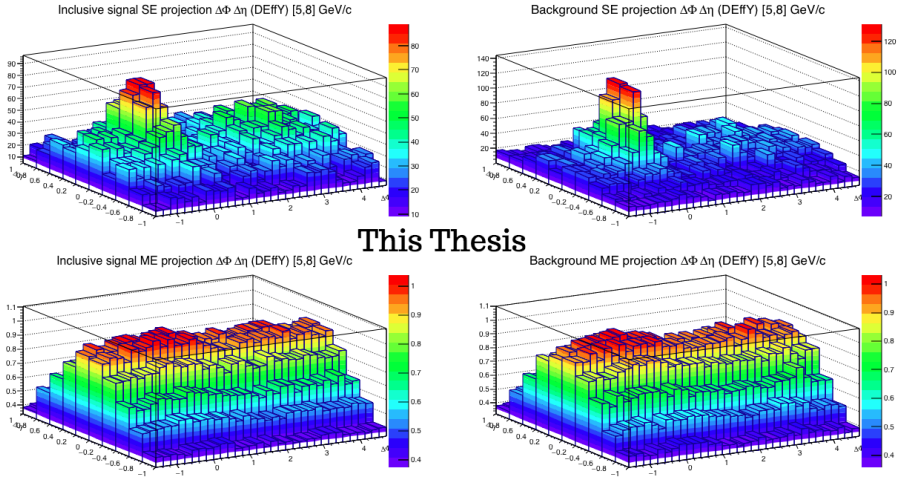

FIGURE 4.30: Top row: Single event distribution in the signal region (left) and sideband region (right). Bottom row: Mixed Event distribution in the signal region (left) and sideband region (right) in the p_T range [5,8] GeV/c.

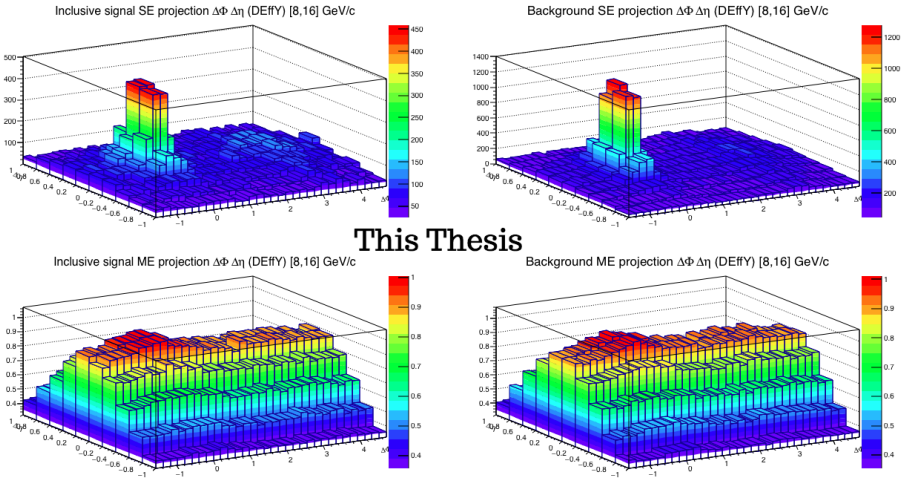

FIGURE 4.31: Top row: Single event distribution in the signal region (left) and sideband region (right). Bottom row: Mixed Event distribution in the signal region (left) and sideband region (right) in the p_T range [8,16] GeV/c.

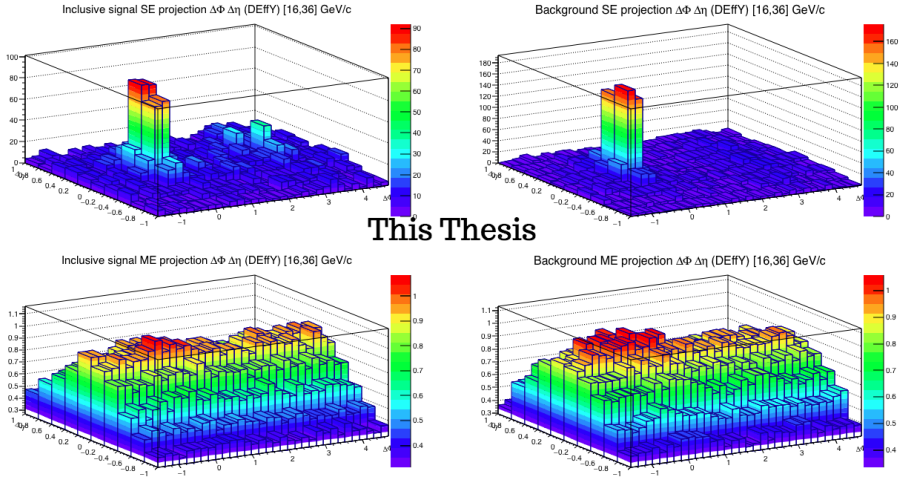

FIGURE 4.32: Top row: Single event distribution in the signal region (left) and sideband region (right). Bottom row: Mixed Event distribution in the signal region (left) and sideband region (right) in the p_T range [16,36] GeV/c.

With the data collected in pp collisions at 8 TeV, the Mixing Event (ME) distributions are different compared to those obtained in minimum bias .i.e pp collisions at 7 TeV. The difference is manifested by the presence of a bump (or an enhancement) around ($\Delta\phi$,$\Delta\eta$)=(0,0). In minimum bias, this feature does not exist. The distributions are rather flat in $\Delta\phi$. This is visible in the bottom rows of figure.4.30, figure.4.31 and figure.4.32 either in the signal region or in the sideband region. In minimum bias, the detection of particles (or jets of particles) is isotropic in all ϕ directions (the azimuthal plane). This leads to flat mixing events distributions where the physics features disappear. If only a part of the azimuthal plane is considered, such as the data collected by the EMCal trigger, the particles will be considered only in the pseudo-rapidity range $-0.7 < \eta < 0.7$ and the azimuthal angle range $80° < \phi < 180°$ with photons and electrons accepted with $p_{\mathrm{T}} > 5$ GeV/c. An illustrative scheme is shown in figure.4.33.

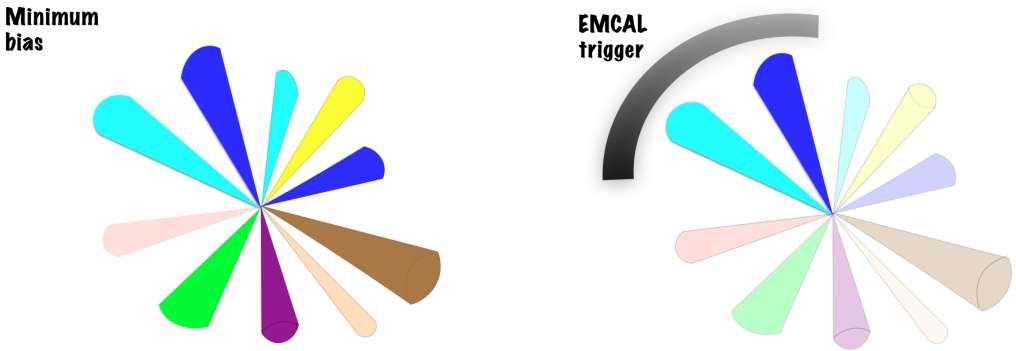

FIGURE 4.33: Illustration of detected jets in the transverse plane for Minimum bias (left) and EMCal trigger (right).

Having such criteria on the transverse momentum, pseudo-rapidity, and azimuthal angle will probably give different distributions in addition to the impact on the reconstruction of particles requiring electrons and photons in their decay channels. Consequently, the mixing events are expected to be different as well. According to the mixing event distribution, what is favoured the most are the jets of particles created in the same direction and match the EMCal acceptance which is limited in the azimuthal and longitudinal plane, and that's why a peak is observed in the mixing event distributions.

These features can be reproduced via a Monte Carlo Toy by generating the ϕ, $\Delta\phi$, η, $\Delta\eta$ distributions randomly. The distributions are constrained by the EMCal trigger acceptance .i.e thresholds on the transverse momentum of electrons and photons, the azimuthal angle, and pseudo-rapidity. The resulted distributions in one dimension are presented for the ranges [3,5], [5,8], and [8,16] GeV/c in figure.4.34, figure.4.35 and figure.4.36, respectively. The top rows correspond to the ϕ and $\Delta\phi$ distributions. Whereas, the bottom rows correspond to the η and $\Delta\eta$ distributions. The left column presents the distributions of D mesons, the middle column the associated hadron distributions, and correlations are presented in the right column.

For both D mesons and hadrons (associated tracks), the distributions are similar in the three p_T ranges. The η distribution is almost flat, which leads to the expected triangular distributions in $\Delta\eta$. As for ϕ distributions, they are not flat, and they show some inhomogeneities. This behaviour is due to the limited acceptance imposed by the EMCal trigger in the azimuthal plane. Concerning the $\Delta\phi$ distributions, they show 2 bumps around $\Delta\phi = 0, \pi$. This feature shows that the produced jets of particles are privileged, even if they are from different events and collected within the EMCal trigger acceptance.

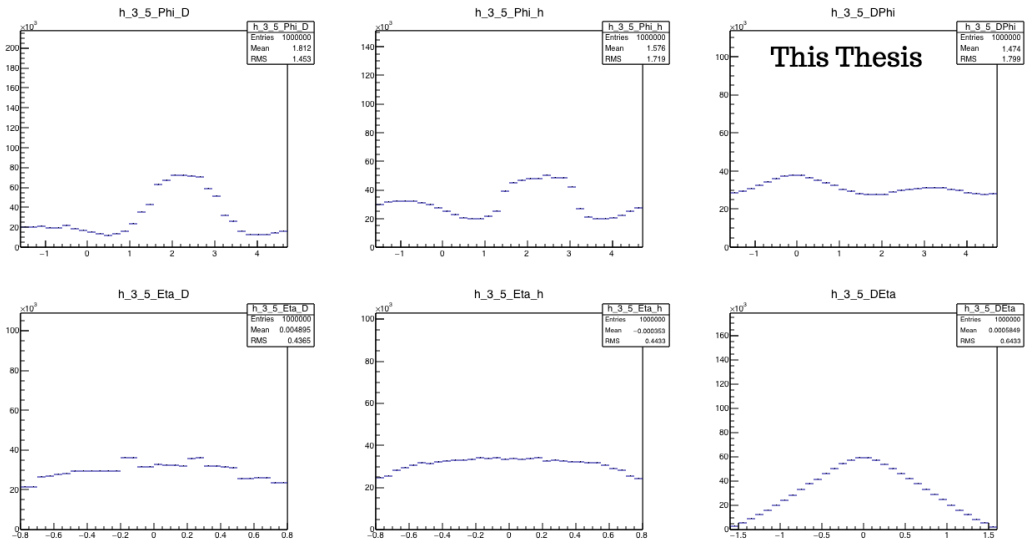

FIGURE 4.34: Simulations of the ϕ distributions of D mesons (top left), hadrons (top middle) and $\Delta\phi$ (top right), η distributions of D mesons (bottom left), hadrons (bottom middle) and $\Delta\eta$ (bottom right) using Monte Carlo Toy in the p_T range [3,5] GeV/c.

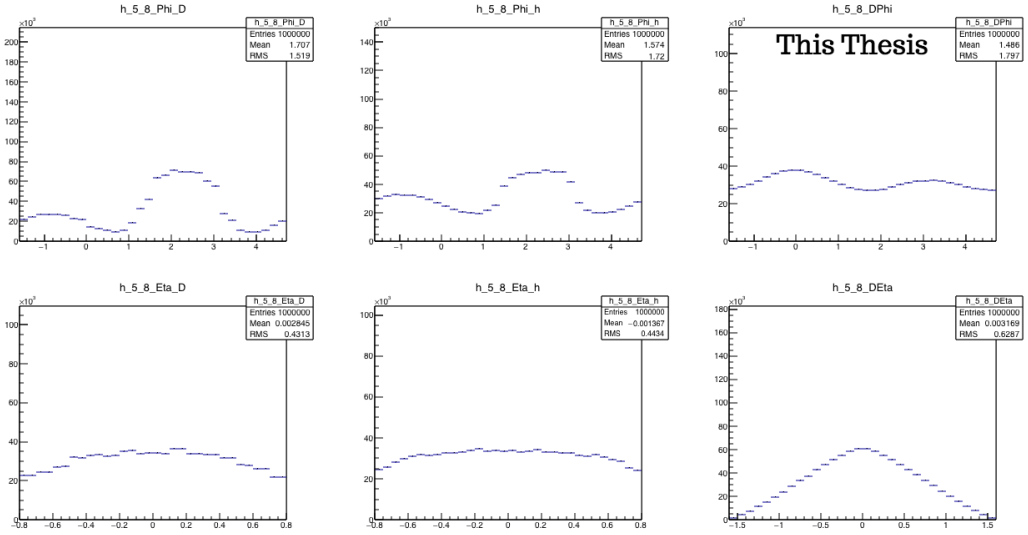

FIGURE 4.35: Simulations of the ϕ distributions of D mesons (top left), hadrons (top middle) and $\Delta\phi$ (top right), η distributions of D mesons (bottom left), hadrons (bottom middle) and $\Delta\eta$ (bottom right) using Monte Carlo Toy in the p_T range [5,8] GeV/c.

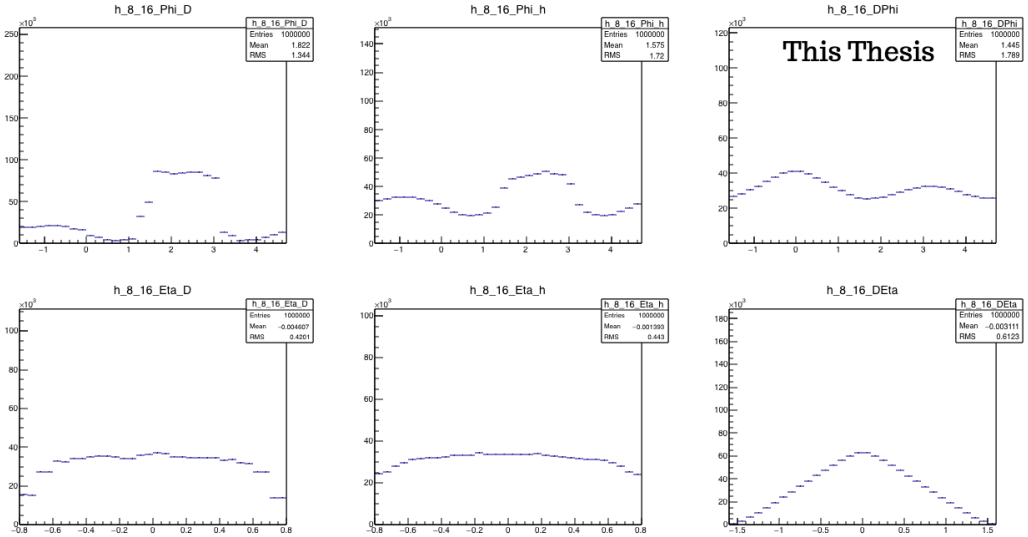

FIGURE 4.36: Simulations of the ϕ distributions of D mesons (top left), hadrons (top middle) and $\Delta\phi$ (top right), η distributions of D mesons (bottom left), hadrons (bottom middle) and $\Delta\eta$ (bottom right) using Monte Carlo Toy in the p_T range [8,16] GeV/c.

The correspondent Mixing Events distributions in two-dimensions using Monte Carlo Toy simulations are presented in figure.4.37 for the three p_T ranges of D mesons. The resulting behaviour is reasonable regarding the one-dimensional distributions of $\Delta\phi$ and $\Delta\eta$. By comparing the mixing event from the data and simulations, one can deduce that the observed peak around $(\Delta\phi, \Delta\eta) = (0,0)$ from the collected data (shown earlier in figures.4.29-4.32) is probably due to the presence of the EMCal trigger.

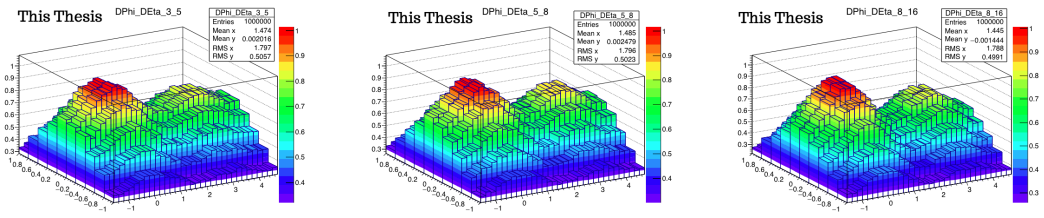

FIGURE 4.37: Mixing Event distributions obtained from Monte Carlo Toy in the p_T ranges [3,5] GeV/c (left), [5,8] GeV/c (middle), [8,16] GeV/c (right).

To Verify this interpretation, the bias due to the EMCal trigger can be studied in a different perspective by modifying the task AliAnalysisTaskDStarCorrelations. The code is modified (but not committed) to consider the electrons and photons with $p_T > 5$ GeV/c. The other particles are detected via the EMCal within a pseudo-rapidity range $-0.7 < \eta < 0.7$ and an azimuthal angle in the range $80° < \phi < 180°$. After that, the usual analysis procedure is applied. The resulting single events and mixed events in the three p_T ranges in the signal region are presented in figure.4.38, figure.4.39 and figure.4.40. The top rows present the single event distributions for minimum bias (left) and EMCal trigger (right). The bottom rows show the mixed event distributions for the minimum bias case (left) and the EMCal trigger case (right).

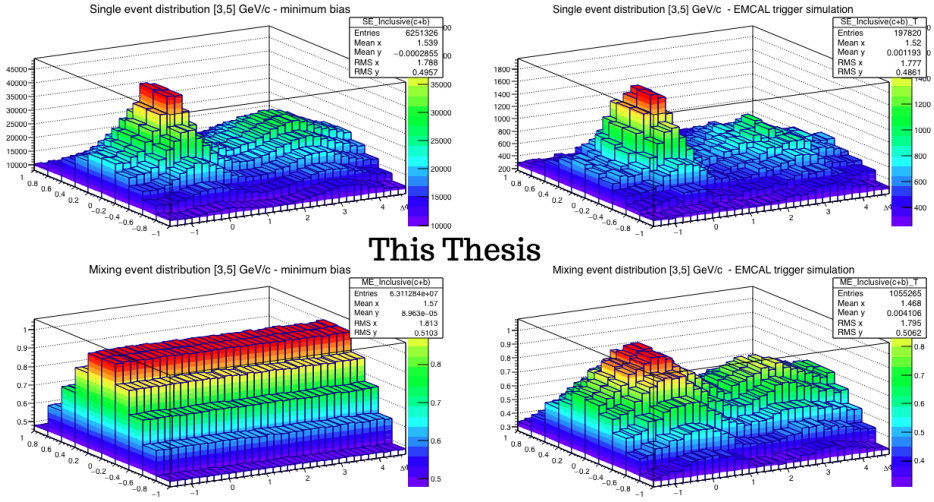

FIGURE 4.38: Single Event distributions obtained in minimum bias (top left) and EMCal trigger (top right) and Mixed Event distributions in minimum bias (bottom left) and EMCal trigger (bottom right) in the p_T ranges [3,5] GeV/c.

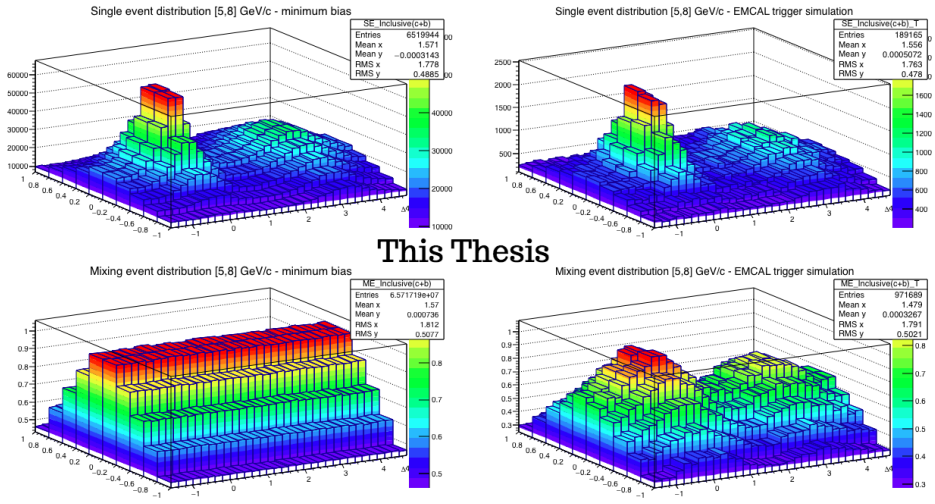

FIGURE 4.39: Single Event distributions obtained in minimum bias (top left) and EMCal trigger (top right) and Mixed Event distributions in minimum bias (bottom left) and EMCal trigger (bottom right) in the p_T ranges [5,8] GeV/c.

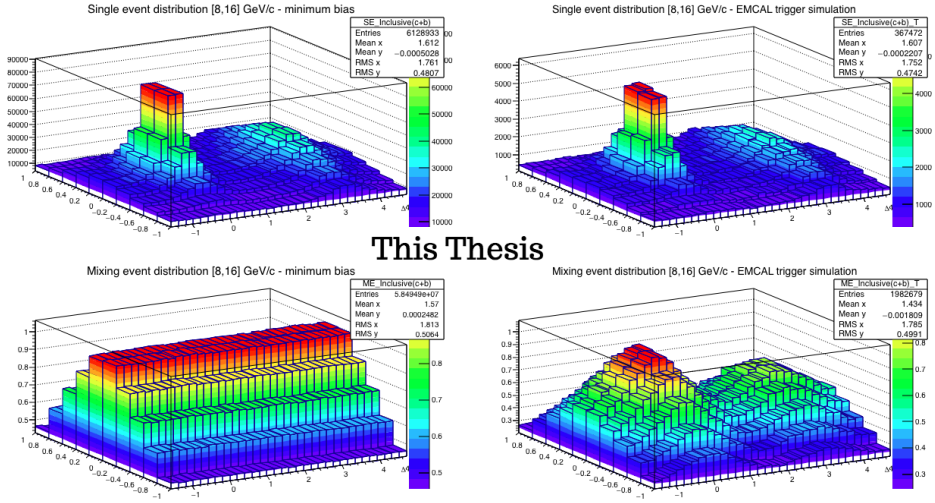

FIGURE 4.40: Single Event distributions obtained in minimum bias (top left) and EMCal trigger (top right) and Mixed Event distributions in minimum bias (bottom left) and EMCal trigger (bottom right) in the p_T ranges [8,16] GeV/c.

The criteria imposed by the presence of the EMCal trigger does not influence only the Mixing Event distribution but other observables as well. The fraction of D^{*+} mesons coming only from the fragmentation of charm quarks (prompt) is extracted by taking advantage of several MC samples generated for different purposes. The resulting fractions are shown in figure.4.41 for the minimum bias case (blue points) and the EMCal trigger case (green points).

The top left panel presents the fraction of prompt D^{*+}. It was obtained by exploiting the sample LHC106a which is a MC sample simulated with PYTHIA event generator in p-p

collisions at 7 TeV. In the top right panel, a summation of the distributions from the 2 Monte Carlo samples (LHC10f6a and LHC10d) is performed to deal with more statistics.

According to the distributions in the top row of figure.4.41, the behaviour of the fraction f_c in minimum bias is the expected one. As for the resulting one for the EMCal case, the bias is more important at low p_T. This is a piece of reliable evidence in the case of the summed samples where more statistics are exploited. Down to 15 GeV/c, it is clear that there is an agreement between the fraction obtained in the minimum bias and EMCal trigger.

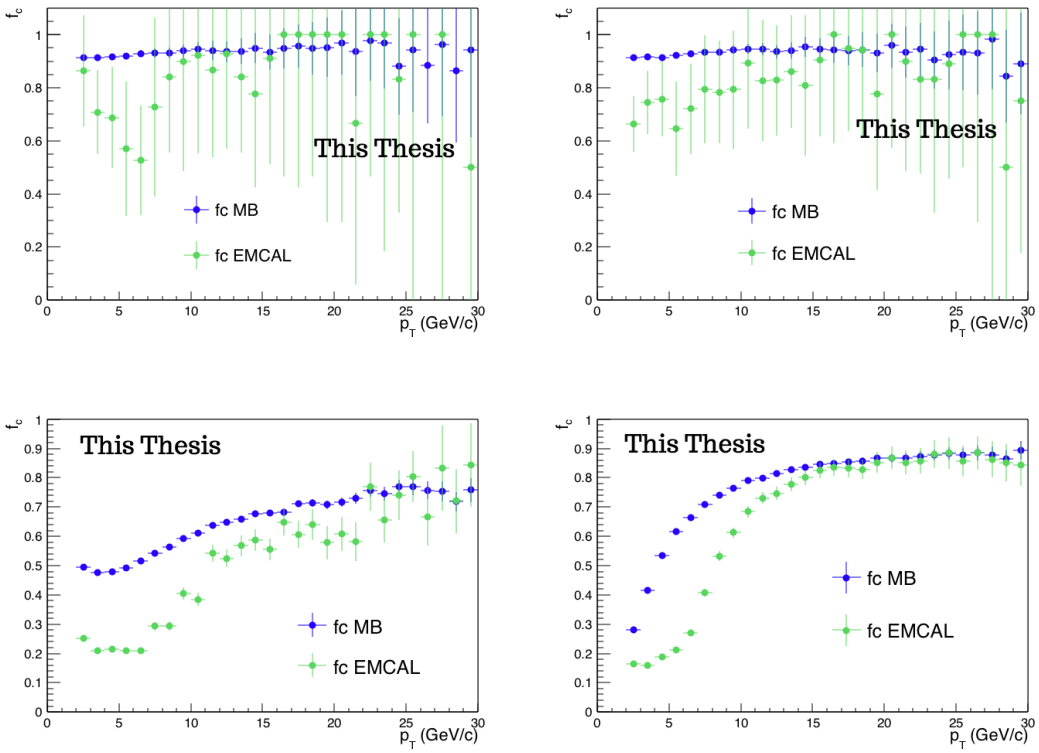

FIGURE 4.41: Fraction of charm quarks as a function of p_T in the case of minimum bias (blue points) and EMCal trigger (green points) using different MC samples: LHC10f6a (top left), LHC10d4+LHC10f6a (top right), LHC10f7a (bottom left) obtained in pp collisions at 7 TeV and LHC12d2 (bottom right) in pp collisions at 8 TeV.

For the samples, LHC10f7a and LHC12d2 simulated with PYTHIA in pp collisions at 7 TeV and 8 TeV, respectively, the production of charm quark pairs is forced in each event. The fraction shapes are different from the expected shape in minimum bias since the production of charm quarks is biased by forcing charm quark production. Concerning the EMCal trigger simulations, the bias is more important at low and intermediate p_T. From 15 GeV/c, the agreement is established between the two cases.

As a title of comparison, the p_T shape of D^{*+} obtained with the EMCal trigger simulations is compared to the simulated p_T shape of D^0 and D^+ with the EMCal trigger in p-p collisions at 8 TeV (provided by Ankita). For all D mesons, the distributions are obtained

in the hadronic channel. They were scaled as well by the number of events, the correspondent fragmentation fraction, and the branching ratio. The distributions are presented in figure.4.42. Qualitatively, the behaviour of the distributions is similar between the 3 D mesons. Quantitatively, the distribution of D^{*+} is in agreement with D^{+} using the sample LHC10f7a. Concerning the sample LHC12d2, the D^{*} p_T shape is in agreement with D^{0}.

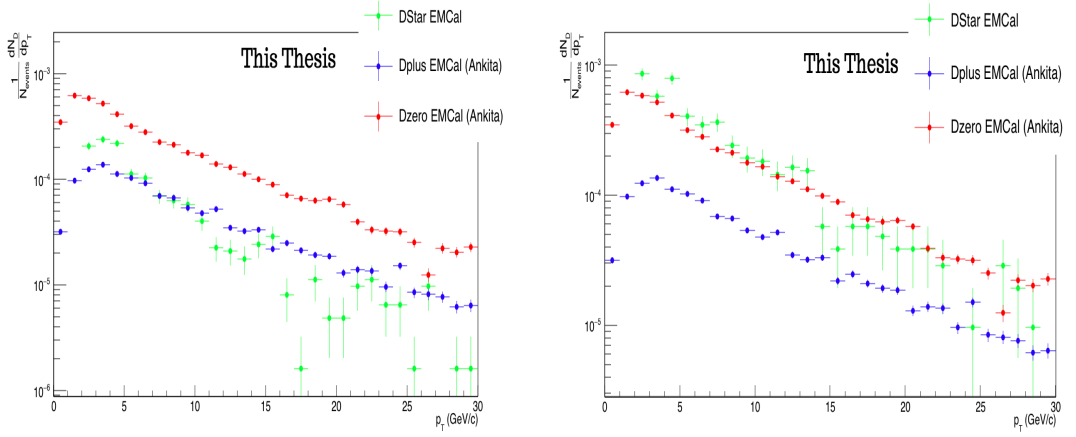

FIGURE 4.42: Transverse momentum distributions of D^{*} (green points), D^{0} (red points) and D^{+} (blue points) in the hadronic channel and normalised to the number of events for the MC samples : LHC10f7a (left) and LHC12d2 (right).

The previous part was a short parenthesis to discuss the impact of the EMCal trigger presence on the collected data and consequently on the different observables/distributions such as the mixing event distributions, the p_T spectrums, and the fraction of the charm quarks.

After obtaining the mixing and single events, the corrected single events can be extracted in both signal region and sideband region in the four considered p_T bins. Each resulting 2-dimensional corrected single event distribution is projected along $\Delta\phi$-axis, and the obtained one-dimensional distributions are presented in figure.4.43. The correlation distributions in the signal region are presented by the blue points and in the sideband region by red points. The distributions are shown for the 4 p_T ranges: [3,5] GeV/c (top left), [5,8] GeV/c (top right), [8,16] GeV/c (bottom left), [16,36] GeV/c (bottom right).

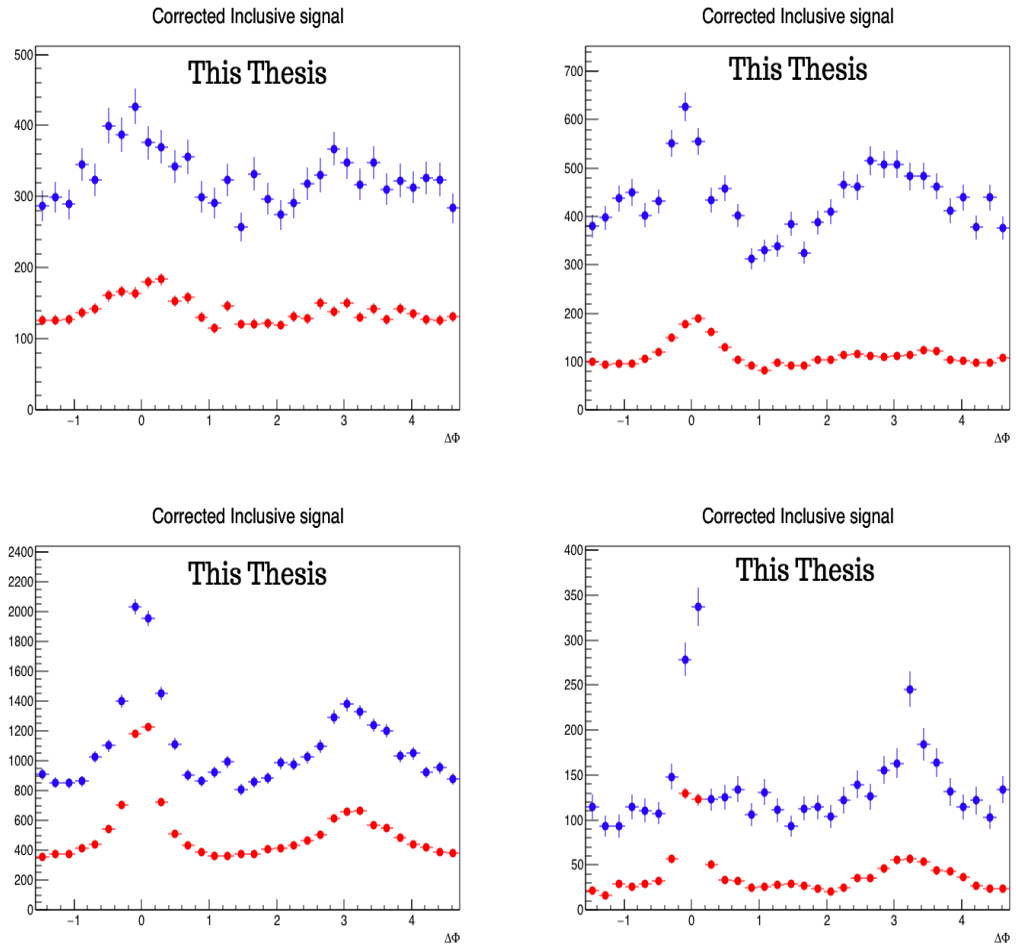

FIGURE 4.43: Correlation distributions in the signal region (blue points) and the sideband region (red points) projected on $\Delta\phi$-axis in the p_T ranges : [3,5] GeV/c (top left), [5,8] GeV/c (top right), [8,16] GeV/c (bottom left), [16,36] GeV/c (bottom right) obtained in pp collisions at 8 TeV.

Finally, the correlations in the sideband region are subtracted from those in the signal region to get the distributions presented in figure.4.44 also in the 4 p_T regions [3,5] GeV/c (top left), [5,8] GeV/c (top right), [8,16] GeV/c (bottom left), [16,36] GeV/c (bottom right). So far, the results are promising. However, they are not fully corrected due to some missing ingredients at the time of the performance of the analyses and because of the reasons mentioned at the beginning of this section.

Concerning the normalised angular-correlation distributions, it is not straightforward to deduce a conclusion from the low p_T distributions because of the dominance of fluctuations. At intermediate p_T [5,8] GeV/c, the near-side, and the away side peaks are visible, and the same can be stated for the range [8,16] GeV/c although they are not large in magnitude. For the interval [16,36] GeV/c, the magnitude of both peaks is large enough, and that gives better visibility to the distribution in that p_T range.

The baseline that represents the underlying events is around 3 (on average). This value was already inferred for correlation distributions in p-p collisions at 7 and 13 TeV. As concluded

from the analyses for the preceding energies, the baseline is dependent on the p_T range of the associated tracks, and here we are dealing with the integrated one $p_T(h) > 0.3$ GeV/c. The baseline will be lower if a subrange of p_T(h) is considered.

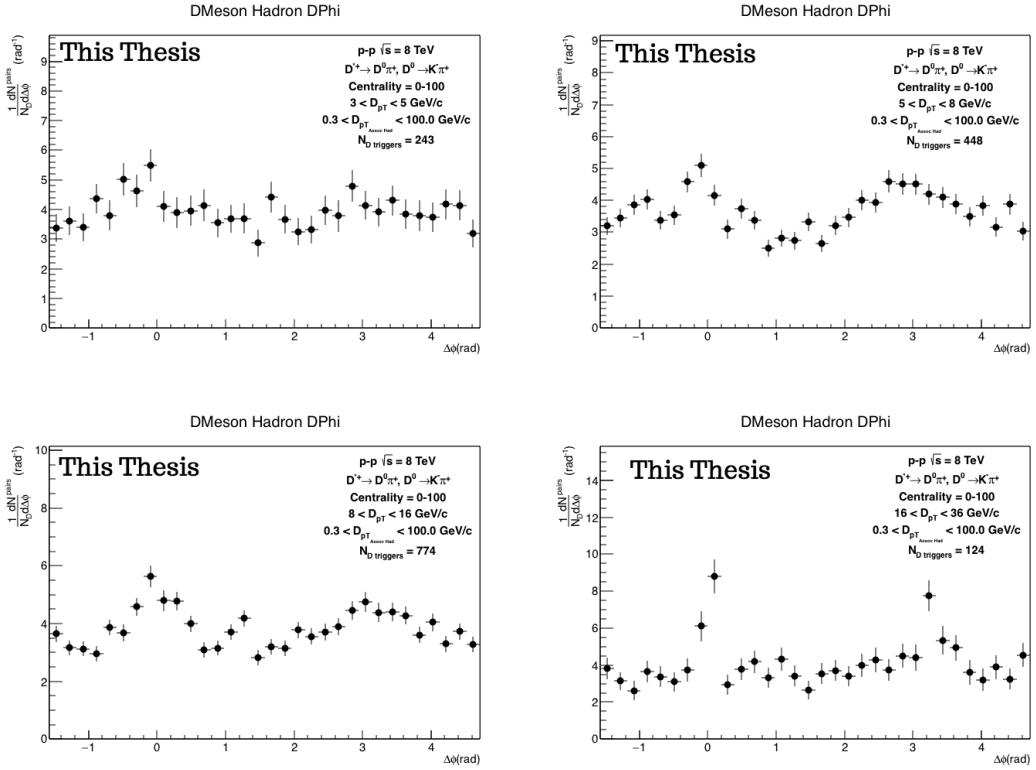

FIGURE 4.44: Normalised correlation distributions projected on $\Delta\phi$-axis after background subtraction in the p_T ranges : [3,5] GeV/c (top left), [5,8] GeV/c (top right), [8,16] GeV/c (bottom left), [16,36] GeV/c (bottom right) obtained in pp collisions at 8 TeV.

4.4 Chapter conclusion

In this chapter, the adopted strategy to analyse the collected data in pp collisions at 13 TeV was presented to get the fully corrected correlations of prompt D^{*+} mesons with primary charged particles. The resulting intermediate distributions were presented in addition to the estimation of systematic uncertainties. An overview is also given on the average D-hadron correlation distributions. D mesons were reconstructed in the range $3 < p_T < 16$ GeV/c and the associated tracks in the range $p_T > 0.3$ GeV/c. Correlation distributions for D^{*+}-hadron or average D-hadron show a flat baseline that depends on the p_T of associated tracks reflecting the underlying events. The distributions are characterised by two prominent peaks, one around $\Delta\phi$ =0 (near side peak) and the other around $\Delta\phi = \pi$ (away side peak) which reflects the jet-like behaviour for D mesons and their associated charged particles. Within the PWG-HFCJ, the average D-hadron correlations were compared to the distributions obtained from different models based on different physics treatments. The models described

qualitatively well the data and the quantitative agreement was established with PYTHIA8 and POWHEG+PYTHIA6 especially at high p_{T}. A similar analysis strategy was applied in pp collisions at 8 TeV without reaching the steps of efficiency, purity, and B feed-down correction. The obtained distributions are promising especially that no specific treatment was adapted to deal with the presence of the EMCal trigger.

Chapter 5

PYTHIA event generator

In this chapter, the PYTHIA event generator is introduced through the main theoretical principles on which it is based. Next, the correlation results obtained using this event generator are presented.

5.1 Introduction

PYTHIA is an event generator that exploits Monte Carlo methods. It is based on several physics models from theory and phenomenology to study high-energy collisions. Those collisions are evolving from a few-body hard process to a complex multi-hadronic final state. The colliding beams are limited by a set of particle species which can be protons (p, $\bar{p}$), neutrons (n, $\bar{n}$), pions (π^+, π^-, π^0), electrons (e^-, e^+) and muons (μ^-, μ^+) to study the systems hadron-hadron or lepton-lepton collisions. The energy in the centre of mass system should be larger than 10 GeV and smaller than 100 TeV. In this thesis, PYTHIA is used as a standalone event generator to study correlations in pp collisions at RHIC energies (200 GeV) and LHC energies (7 TeV). The version 8.226 (written in C++) including the default tune $Monash$ 2013 was used in the current work [100].

PYTHIA, like any event generator, passes by 3 levels to simulate the hadronic collisions: process level, parton level and hadron level.

- in the **Process level**, the nature of the event is specified, and it can be
  - $Soft\ QCD$: it includes the elastic and inelastic processes. The latter can be either a (single, double, central) diffractive or non-diffractive.
  - $Minimum\ Bias$: it is a process in experiments that refers to accepting all detected particles and it is equivalent to inelastic non-diffractive events.
  - $Hard\ QCD$: includes the necessary processes for jet production above some p_{T} thresholds. Among the main processes, one can mention the following scatterings $gg \to gg$, $gg \to q\bar{q}$, $qg \to qg$, $\bar{q}g \to \bar{q}g$, $qq \to qq$, $q\bar{q} \to q\bar{q}$.
- at the **Parton level**, the subsequent processes will take place. For example, one can mention initial and final state radiation, multiple interactions and beam remnants.

- at the **Hadron level**, the Lund string model of hadronisation is applied to generate the final state particles that are supposed to be detected by experiments.

From the technical side, the procedure can be described by:

- Initialisation by setting the initial conditions.
- Event generation according to the initial conditions.
- Finishing by getting statistics information on all generated particles.

In this procedure, one can access information from different levels. It may concern the partons, the final hadrons or their kinematical variables.

5.2 Basics and physics features

In Monte Carlo event generators, the evolution of a collision/event takes place according to a determined procedure, as summarised briefly in the following [101]:

- A collision occurs between two hadrons (bags of partons). As a result, it takes place between partons with different chosen processes.
- Colour and electromagnetic charges are accelerated due to the collision. Consequently, incoming partons can emit Bremsstrahlung/Gluonstrahlung radiations .i.e Initial-State Radiation (ISR) which is classified as a space-like parton shower.
- Outgoing partons also can emit radiations or what is called Final-State Radiation (FSR), and it is classified as a time-like shower.
- The colliding hadrons are a bunch of incoming partons. Consequently, several collisions between partons can occur. This aspect led to the introduction of the term Multiparton Interactions (MPI).
- The partons do not acquire the whole energy, and the biggest fraction remains in the beam remnants that are colourful due to the colour conservation principle.
- When the colourful partons and beam remnants move away from each other, confinement forces become important. It was suggested that, between each colour and its anti-colour, a confinement field is created and can be broken when a pair of quark-antiquark is produced. An (anti)quark can combine with another (anti)quark from an adjacent break to form a hadron (Hadronisation).
- The generated hadrons can be either long-lived enough to be detected or unstable to decay shortly after their production. At this stage only, event generators are dealing with experimental observables.

The partonic cross-section is a combination of the phase space with the matrix elements derived from Feynman rules using the Lagrangian of the concerned theory. For example, one can consider from QCD the simple scattering $u(1)d(2) \rightarrow u(3)d(4)$ where quarks exchange

a gluon. The total cross-section is obtained by convoluting the partonic cross-section with the constituents of the incoming hadrons. This is expressed by the equation,

$$\sigma = \sum_{i,j} \int\int\int dx_1\, dx_2\, d\hat{t}\, f_i^{(A)}(x_1, Q^2)\, f_j^{(B)}(x_2, Q^2)\, \frac{d\hat{\sigma}_{ij}}{d\hat{t}} \tag{5.1}$$

A and B represent the incoming hadrons. The indices i and j refer to the partons in the hadrons A and B. $\frac{d\hat{\sigma}_{ij}}{d\hat{t}}$ is the partonic cross section where $\hat{t}$ is a Mandelstam variable defined by $\hat{t} = (p_1 - p_3)^2$. x_1 and x_2 are the momentum fractions, defined respectively as E_i/E_A and E_j/E_B. $f_i^{(A)}(x_1, Q^2)$ and $f_j^{(B)}(x_2, Q^2)$ are the parton distribution function (PDF).

There are 16 Partonic Distribution Functions (PDF) integrated within PYTHIA8. At the Leading Order (LO), the default PDF exploited in the current work for proton is the CTEQ5L. It involves the strong coupling constant $\alpha_s(M_Z) = 0.127$. The evolution as a function of x and Q covers the ranges $10^{-6} < x < 1$ and 1.1 GeV $< Q <$ 10 TeV, respectively. Some other external parton distribution functions can be used as well.

5.2.1 Parton showers (ISR/FSR)

Parton showers in QCD can take place according to three different patterns: q $\rightarrow$ qg, g$\rightarrow$ gg, g $\rightarrow q\bar{q}$ which can contribute to both Initial State Radiation (ISR) and Final State Radiation (FSR). In PYTHIA, the algorithms of ISR and FSR are based on the principle of p_T-ordered evolution, and that was already implemented for PYTHIA 6.3. This sequence is not only interleaved with the initial state radiation evolution and multiple interactions (MPI), but with the Final state radiation evolution as well. In this approach, the process of the interaction is split from a complex 2 $\rightarrow$ n process with a large number of final states into a simple process 2 $\rightarrow$ 2 + successive radiations in the initial/final states (ISR/FSR) as presented in figure.5.1 where the incoming partons radiate harder gluons and outgoing partons radiate softer gluons. This can be expressed differently using the parameter $Q^2 \sim |p^2| = |E^2 - \vec{p}^2|$. The incoming partons (ISR) are generated with the virtualities $Q^2 < 0$ and the term "space-like shower" is attributed. The outgoing partons (FSR) are generated with the virtualities $Q^2 > 0$ and the term "time-like shower" is used in this case.

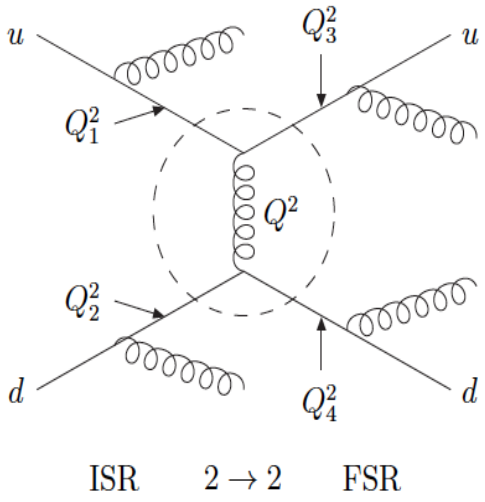

FIGURE 5.1: Shower approach : the factorisation $2 \to$ n.

The evolution of the partonic shower is based on the standard LO DGLAP splitting kernel in QCD. It can be presented for three patterns by the following equations:

$$P_{q\to qg}(z) = C_F \frac{1+z^2}{1-z} \tag{5.2}$$

$$P_{g\to gg}(z) = C_A \frac{(1-z(1-z))^2}{z(1-z)} \tag{5.3}$$

$$P_{g\to q\bar{q}}(z) = T_R \left(z^2 + (1-z)^2\right) \tag{5.4}$$

where z is the fraction of the shared energy between the daughter partons, $\mathrm{C}_F = \frac{4}{3}$, $\mathrm{C}_A = \mathrm{N}_C = 3$, $\mathrm{T}_R = \frac{1}{2}$.

The evolution of the shower, in the final states (FSR), is presented by the DGLAP equation,

$$dP_{a\to bc} = \frac{\alpha_s}{2\pi} \frac{dQ^2}{Q^2} P_{a\to bc}(z)\, dz\, exp\left(-\sum_{b,c} \int_{Q^2}^{Q^2_{max}} \frac{dQ'^2}{Q'^2} \int \frac{\alpha_s}{2\pi} P_{a\to bc}(z')\, dz'\right), \tag{5.5}$$

The exponent is the Sudakov form factor [102] which was introduced to conserve the total probability to deal with the cancellation between real and virtual divergences. Briefly, the Sudakov factor is an approximation representing the complete virtual corrections from loop graphs. For initial state radiation (ISR), the evolution of the shower according to the DGLAP equation is expressed by,

$$\frac{df_b(x,Q^2)}{d(lnQ^2)} = \sum_a \int_x^1 \frac{dz}{z} f_a(x',Q^2) \frac{\alpha_s}{2\pi} P_{a\to bc}\left(z = \frac{x}{x'}\right) \tag{5.6}$$

Equation.5.6 indicates the branching probability of a parton a to bc for an exchange dQ^2, in other word, it illustrates how the distribution will evolve for different possible branchings a to bc.

For FSR, the outgoing partons kicked by the hard process form a cascade toward the mass shell with large timelike virtualities. As for ISR, it starts with a simple proton, so the closer we get to the hard interaction the larger the spacelike virtualities are.

The evolution of the ISR and FSR parton showers is expressed by the differential branching probability per unit evolution time:

$$\frac{dP_{FSR}}{dp_\perp^2} = \frac{1}{p_\perp^2} \int dz \frac{\alpha_s}{2\pi} P(z) \tag{5.7}$$

$$\frac{dP_{ISR}}{dp_\perp^2} = \frac{1}{p_\perp^2} \int dz \frac{\alpha_s}{2\pi} P(z) \frac{f'(x/z, p_\perp^2)}{z f(x, p_\perp^2)} \tag{5.8}$$

where $z = x/x'$ with $x < x'$ for ISR and $p_\perp^2$ is the PYTHIA transverse-momentum evolution variable, defined by:

$$p_\perp^2 = p_{\perp evol}^2 = \begin{cases} (1-z)\, Q^2 : ISR \\ z(1-z)\, Q^2 : FSR \end{cases} \tag{5.9}$$

FSR are characterised by time-like virtualities ($p^2 > 0$) while ISR are characterised by space-like virtualities ($p^2 < 0$)

5.2.2 Multi-Parton Interactions (MPI)

The Multi-Parton Interaction (MPI) is the consequence of the hadron constitution. It has been proven that this process is involved in small systems like pp collisions or systems such as p-Pb and Pb-Pb through different studies. For what concerns the heavy-flavour sector, the multiplicity dependence of the average transverse momentum and heavy-flavour hadron yield was studied in [103] [104] [105]. It was inferred that the multiplicity is proportional to multiple Parton Interactions that was, indeed, dependent on the increased yield of D mesons with the multiplicity. The multiplicity itself increases with the hardness of the scatterings (.i.e high p_T). The regularised parton-parton cross-section, is expressed by the equation:

$$\frac{d\hat{\sigma}_{2\to2}}{dp_\perp^2} \propto \frac{\alpha_s^2(p_\perp^2)}{p_\perp^4} \to \frac{\alpha_s^2(p_\perp^2 + p_{\perp 0}^2)}{(p_\perp^2 + p_{\perp 0}^2)^2} \tag{5.10}$$

to avoid the divergence due to the $p_\perp \to 0$ limit (low momentum transfer) which is the case for low-x partons accessible at high energies $\sqrt{s}$. This cross-section depends on three parameters: the effective $p_{\perp 0}$ which is a free parameter of the model, $\alpha_s(M_Z)$ (a dampening scale around 2 GeV) and the PDF that defines the parton luminosity in the MPI. The typical average number of interactions per event is around 2-3 at the Tevatron and 4-5 at the LHC.

The probability for the MPI i to take place is expressed by the equation,

$$\frac{dP_{MPI}}{dp_\perp} = \frac{1}{\sigma_{ND}} \frac{d\sigma_{2\to2}}{dp_\perp} \exp(-\int_{p_\perp}^{p_{\perp i-1}} \frac{1}{\sigma_{ND}} \frac{d\sigma_{2\to2}}{dp'_\perp} dp'_\perp) \tag{5.11}$$

In PYTHIA, the number of MPI depends on the impact parameter .i.e the average number of MPI is large when collisions are more central [103].

By combining all ingredients (ISR, FSR, MPI), The master evolution equation of PYTHIA 8 can be expressed by,

$$\begin{aligned} \frac{dP}{dp_\perp} = &(\frac{dP_{MPI}}{dp_\perp} + \sum \frac{dP_{ISR}}{dp_\perp} + \sum \frac{dP_{FSR}}{dp_\perp}) \\ &\times \exp(-\int_{p_\perp}^{p_{\perp i-1}} (\frac{dP_{MPI}}{dp'_\perp} + \sum \frac{dP_{ISR}}{dp'_\perp} + \sum \frac{dP_{FSR}}{dp'_\perp}) dp'_\perp) \end{aligned} \tag{5.12}$$

5.2.3 Color Reconnection (CR)

The Colour Reconnection (CR) mechanism is the interaction and interference between the decay products of any quark (chromoelectric fields) during hadronisation. The contribution of such a mechanism is expected at a high rate, especially at the LHC, due to the presence of a large number of coloured partons combined through MPI, Parton Showers (PS) and Beam Remnants (BR). This mechanism was introduced the first time to explain the increase of $< p_T >$ as a function of n_{ch} in UA1 [106] [107]. This is because the rising trend with multiplicity is not p_T dependent but MPI dependent instead [108]. Studies such as [109] have proven the sensitivity of underlying events to colour reconnection. The common scenario for colour reconnection suggests a probability of colour inter-arrangement (colour flow of different MPI's) between the partons of two sub-scatterings in such a way that the total string length (λ) is reduced. λ can be defined as,

$$\lambda \approx \sum_{i,j} ln \left(\frac{m_{ij}^2}{m_0^2} \right), \tag{5.13}$$

$m_0 (\approx 1$ GeV/c) is a reference scale (of the order of hadronic mass). i, j are indices running over all parton pairs which are colour-string-connected.

The transverse velocity of the string piece is transferred to the particles produced from it. The favoured reduced string length that refers to longer timescales is the consequence of closer endpoint partons. As a result, the string pieces will have high transverse velocity.

5.2.4 Beam Remnants (BR)

After MPI (with colours contribution) took place due to the collisions of several incoming hadrons, as compensation, they leave behind a complicated structure manifested by the Beam Remnants (BR). BR consist of any remaining valence content in the incoming

hadrons where they will be carrying the remaining fraction of the longitudinal momentum. In PYTHIA, the default model that describes the beam remnant is based on the principle that gluons are attached to colour lines in such a way that the total colour charge of the remnant is reduced. Whereas for the x values of BR, valence contents are chosen to be harder (large carried momentum) [103] [106].

5.2.5 Hadronisation

The Lund String Fragmentation framework [110] [111] is the adopted approach for hadronization processes in PYTHIA. Hadronization is a mechanism where coloured partons become a bounded state of partons and transform into colourless particles (hadrons). Hadronization is based on the linear confinement picture .i.e the larger the distance between the charge and the anti-charge in a colour dipole field, the higher is the stored energy (linear increase). The production of $q\bar{q}$ pair is a good example where this mechanism can take place. The tension in the string between q and $\bar{q}$ increases when the pairs move away from each other. If the tension is large enough, a new pair can be created in between. This results in 4 quarks $q\bar{q'}$ and $q'\bar{q}$ and so on. The previous process will be repeated till the string mass is not enough to create new pair, consequently, the last pairs will be transformed into hadrons in this evolution chain [101] [112] [29] [113] [114].

5.3 Heavy flavours in PYTHIA

In PYTHIA, heavy-flavours are treated perturbatively concerning their production and in a non-perturbative way to deal with their hadronisation. By considering QCD processes in hadron-hadron collisions, the parton shower evolution ($2 \rightarrow$ n) is subdivided into three stages as already explained, the initial state radiation followed by the hard scattering sub-process then the final state radiation. The hard sub-process is represented by a scattering $2 \rightarrow 2$ and characterised by the shortest distance (the largest virtualities in the whole process of evolution).

The same procedure is applicable for heavy-flavours at the level of the hard sub-process where they can be produced,

- at the **leading-order LO** $\mathcal{O}(\alpha_s^2)$ through **flavour creation** : $q\bar{q}$ annihilation ($q\bar{q} \rightarrow Q\bar{Q}$) and gluon fusion ($gg \rightarrow Q\bar{Q}$). This mechanism is included by default when PYTHIA8 is used as a standalone event generator. The correspondent Feynman diagrams are shown in figure.5.2 as an illustration.

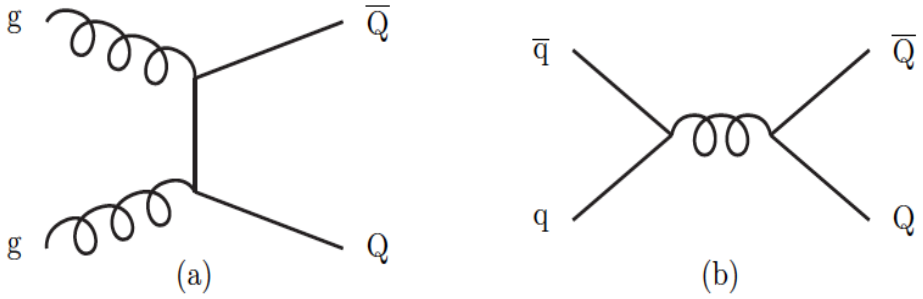

FIGURE 5.2: Leading-Order : (a) Flavour creation through gluon fusion. (b) Flavour creation through the annihilation of $q\bar{q}$ pair [111].

- at the **next-to-leading-order NLO** $\mathcal{O}(\alpha_s^3)$ through **flavour excitation** (Qq(g) $\rightarrow$ Qq(g)) where the heavy quark Q from a beam is put on-shell to interact with a parton (q,g) from the other beam. The other process is the **gluon splitting** ($g \rightarrow Q\bar{Q}$) where gluon can branch either in the initial-state or in the final-state in such a way that it does not contribute to the hard sub-process. A radiative correction can be added to the pair creation process through gluon emission ($gg \rightarrow Q\bar{Q}$g) which is allowed in the parton shower to compensate for the recoil due to the back-to-back production of the heavy-flavour pair (see figure.5.3).

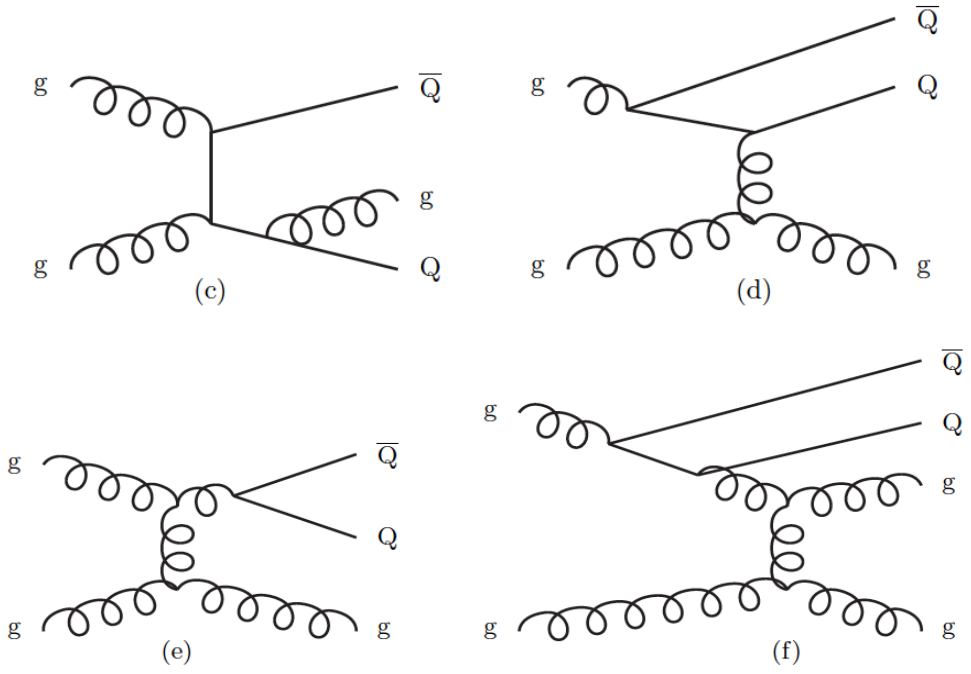

FIGURE 5.3: Next-to-Leading-Order : (c) Flavour creation + radiative correction (gluon emission), (d) Flavour excitation, (e) Gluon splitting (final-state), (f) Gluon splitting (initial-state) [111].

In addition to PYTHIA8 and in order to exploit the NLO, one needs to add merging of the Matrix Element / Parton Shower (ME / PS) using, for instance, POWHEG-BOX event generator that is an option among several others so that the NLO processes

can be considered which is beyond the time and the resources allowed to finish this thesis.

In addition to the previous production mechanisms, heavy flavours can be produced from other sources, such as the decays of resonances (Z, W, H).

At lower energies in the centre of mass frame $\sqrt{s}$, the production cross-section of heavy-flavours via pair creation is the most dominant and followed by flavour excitation and gluon splitting. At higher energies, the contribution of pair creation decreases and the gluon splitting becomes the dominant one. This is due to the fact that the number of branchings increases with energy which is the case for gluon splitting. This mechanism becomes dominant in comparison to pair creation that remains a process $2 \rightarrow 2$ scattering whatever the energy $\sqrt{s}$. Concerning flavour excitation, the number of branchings is more restrictive at higher energies. At lower energies, kinematical requirements are less, and the mechanism (FEX) becomes dominant compared to gluon splitting in this case.

For heavy flavour hadronization, the string is a very important entity in the process. It satisfies the Lorentz-invariance principle applied on a linear confinement potential with a tension of 1 GeV/c. In this model, the confinement of partons inside the hadrons is ensured by the string that spans between the outgoing partons. It consists of colour and anti-colour charges on its two ends. The quark can be attached to one string piece, and the gluon can be attached to two of them.

As mentioned earlier and taking advantage of the string properties, the Lund string fragmentation model can describe the non-perturbative hadronization of partons. Accordingly, the process depends pretty much on the invariant mass of the string. Consequently, it will lead to different hadronisation scenarios.

- **Normal string fragmentation** The string invariant mass is large enough as well as its length which results in larger average multiplicities. A continuum of phase-space is assumed as a standard iterative scheme. This approach is only applicable for some cut-off on the mass.
- **Cluster decay** The continuum assumption is not anymore applicable and from the kinematic side, only two body final states are reachable. This is due to the fact that the string is produced with a small invariant mass, and it is called a cluster.
- **Cluster collapse** The invariant mass of the string is too small then it will not decay into two bodies, but it will collapse into one hadron. In this case, a discrete phase-space of hadrons is considered instead of the continuum one [111].

5.4 Results and discussions

The goal of these analyses is to study heavy-flavour correlations $B - \bar{B}$ and $D - \bar{D}$ in pp collisions for different energies (7 TeV and 200 GeV). For this purpose, the acceleration

of two beams of protons is simulated at the energies of 7 TeV and 200 GeV in the centre of mass frame using the event generator PYTHIA8 (version 8.226). Heavy-flavour mesons were generated by forcing the production of a heavy flavour pair in each event. this process will be referred to as "Forced" for the rest of this chapter. One million is the number of events set in these simulations.

B (D) mesons are correlated with $\bar{B}(\bar{D})$ in such a way that the pairs should be in the same event. The opening angle between the correlated pairs is computed by applying the equation,

$$\Phi = acos\left(\frac{P_x^D P_x^{\bar{D}} + P_y^D P_y^{\bar{D}}}{P_T^D \times P_T^{\bar{D}}}\right) \tag{5.14}$$

Where P_x, P_y, P_T are the momentum along x, y and the transverse plane directions, respectively. The opening angle is computed for all possible combinations $B - \bar{B}$ ($D - \bar{D}$) to obtain the $\Delta\phi$, $\Delta\eta$, ΔY, Δp_T distributions. The transverse momentum distributions of these mesons are obtained as well as a check.

5.4.1 $D - \bar{D}/B - \bar{B}$ correlations obtained with different configurations

It is important to compare the correlation distributions obtained for different configurations with PYTHIA. Later, one configuration is considered to get the final results of this chapter. The physics properties for each of the 3 configurations are explained in the following:

- **HardQCD:all=on** where all QCD processes are involved. The most relevant ones in this analysis are those responsible for the production of the pair of charm/bottom quarks through $q\bar{q}$ annihilation or gluon fusion. However, gluon splitting contributes to the initial and final-state radiation even if the NLO is not activated.
- **Forced**. In each event, a pair of heavy flavours are forced to be created, so one should have one pair at least in each event. The number of heavy flavours will be larger than the natural number.
- **Minimum Bias (MB)** is the ideal process for comparisons with respect to experimental data. Briefly, this mode is suitable to simulate a realistic experiment where the number of generated particles can be closer to the one measured in experiments or with a similar scale.

Some considerations were taken into account to make the analysis simpler. All decay channels were treated equally, so no decay channel was privileged. In addition, all decay channels of the concerned particles for the analysis were switched off (B and D mesons). This way, the heavy mesons will be identified via their PDG numbers.

Correlations were obtained for both D and B mesons at the energies 200 GeV and 7 TeV. $B\bar{B}$ correlations in pp collisions at 200 GeV won't be presented since the number of events was not enough to get some conclusions, especially the two configurations HardQCD and MB that have shown statistical fluctuations.

The obtained $D\bar{D}$ correlations in pp collisions at 200 GeV are presented in figure.5.4. The red curve presents the correlation distributions for the "Forced" case, the green one for "All HardQCD" processes and the blue one for the Minimum bias (MB) case. For each configuration, the distributions $\Delta\phi$, Δp_T, $\Delta\eta$, ΔY, p_T are presented. According to figure.5.4, the correlation distributions show similar quantitative behaviour for the two cases "MB" and "HardQCDall". The same behaviour is observed for the "Forced" case, but with a quantitative difference and a light qualitative difference, and that does not change the physics interpretation. These features are observed in Δp_T, $\Delta\eta$, ΔY, p_T distributions but not in $\Delta\phi$ distribution. Correlations are sensitive observable to the number of created heavy flavours and correlated pairs. This is due to the fact that in the "Forced" case, the number of created heavy flavour pairs is enhanced compared to the cases MB, HardQCDall which leads to larger distributions in magnitude in the "Forced" case. Otherwise, the physical conclusions and interpretations for the cases should be the same. For this reason and time matter, the configuration "Forced" will be used in these analyses.

$B\bar{B}$ correlations in pp collisions at 7 TeV are presented in figure.5.5 and $D\bar{D}$ correlations in pp collisions at 7 TeV are presented in figure.5.6. The same conclusions can be deduced from these figures as well. The difference with respect to 200 GeV is that correlations distributions at 7 TeV are more disentangled due to the large multiplicities generated at higher energies. Correlation distributions in the "Forced" configurations have the largest magnitude in comparison to the case of "HardQCDall" which in its turn has a larger magnitude than the case of "MB".

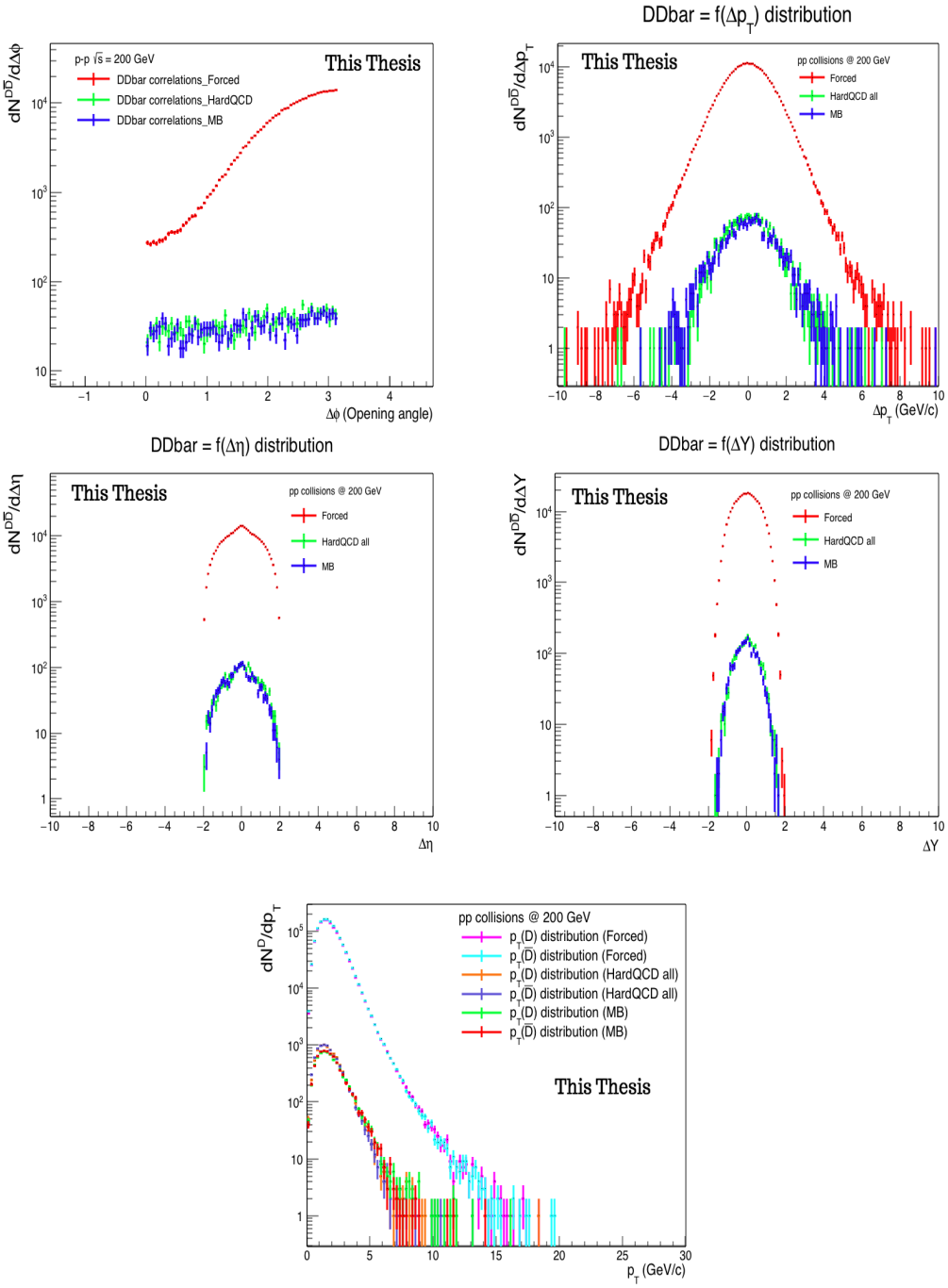

FIGURE 5.4: $D-\bar{D}$ correlation distributions of $\Delta\phi$ (top left), Δp_T (top right), $\Delta\eta$ (middle left), ΔY (middle right) in pp collisions at 200 GeV for the 3 configurations : Forced (red), HardQCD all (green) and MB (blue). p_T distributions of $D(\bar{D})$ mesons for the 3 configuration cases (bottom).

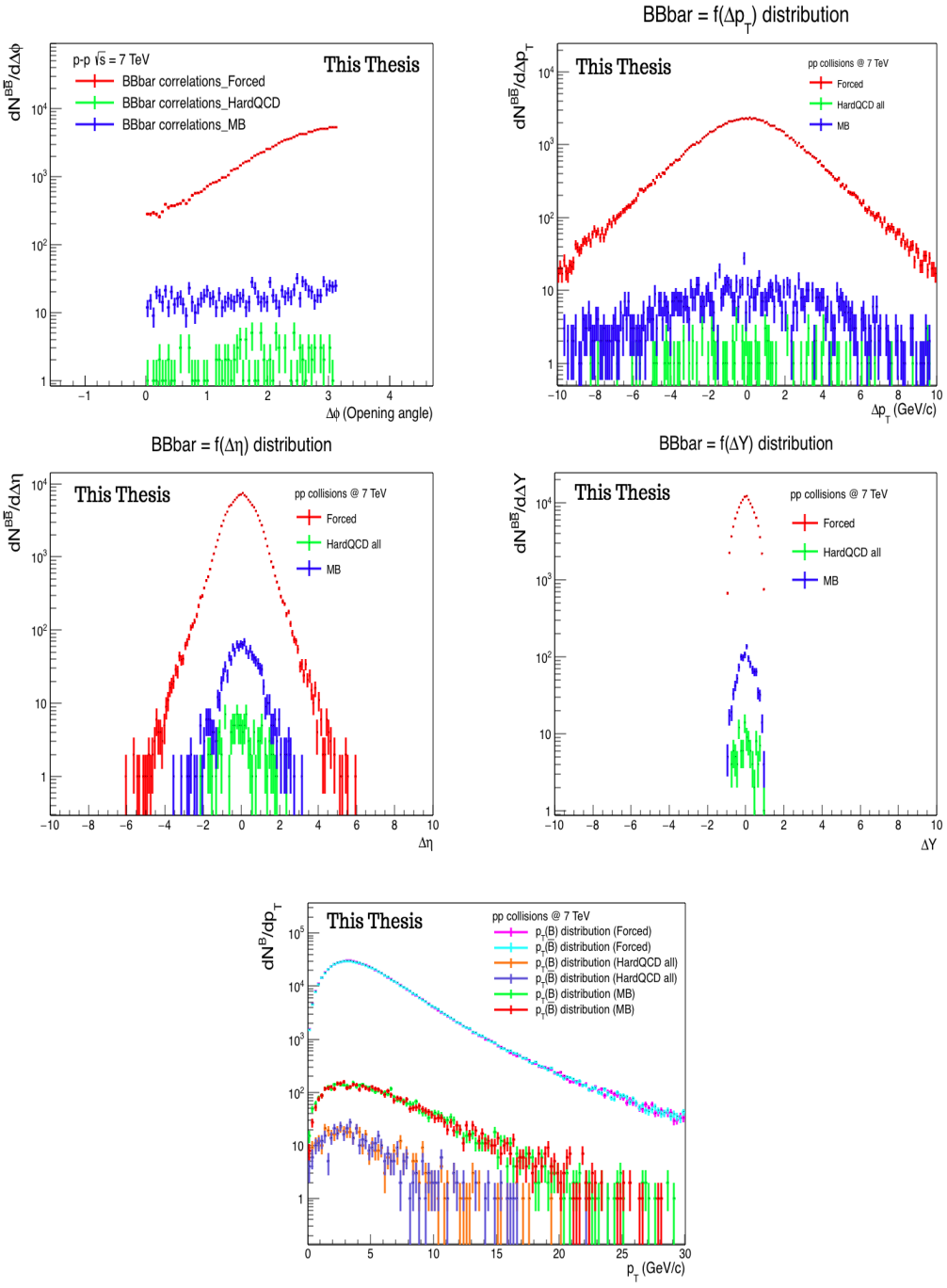

FIGURE 5.5: $B-\bar{B}$ correlation distributions of $\Delta\phi$ (top left), Δp_T (top right), $\Delta\eta$ (middle left), ΔY (middle right) in pp collisions at 7 TeV for the 3 configurations : Forced (red), HardQCD all (green) and MB (blue). p_T distributions of $D(\bar{D})$ mesons for the 3 configuration cases (bottom).

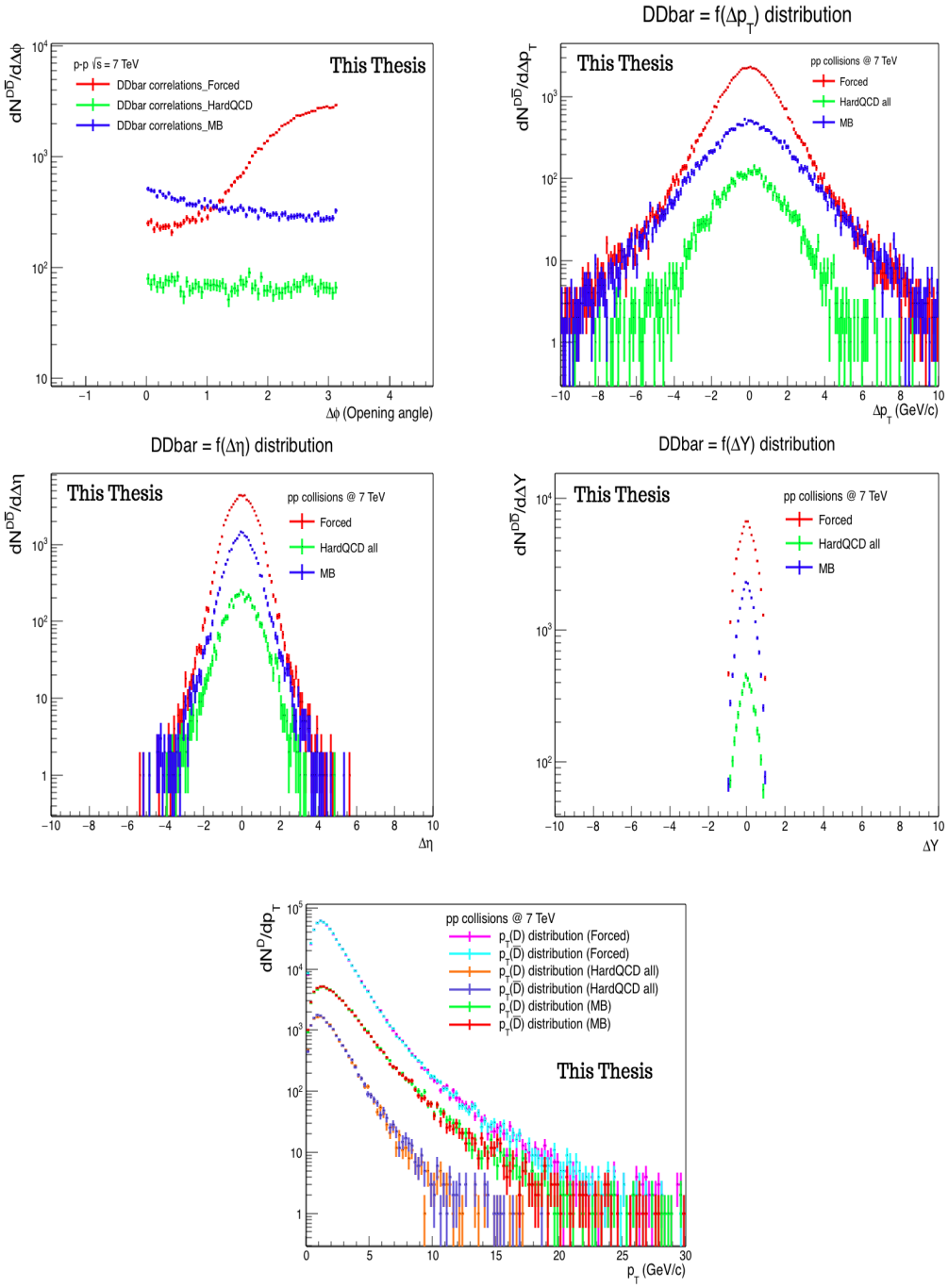

FIGURE 5.6: $D-\bar{D}$ correlation distributions of $\Delta\phi$ (top left), Δp_T (top right), $\Delta\eta$ (middle left), ΔY (middle right) in pp collisions at 7 TeV for the 3 configurations : Forced (red), HardQCD all (green) and MB (blue). p_T distributions of $D(\bar{D})$ mesons for the 3 configuration cases (bottom).

5.4.2 $B-\bar{B}/D-\bar{D}$ correlations in pp collisions at 7 TeV and 200 GeV

In this section, $B-\bar{B}$ and $D-\bar{D}$ correlation distributions are obtained for the full p_T range and for the subranges : $0 < p_T(B/D) + p_T(\bar{B}/\bar{D}) < 10$ GeV/c, $10 < p_T(B/D) + p_T(\bar{B}/\bar{D}) < 20$ GeV/c, $20 < p_T(B/D) + p_T(\bar{B}/\bar{D}) < 30$ GeV/c and $p_T(B/D) + p_T(\bar{B}/\bar{D}) > 30$ GeV/c. The correspondent distributions of $B-\bar{B}$ correlation

in pp collisions at 200 GeV are presented in figure.5.7. The $\Delta\phi$ distribution is presented in the top left panel of figure.5.7. The black curve represents the correlations of $B - \bar{B}$ pairs in the integrated p_T range, the red curve represents the correlations in the range 0 $< p_T(B) + p_T(\bar{B}) <$ 10 GeV/c, the green curve in the range 10 $< p_T(B) + p_T(\bar{B}) <$ 20 GeV/c, the blue curve in the range 20 $< p_T(B) + p_T(\bar{B}) <$ 30 GeV/c and the yellow one in the range $p_T(B) + p_T(\bar{B}) >$ 30 GeV/c.

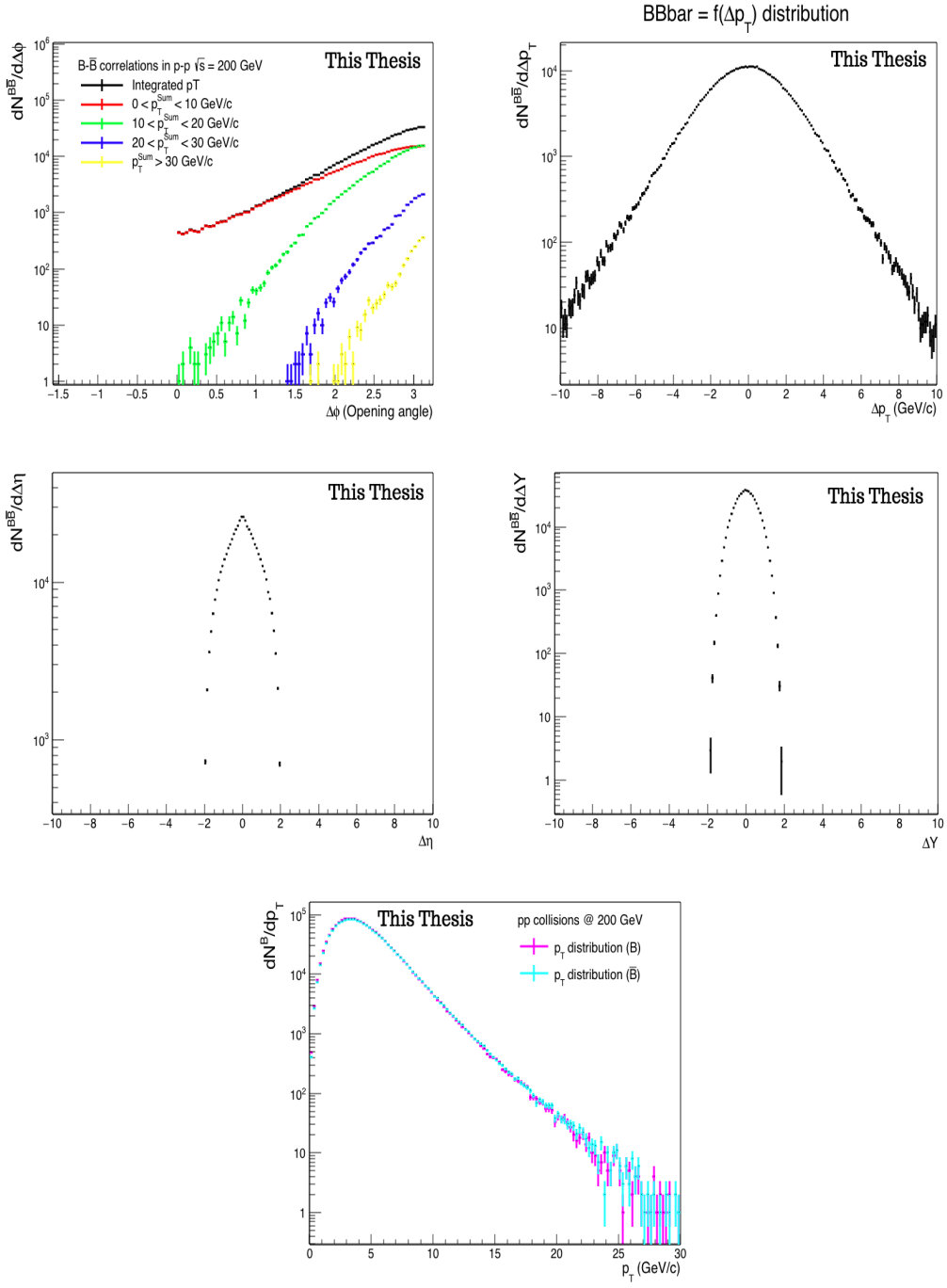

FIGURE 5.7: $B-\bar{B}$ correlation distributions of $\Delta\phi$ (top left), Δp_T (top right), $\Delta\eta$ (middle left), ΔY (middle right) and p_T spectrum of B (magneta) and $\bar{B}$ (cyan) (bottom) in pp collisions at 200 GeV.

First, an observed enhancement of the correlation distributions around $\Delta\phi = \pi$, shows that B mesons are mainly produced back-to-back in pp collisions at 200 GeV whatever the considered range of transverse momentum. Secondly, one can see that the dominant distributions are those with the low p_T range. However, correlations get stronger at high transverse momentum. The distributions for high p_T B mesons are less broadened in comparison to those at low p_T. From this observation, one can deduce that at high p_T, the generated bottom quark pairs through flavour creation becomes important compared to those generated via the NLO processes (Flavour Excitation and Gluon Splitting). The opposite is observed for low$_T$ pairs where events with NLO processes are not negligible.

An interpretation can be given based on either processes or the number of created pairs and their transverse momentum as presented in the p_T distribution in the bottom panel of figure.5.7. From one side, it is clear that there are more produced/generated B mesons at low p_T compared to those at high p_T which confirms the deduction from the $\Delta\phi$ distributions. On the other side, flavour creation is a reflection to the Leading Order QCD calculations which is supposed to lead to a back-to-back production of heavy flavour. This is true, according to the $\Delta\phi$ distributions, since PYTHIA8 (standalone event generator) is based on LO QCD calculations. As a side note, the transverse momentum spectrum of $B/\bar{B}$ mesons (and $D/\bar{D}$) were obtained separately to have a separate visualisation.

In the top right panel of figure.5.7, the Δp_T correlation distribution of $B\bar{B}$ pair in the integrated p_T range is presented. One can notice a prominent peak around $\Delta\phi = 0$. This shows that that an important number B-meson pairs is produced with similar transverse momentum whether the pairs are produced in the same direction or with opposite ones.

In the left plot in the middle row of figure.5.7, the $\Delta\eta$ correlation is presented where the cut $|\eta| < 1$ was applied. The same for ΔY correlation presented in the right plot in the middle row of figure.5.7 where the cut $|Y| < 1$ was applied.

A peak (enhancement) around $\Delta\eta = 0$ (ΔY = 0) means that B and $\bar{B}$ pairs are produced either in the same direction ($\Delta\phi$ =0) or in opposite directions ($\Delta\phi = \pi$) which is visible and in agreement with respect to the distributions of $\Delta\phi$ correlations.

Correlations of $D\bar{D}$ in pp collisions at 200 GeV are presented in figure.5.8. The difference with respect to $B\bar{B}$ lies in the $\Delta\phi$ distributions where the correlations were obtained for five p_T subranges instead of 4. The range $0 < p_T(D) + p_T(\bar{D}) < 10$ GeV/c was split into 2 ranges : $0 < p_T(D) + p_T(\bar{D}) < 5$ GeV/c and $5 < p_T(D) + p_T(\bar{D}) < 10$ GeV/c for a better visualisation and in order to distinguish between the integrated p_T and the range [0-10] GeV/c. Similar conclusions can be deduced for $D\bar{D}$ correlations concerning the $\Delta\phi$ distributions and the involved processes for this order of energy, as well as their connection with the transverse momentum. The interpretations are not different also for the distributions of $\Delta\eta$ and ΔY. The difference between the two meson species lies in the p_T spectrum. The distribution of B mesons reaches 30 GeV/c, while the one of the D mesons extends up to 20 GeV/c. Either the number of events set in the analysis was not enough, or

the number of generated/produced D mesons at energies of the order of 200 GeV is smaller than B mesons.

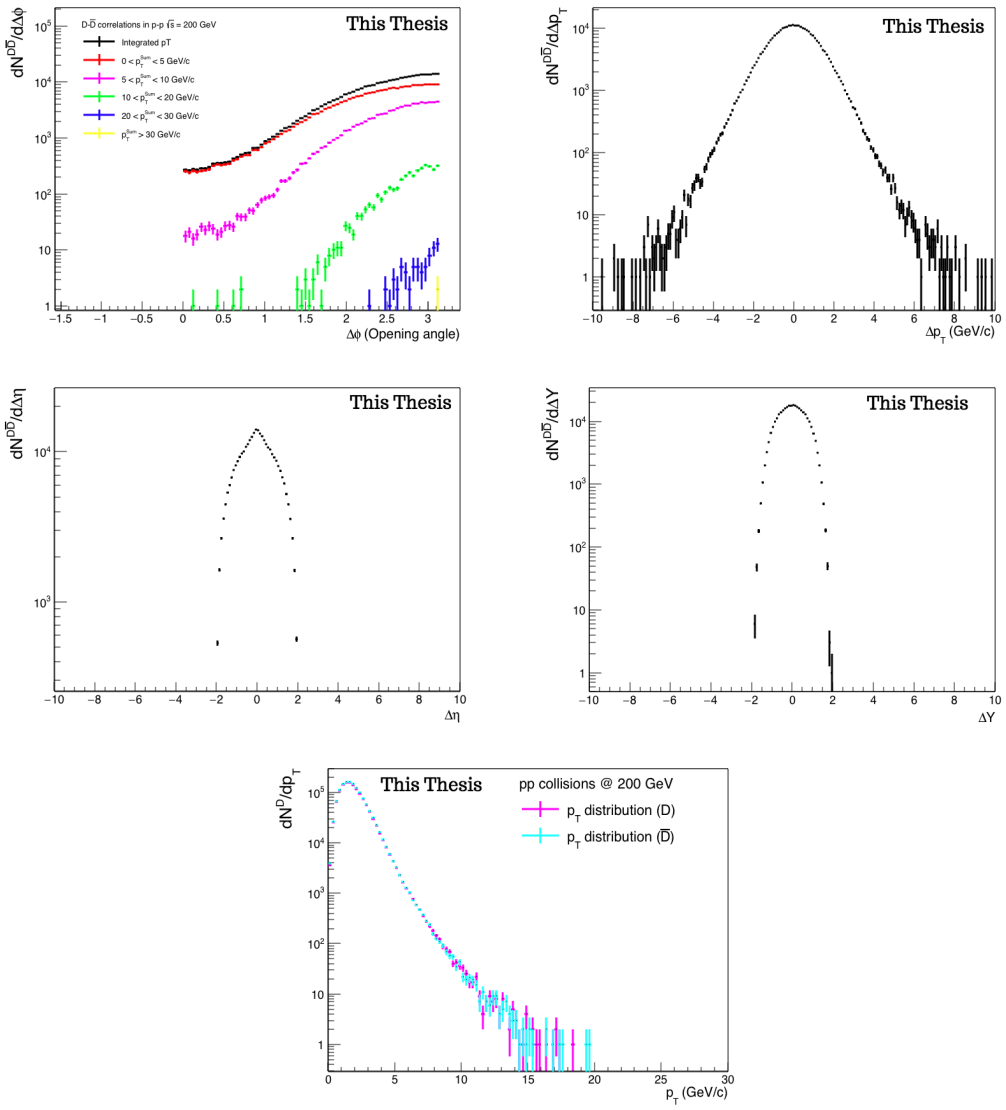

FIGURE 5.8: $D-\bar{D}$ correlation distributions of $\Delta\phi$ (top left), Δp_T (top right), $\Delta\eta$ (middle left), ΔY (middle right) and p_T spectrum of D (magneta) and $\bar{D}$ (cyan) (bottom) in pp collisions at 200 GeV.

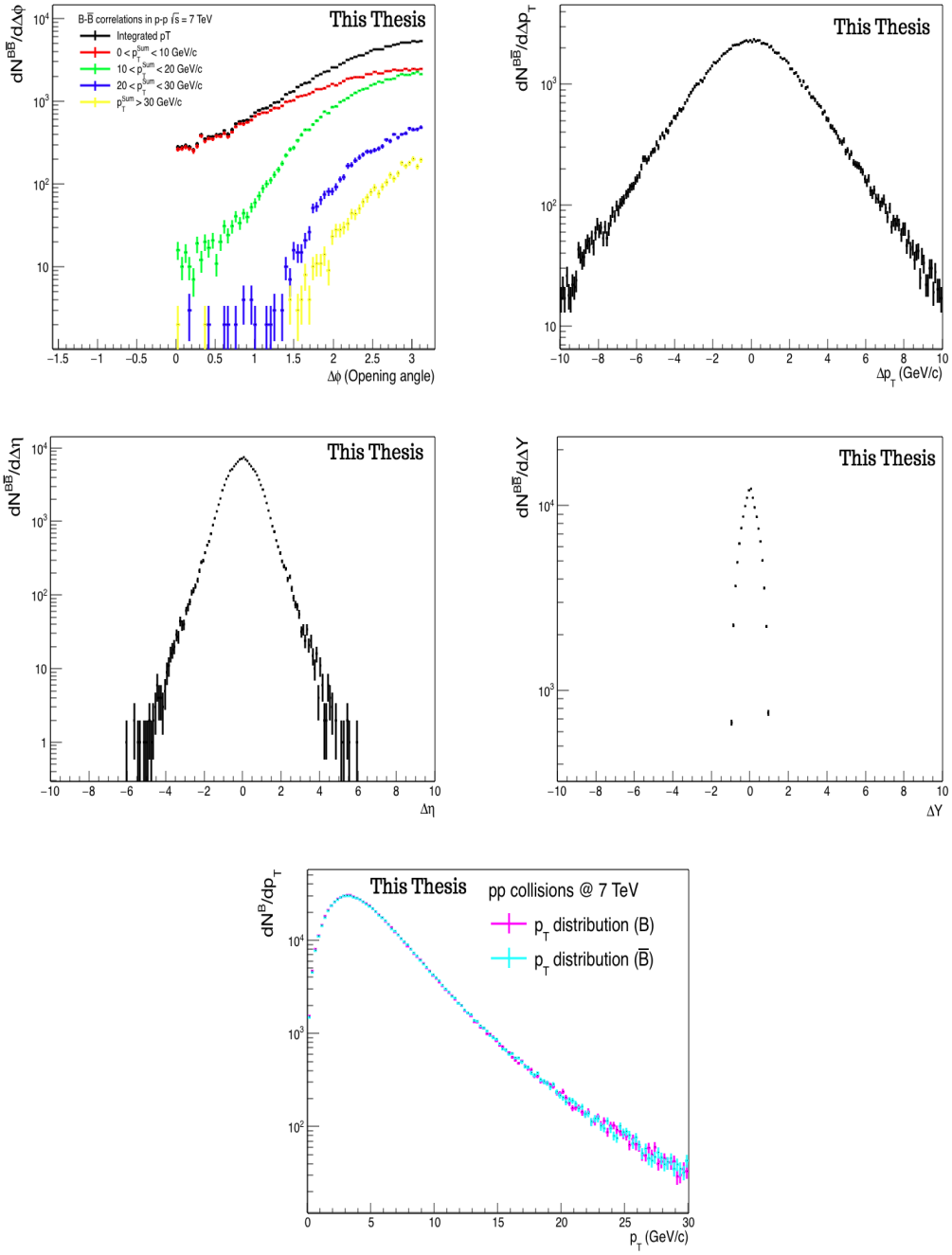

FIGURE 5.9: $B-\bar{B}$ correlation distributions of $\Delta\phi$ (top left), Δp_T (top right), $\Delta\eta$ (middle left), ΔY (middle right) and p_T spectrum of B (magneta) and $\bar{B}$ (cyan) (bottom) in pp collisions at 7 TeV.

$B\bar{B}$ correlations in pp collisions at 7 TeV are presented in figure.5.9 and $D\bar{D}$ correlations in pp collisions at 7 TeV are presented in figure.5.10. The observed features are similar between the two mesons. Consequently, similar conclusions are inferred from distributions in pp collisions at 7 TeV compared to those in pp collisions at 200 GeV.

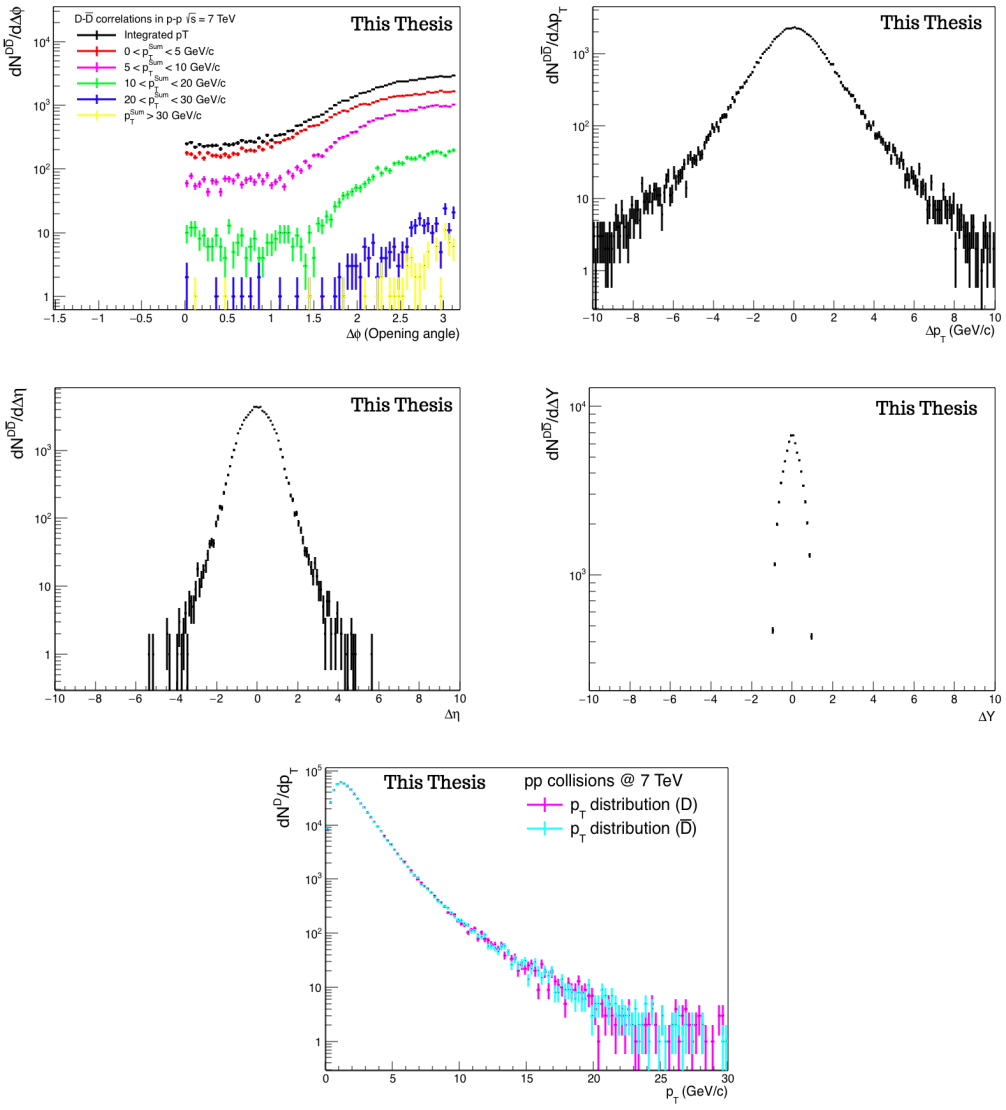

FIGURE 5.10: $D - \bar{D}$ correlation distributions of $\Delta\phi$ (top left), Δp_T (top right), $\Delta\eta$ (middle left), ΔY (middle right) and p_T spectrum of B (magneta) and $\bar{B}$ (cyan) (bottom) in pp collisions at 7 TeV.

Apart from the difference in the p_T subranges between the two mesons, another difference is observed in $\Delta\phi$ distributions. More contribution is observed in $B\bar{B}$ correlations at $\Delta\phi = 0$ with respect to $D\bar{D}$ correlation distribution. This contribution at smaller angles is relatively larger in pp at 7 TeV than at 200 GeV. This can be interpreted based on the energy scale which is of the order of the TeV where more D/B mesons are generated and this is confirmed according to the p_T distributions. Consequently, a larger number of heavy flavour pairs is generated per event with similar directions ($\Delta\phi = 0$). Basically, this is related to the production mechanism called gluon splitting that is expected to be dominant at LHC energies where heavy flavours are created with (almost) identical momentum in the same direction. This is not exactly the case in these analyses because PYTHIA is used as a standalone event generator where the LO QCD calculations are the adopted ones. The production of heavy flavour at smaller angles at this energy scale is probably coming from

the gluon splitting that can take place in the ISR and FSR.

5.4.3 $c - \bar{c}$ vs $D - \bar{D}$ correlations and $b - \bar{b}$ vs $B - \bar{B}$ correlations

The main goal in this part is to do the comparison $c - \bar{c}$ vs $D - \bar{D}$ correlations and $b - \bar{b}$ vs $B - \bar{B}$. Figure.5.11 shows $b\bar{b}$ vs $B\bar{B}$ correlations in pp collisions at 200 GeV. Correlations of $c\bar{c}$ vs $D\bar{D}$ in pp collisions at 200 GeV are presented in figure.5.12. $b\bar{b}$ vs $B\bar{B}$ correlations in pp collisions at 7 TeV are shown in figure.5.13 and $c\bar{c}$ vs $D\bar{D}$ correlations in pp collisions at 7 TeV are presented in figure.5.14.

In each figure, the following distributions are presented : $\Delta\phi$ (top left), Δp_T (top right), $\Delta\eta$ (middle left), ΔY (middle right) and p_T distributions (bottom).

For the first four distributions, a ratio was computed between the correlations of the mesons and the quarks. The correspondent distributions for mesons ($D\bar{D}$ and $B\bar{B}$) are presented in black and those of quarks ($c\bar{c}$ and $b\bar{b}$) are presented in purple.

For both energies (200 GeV and 7 TeV), the distributions of $b\bar{b}$ ($c\bar{c}$) correlations are larger in magnitude than those of $B\bar{B}$ ($D\bar{D}$). This is reasonable since not all b (c) quarks will hadronise into B (D) mesons, and there will be a fraction of b (c) quarks that will hadronise into baryons. The same information can be inferred from the ratio plots in the lowest panels in each figure where the ratio is always less than 1. In addition, the exhibited behaviour of heavy quarks is reproduced by heavy mesons which is illustrated by the qualitative resemblance between the distributions of quarks and mesons.

Except for $b\bar{b}$ vs $B\bar{B}$ correlations in pp collisions at 200 GeV, the other 3 cases exhibit a different behaviour at smaller angles concerning the $\Delta\phi$ distributions. This is probably due to the number of generated quarks (c/b) or mesons (D/B).

For one side, smaller angles is a sensitive region, especially that PYTHIA is used as a standalone event generator. On the other side, the energy scale of the order of the TeV is the most impacted where it is expected to have a difference compared to energies of the order of the GeV. Still, we stick with PYTHIA as a standalone event generator so that we won't go beyond the plan of the thesis.

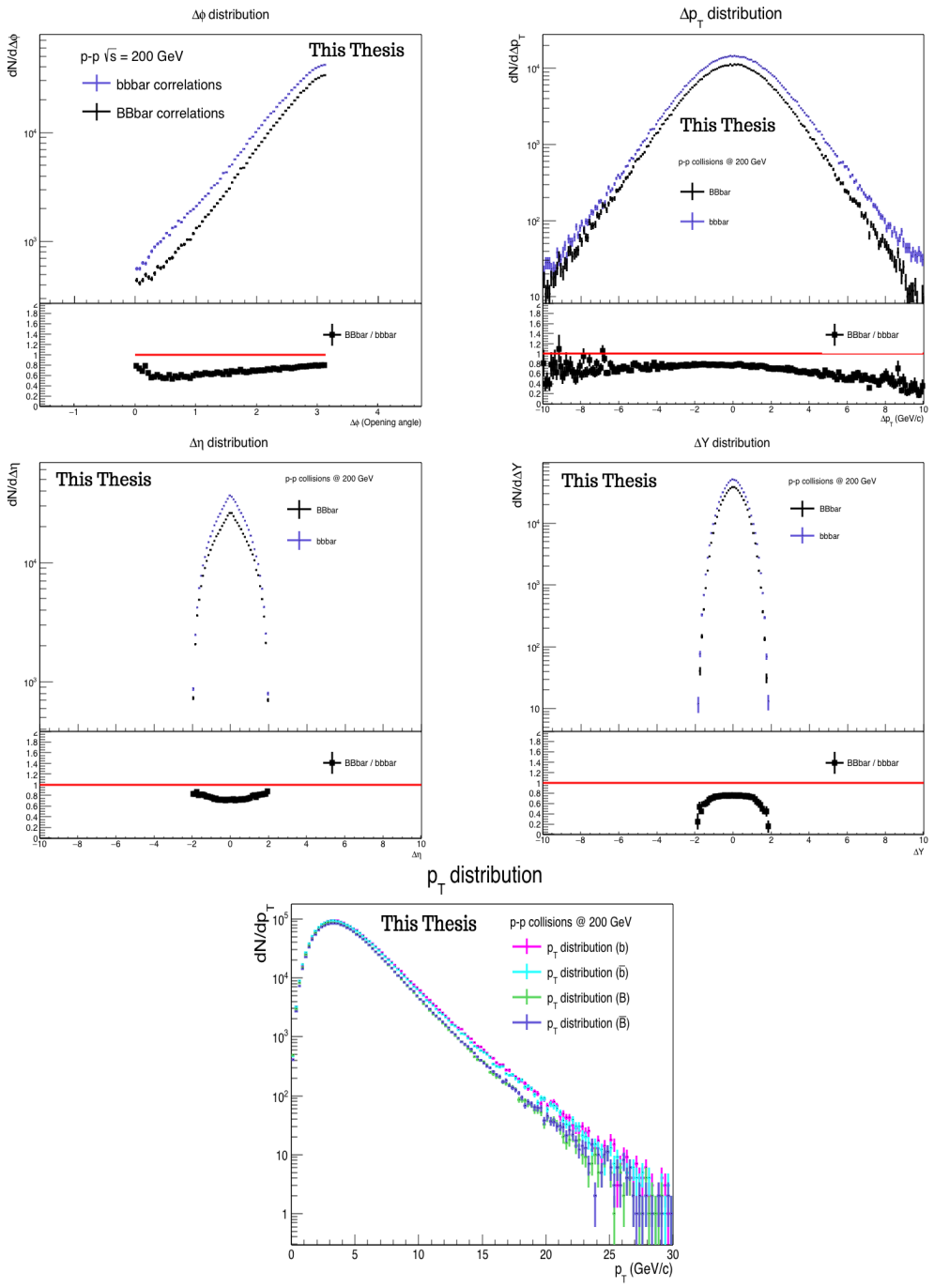

FIGURE 5.11: $B - \bar{B}$ (black) vs $b - \bar{b}$ (purple) correlation distributions for $\Delta\phi$ (top left), Δp_T (top right), $\Delta\eta$ (middle left), ΔY (middle right) and p_T spectrum (bottom) of b quarks (magenta), $\bar{b}$ quarks (cyan), B mesons (light green), $\bar{B}$ mesons (purple) in pp collisions at 200 GeV.

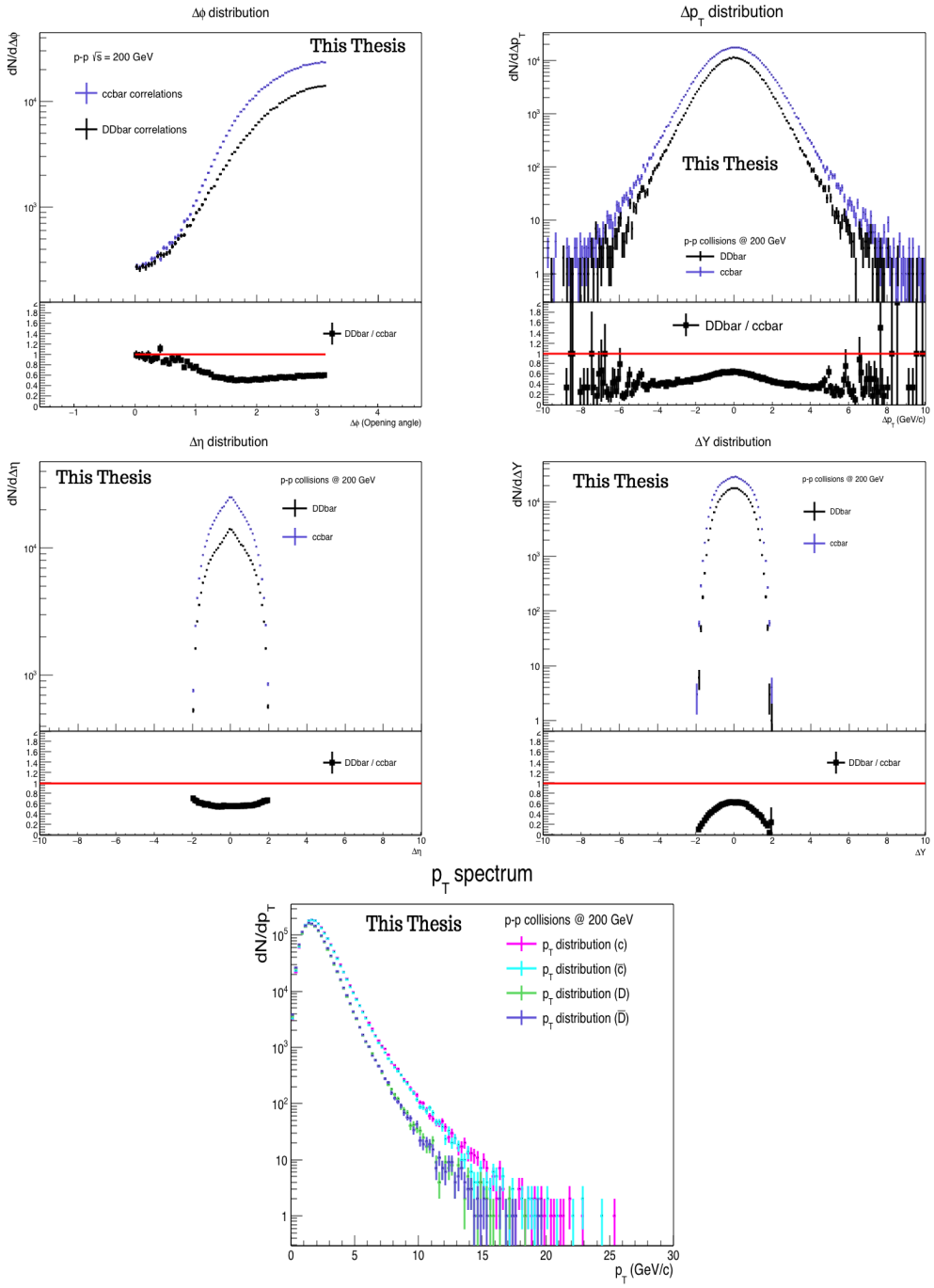

FIGURE 5.12: $D - \bar{D}$ (black) vs $c - \bar{c}$ (purple) correlation distributions for $\Delta\phi$ (top left), Δp_T (top right), $\Delta\eta$ (middle left), ΔY (middle right) and p_T spectrum (bottom) of c quarks (magenta), $\bar{c}$ quarks (cyan), D mesons (light green), $\bar{D}$ mesons (purple) in pp collisions at 200 GeV.

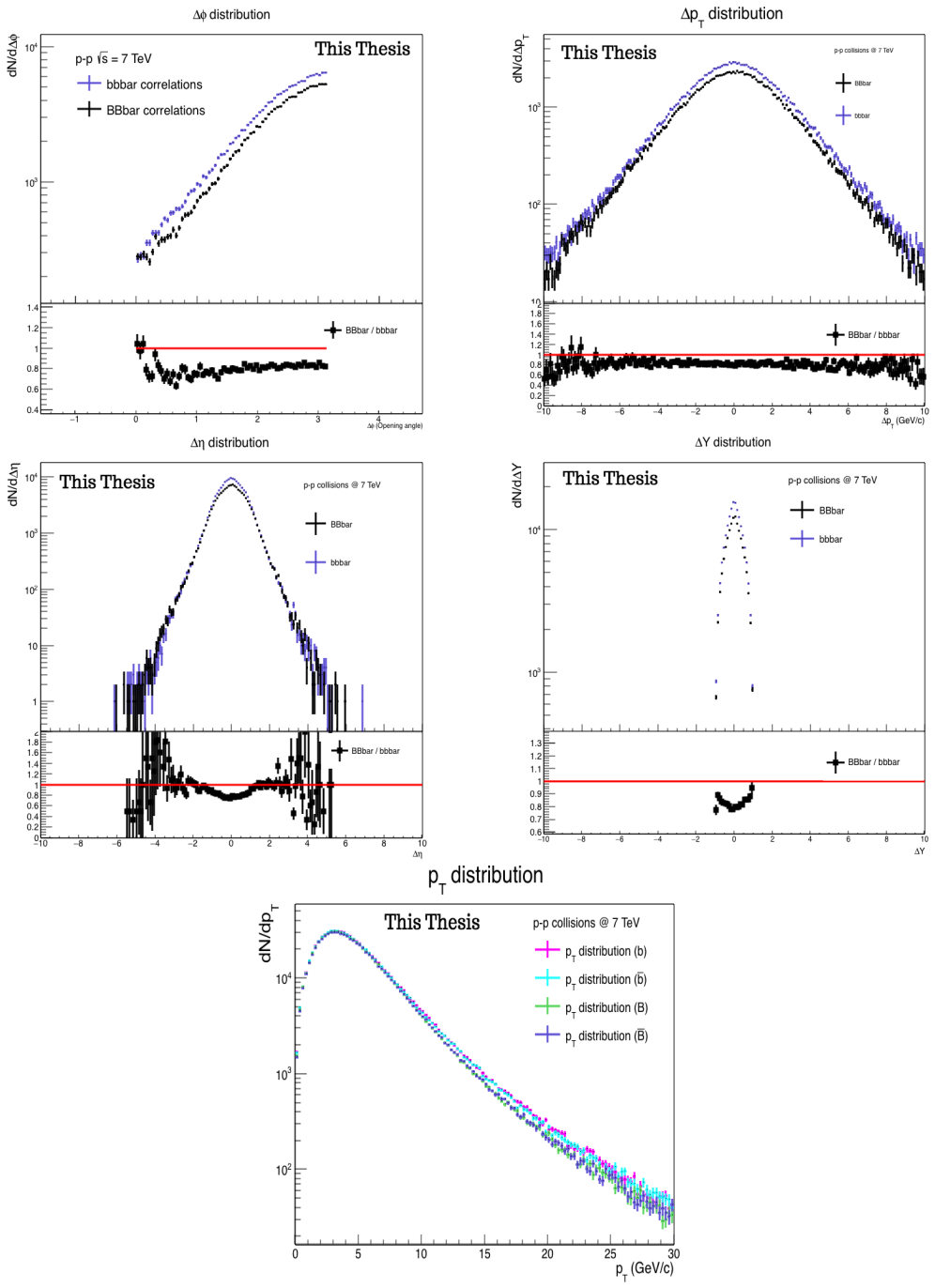

FIGURE 5.13: $B - \bar{B}$ (black) vs $b - \bar{b}$ (purple) correlation distributions for $\Delta\phi$ (top left), Δp_T (top right), $\Delta\eta$ (middle left), ΔY (middle right) and p_T spectrum (bottom) of b quarks (magenta), $\bar{b}$ quarks (cyan), B mesons (light green), $\bar{B}$ mesons (purple) in pp collisions at 7 TeV.

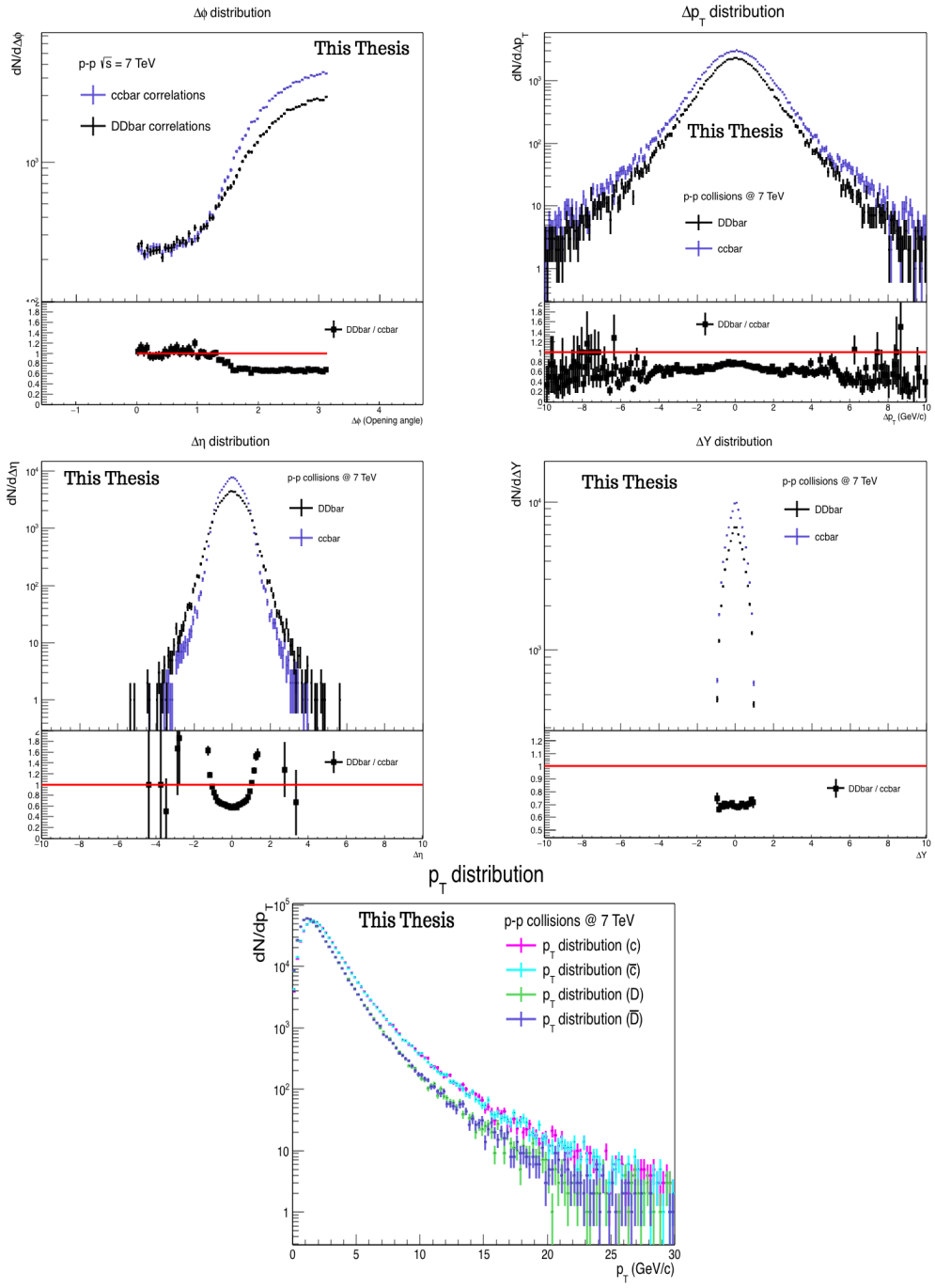

FIGURE 5.14: $D - \bar{D}$ (black) vs $c - \bar{c}$ (purple) correlation distributions for $\Delta\phi$ (top left), Δp_T (top right), $\Delta\eta$ (middle left), ΔY (middle right) and p_T spectrum (bottom) of c quarks (magenta), $\bar{c}$ quarks (cyan), D mesons (light green), $\bar{D}$ mesons (purple) in pp collisions at 7 TeV.

5.4.4 $D - \bar{D}/B - \bar{B}$ correlations with/without Initial State Radiation and Final State Radiation (ISR/FSR)

In this part, correlation distributions of mesons are investigated and compared to each other for the two cases:

- Parton shower (ISR/FSR) = on
- Parton shower (ISR/FSR) = off

Except for p_T spectrums, all correlation distributions with ISR/FSR switched "On", are presented in black curves, and the distributions with ISR/FSR switched "Off" are presented in green curves. The plots are organised in the same way as in the previous sections. Per energy and meson species, the $\Delta\phi$, Δp_T, $\Delta\eta$, ΔY, p_T distributions are presented in each figure in the top left, top right, middle left, middle right and bottom panels, respectively.

$B\bar{B}$ correlations in pp collisions at 200 GeV are presented in figure.5.15. The p_T spectrums (bottom panel) show similar distributions between the two cases with ISR/FSR switched "On" and "Off". Similarly, $\Delta\eta$ and ΔY distributions do not exhibit any different behaviour between the 2 cases, they show similar distributions, instead. This information can be deducted directly from the computed ratios in the correspondent lower panel.

This is not the case for the rest of the distributions. One can see clearly that the Δp_T distribution with ISR/FSR switched "On" is broader than the one with ISR/FSR switched "Off". This feature stems most likely from the small number of correlated pairs because there are less generated mesons due to the absence of parton showers. Otherwise, it is clear that the absence of ISR/FSR leads to the production of more pairs with similar p_T which is visible in the peak around $\Delta p_T = 0$.

The $\Delta\phi$ correlation distributions are also different between the 2 cases. When ISR/FSR are switched "Off", correlations are more important at larger angles ($\Delta\phi = \pi$) and smaller in general for the rest of $\Delta\phi$ range compared to the case of ISR/FSR switched "On" where the opposite behaviour is observed. These aspects are obviously due to the presence/absence of radiations in the initial and final states. As a result, ISR/FSR affect the number of produced pairs becayse they contribute partially via the gluon splitting which can be the cause of the observed difference at smaller angles in $\Delta\phi$ distributions.

Similar conclusions can be inferred from $D - \bar{D}$ correlations in pp collisions at 200 GeV presented in figure.5.16 for the p_T spectrums, $\Delta\eta$ and ΔY distributions. As for $\Delta\phi$ and Δp_T distributions, less discrepancy is observed between the cases where ISR/FSR are On and Off.

Figure.5.17 presents the correlation distributions of $B - \bar{B}$ in pp collisions at 7 TeV. Similar features are observed compared to the distributions at 200 GeV either the similarities found for $\Delta\eta$, ΔY, p_T distributions or the differences found for $\Delta\phi$ and Δp_T distributions. Figure.5.18 shows the $D\bar{D}$ correlations in pp collisions at 7 TeV. The distributions exhibit similar behaviour as those observed in $D\bar{D}$ correlations at 200 GeV. The discrepancy for $\Delta\phi$ correlations between the 2 cases (ISR/FSR On/Off) is pretty clear compared to the case of 200 GeV. Concerning the Δp_T distributions, the difference between the 2 cases appears to be more quantitative than a qualitative one for $D\bar{D}$. While for $B\bar{B}$, the difference between the 2 cases is rather a qualitative one.

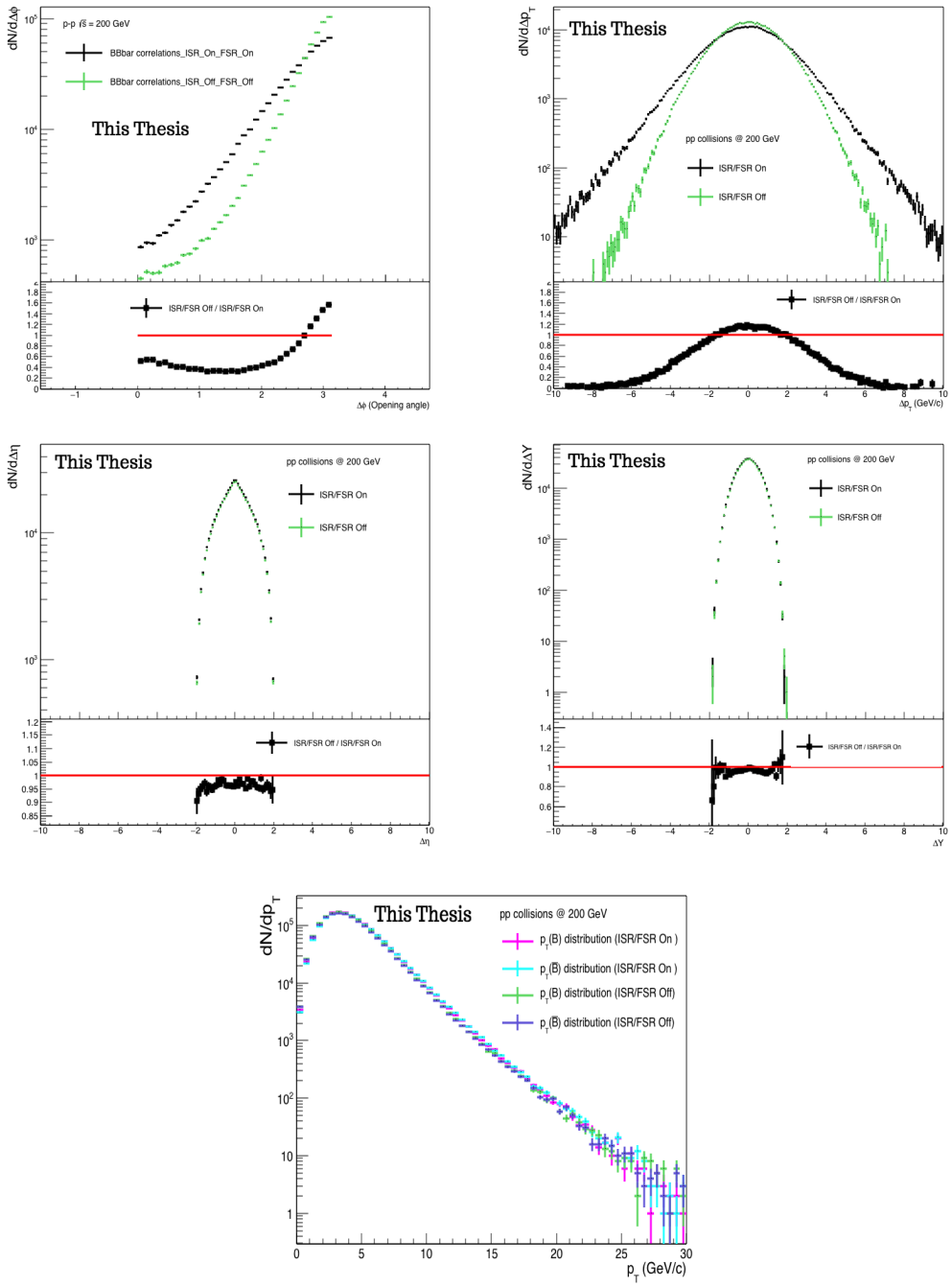

FIGURE 5.15: $B - \bar{B}$ correlation distributions of $\Delta\phi$ (top left), Δp_T (top right), $\Delta\eta$ (middle left), ΔY (middle right) in pp collisions at 200 GeV for ISR/FSR On (black) and ISR/FSR Off (green) and p_T distributions (bottom) for ISR/FSR On, of B mesons (magenta), $\bar{B}$ mesons (cyan) and for ISR/FSR Off, of B mesons (green), $\bar{B}$ mesons (purple).

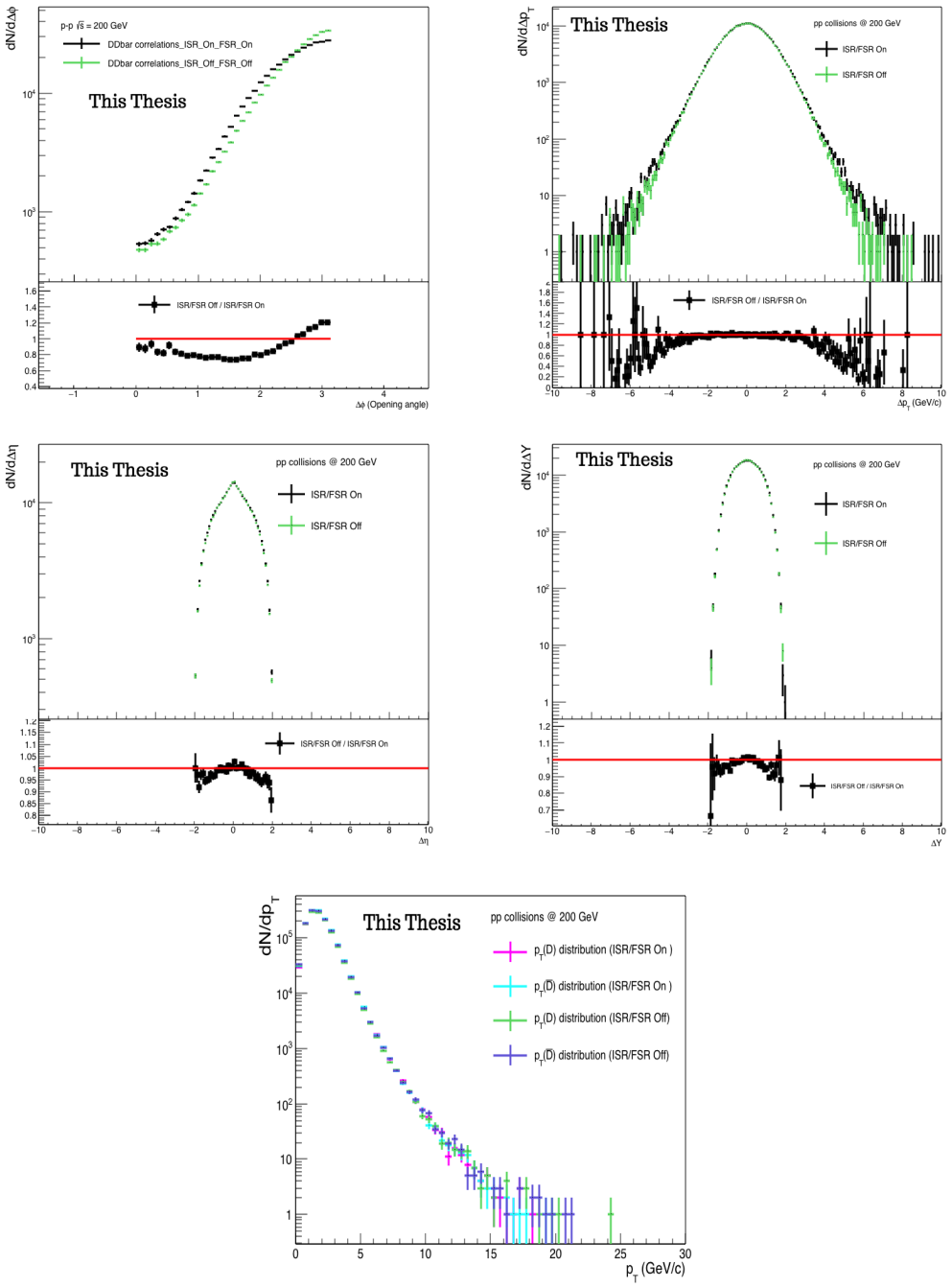

FIGURE 5.16: $D - \bar{D}$ correlation distributions of $\Delta\phi$ (top left), Δp_T (top right), $\Delta\eta$ (middle left), ΔY (middle right) in pp collisions at 200 GeV for ISR/FSR On (black) and ISR/FSR Off (green) and p_T distributions (bottom) for ISR/FSR On, of D mesons (magenta), $\bar{D}$ mesons (cyan) and for ISR/FSR Off, of D mesons (green), $\bar{D}$ mesons (purple).

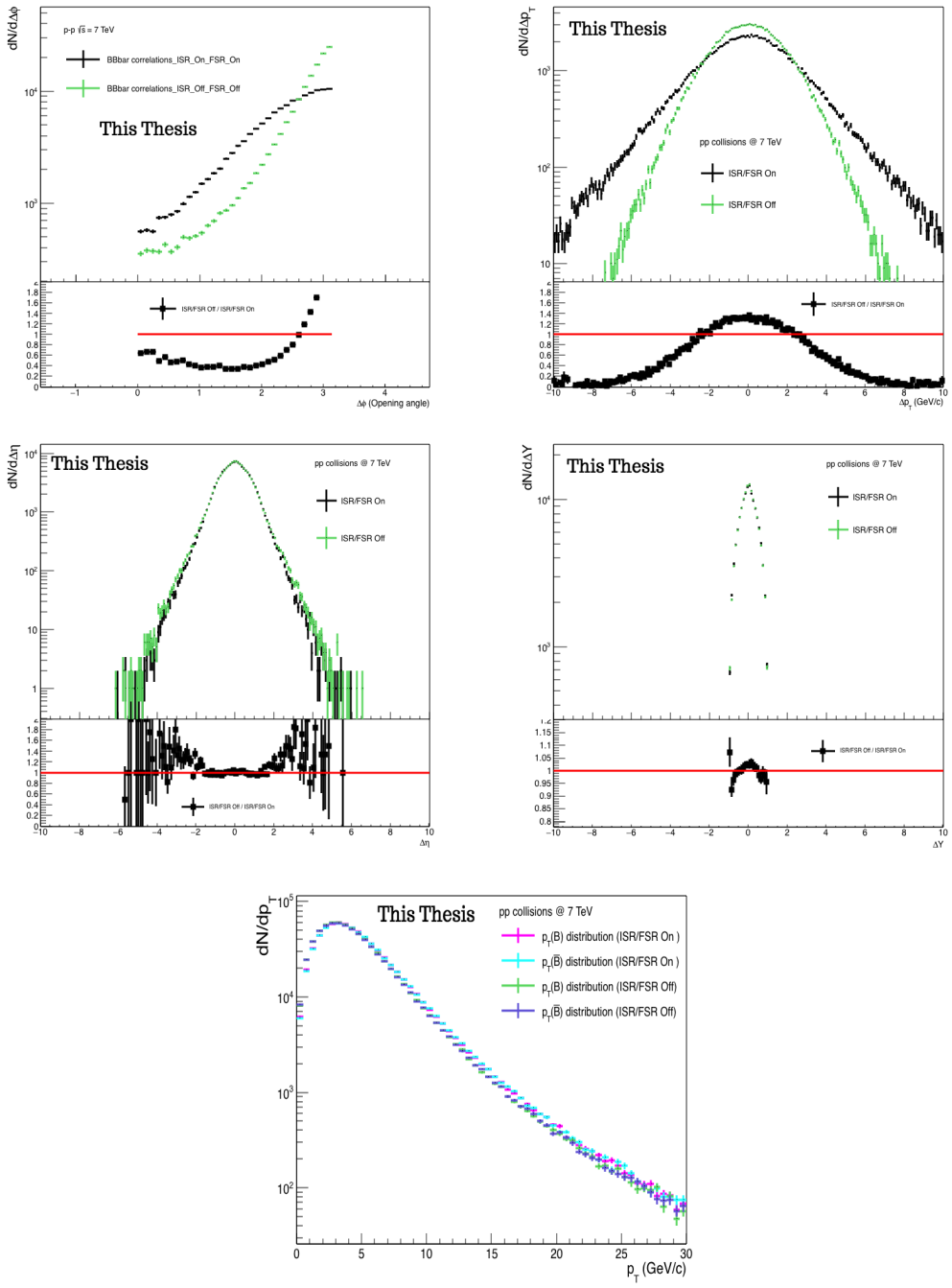

FIGURE 5.17: $B - \bar{B}$ correlation distributions of $\Delta\phi$ (top left), Δp_T (top right), $\Delta\eta$ (middle left), ΔY (middle right) in pp collisions at 7 TeV for ISR/FSR On (black) and ISR/FSR Off (green) and p_T distributions (bottom) for ISR/FSR On, of B mesons (magenta), $\bar{B}$ mesons (cyan) and for ISR/FSR Off, of B mesons (green), $\bar{B}$ mesons (purple).

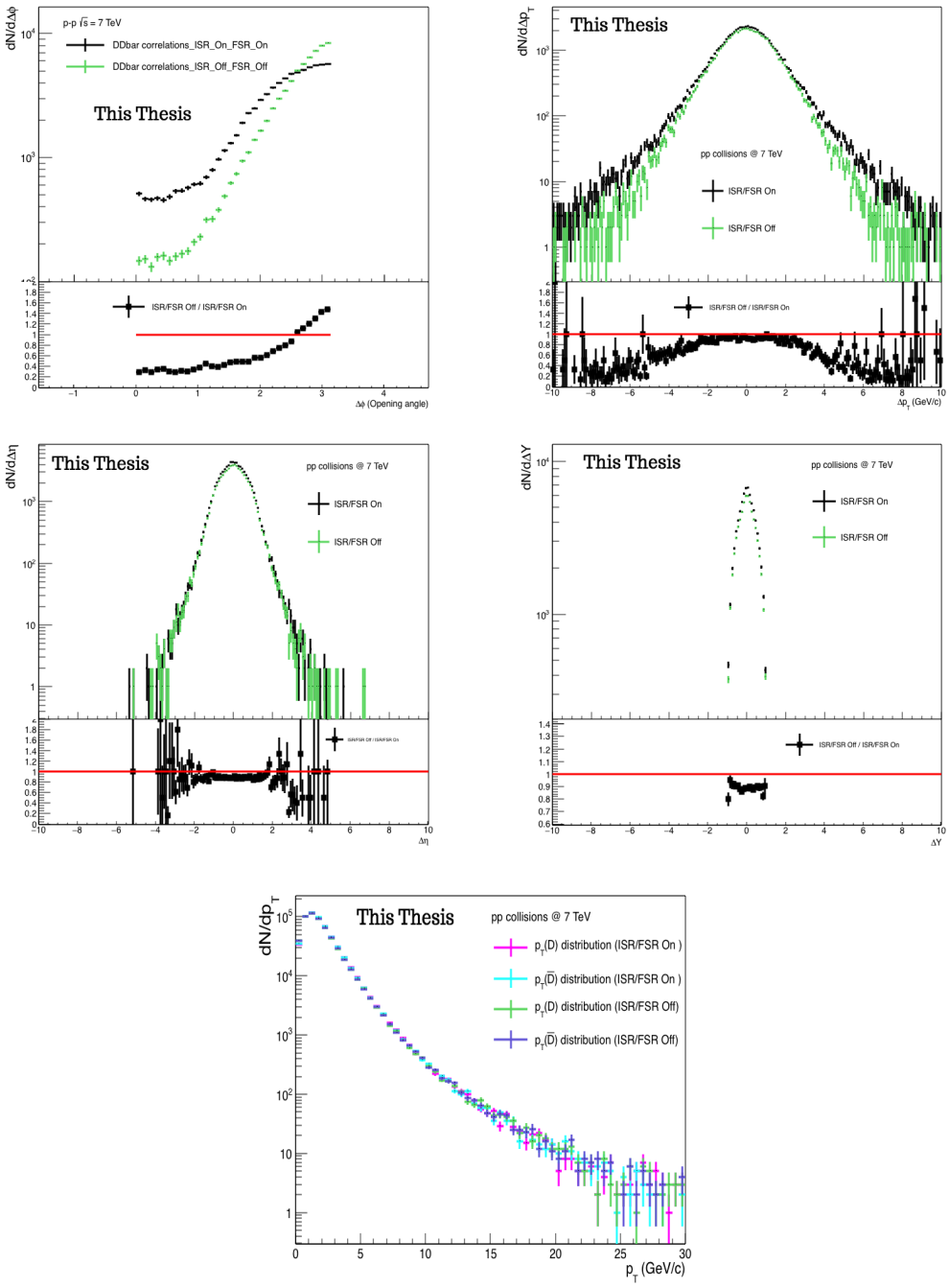

FIGURE 5.18: $D - \bar{D}$ correlation distributions of $\Delta\phi$ (top left), Δp_T (top right), $\Delta\eta$ (middle left), ΔY (middle right) in pp collisions at 7 TeV for ISR/FSR On (black) and ISR/FSR Off (green) and p_T distributions (bottom) for ISR/FSR On, of D mesons (magenta), $\bar{D}$ mesons (cyan) and for ISR/FSR Off, of D mesons (green), $\bar{D}$ mesons (purple).

5.4.5 $D - \bar{D}/B - \bar{B}$ correlations with/without Multiple Parton Interaction (MPI)

In this part, correlation distributions obtained with the default configuration are presented and compared to those distributions for which the Multiple Parton Interactions (MPI) was

switched Off. $B - \bar{B}$ correlations in pp collisions at 200 GeV are presented in figure.5.19. $D - \bar{D}$ correlations in pp collisions at 200 GeV are presented in figure.5.20. $B\bar{B}$ correlations in pp collisions at 7 TeV are displayed in figure.5.21 and those of $D\bar{D}$ correlations at 7 TeV are displayed in figure.5.22.

The same order of distributions is kept in each figure : $\Delta\phi$ (top left), Δp_T (top right), $\Delta\eta$ (middle left), ΔY (middle right), p_T (bottom) with their ratios in the bottom panels (except for the p_T spectrum). The black curves refer to the distributions obtained with MPI switched "On" and the green ones refer to those obtained with MPI switched "Off".

Correlation distributions have similar behaviour for the 2 cases of MPI switched "On" and "Off" with a quantitative difference for the Δp_T, $\Delta\eta$, ΔY and p_T distributions for both energies (200 GeV and 7 TeV) and both mesons (B and D mesons). Quantitatively, the distributions obtained with MPI "Off" are lower than those obtained with MPI "On". This is probably due to the mechanism of MPI which leads to more interactions between partons .i.e the production of more particles. Consequently, a large number of heavy flavour pairs is created which means a larger number of correlated pairs ($B - \bar{B}$, $D - \bar{D}$). The ratios deliver the same message about this quantitative difference.

Concerning the $\Delta\phi$ distributions, a quantitative difference between the two cases (MPI On/Off) is observed. The difference in $\Delta\phi$ distribution lies at larger angles ($\Delta\phi = \pi$) where correlation distributions are closer in magnitude in both cases (MPI On/Off), and the similarity is more prominent in the case of $B\bar{B}$ correlations for both energies (200 GeV and 7 TeV). As for smaller angles, the difference in magnitude is larger, especially for the case of $D - \bar{D}$ correlations for both energies (200 GeV and 7 TeV).

These observed features dictate that MPI affects the production mechanism of heavy flavour. Without MPI, there are less created heavy-flavours via gluon splitting .i.e less created pairs with smaller angles. D mesons (Charm quarks) are more impacted whereas the effect is minor for B mesons (bottom quarks).

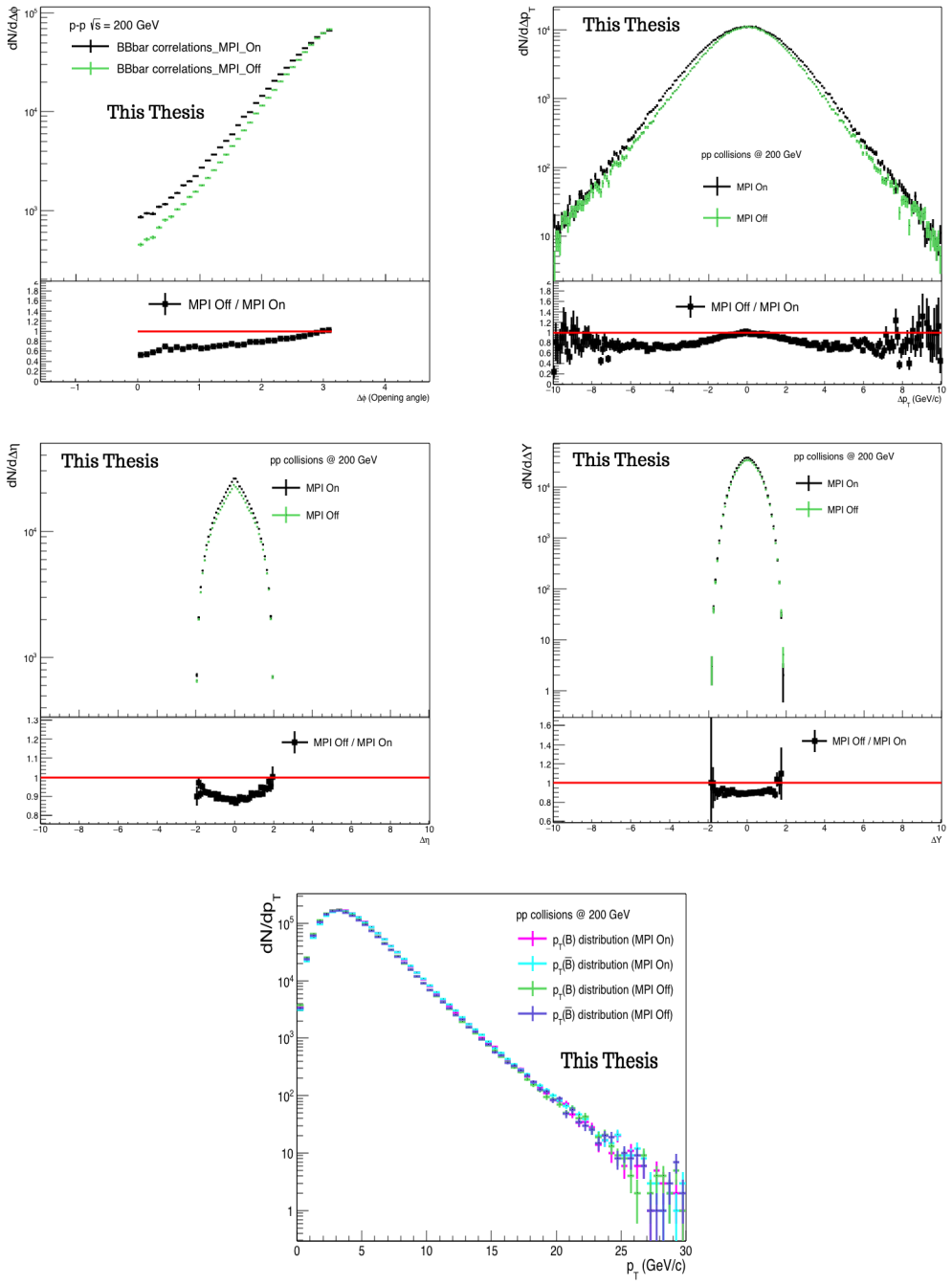

FIGURE 5.19: $B - \bar{B}$ correlation distributions of $\Delta\phi$ (top left), Δp_T (top right), $\Delta\eta$ (middle left), ΔY (middle right) in pp collisions at 200 GeV for MPI "On" (black) and MPI "Off" (green). p_T distributions (bottom) for MPI "On" of B mesons (magenta) and $\bar{B}$ mesons (cyan) and for MPI "Off" of B mesons (green) and $\bar{B}$ mesons (purple).

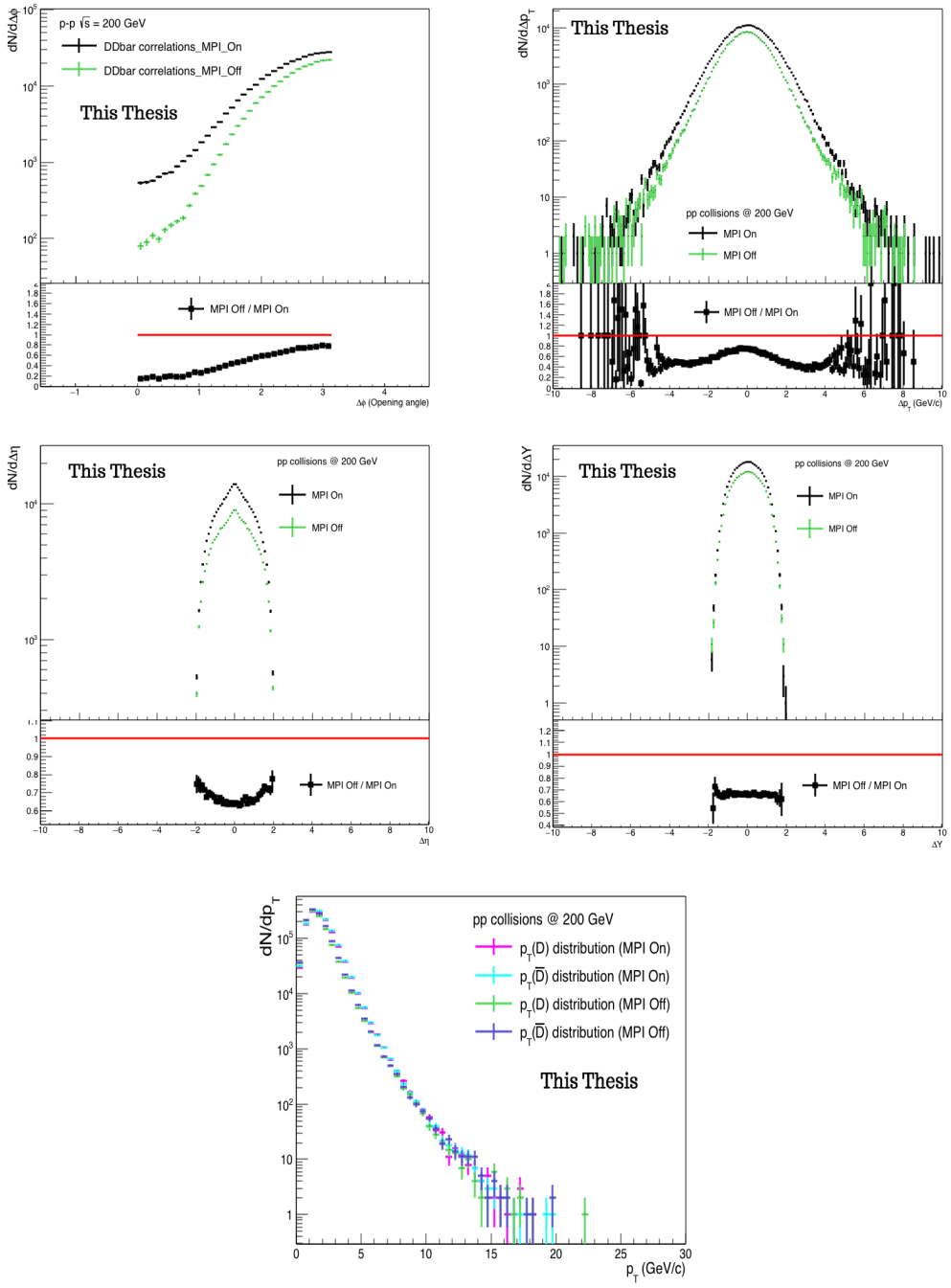

FIGURE 5.20: $D - \bar{D}$ correlation distributions of $\Delta\phi$ (top left), Δp_T (top right), $\Delta\eta$ (middle left), ΔY (middle right) in pp collisions at 200 GeV for MPI "On" (black) and MPI "Off" (green). p_T distributions (bottom) for MPI "On" of D mesons (magenta) and $\bar{D}$ mesons (cyan) and for MPI "Off" of D mesons (green) and $\bar{D}$ mesons (purple).

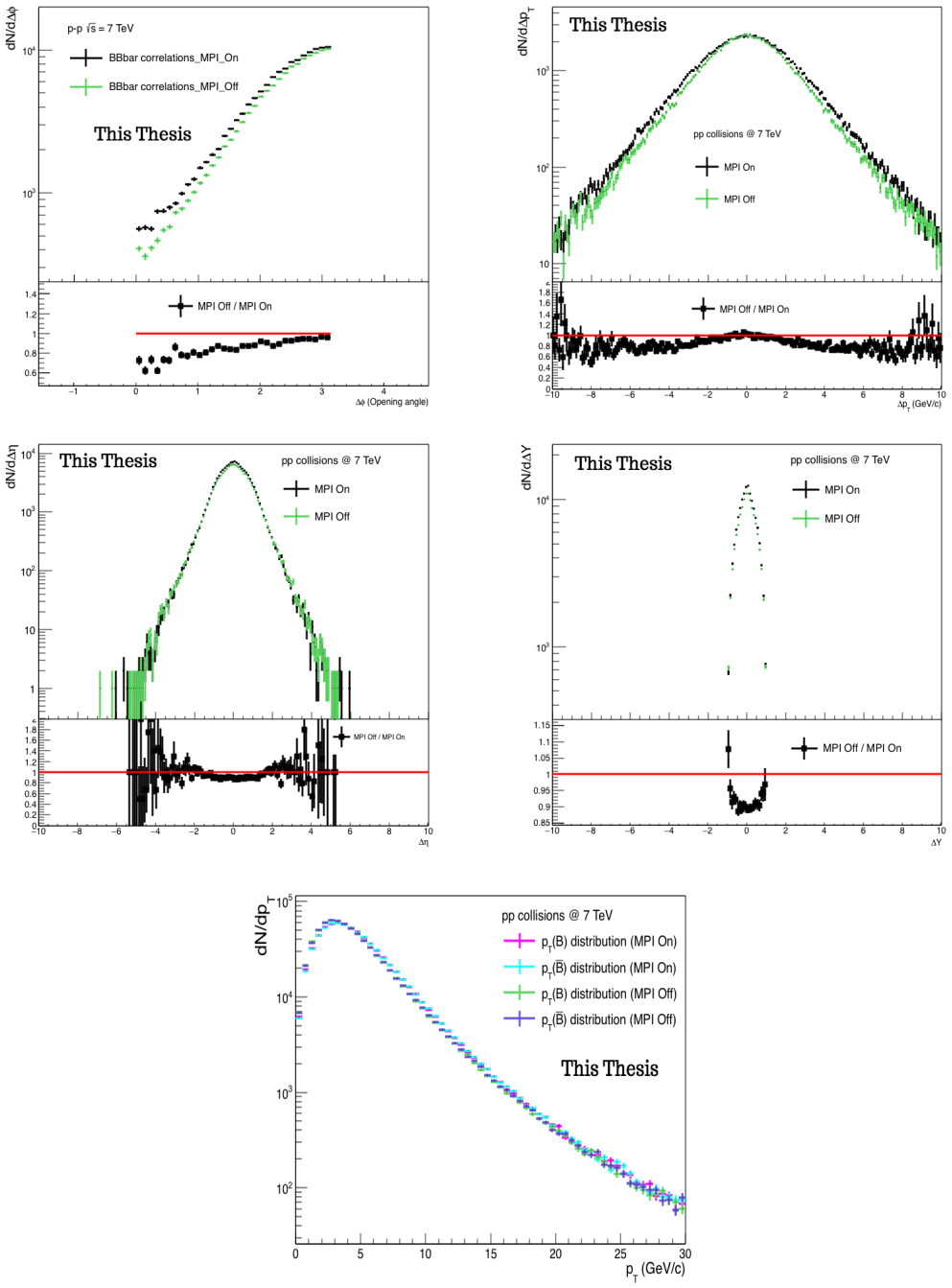

FIGURE 5.21: $B - \bar{B}$ correlation distributions of $\Delta\phi$ (top left), Δp_T (top right), $\Delta\eta$ (middle left), ΔY (middle right) in pp collisions at 7 TeV for MPI "On" (black) and MPI "Off" (green). p_T distributions (bottom) for MPI "On" of B mesons (magenta) and $\bar{B}$ mesons (cyan) and for MPI "Off" of B mesons (green) and $\bar{B}$ mesons (purple).

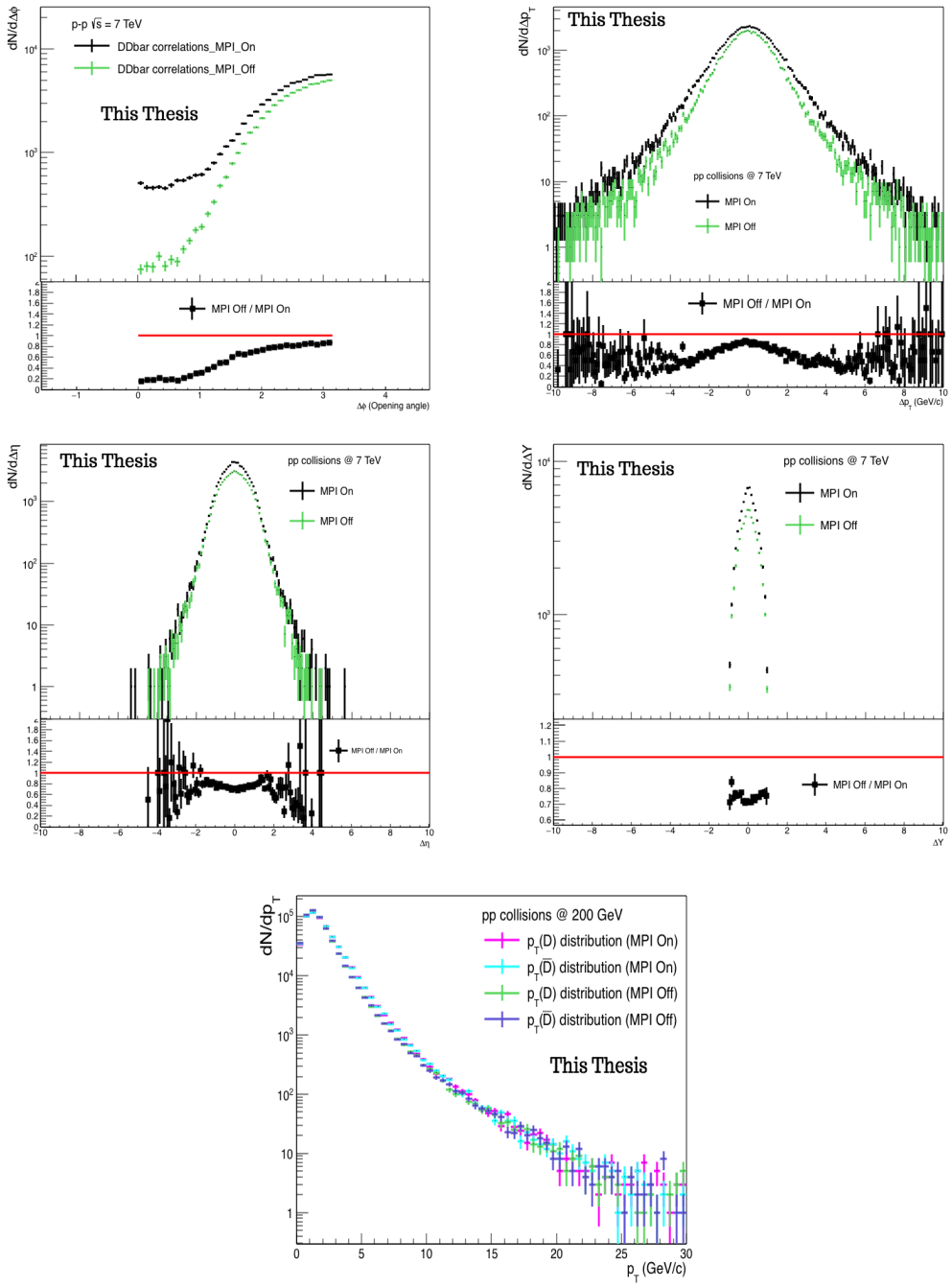

FIGURE 5.22: $D - \bar{D}$ correlation distributions of $\Delta\phi$ (top left), Δp_T (top right), $\Delta\eta$ (middle left), ΔY (middle right) in pp collisions at 7 TeV for MPI "On" (black) and MPI "Off" (green). p_T distributions (bottom) for MPI "On" of D mesons (magenta) and $\bar{D}$ mesons (cyan) and for MPI "Off" of D mesons (green) and $\bar{D}$ mesons (purple).

5.4.6 $D - \bar{D}/B - \bar{B}$ correlations with/without Colour Reconnection (CR)

In this part, correlation distributions are obtained for the case of Colour Reconnection (CR) switched "Off" and compared to those obtained with CR switched "On". The correspondent $B - \bar{B}$ correlation distributions in pp collisions at 200 GeV are presented in figure.5.23.

$D - \bar{D}$ correlations in pp collisions at 200 GeV are presented in figure.5.24. $B - \bar{B}$ correlations in pp collisions at 7 TeV are presented in figure.5.25 and those of $D - \bar{D}$ correlations in pp collisions at 7 TeV are presented in figure.5.26.

For each figure, the distributions $\Delta\phi$, Δp_T, $\Delta\eta$, ΔY, p$_T$ are presented. Black curves represent correlations in the standard case where CR is switched "On". The green curves represent correlations with CR switched "Off".

One can see clearly that, whatever the energy or the meson species, the distributions obtained for the 2 cases (CR is switched "On" or "Off") are similar in behaviour and magnitude. This is clear through the computed ratios shown in the bottom panels for each distribution.

Apart from the similarities, there is a discrepancy in $\Delta\phi$ distributions at smaller angles between correlations with CR switched "On" and "Off" for both energies (200 GeV and 7 TeV). This difference is more visible for $D - \bar{D}$ correlations in pp collisions at 200 GeV and less visible at 7 TeV.

This observation is either associated with the energy scale for D mesons, or it might be the number of events that were not enough to give some firm conclusions. Otherwise, based on what is available, the discrepancy is due to the absence of CR that lead to less gluon splitting at an energy of the order of GeV, but it does not influence that much the production mechanisms of heavy flavour at energies of the order of TeV.

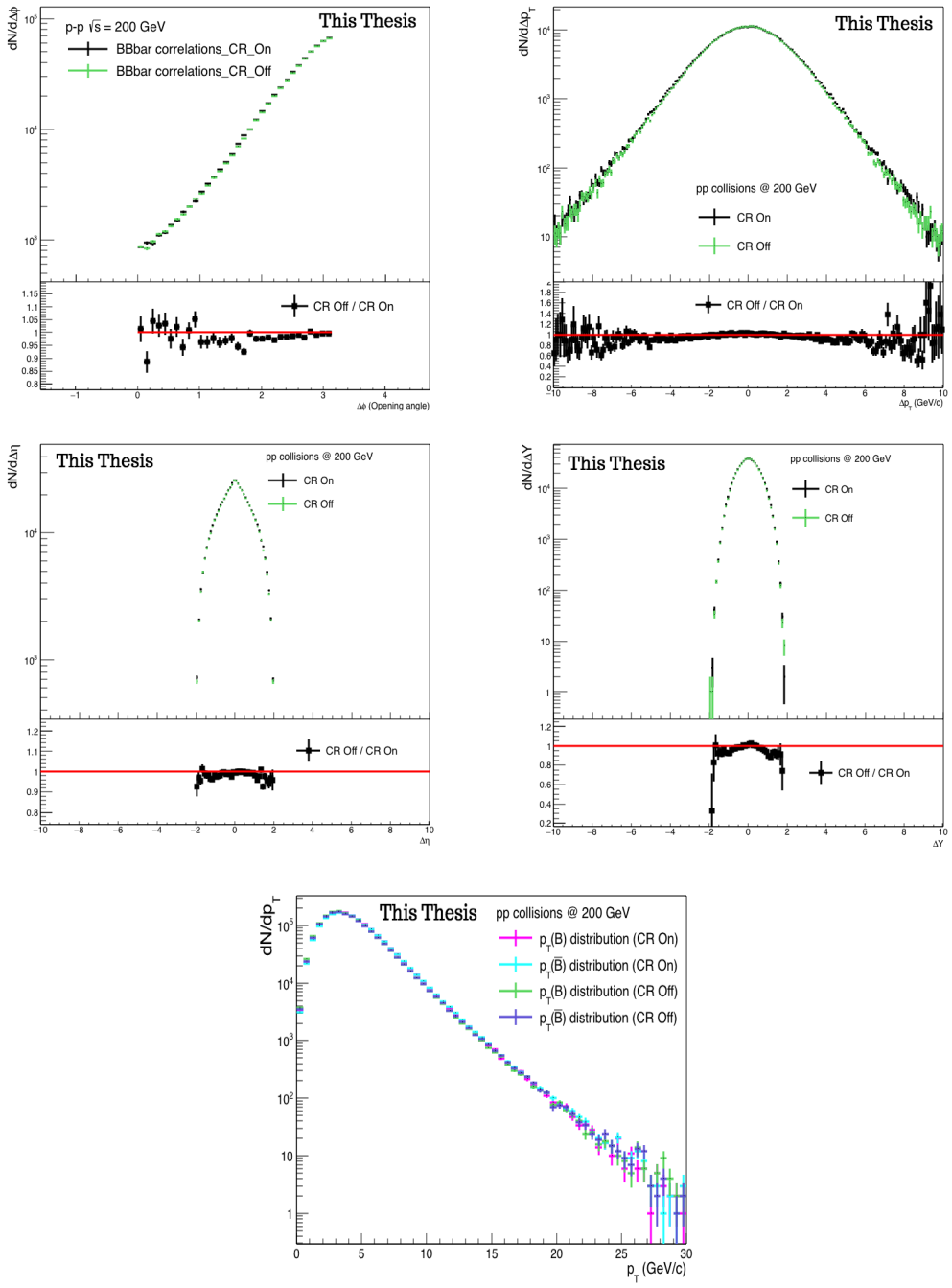

FIGURE 5.23: $B - \bar{B}$ correlation distributions of $\Delta\phi$ (top left), Δp_T (top right), $\Delta\eta$ (middle left), ΔY (middle right) in pp collisions at 200 GeV with CR (black) and without CR (green). p_T distributions (bottom) with CR for B mesons (magenta) and $\bar{B}$ mesons and without CR for B mesons (green) and $\bar{B}$ (purple).

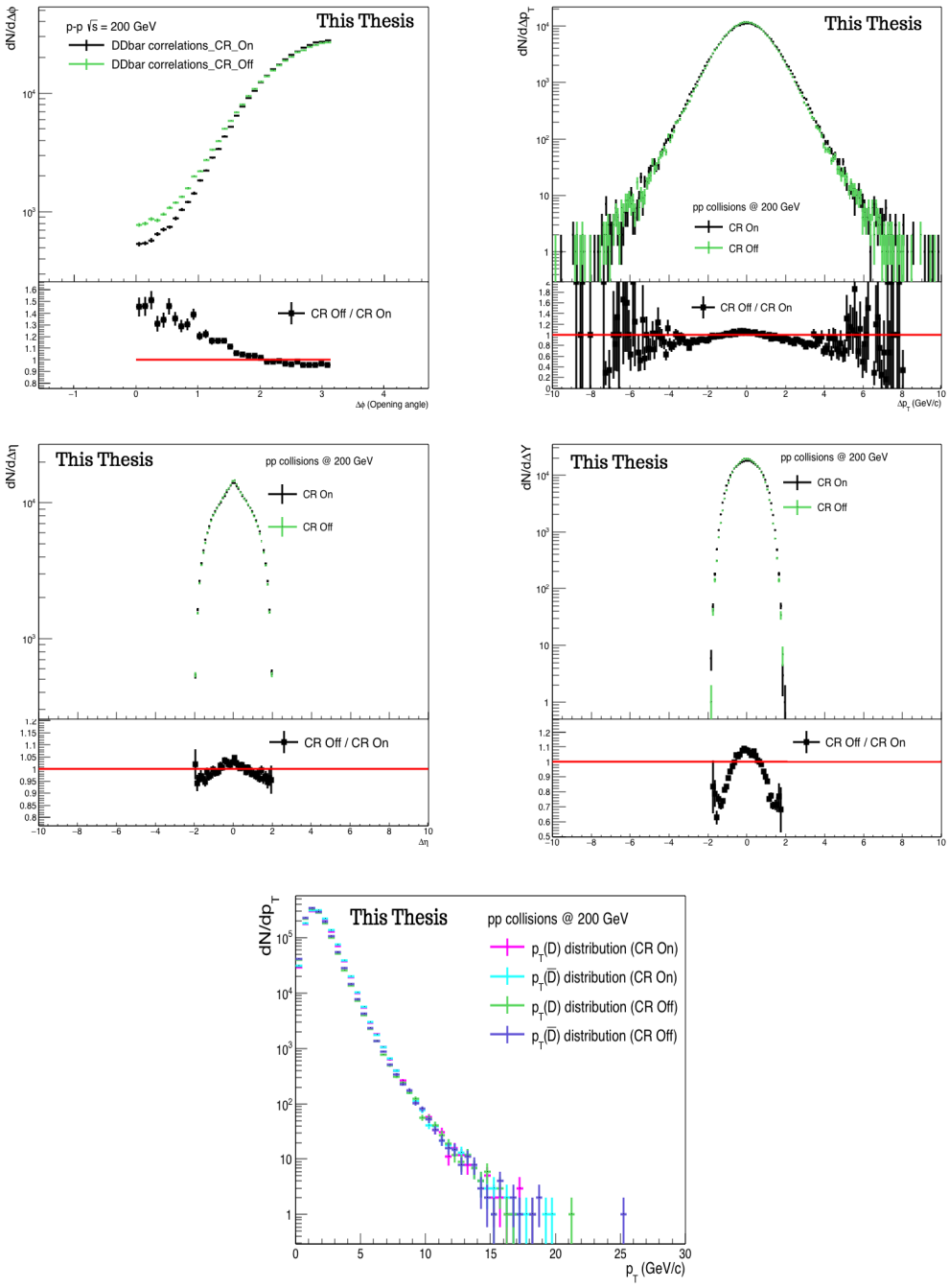

FIGURE 5.24: $D - \bar{D}$ correlation distributions of $\Delta\phi$ (top left), Δp_T (top right), $\Delta\eta$ (middle left), ΔY (middle right) in pp collisions at 200 GeV with CR (black) and without CR (green). p_T distributions (bottom) with CR for D mesons (magenta) and $\bar{D}$ mesons and without CR for D mesons (green) and $\bar{D}$ (purple).

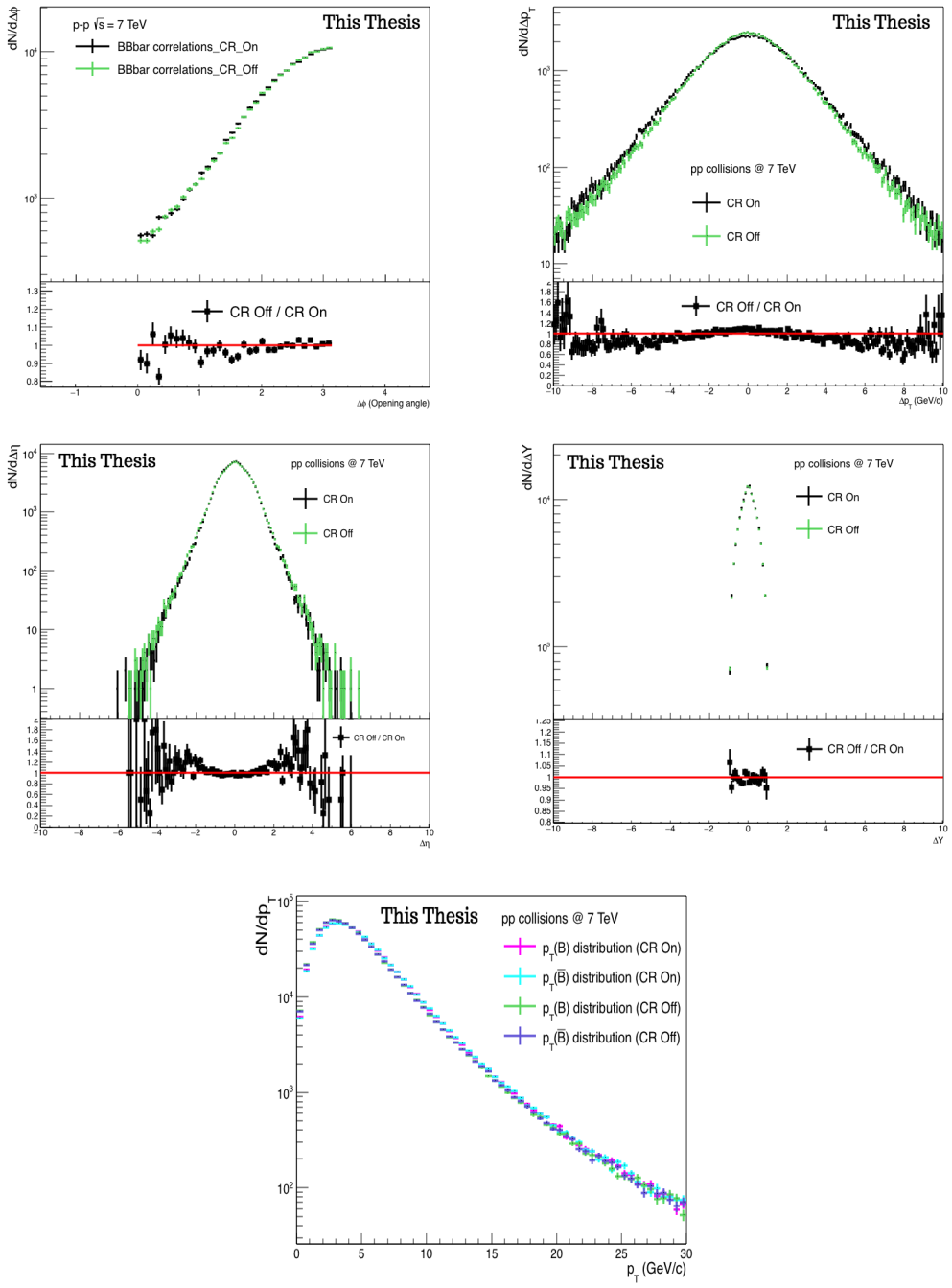

FIGURE 5.25: $B - \bar{B}$ correlation distributions of $\Delta\phi$ (top left), Δp_T (top right), $\Delta\eta$ (middle left), ΔY (middle right) in pp collisions at 7 TeV with CR (black) and without CR (green). p_T distributions (bottom) with CR for B mesons (magenta) and $\bar{B}$ mesons and without CR for B mesons (green) and $\bar{B}$ (purple).

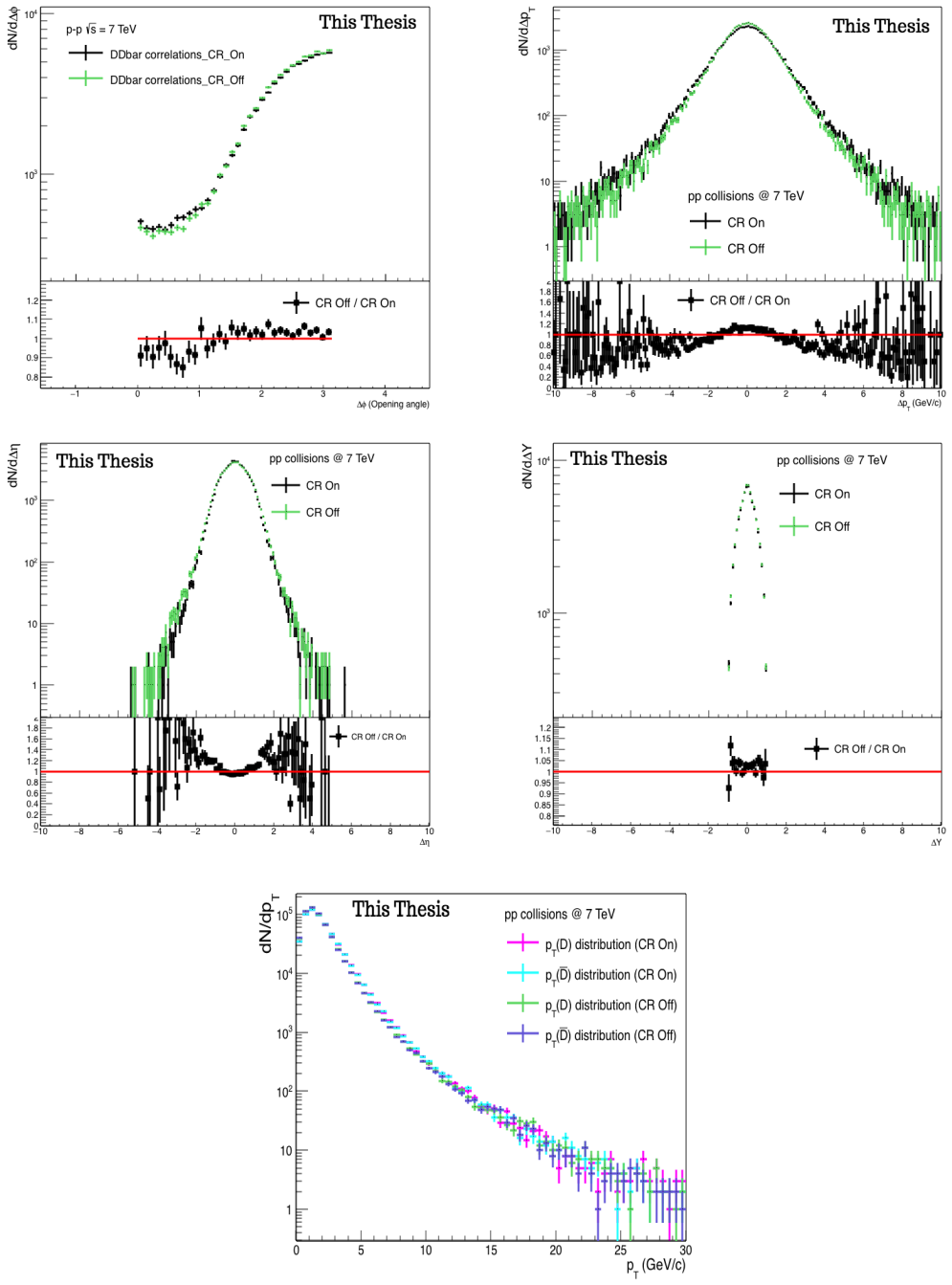

FIGURE 5.26: $D - \bar{D}$ correlation distributions of $\Delta\phi$ (top left), Δp_T (top right), $\Delta\eta$ (middle left), ΔY (middle right) in pp collisions at 7 TeV with CR (black) and without CR (green). p_T distributions (bottom) with CR for D mesons (magenta) and $\bar{D}$ mesons and without CR for D mesons (green) and $\bar{D}$ (purple).

5.4.7 $D - \bar{D}/B - \bar{B}$ correlations Monash2013 versus 4C Tune

In this part, the correlation distributions obtained with the default tune ($Monash$ 2013) are compared to those obtained using the tune $4C$. The general difference between the tunes comes from the different implemented ways to deal with the processes and the description of

the experimental data. For instance, the tune $Monash$ 2013 was configured to describe the minimum-bias physics and underlying events (UE). The $tune$ $4C$ was parametrised based on the early LHC data. Otherwise, among the main difference between these two tunes, one can mention the shape of the hadron-hadron overlap profile, and colour reconnection simulations and multiple interactions parametrisation [100].

The distributions, as presented earlier, are shown in this part for both energies and meson species and this is for both tunes. The black curves represent the distributions obtained using the $Monash$ 2013 tune and those in blue for correlations obtained using tune 4C.

$B-\bar{B}$ correlations in pp collisions at 200 GeV are shown in figure.5.27. $D-\bar{D}$ correlations at 200 GeV are presented in figure.5.28. In pp collisions at 7 TeV, $B\bar{B}$ correlations are presented in figure.5.29 and those of $D\bar{D}$ correlations are presented in figure.5.30.

One can notice that both tunes similarly describe correlations, qualitatively and quantitatively, especially in pp collisions at 7 TeV for both D and B mesons which is visible through the computed ratios presented in the bottom panel of each distribution. In pp collisions at 200 GeV, there is a quantitative difference in the distributions between both tunes. The obtained correlations using the $tune$ $4C$ are larger in magnitude than those obtained using the tune $Monash$ 2013. It is not fair to say that one of them is not correct since no comparison to experimental data was performed and which was not among the to-do list in this chapter of the thesis.

Besides the difference between the correlations with these two tunes which is more visible in the $\Delta\phi$ distributions for both B and D mesons in pp collisions at 200 GeV, the description given in the 2 cases is similar at least qualitatively. Anyway, similar comparison was already performed exhaustively in [100] and the focus was not on correlations only, but several observables were considered, and similar comparison features were concluded.

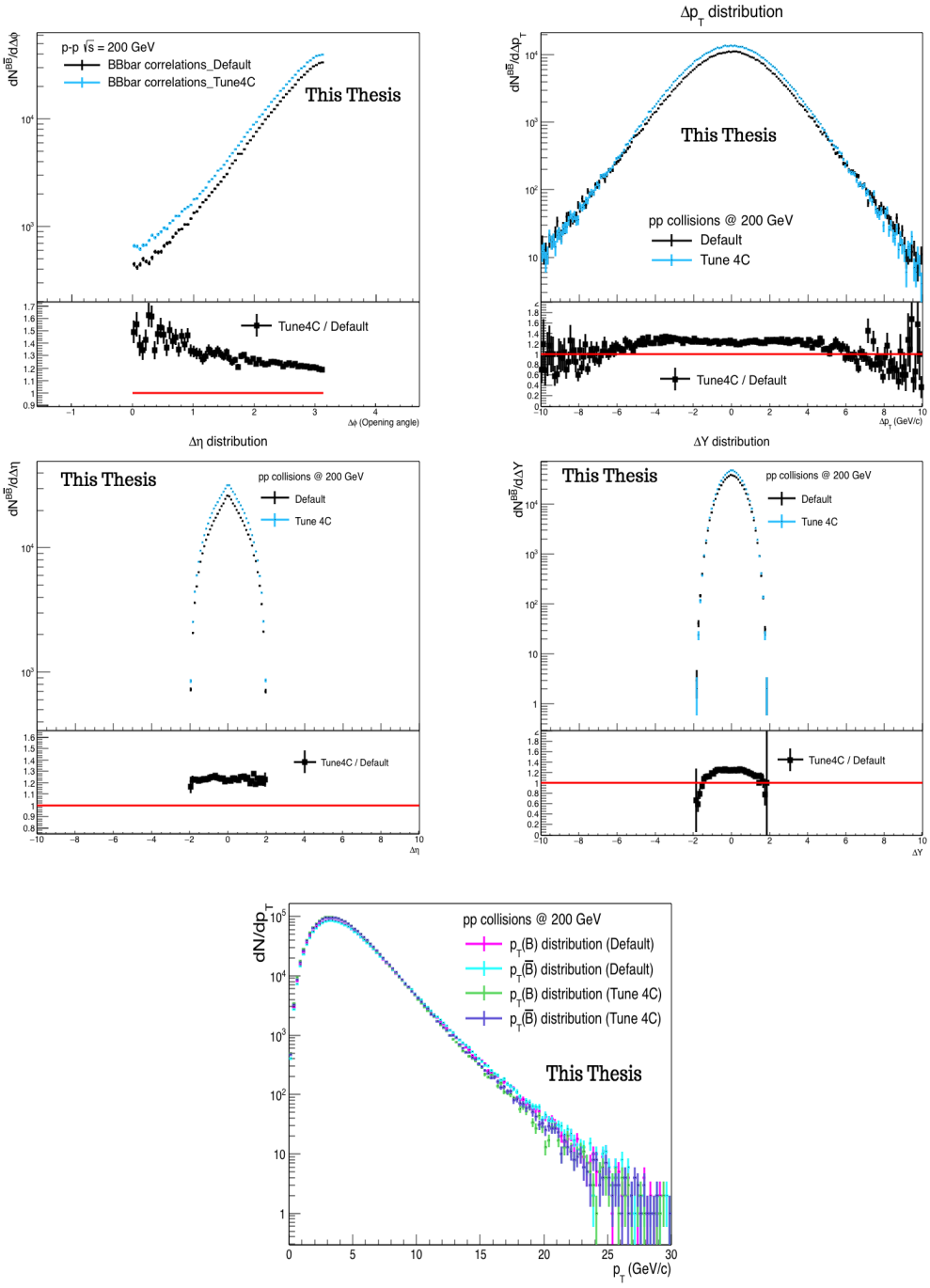

FIGURE 5.27: $B - \bar{B}$ correlation distributions of $\Delta\phi$ (top left), Δp_T (top right), $\Delta\eta$ (middle left), ΔY (middle right) with the default tune $Monash$ 2013 (black) and the the tune 4C (blue) in pp collisions at 200 GeV (Tunes). p_T spectrum (bottom) with the tune Monash2013 for B (magenta) and $\bar{B}$ (cyan) and with the tune 4C of B (green) and $\bar{B}$ (purple).

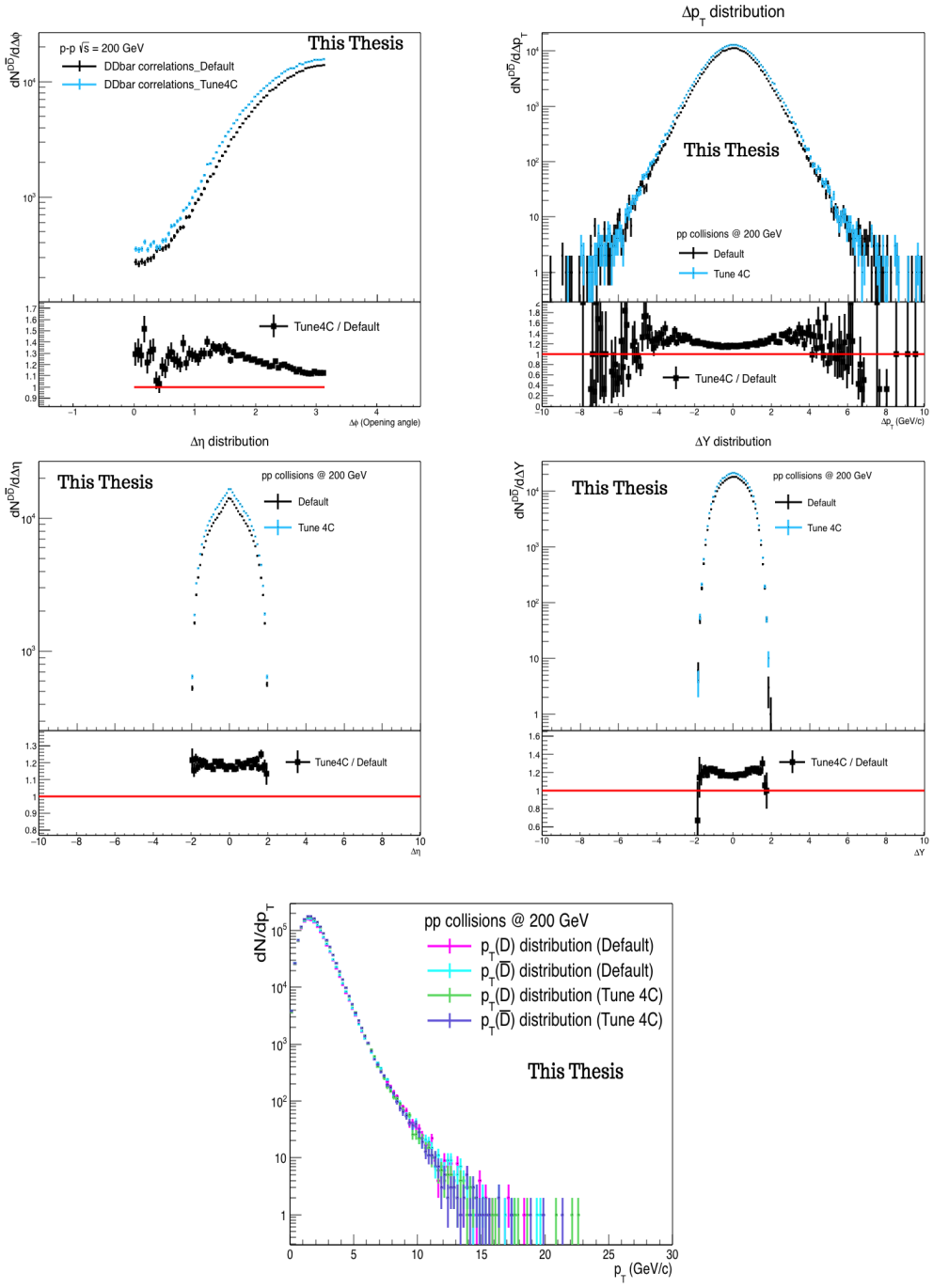

FIGURE 5.28: $D - \bar{D}$ correlation distributions of $\Delta\phi$ (top left), Δp_T (top right), $\Delta\eta$ (middle left), ΔY (middle right) with the default tune $Monash$ 2013 (black) and the the tune 4C (blue) in pp collisions at 200 GeV (Tunes). p_T spectrum (bottom) with the tune Monash2013 for D (magenta) and $\bar{D}$ (cyan) and with the tune 4C of D (green) and $\bar{D}$ (purple).

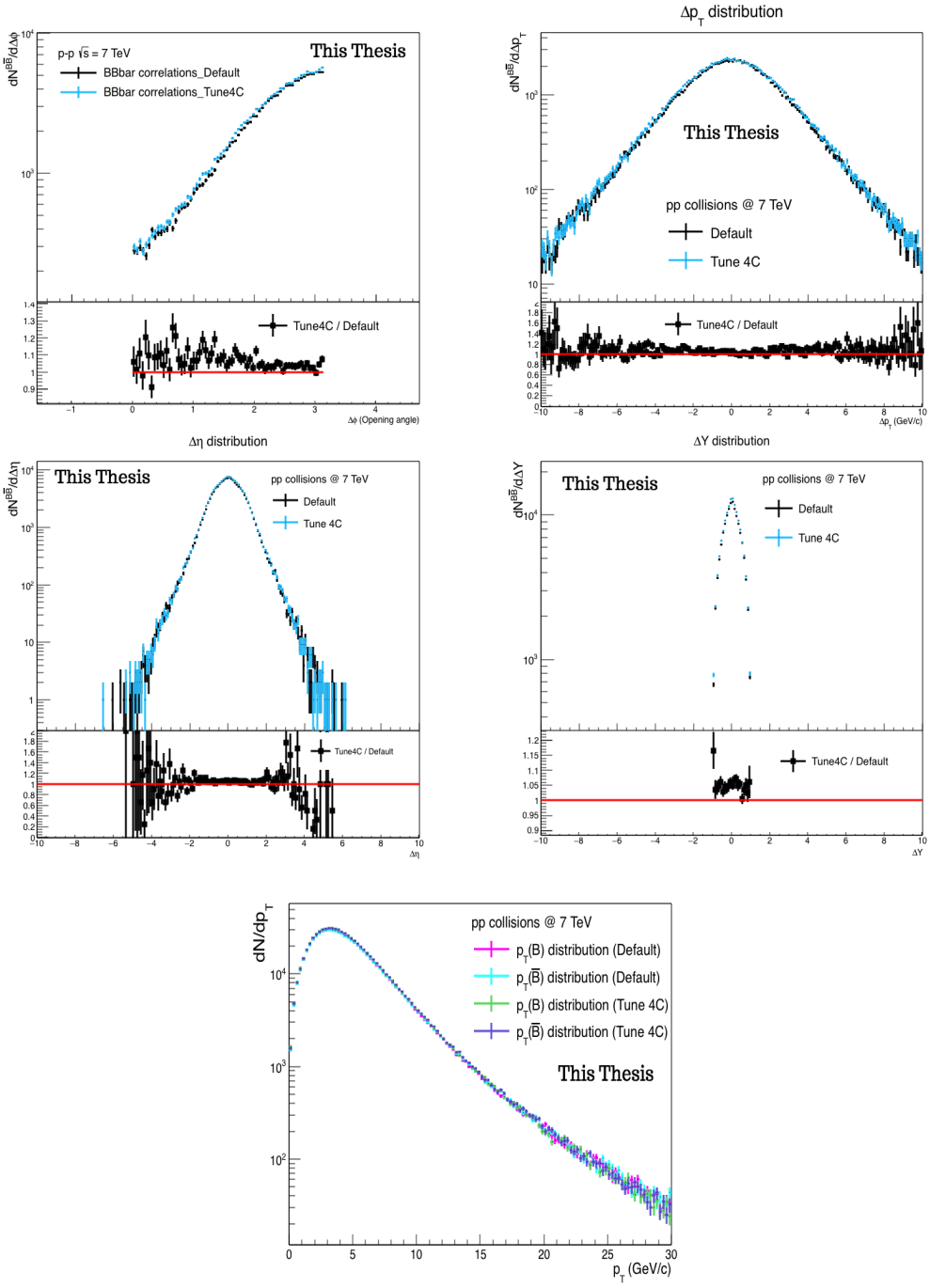

FIGURE 5.29: $B - \bar{B}$ correlation distributions of $\Delta\phi$ (top left), Δp_T (top right), $\Delta\eta$ (middle left), ΔY (middle right) with the default tune $Monash$ 2013 (black) and the the tune 4C (blue) in pp collisions at 7 TeV (Tunes). p_T spectrum (bottom) with the tune Monash2013 for B (magenta) and $\bar{B}$ (cyan) and with the tune 4C of B (green) and $\bar{B}$ (purple).

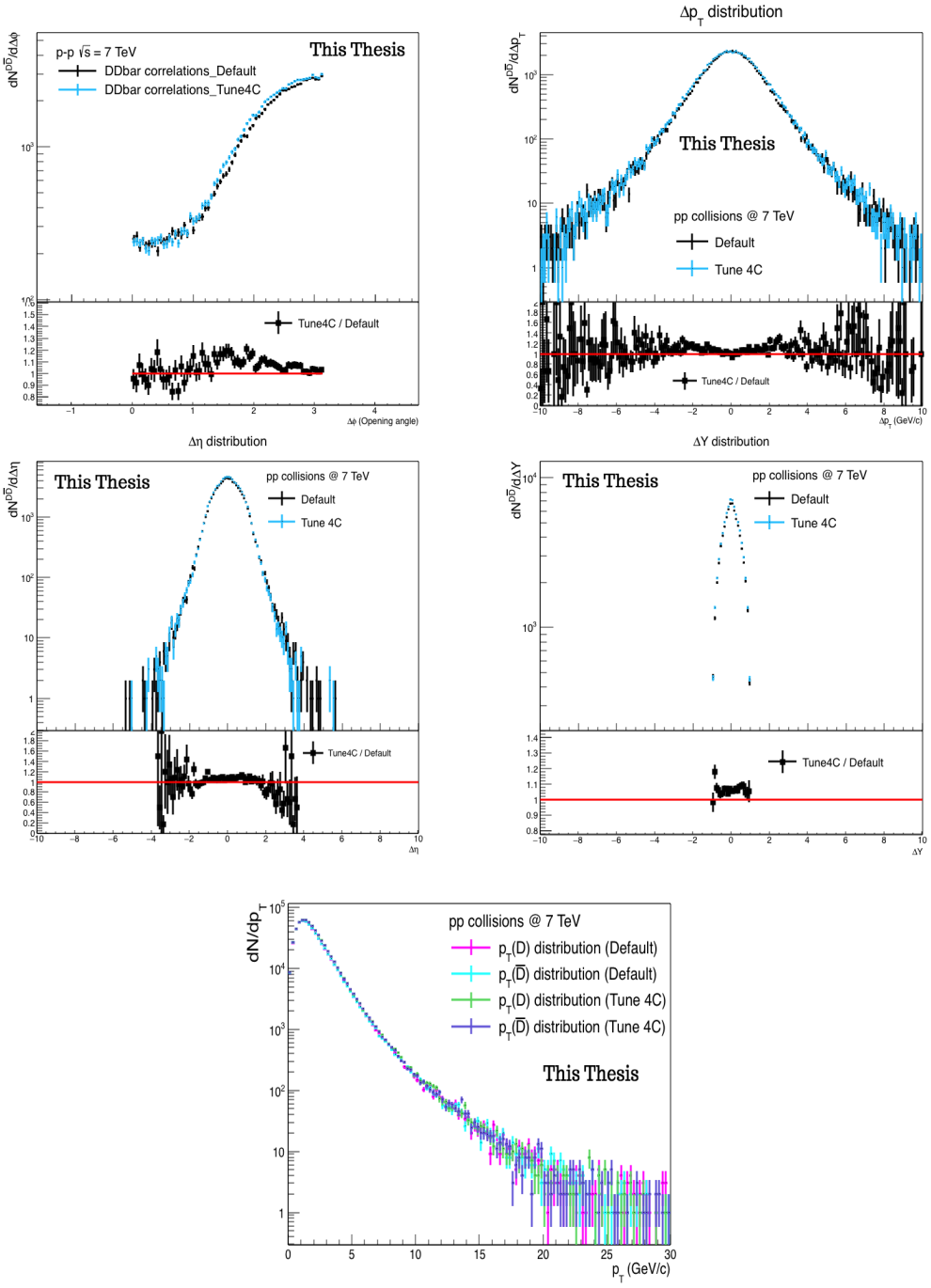

FIGURE 5.30: $D - \bar{D}$ correlation distributions of $\Delta\phi$ (top left), Δp_T (top right), $\Delta\eta$ (middle left), ΔY (middle right) with the default tune $Monash$ 2013 (black) and the the tune 4C (blue) in pp collisions at 7 TeV (Tunes). p_T spectrum (bottom) with the tune Monash2013 for D (magenta) and $\bar{D}$ (cyan) and with the tune 4C of D (green) and $\bar{D}$ (purple).

5.5 Chapter Conclusion

The configuration labelled "Forced" was exploited to perform the current analysis for a matter of time, and due to the similarities exhibited compared to the two other configurations.

We learnt that heavy flavours are generated back-to-back for energies of the order of GeV via flavour creation, and for energies of the order of TeV, gluon splitting contribute effectively although no NLO procedure was integrated into the analysis. In addition to that, high p_T pairs are mainly created at larger angles while low-p_T pairs are generated even at smaller angles. Then, it was concluded that mesons correlations are a reflection of quark correlations because the kinematic pattern is similar between the parton level and the hadron level for different energy scales. After that, we have seen that ISR/FSR have a non-negligible effect on correlations because less heavy flavours were generated which has influenced the production mechanism, especially at larger and smaller angles. It was not the case for MPI whose absence minimised the gluon splitting mechanism. As for CR, the impact was not prominent except for D mesons and their production at smaller angles.

Chapter 6

EPOSHQ Event generator

In this chapter, the theoretical principles of EPOS / EPOSHQ event generators as well as the Heavy Quark package are presented. Then, the results obtained are presented and discussed, in addition to the comparisons made with the experimental data.

6.1 Theoretical basics

The EPOS event generator integrates several approaches from which it derives its abbreviation. It is an **E**nergy conserving quantum mechanical multiple scattering approach based on,

- **P**artons, parton ladders, strings,
- **O**ff-shell remnants,
- **S**plitting of parton ladder.

and it is based on the Parton-Based Gribov-Regge Theory (PBGRT), an approach that combines the two theories: Gribov-Regge theory (GRT) and the parton model. In this merged picture, the issues of multiparton interactions and energy conservation were solved.

The parton model exploits factorization to compute the inclusive cross-section. As for the Gribov-Regge theory (multiple scattering theory), multiparton interactions are allowed to take place. In GRT, the elementary interaction is represented by an exchange of a "Pomeron" which is a phenomenological object with an unknown nature. It is parametrised by an elastic amplitude presented by the equation,

$$T(s,t) \sim is^{\alpha_0+\alpha' t}, \tag{6.1}$$

The inelastic cross section can be expressed by the equation,

$$\sigma_{inel}^{h_1 h_2} = \int d^2b \, \{1 - exp(-G(s,b))\}, \tag{6.2}$$

where $G(s,b)$ is an elementary interaction, proportional to the Fourier transform of $T(s,t)$. It is presented by a thick line as shown in figure.6.1. An interesting discussion about pomeron physics can be found in [115] [116].

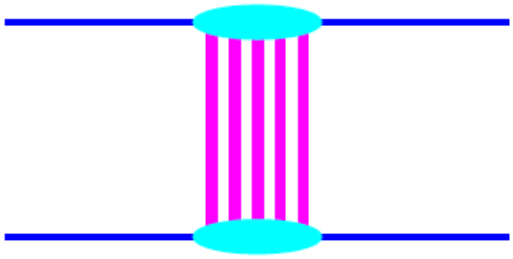

FIGURE 6.1: Hadron-Hadron scattering according to GRT. Pomeron: thick pink lines [117].

In the parton model, the partons of the projectile or the target can be presented by the distribution functions f_{h_1} and f_{h_2}. The production cross-section of partons is factorized by these two latter functions to get the inclusive cross-section, as it is done in PYTHIA and other MC event generators. The inelastic cross-section can be described by the equation,

$$\sigma_{inel}^{h_1 h_2} = \sum_{ij} \int dp_T^2 \int dx^+ \int dx^- \, f_{h1}^i(x^+, p_T^2) \, f_{h2}^j(x^-, p_T^2) \, \frac{d\hat{\sigma_{ij}}}{dp_T^2}(x^+ x^- s) \, \theta(p_T^2 - Q_0^2) \tag{6.3}$$

where Q_0 is a cutoff and $\frac{d\hat{\sigma_{ij}}}{dp_T^2}$ is the parton-parton elementary cross-section, the indices i and j refer to the flavour of partons

The PBGRT is developed in such a way that the energy conservation follows the rules of Quantum Field Theory (QFT) for both the cross-section and the particle production calculations. The energy is properly shared between the different interactions happening in parallel for different systems (pp, p-A, A-A), as displayed in figure.6.2. The thick lines in these schemes represent the sum of the elementary interactions for soft, hard and semi-hard contributions. For the three collisional systems, the nucleon constituents carry an incident momentum fraction so that the sum of the fractions equals one to satisfy the principle of momentum conservation. The constituents of the nucleon can be either participants in the elementary interactions (with the participants of other nucleons) or can be spectators (remnant which represents the rest of all nucleons).

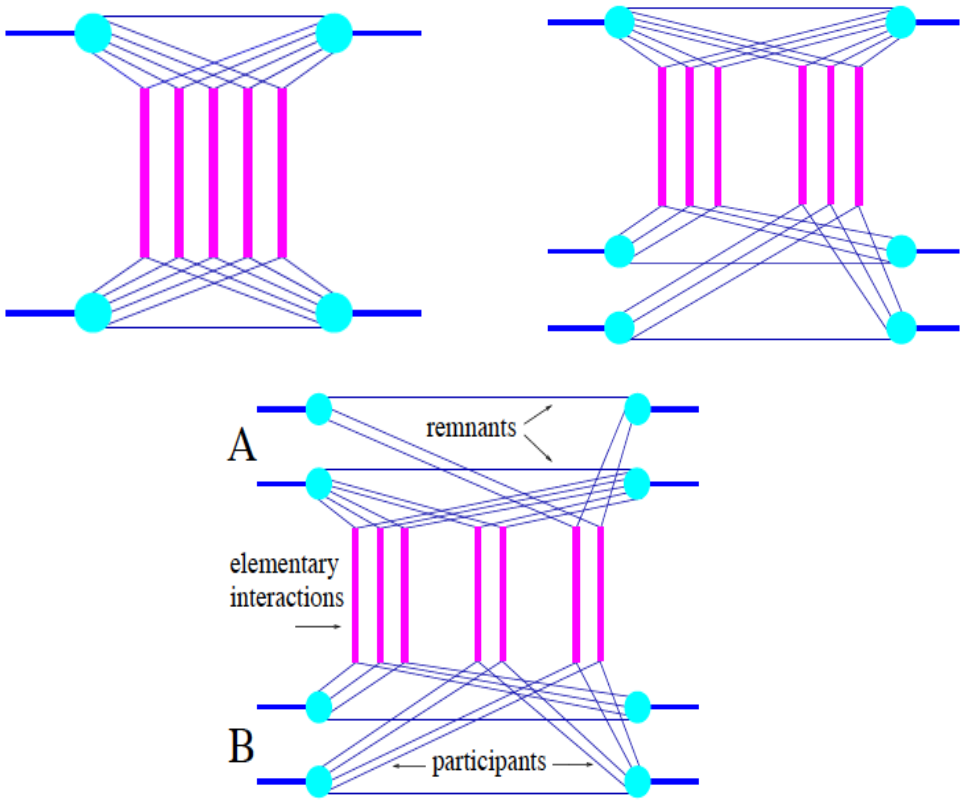

FIGURE 6.2: Elastic amplitude contribution in proton-proton scattering (top left), proton-nucleus (top right) and nucleus-nucleus scattering (bottom) scattering [117].

It is important to mention the profile function included in cross-section calculations to express the contribution of the soft, hard and semi-hard processes. The profile function is symbolised by $G(s,b)$ and associated to the cross-section through the equation,

$$\sigma_{tot} = \int d^2b\, G(s,b) \tag{6.4}$$

where σ_{tot} is the total cross-section for two-body scattering, s is a Mendelstam variable (energy squared in the cms), b is the impact parameter and $G(s,b)$ is the profile function or in an other word, the probability of an interaction with an impact parameter b and an energy $\sqrt{s}$. More information can be found in Appendix.C about the profile function and the contribution for different processes.

Each time the term "Pomeron" is mentioned, one should associate it with the amplitude of elementary parton-parton scattering. The pomeron can be imagined as two layers of parton ladders where the two layers are connected to the remnants of the projectile and the target by two legs (leg=colour singlet=$q\bar{q}$=qqq=$\bar{q}\bar{q}\bar{q}$) and the cut pomeron can be thought of as two strings [118]. According to the nature of the scattering, four types of pomerons are distinguished: soft, val-val (hard), sea-sea (semi-hard), val-sea and sea-val (mixed semi-hard). For each pomeron type, there is a correspondent profile function. More details can be found

in [117]. Perturbative pomerons are treated in this approach using the DGLAP evolution equations where the virtualities in the ladder are ordered. Non-perturbative pomerons are included as well, and they are treated using non-perturbative, finite-range gluon propagators. The general expression of the hadron-hadron scattering amplitude, where multiple scattering and kinematics are taken into account, is displayed in figure.6.3.

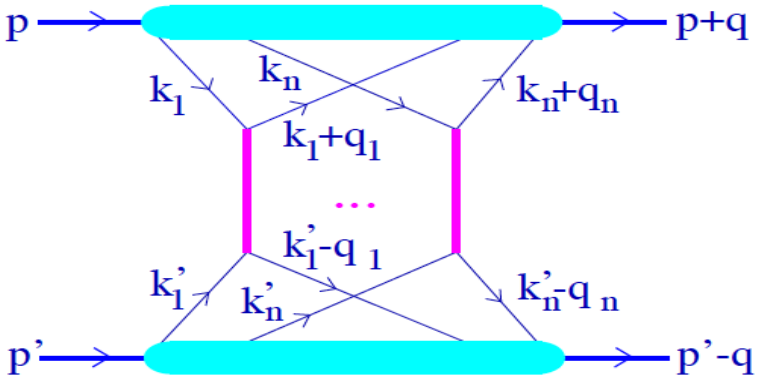

FIGURE 6.3: Hadron-hadron interaction amplitude [117].

and can be expressed by the equation,

$$
\begin{aligned}
i\,T_{h_1h_2}(s,t) = \sum_{n=1}^{\infty} \frac{1}{n!} \int \prod_{t=1}^{n} \left[\frac{d^4k_l}{(2\pi)^4} \frac{d^4k'_l}{(2\pi)^4} \frac{d^4q_l}{(2\pi)^4} \right] N_{h_1}^{(n)}(p, k_1, ..., k_n, q_1, ..., q_n) \\
\times \prod_{l=1}^{n} \left[i\,T_{1\mathbb{P}}(\hat{s}_l, q_l^2) \right] N_{h_2}^{(n)}(p', k'_1, ..., k'_n, -q_1, ..., -q_n)(2\pi)^4 \delta^{(4)} \left(\sum_{k=1}^{n} q_i - q \right)
\end{aligned}
\tag{6.5}
$$

where t=q^2, s=$(p+p')^2$ and p, p' are the 4-momenta of the initial hadrons, $\hat{s}_l = (k_l + k'_l)^2$ and k_l, k'_l are the 4-momenta of the initial partons for the lth scattering and q_l is the 4-momentum transfer. The factor $\frac{1}{n!}$ is included to account for the n identical re-scattering contributions. $N_h^{(n)}(p, k_1, ..., k_n, q_1, ..., q_n)$ represents the contribution of the vertex for the coupling (n)parton-hadron h. $T_{1\mathbb{P}}$ is the partonic scattering amplitude from all contributions and can be expressed by the equation,

$$
T_{1\mathbb{P}}^{h_1h_2} = T_{soft}^{h_1h_2} + T_{sea-sea}^{h_1h_2} + T_{val-val}^{h_1h_2} + T_{val-sea}^{h_1h_2} + T_{sea-val}^{h_1h_2} \tag{6.6}
$$

The hadronic profile function γ is defined by :

$$
\gamma_{h_1h_2}(s,b) = \frac{1}{2\,s}\, 2Im\,\tilde{T}_{h_1h_2}(s,b) \tag{6.7}
$$

where $\tilde{T}$ is the Fourier transform of the scattering amplitude T. $2Im\,\tilde{T}_{h_1h_2}(s,b)$ can be

presented by a cut elementary diagram and $-2Im\,\tilde{T}_{h_1h_2}(s,b)$ by an uncut elementary diagram (see figure.6.4). The partonic scattering amplitude can be expressed as a function of the partonic profile function that satisfies the equation,

$$G_{1\mathbb{P}}^{h_1h_2} = G_{soft}^{h_1h_2} + G_{sea-sea}^{h_1h_2} + G_{val-val}^{h_1h_2} + G_{val-sea}^{h_1h_2} + G_{sea-val}^{h_1h_2} \tag{6.8}$$

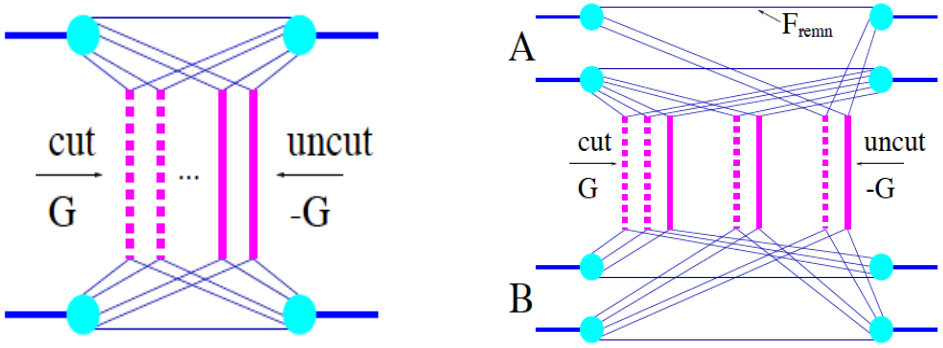

FIGURE 6.4: The hadronic profile function expressed as a function of the partonic profile function $G_{1\mathbb{P}}^{h_1h_2}$ in pp scattering (left diagram) and nucleus-nucleus scattering (right diagram) [117].

The cut elementary diagram (dashed vertical line) represents virtual emissions (particles off-shell) while the uncut elementary diagram (full vertical line) represents realistic elementary interactions .i.e pomerons that will hadronise later into particles on-shell.

One of the important features of this approach is that the AGK cancellations in hadron-hadron scattering are applicable. The AGK cancellations mean that the contributions of multiple scattering diagrams with more than one elementary interaction cancel each other. This principle is applicable in nucleus-nucleus scatterings. This leads to the fact that the cross-section is nothing but the proton-proton cross-section times the mass number associated with the nature of the scattered nucleus (target and the projectile). The last statement can be expressed by the equation,

$$\frac{d\sigma_{incl}^{AB}}{dq}(q,s,b) = AB\frac{d\sigma_{incl}^{pp}}{dq}(q,s,b) \tag{6.9}$$

More details on Parton-Based Gribov-Regge Theory, the integrated approach in EPOS event generator, can be found in [117].

EPOS was already tested through the reproduction of simple and sophisticated observables. They were found in reasonable agreement with experimental data. Examples of such comparisons to data can be checked in [119] [120] [121] [122] and many others. EPOS had been used even in cosmic rays studies as it was done in [118] where those studies helped to improve EPOS in energy intervals not accessible in colliders and accelerators on the earth.

6.1.1 Initial conditions

Within the EPOS event generator, the same procedure is followed for different collisional systems (pp, p-A or A-A). For this reason, it is called a universal model. The starting point is the initial conditions like most event generators. From the technical side and according to EPOS user's guide [124], the main mandatory parameters to initialise are the following :

- Number of events
- Energy per nucleon-nucleon in centre of mass system (cms).
- Atomic number (Z) and mass number (A) of the projectile.
- Atomic number (Z) and mass number (A) of the target.
- Activate/deactivate the nuclear effects due to parton splitting and fusion which leads to screening (saturation) and so on ...
- Activate/deactivate some specific decay channels.

In addition to the technical details, some other physical aspects are worth mentioning, for example :

- The number of each type of exchanged pomerons between the projectile and the target
- Activate/deactivate the energy sharing between the pomerons and the two remnants (which leads to the production of particles either from remnants decays or cut pomerons).

6.1.2 Parton ladders

(Splitting of) Parton ladder is an essential aspect in EPOS, and it was a partial factor of success to predict until now many experimental data. As is mentioned earlier, parton ladders contribute as pairs to form the pomerons which is another way to represent colour flux tubes. Figure.6.5 represents the structure of the parton ladder. The left diagram shows the parton-parton elementary interaction where the hard scattering takes place in the middle after the emission of partons due to the initial space-like cascade. The right diagram shows a simple schematic representation for a parton ladder [125].

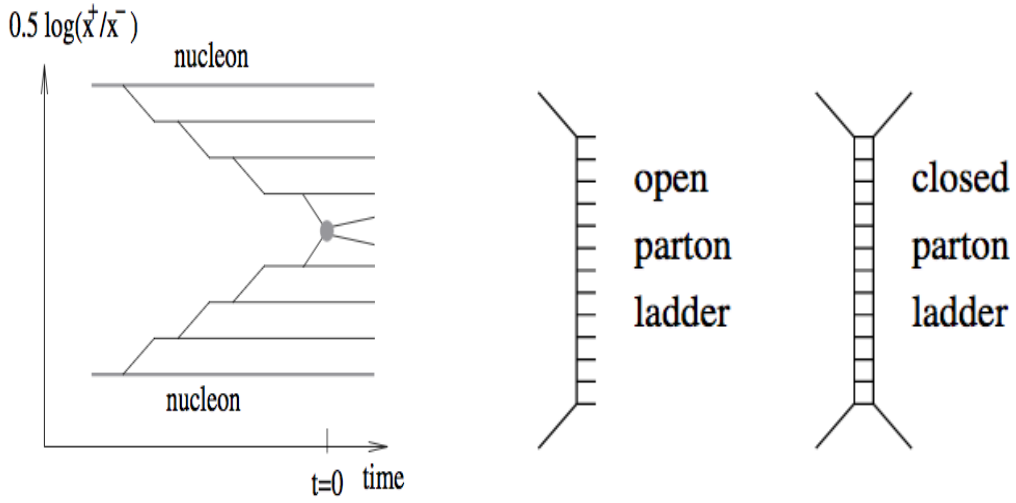

FIGURE 6.5: Left: Parton-Parton elementary interactions. Right: Symbolic scheme for open and closed parton ladders [125].

A parton ladder is supposed to consist of 2 parts: the soft one and the hard one and they can be either open or closed ladders (right diagram of figure.6.5). The open parton ladders contribute to the inelastic scattering amplitude while the closed ones contribute to the elastic scattering amplitude. The latter does not participate in particle production, but it affects the partial cross-section significantly by producing several interfering contributions.

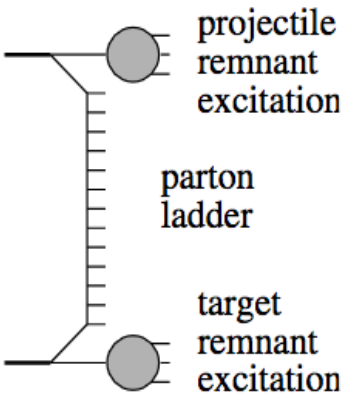

FIGURE 6.6: Complete picture : parton ladders and beam remnants [125].

The interacting partons (quark-antiquark or quark-diquark) leave behind colourless off-shell remnants from the projectile and the target (generally excited). This induces the deceleration of the target which is not the case if the interacting partons are just some simple quarks. The full picture can be visualised by the diagram shown in figure.6.6. In the end, all objects are colourless (or white): the remnants and the parton ladders. More details about the importance of parton ladders and their splitting can be found in [126] [127].

6.1.3 Core-Corona approach

The Core-Corona approach is another essential aspect integrated into the EPOS event generator. At an early proper time τ_0 and after the collisions take place, the partons/hadrons density is not the same everywhere, and so do the string segments. To separate the high-density region (central part/the fluid) in the collision zone from the low density one (peripheral part/escaping hadrons including jet hadrons), the geometrical properties of the medium were considered in addition to the momentum, and the density of the string segments. The idea of separation came up because of the necessity to remove the background (for some observables) to get only the concerned signal in the analysis. For instance, one can mention the collectivity through the radial flow that takes place in a high-density medium in heavy-ion collisions. Meanwhile, the peripheral particles/partons do not contribute in such expansion (at least in the same way as those from the central part), but they behave as independent pp/pA collisions. Hence, it comes the necessity for the core-corona separation [128].

In this approach, the nucleus-nucleus peripheral collisions are considered to behave as pp or p-A like collisions. The created partons before hadron formation are split into two kinds. The first one is string segments created in a dense area or what is called "core". For the second one, string segments are formed in an area with low density or the so-called "corona". This is illustrated by the Monte Carlo simulations done in 40-50% semi-peripheral Au-Au collisions presented in figure.6.7 [125].

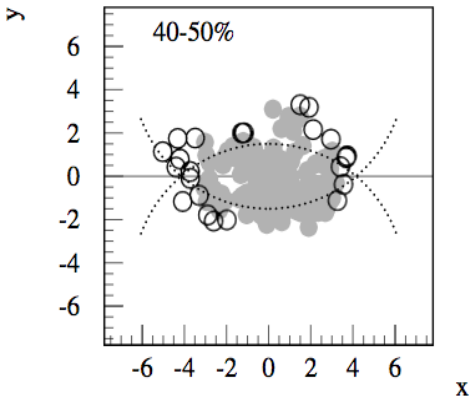

FIGURE 6.7: Monte Carlo simulations for Au-Au collisions at 200 GeV in 40-50% centrality [125].

This picture is displayed in the XY plane. The dotted half-circles symbolise the two colliding nuclei. The grey area represents the string segments at the high-density region or the reaction zone (core) where the local equilibrium is reached through the sufficiently large number of collisions of the partons. The open circles are the string segments at low-density regions

or surface partons (corona) where the local equilibrium is not reached because partons undergo fewer collisions/interactions, and they are treated as elementary proton-proton collisions. Consequently, this region will not contribute to the hydrodynamical evolution of the system [129].

At low density, string fragments hadronise without interactions which is similar to pp or p-A scattering. For the high-density area, the treatment is similar to the one in heavy-ion collisions via hydrodynamical evolution. This approach will be discussed in the following subsection (section.6.1.4).

The previous description can be visualised differently in figure.6.8. The blue area represents the bulk matter where the energy density is high. Anything else outside this area, one can find jets or escaping hadrons. Three possible scenarios can take place. The string piece can be formed inside the core (represented in pink) because it does not have enough energy to escape the created medium which evolves under the restrictions of hydrodynamic laws. The string piece can be formed outside the core (represented by red) to produce particles/jets or corona. The string piece can be formed inside the core, but it escapes the medium (presented in blue) because it possesses enough energy to form a jet that has already interacted with the medium [130]. Based on what has been mentioned, particles can come from two sources: the core, or the corona. The contribution from the corona is dominant at high p_T while at low p_T the contribution from the two sources is a bit similar. As for intermediate p_T, the contribution depends on the particle species.

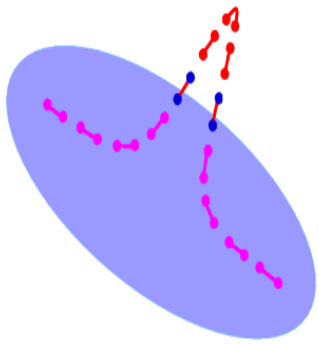

FIGURE 6.8: Colour flux tube fragmentation into string fragments in the core-corona approach [130].

The integration of the core-corona approach in EPOS had given an enough good description to the data for different observables as it was done using EPOS 1 [128], EPOS 2 [131] with the ideal hydrodynamic evolution or the viscous one using EPOS3 [132] [133]. This approach was also verified for both high and low energy beams where an acceptable agreement was found between data and predictions [129].

6.1.4 Hydrodynamic evolution

The hydrodynamic evolution can occur either in high multiplicity pp collisions [134] or in heavy-ion collisions [135]. The starting point is the parton ladders (section.6.1.2) .i.e the elementary colour flux tubes that are longitudinal strings. These strings can be imagined as 3 dimensional objects with a surface X(α,β) in space-time as displayed in figure.6.9(a). The flux tube is moving in parallel to the z-axis. Due to the kinky string part, another movement is considered in the transverse direction parallel to the y-axis.

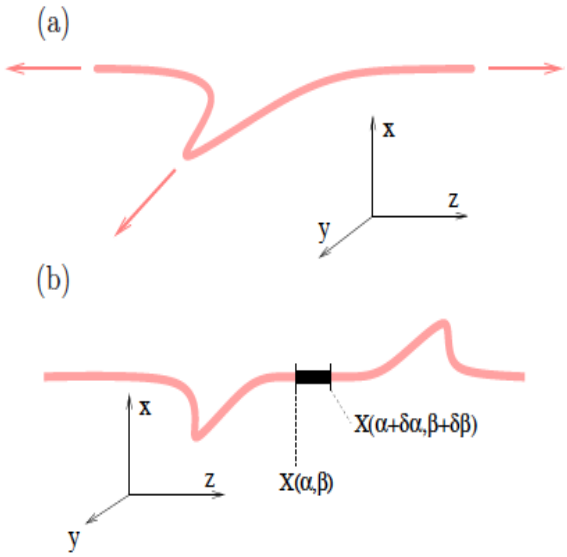

FIGURE 6.9: (a) Flux tube with a kink moving along the y-axis. (b) String segment at a determined proper time [134].

At moderate relativistic energies, string density is not too high, and the hadronisation takes place through string breaking. The resulting string segments will form hadrons at the end of the process. If the collision energy is high enough, the resulting string density will be high so that the hadronisation of different segments will not be independent. For this reason, strings will be split into segments with a proper time τ_0 and widths $\delta\alpha$, $\delta\beta$. Certainly, there will be a region where the string segment density is low (corona) and a region with a larger density of string segments (core) as was already discussed in section.6.1.3.

At this stage, the four-momenta of the string segments can be extracted as well as the initial condition for the hydrodynamic evolution by determining a local energy density $\epsilon(\tau_0, \vec{x})$ and a local flow velocity $\vec{v}(\tau_0, \vec{x})$ where both are dependent on the initial proper time τ_0 and space. An example of the initial energy density is displayed in figure.6.10.

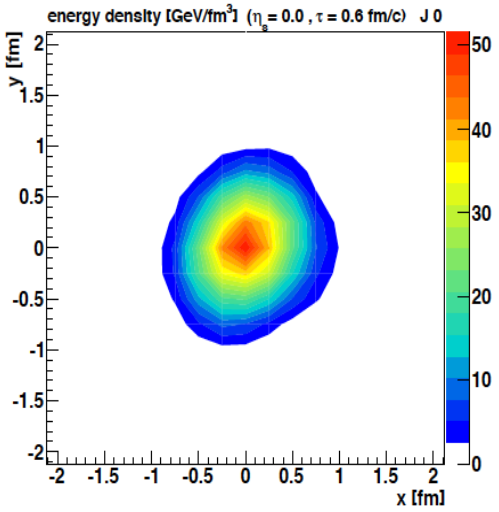

FIGURE 6.10: Example of an initial energy density in high multiplicity pp collisions at an energy of 900 GeV at $\tau_0 = 0.6$ fm/c [134].

By considering these initial conditions with the ideal (or the viscous) hydrodynamical evolution, the created medium will evolve according to the local energy-momentum conservation equation,

$$\partial_\mu T^{\mu\nu} = 0, \qquad T^{\mu\nu} = (\epsilon + p)u^\mu u^\nu - pg^{\mu\nu}, \quad \nu = 0, ..., 3 \tag{6.10}$$

and the equation of net charges conservation,

$$\partial N_k^\mu = 0, \qquad N_k^\mu = n_k u^\mu, \quad k = B, S, Q \tag{6.11}$$

where u is the four-velocity in the local rest frame, B is the baryon number, S the strangeness, and Q is the electric charge. After solving these equations, the obtained solutions are the space-time dependent quantities : energy density $\epsilon(x)$, collective flow velocity $\vec{v}(x)$ and the net flavour densities $n_k(x)$.

As a Summary concerning the hydrodynamic evolution, at an initial proper time τ_0, the created medium expands with determined initial conditions until it reaches a defined temperature T_H where hadronisation (section.6.1.5) takes place (switch from matter to particles) by applying the procedure of Cooper-Frye. After that, hadrons undergo re-scatterings where hadronic cascades evolve in the scope of the UrQMD model [136]. Under these circumstances, the energy density shown in figure.6.10 can evolve with time as presented in figure.6.11. A similar procedure is considered for simulations with viscous effects [137] instead of the ideal hydrodynamics evolution.

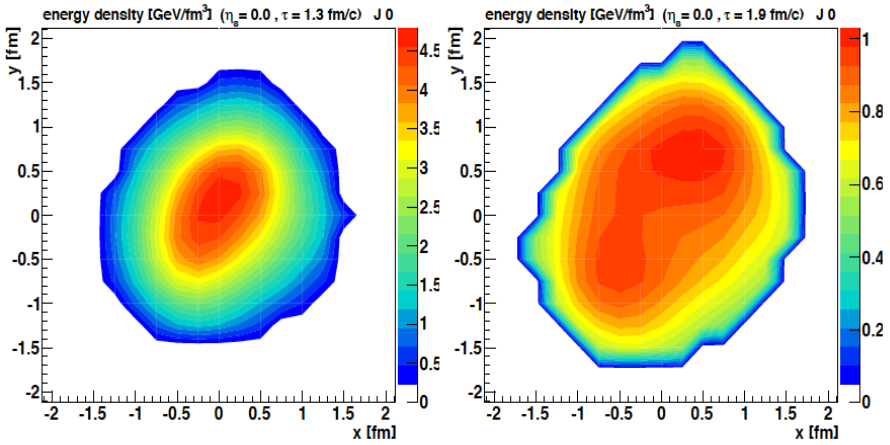

FIGURE 6.11: Same as figure.6.10 at later proper times : $\tau = 1.3$ fm/c (left) and $\tau = 1.9$ fm/c (right) [134].

By integrating such fluid hydrodynamic expansion in EPOS, the obtained results have shown an acceptable agreement with data by reproducing correlation distributions and mass splitting observed through the elliptic flow (v_2) [133] [138]. The latter is among the proof of the existence of collective behaviour in p-A systems.

6.1.5 Hadronisation

In the EPOS approach, the hadronisation mechanism is dependent on the structure of the cut pomeron. If the pomeron is soft, then hadronisation is hidden in a simple parametrisation of the characteristics of the soft pomeron. If the pomeron is hard, then hadronisation is based on the fact that summing over the hadronic final states is similar to summing over the partonic final states, and the parametrisation used is called the "String model". It is not considered a microscopic hadronisation model due to the parametrisation of the hadronic structure of the cut pomeron, and it should be in agreement with the principle laws of physics and experimental observations.

The simplest representation of a cut pomeron is displayed in figure.6.12. The cut pomeron is presented by the dashed thick vertical line which is connected to the nucleons (quark - anti-quark) and symbolised by the external legs. More details, about the hadronisation mechanism using this approach for the different processes (dependent on pomeron structure), can be found in Appendix.D.

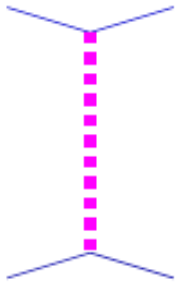

FIGURE 6.12: Schematic representation of a cut pomeron [117].

The main difference between the hadronisation process in EPOS and PYTHIA (based on the Lund String Model) is that in EPOS, hadrons are produced directly from strings using the area law, while in PYTHIA, hadrons are produced from mass clusters using the fragmentation function.

The area law deals with the string breaking to produce final state hadrons. This law is based on the same principle of unstable particles decay. The same principle is considered for strings through the equation,

$$dP = \lambda\, dA \tag{6.12}$$

where dP is the probability of string breaking with a breaking constant λ and dA is the proper surface in the Minkowski space. dA can be written in a more simplified formula as,

$$dA = \frac{1}{2}\,(1 - cos\phi)\, d\sigma\, d\tau \tag{6.13}$$

σ and τ are space-like and time-like parameters, ϕ is the angle between the partons. The maximum contribution to the string breaking is coming from partons moving in opposite directions. For partons with $\phi = 0$, the contribution is zero. The location of string breaking has to be determined. First, this relies on equation 6.12 and secondly on the expression,

$$P_0(A) = e^{\lambda\, A} \tag{6.14}$$

P_0 is the probability of having zero break in the area A. Several surfaces A_i are generated as well according to the expression,

$$A_i = -log(r_i)/\lambda \tag{6.15}$$

where r_i is a random number between 0 and 1. The area A_i has no precise shape as long as causality is preserved. This procedure of string breaking can be symbolised in a simple concrete way by the diagram displayed in figure.6.13. P_i are the breaking points, and L_i are the lines defined by the surfaces A_i.

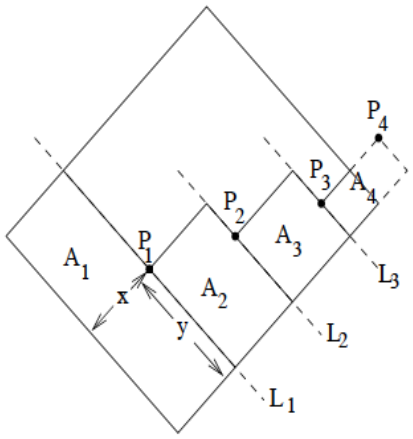

FIGURE 6.13: Search for breaking points (simple representation) [117].

The procedure starts with a first breaking point P_1 that is chosen randomly on the line L_1 defined by the surface A_1. The second breaking point is selected according to the first one (considered as a constraint) and so on. This procedure is over if the last surface is too large so that it is not anymore in the surface of the string or if the resulting pieces are not heavy enough to produce hadrons.

Concerning the flavour of the string fragments (partons), it is suggested that at each breaking point, new associated flavours are created with some probabilities (free parameters) to create pairs of quark-antiquark or diquark-antidiquark. For the case of quark-antiquark, the probability of creating u/d and s quarks are p_{ud} and 1 - 2 p_{ud}, respectively. For the case of diquark-antidiquark, the parameter $p_{diquark}$ is considered. For the mass, the string momentum is computed first. Consequently, the momentum of the string fragments can be deduced, as well as their masses. For what concerns the type of hadron, it is determined using a table (already established in this approach) where for each string fragment with a determined flavour and a mass range, a hadron type is associated.

The "Parton-Based Gribov-Regge Theory" was tested at the time of the establishment by comparing the spectrum of different observables obtained with EPOS event generator to those measured within different experiments/energies (LEP, RHIC, HERA, PETRA, SLAC, ...) and a good agreement was found compared to the data.

More details on the parameters used to build this approach can be found in [117]. These parameters are connected to different mechanisms such as hadronisation, time-like cascade, parton-parton scattering, hadron-hadron scattering and others.

The previously described hadronisation procedure is used generally at the level of the matter created in heavy-ion collisions (core). Regardless of the collisional system, hadronisation takes place at the hyper-surface of the core where the temperature should be close to the one of hadronisation T_H. This is treated using the Cooper-Frye procedure [139] which was

already exploited in separated studies and shown reasonable agreement in comparison to the experimental measurements [140] [141].

6.2 MC@sHQ approach

MC@sHQ is an approach based on Monte Carlo simulations where HQ is an abbreviation for **H**eavy **Q**uark, and it is a package that was developed and dedicated to the study of heavy flavours and how they interact with the created medium in heavy-ion collisions and other small systems like pp or p-A collisions. The complete picture of the evolution of heavy quarks from production to hadronisation using MC@sHQ as a standalone event generator consists of 3 principal stages,

- Initialisation of the nucleus-nucleus collisions, as well as heavy flavour spectrums based on FONLL predictions.
- Then, MC@sHQ is coupled with 3+1 dimension (viscous or ideal) fluid dynamical evolution from EPOS. Heavy flavours are propagated according to the equation of Boltzmann where the properties of the gluon and light quarks are taken from the local background medium properties (temperature, velocities). At this stage of the evolution, the heavy quarks undergo an energy loss through 2 mechanisms: collisional and/or radiative.
- Finally, the hadronization of heavy flavour can take place either via the fragmentation (high p_T) or the coalescence (low p_T) at T=155 MeV.

More details about the heavy flavour production, interaction with the medium and finally hadronisation can be found in [142].

The collisional process is an elastic scattering $2 \rightarrow 2$ which can be expressed by the interaction equation : Q + q $\rightarrow$ Q' + q' and Q + g $\rightarrow$ Q' + g' while the radiative process is an inelastic scattering and can be expressed by : Q + q $\rightarrow$ Q' + q' + g and Q + g $\rightarrow$ Q' + g' + g".

Among the crucial features of the MC@sHQ approach is the use of a K-factor (temperature-independent) to rescale the corresponding scattering rates/cross-section in such a way that the predicted nuclear modification factor (R_{AA}) obtained with this approach will be in agreement with the R_{AA} measured from the data within experimental uncertainties [143]. Once the K-factor is fixed according to the concerned scenario, this same value is used to deduce other observables distributions such as the elliptic flow v_2, azimuthal correlations or cross-section. The latter, for example, can be extracted for the purely collisional mechanism (K=1.5), the purely radiative mechanism (K=1.8) (which was integrated and tested for the first time in MC@sHQ in [2]) or the collisional+radiative scenario (K=0.8).

6.3 EPOSHQ event generator

EPOS-HQ is a framework resulted from the combination of EPOS3 and MC@sHQ event generators to predict the observables of heavy flavours in different collisional systems [144]. The evolution of heavy-flavours in EPOS-HQ differs from the one in MC@sHQ by the initial conditions. With MC@sHQ, as mentioned in section.6.2, initial heavy flavour spectrums are based on FONLL predictions. While for EPOSHQ, heavy quarks are generated in the initial conditions of EPOS3.

Briefly, heavy quarks are produced in $2 \rightarrow 2$ partonic collisions/cascades (born level). According to Regge theory, 2 partons will undergo a soft interaction. A spacelike cascade takes place once the virtuality is larger than the saturation scale ($Q^2 > Q_s^2$). In such a cascade, the virtuality increases by emitting timelike partons. When radiations are over from spacelike partons, the collision takes place. This is called the born process, and it is treated using a partonic cross-section from pQCD. In their turn, radiated partons from the born process and spacelike cascades will initiate timelike cascades. More advanced details can be found in [145].

The approach EPOSHQ was tested in several analyses by comparing its predictions to data where an agreement was established within experimental systematic uncertainties for different observables [146] [3] [147] [148] [149] [150] [151] [152]. In the upcoming sections, the notation EPOSHQ refers to EPOS3 + MC@sHQ .i.e both notation are equivalent.

6.4 Correlation analysis and Results for p-p and p-Pb collisions

In this section, correlation analyses are carried out using the event generator EPOSHQ (with EPOS version 3.210). In some cases, EPOS is exploited instead because of the missing particles D^* in the current version of EPOSHQ. D ($\bar{D}$) mesons are correlated with charged particles in pp / $p - \bar{p}$ and p-Pb collisions.

In these analyses, some selection criteria - similar to those considered in the experimental measurements - were applied :
- Only events with tagged D mesons - that pass the kinematical criteria - are considered.
- the pair D meson - hadron should be in the same event (event-by-event analysis)
- D mesons from B-mesons decays are removed
- The daughters of D mesons are removed from the set of associated charged particles.

Once the above criteria are satisfied, both D mesons and associated charged tracks should pass the kinematical cuts, also similar to those applied in the correspondent experiment

selected for the comparison. Several experiments from different collaborations were considered, and the output from predictions and experiments will be presented in the next sections.

6.4.1 D-h correlations in p-p collisions at $\sqrt{s}$ = 7 TeV

In this part, correlation analyses are done with EPOSHQ event generator between D mesons (D^{*+}, D^{+} and D^{0} and their anti-particles) and charged particles (the most abundant ones are: protons, kaons, pions, muons, electrons and their anti-particles) generated in pp collisions at 7 TeV. D mesons were considered in the 3 p_T ranges [3-5], [5-8] and [8-16] GeV/c. For the associated charged particles, the considered p_T ranges are [0.3-1], [1-99] and the integrated one [0.3-99] GeV/c. In the end, the distributions are normalised by the number of D mesons in the selected p_T range. D mesons should have a rapidity within the range $|y| < 0.5$, and charged particles should be within the pseudo-rapidity range $|\eta| < 0.8$. In this procedure, D mesons are correlated with all charged particles in each event. The differences in azimuthal angle and pseudo-rapidity are computed. Finally, only pairs with $|\Delta\eta| < 1$ are considered. The obtained distributions with EPOSHQ are presented in blue circles in figure.6.14.

The comparison is performed with respect to the measurements done by the ALICE experiment (presented in black squares in figure.6.14).

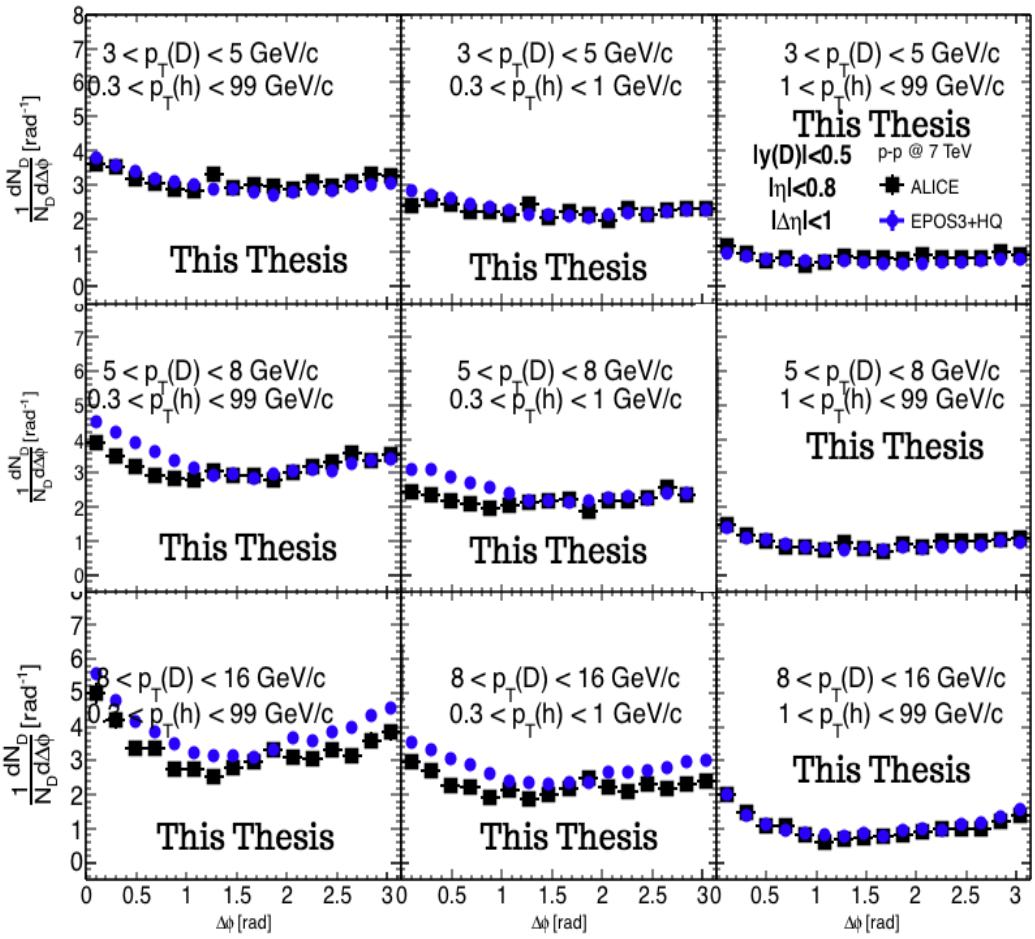

FIGURE 6.14: D-h correlations in pp collisions at $\sqrt{s}$ = 7 TeV : ALICE Data (black squares) vs EPOSHQ (blue cicles). The baseline is included.

As already stated, the predicted correlations with EPOSHQ and the measured ones from the ALICE experiment are presented in figure.6.14 in blue circles and black squares, respectively. From the distributions, one can notice a qualitative agreement between the predictions and the measurements. A more visible discrepancy appears at high p_T of D mesons and for the integrated p_T intervals of associated tracks, especially at smaller angles. The correlations obtained with EPOSHQ describes the data qualitatively well but not quantitatively. The estimated difference reaches an average varying from 2% up to 18%. Regardless of the differences, similar behaviour is observed for D-hadron correlations in both experimental measurements and theoretical predictions. A prominent peak is visible around smaller angles due to the formation of a jet of particles in the direction of the charm quark production. This is partially due to the mechanism called gluon splitting, which is expected to take place at energies of the order of the TeV, in addition to the contribution of pair creation. On the other hand, in the opposite direction of the produced charm quark, less charged particles are produced around the angle $\pi/2$.

A baseline subtraction was performed to the previous distributions (figure.6.14). The newly

obtained correlations from EPOSHQ predictions and measurements from ALICE, are presented in figure.6.15. Similar conclusions can be deduced from the comparison with subtracted baseline.

A discrepancy is observed at smaller angles, especially at larger angles for the three p_T ranges of D mesons and the integrated p_T of associated tracks. This can be partially due to the fluctuations of the experimental data and the predictions. However, the overall behaviour is similar and delivers the same information.

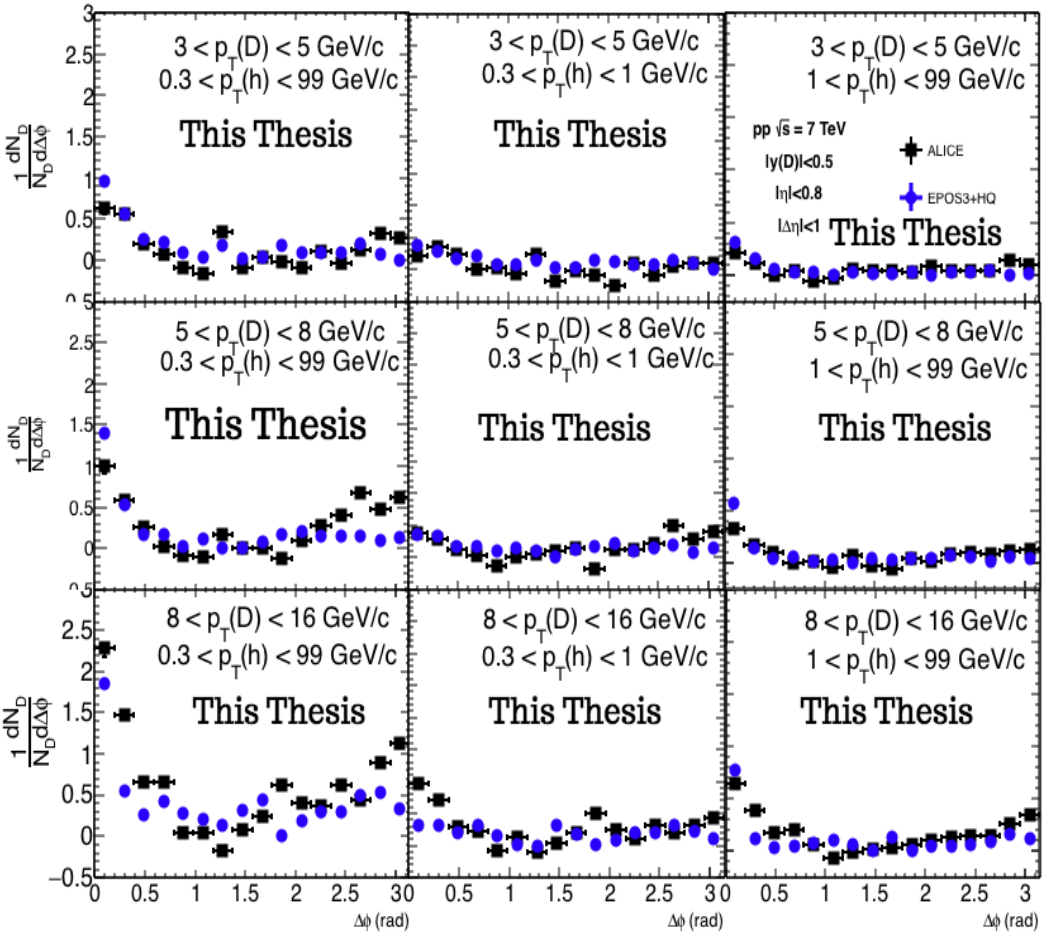

FIGURE 6.15: D-h correlations in pp collisions at $\sqrt{s}$ = 7 TeV : ALICE Data (black squares) vs EPOSHQ (blue cirles) with subtracted baseline.

With EPOS3 coupled to MC@sHQ, not only correlations between D mesons and charged hadrons can be extracted but D mesons during their different production stages including charm quarks, as well. Accordingly, we can get five distributions of correlations with the following species of heavy flavours / D mesons,

1. heavy quarks at creation (provided by EPOS)
2. heavy quarks after the propagation through the QGP (before hadronisation)
3. heavy mesons after hadronisation

4. heavy mesons after rescattering (by exploiting HQ and UrQMD)
5. heavy mesons provided directly from EPOS3 coming from the fragmentation of heavy quarks.

It is crucial to check whether the correlations with heavy quarks at different evolution stages will agree with the correlations performed with D mesons from EPOS. They are supposed to be identical given that heavy quarks at the creation level are themselves provided by EPOS before being exploited by the transport process HQ afterwards. The correlations distributions obtained for the 5 cases listed above are displayed in figure.6.16.

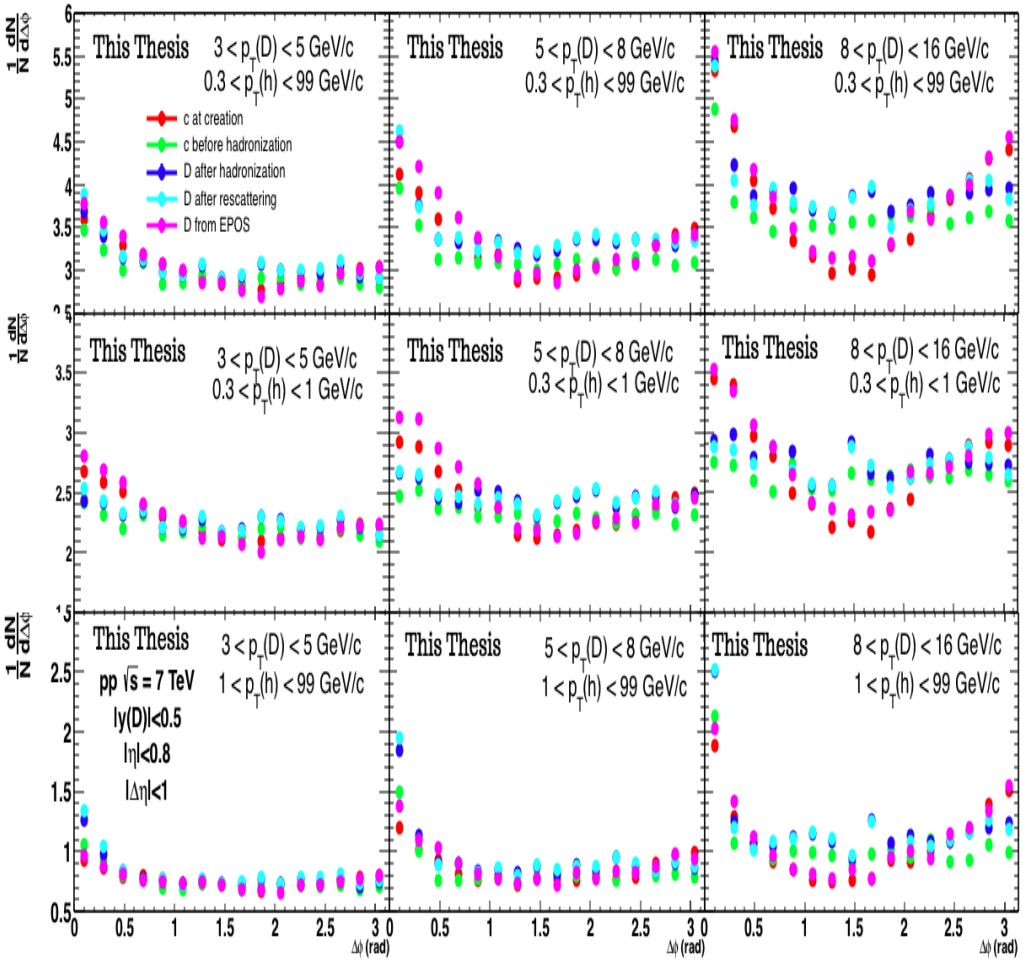

FIGURE 6.16: D-h correlations in pp collisions at $\sqrt{s}$ = 7 TeV with EPOS/EPOSHQ at different D/charm evolution stages : charm at creation (red), charm before hadronisation (green), D mesons after hadronisation (blue), D mesons after rescattering (cyan), D mesons from EPOS (magenta).

The magenta distribution represents the correlations between D mesons (from EPOS) and charged particles. The correlations between charged particles and charm quarks at creation are presented in red, charm quarks before hadronisation in green, D mesons after hadronisation in blue, and after rescattering with the medium in cyan.

One can notice that the distributions of c quarks at creation (red) and D mesons from pure EPOS (magenta) exhibit similar behaviour. It is reasonable since charm quarks at creation are themselves provided by EPOS. Thus, one can deduce that charm quarks follow the pattern of correlations since two peaks around $\Delta\phi = 0, \pi$ are present. The correlations with charm quarks before hadronisation and those with D mesons after hadronisation/rescatterings show similar distributions, but they follow different patterns (broader) with respect to the two previously discussed distributions. For the range 3< $p_T(c/D) <$ 5 GeV/c, the distributions do not show important enhancement at smaller angles, especially around π. This feature disappears at larger p_T. One can notice also that the correlations of charm quarks before/after hadronisation and D mesons after rescattering are strongly correlated with the charged particles compared to the distributions of charm quarks at creation/from EPOS. This is observed for the charged particles at low p_T (middle row of figure.6.16).

6.4.2 D-h correlations in pp collisions at $\sqrt{s} = 13$ TeV

At the beginning of this part, it is interesting to perform a theoretical comparison between the correlation distributions obtained in pp collisions at 7 TeV and those at 13 TeV using EPOSHQ.

Figure.6.17 shows correlation distributions extracted at 7 TeV (blue points) and those at 13 TeV (green points) where the baseline is preserved. Correlation distributions at 13 TeV are a little bit higher than those at 7 TeV which is better visualised in the integrated p_T range of associated charged particles.

This is probably due to the background and underlying events expected at higher energies and larger transverse momentum. Fluctuations are also getting larger with increasing p_T which is probably related to the use of samples with insufficient statistics.

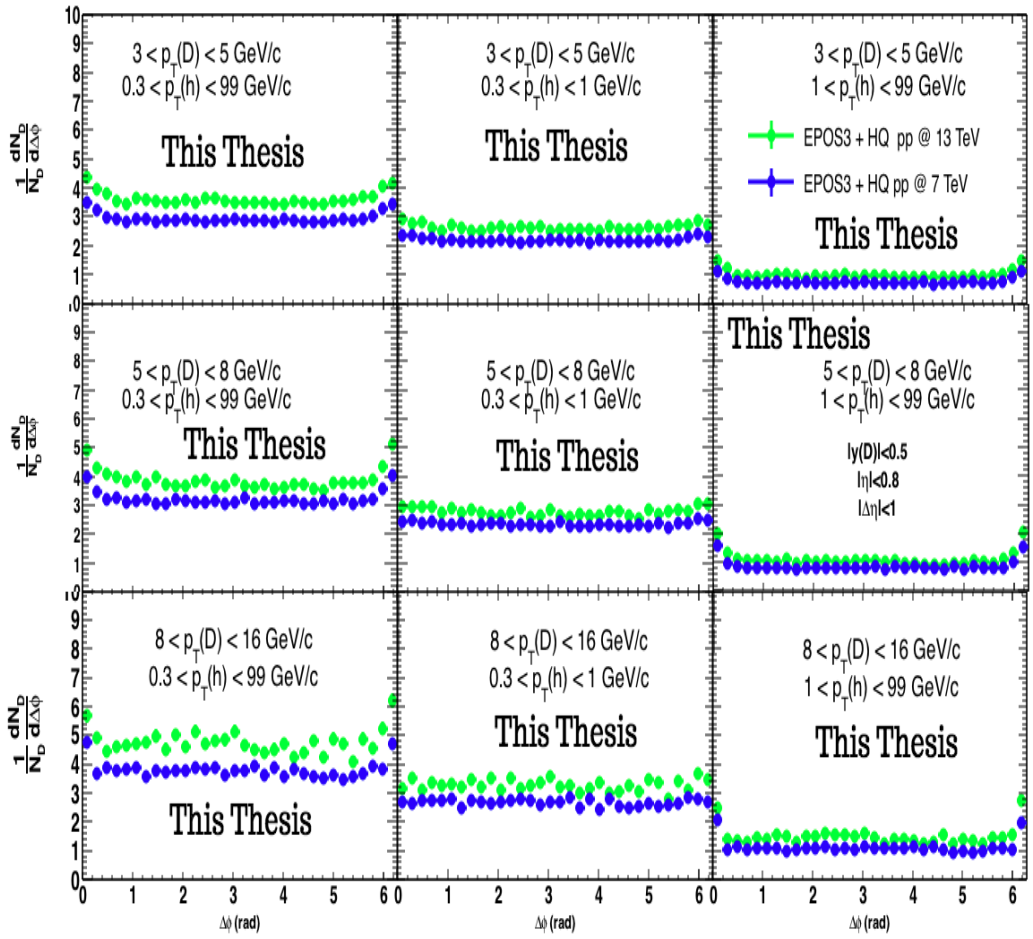

FIGURE 6.17: D-h correlations in pp collisions at $\sqrt{s}$ = 7 TeV (blue) versus 13 TeV (green) with EPOSHQ (including the baseline).

A different comparison is performed by subtracting the baseline in the distributions for both energies. The correspondent correlations are presented in figure.6.18. The difference disappears except for large p_T of D mesons where the fluctuations are dominant. This discrepancy does not prevent the conclusion that the physics principles and phenomena are similar in both energies except for the difference in underlying events, background and multiplicities.

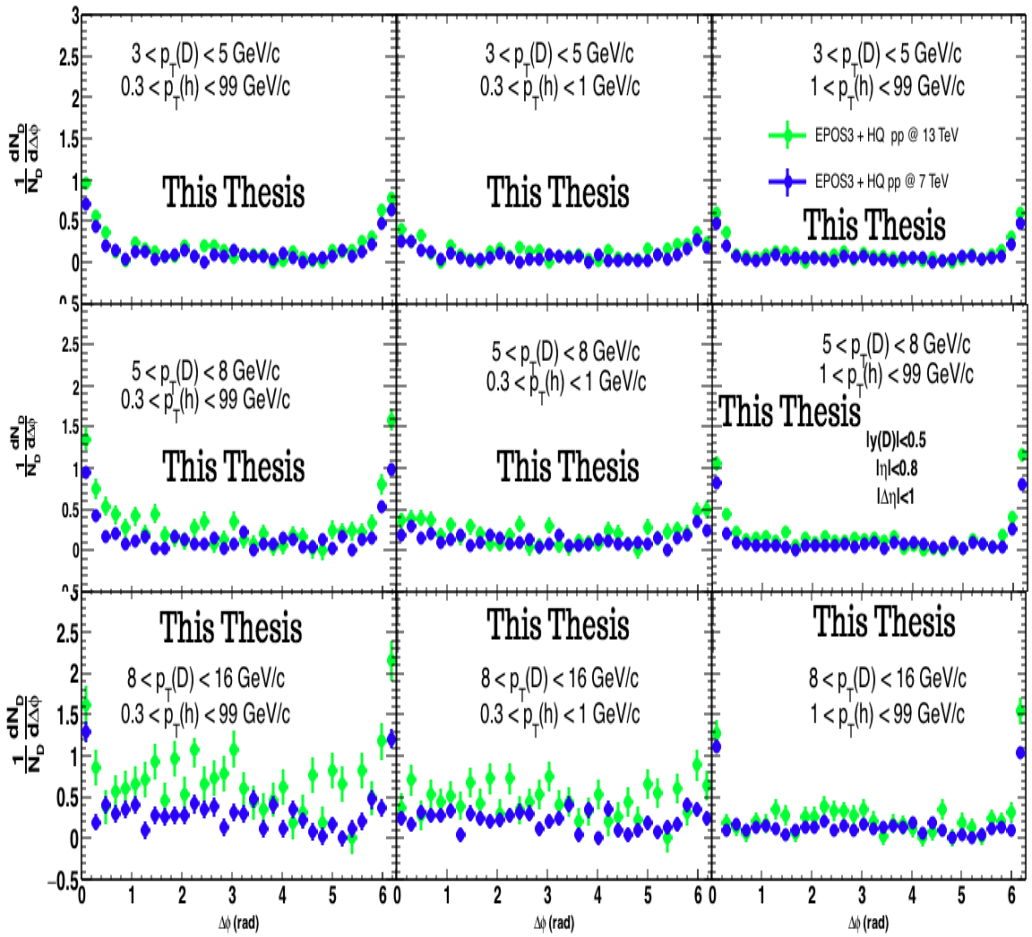

FIGURE 6.18: D-h correlations in pp collisions at $\sqrt{s}$ = 7 TeV (blue) versus 13 TeV (green) with EPOSHQ (subtracted baseline).

6.4.3 $D - \bar{D}$ correlations in pp collisions at $\sqrt{s}$= 7 TeV

Correlations between D and $\bar{D}$ mesons is another interesting study. It was performed at LHCb collaboration in pp collisions at $\sqrt{s}$ = 7 TeV [79] where different combinations of correlated pairs were considered in order to get D^+D^- and $D^0\bar{D}^0$ correlations distributions. EPOS was exploited to obtain the same combinations of D^+-D^- and D^0-$\bar{D}^0$ correlations in pp collisions at $\sqrt{s}$ = 7 TeV. For both experimental and theoretical analyses, the correlated pairs should be in the same event. Each time an event with a tagged D meson is found, the correspondent event is considered in the analysis. D mesons should be within the p_T range $3 < p_T < 12$ GeV/c and within a rapidity range $2 < y < 4$. Once these kinematical criteria are satisfied, the difference in the azimuthal angle (between D and $\bar{D}$) is computed. In these analyses, the concerned observable is the cross-section and not the number of the correlated pairs. The cross-section is defined experimentally by,

$$\sigma = \frac{N_{pair}}{L \times B_1 \times B_2} \tag{6.16}$$

where N_{pair} is the number of correlated pairs in the integrated range of $\Delta\phi$. L is the integrated luminosity considered by LHCb. B_1 is the fragmentation fraction of the charm quarks for the considered D meson (D^+, D^0). B_2 is the branching ratio in the considered decay channel ($K\pi\pi$ for D^+ and $K\pi$ for D^0). The original equation in the LHCb paper included the efficiency which should be ideal (100%) when an event generator is used.

The resulting correlation distributions for D^+-D^- and $D^0\bar{D}^0$ are presented in figure.6.19 and figure.6.20, respectively. The blue histogram refers to the predictions from EPOS, and the green one refers to the measurements from LHCb.

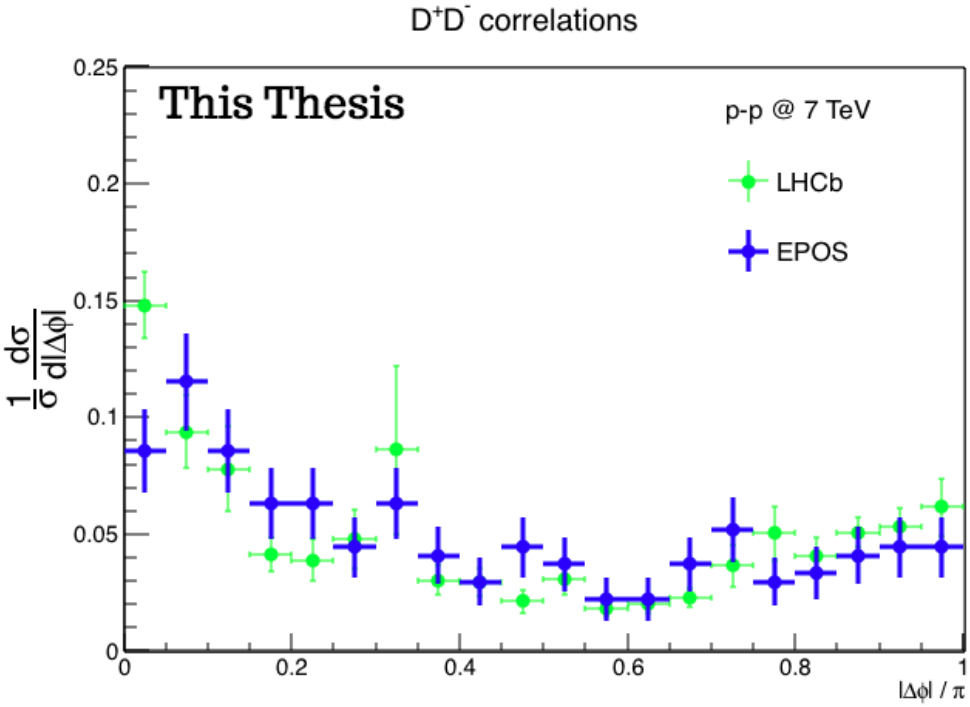

FIGURE 6.19: D^+-D^- correlations in pp collisions at $\sqrt{s}$ = 7 TeV from LHCb data (green) vs EPOS (blue).

Concerning D^+-D^- correlations, in both data and predictions, the distributions are qualitatively similar. The data is described reasonably well by EPOS within uncertainties. This shape shows that charm quarks are produced mainly via gluon splitting where the angle between the created pairs is small and via flavour creation where the angle can be larger or back-to-back with an angle around π. This is clear through the existence of a prominent peak around $\Delta\phi = 0$ and an enhancement around $\Delta\phi = \pi$. Otherwise, the production of D mesons at small angles is underestimated by EPOS. For the rest of the $\Delta\phi$ range, the production is reasonably described.

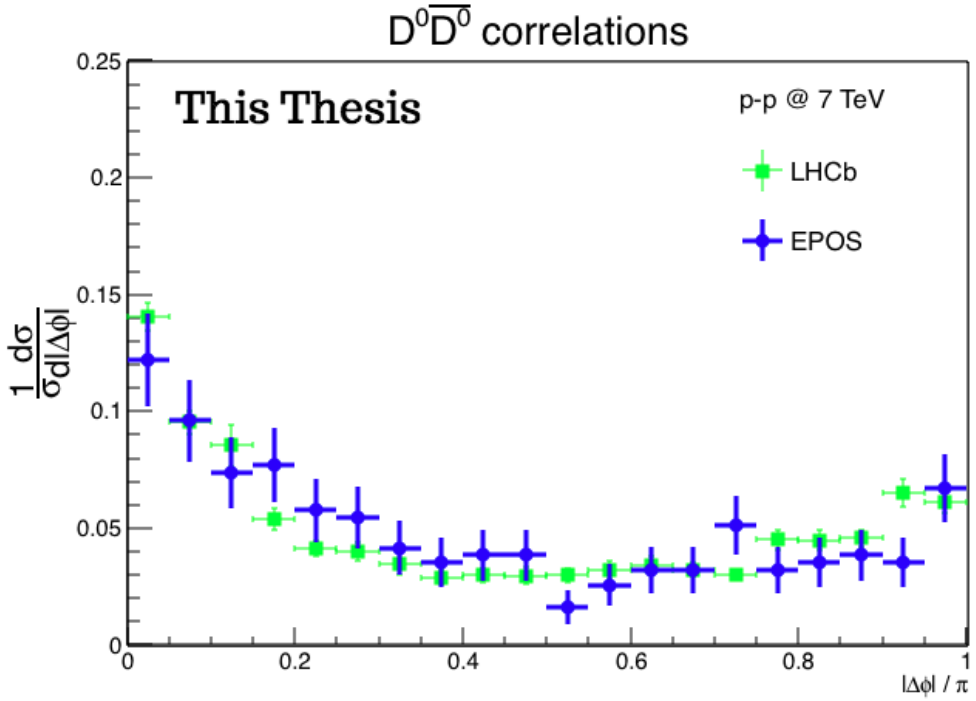

FIGURE 6.20: D^0-$\bar{D}^0$ correlations in pp collisions at $\sqrt{s}$ = 7 TeV with data from LHCb (green) vs EPOS (blue).

As for $D^0\bar{D}^0$, the shape of the correlations from LHCb is nicely described by EPOS. In this case, the data favours the production of charm quarks via gluon splitting (production with small angles) in addition to the contribution of flavour creation (enhancement around $\Delta\phi = \pi$). One can also deduce that D^+ and D^0 (and their antiparticles) behave similarly.

6.4.4 D-h and $D - \bar{D}$ correlations in pp collisions at 500 GeV

In this part, the simulations were performed using EPOS event generator to obtain correlations of D^{*+}-D^{*-} and D^* with charged particles in pp collisions at 500 GeV to compare the predictions from EPOS to the preliminary results from the STAR experiment provided by Jaroslav and Petr [83]. In these analyses, D^* mesons were correlated with charged particles in pp collisions at 500 GeV. The same kinematical cuts, considered in data, are applied where D mesons should have a transverse momentum within the range $8 < p_T < 20$ GeV/c and the charged particles should be with $p_T > 0.5$ GeV/c and within a pseudorapidity range $|\eta| < 1$.

The obtained D-hadron correlation distribution from EPOS simulations is presented in figure.6.21 (blue points) compared to the preliminary STAR results (green points). The baseline is already subtracted in both cases.

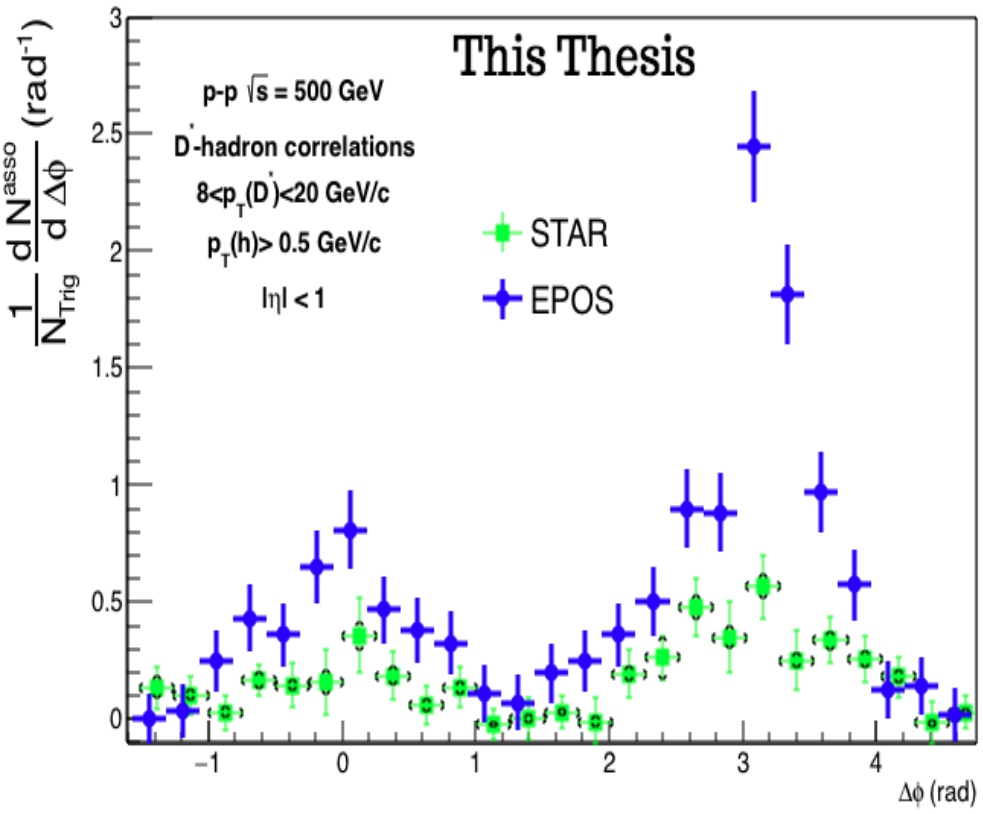

FIGURE 6.21: D-h correlations in pp collisions in pp@500 GeV with EPOS (blue) versus Preliminary STAR (green).

The correlation distribution from STAR preliminary measurements exhibits a different quantitative behaviour compared to the observed one with EPOS. In the latter, the away side peak around $\Delta\phi = \pi$ is larger in magnitude with respect to the near side peak at $\Delta\phi = 0$. EPOS reproduces the general behaviour observed in the experimental data but with a larger magnitude, especially around the peaks. This discrepancy is probably due to the difference in the number of charged particles associated with each D meson between predictions and measurements. Regardless of the difference, the behaviour from predictions suggests that the production of heavy flavour through flavour creation is more important than gluon splitting at RHIC energies. For what concerns the distribution from measurements, it shows also that both mechanisms (flavour creation and gluon splitting) are involved but not with similar magnitude as in EPOS predictions.

Concerning the correlations between D mesons and their antiparticles $\bar{D}$, D mesons are required to be in the range $2.5 < p_T < 20$ GeV/c and $|\eta| < 1$. The resulting correlation distribution from EPOS in pp collisions at 500 GeV is symbolised by the blue points in figure.6.22 while the experimental data are presented in green points.

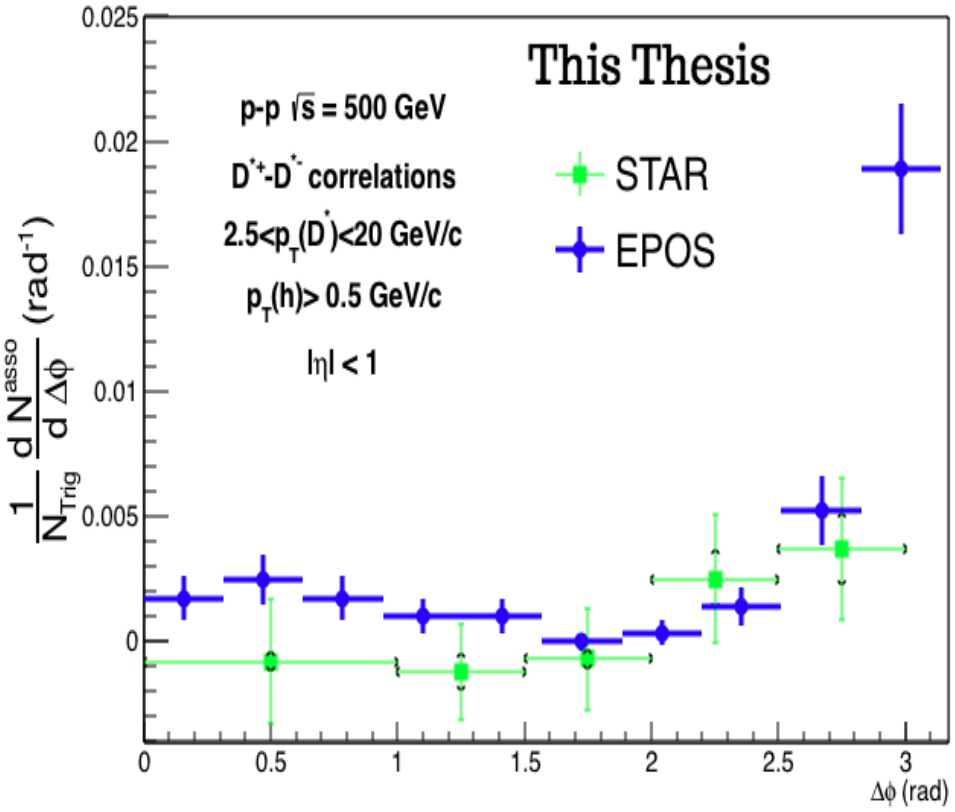

FIGURE 6.22: $D^{*+} - D^{*-}$ correlations in pp collisions in pp collisions at 500 GeV with EPOS (blue) versus STAR Preliminary (green).

There is a peak around $\Delta\phi = \pi$ in the distribution obtained with EPOS which is closer in magnitude to the enhancement observed in the STAR preliminary results. This means that the production of D mesons through pair creation (back-to-back) is the dominant production mechanism in this order of energy (GeV) while gluon splitting (production with smaller angles) is dominant (and flavour excitation with smaller effect) at higher energies (TeV) as it was deduced from LHCb results shown in the previous section.6.4.3. Regarding the comparison between the two curves, EPOS predicts the behaviour of the distribution from STAR, but it underestimates the data at larger angles and with less degree around $\Delta\phi = 0$.

6.4.5 D-h correlations in $p - \bar{p}$ collisions at $\sqrt{s}$= 1.96 TeV

In this part, correlations between D^0-D^{*-} and D^+-D^{*-} are simulated with EPOS in $p - \bar{p}$ collisions at $\sqrt{s}$= 1.96 TeV and the resulting distributions are compared to those measured within CDF collaboration at the Tevatron [82]. In these analyses, the p_T of D^{*-} are selected to be in the range [5.5, 20] GeV/c, D^0 in the range [5.5, 20] GeV/c, and D^+ in the range [7, 20] GeV/c. All correlated D mesons should be within the rapidity range $|y| < 1$. These cuts are also applied for the simulations with EPOS. The distributions from the experimental data and predictions from EPOS are presented in figure.6.23.

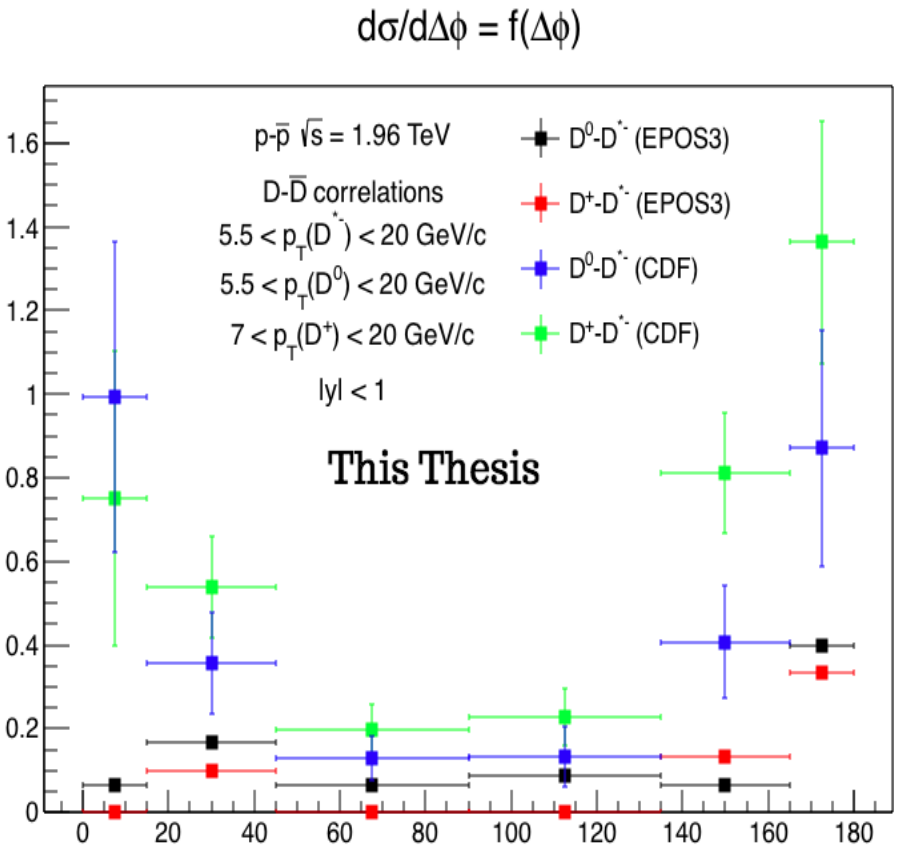

FIGURE 6.23: $D-\bar{D}$ correlations in $p-\bar{p}$ collisions at 1.96 TeV with EPOS3 : D^0-D^{*-} (black squares) and D^+-D^{*-} (red squares) versus CDF : D^0-D^{*-} (blue squares) and D^+-D^{*-} (green squares).

EPOS underestimates the data, especially at smaller angles, although the general behaviour is similar to the measured distributions. The sample used to simulate this collision system was not the best one concerning statistics which can be the reason for this large difference between data and predictions from EPOS. Another reason is that the experimental data were extracted from the HEP data website, but they are not up-to-date compared to the included ones in the paper.

6.4.6 D-h correlations in p-Pb collisions at $\sqrt{s} = 5.02$ TeV

In this final part, EPOSHQ is again exploited to simulate correlations in p-Pb collisions at $\sqrt{s_{NN}} = 5.02$ TeV. The analysis strategy is similar to the one applied in pp collisions at 7 TeV except for the rapidity interval ($-0.96 < y_{cms} < 0.04$). Two sets of experimental data are available to perform the comparison. The first is the collected data of 2013 at CERN-LHC with ALICE experiment where the statistics were not large enough, and it allowed to obtain correlations only at intermediate and high p_T ranges. The predictions from EPOSHQ as well as the measurements from the 2013 data are presented by the black squares and blue circle, respectively, in figure.6.24.

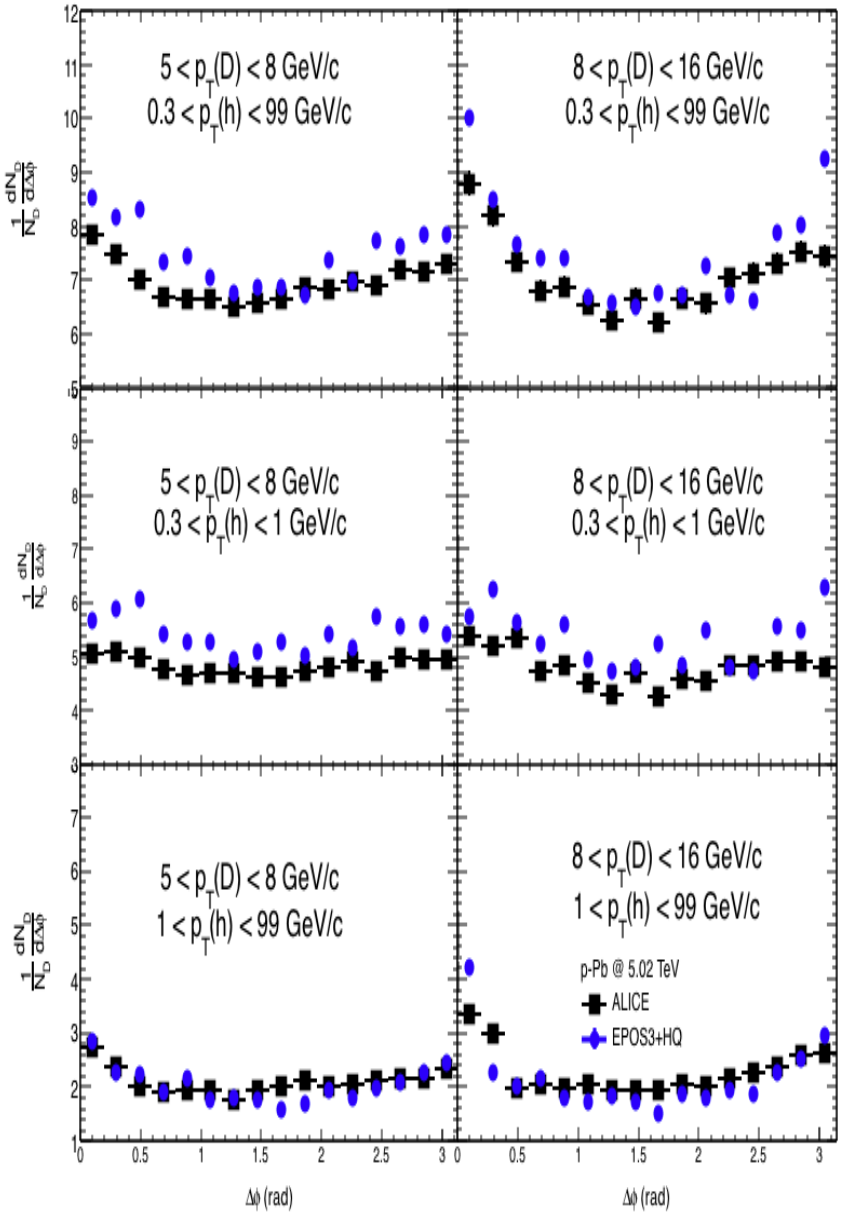

FIGURE 6.24: D-h correlations in p-Pb collisions at $\sqrt{s}$ = 5.02 TeV : ALICE (black squares) vs EPOSHQ (blue circles).

The considered kinematical ranges for D mesons are 5 to 8 GeV/c and 8 to 16 GeV/c presented in the left and right columns, respectively. For the associated tracks, they were considered in the integrated range $p_T > 0.3$ GeV/c (top row) and the two sub-ranges 0.3 to 1 GeV (middle row) and $p_T > 1$ GeV/c (bottom row). The behaviour of correlation distributions generated by EPOSHQ in p-Pb collisions has similar features as those observed in pp collisions. In another word, in both pp and p-Pb collisions, the distributions can be visualised as a baseline and two peaks, a near side and an away side around $\Delta\phi = 0$ and π, respectively. The interesting difference with respect to pp at 7 TeV data lies in the level of the baseline. In p-Pb at 5 TeV, the baseline (representing the underlying events) is higher than

the one observed in the distributions measured in pp at 7 TeV. This is reasonable because of the high produced multiplicity in p-Pb collisions. For the same reason, the magnitude of the peaks or the number of associated particles with one trigger (D meson) is larger compared to the measured one in pp at 7 TeV.

The distributions from EPOSHQ reproduce qualitatively the distributions from measurements. The distributions from data are underestimated at low p_T of associated particles, but the agreement is more promising at high p_T of associated particles. The discrepancy (underestimation of the data) is large around the peak positions in the integrated p_T range of associated particles and over the whole $\Delta\phi$ range for associated particles with $0.3 < p_T <$ 1 GeV/c. These observations are relevant for intermediate and high p_T of D mesons.

In the second data set, collected during 2016 by ALICE experiment for p-Pb collisions, the statistics were large enough to obtain correlations in a wider p_T range, down to 3 GeV/c and up to 24 GeV/c and the considered sub-ranges are 3 to 5 GeV/c, 5 to 8 GeV, 8 to 16 GeV/c and 16 to 24 GeV/c shown in the figure.6.25 and figure.6.26 from the left to the right columns, respectively. Two sets of associated particle thresholds were also considered. The distributions obtained by exploiting the new data with the standard thresholds of associated particles are presented in figure.6.25 with the standard ranges of associated tracks : $p_T >$ 0.3 GeV/c (top row), $0.3 < p_T < 1$ GeV (middle row) and $p_T > 1$ GeV/c (bottom row). The extracted distributions with the new thresholds are shown in figure.6.26 and the considered ranges of associated tracks are $1 < p_T < 2$ GeV/c (top row), $2 < p_T < 3$ GeV/c (middle row) and $p_T > 3$ GeV/c (bottom row). The distributions from the experimental measurements are presented in black squares and those from EPOSHQ simulations in blue points.

The new thresholds give a better qualitative agreement between the data and EPOSHQ predictions compared to the distributions obtained with the standard thresholds. One can notice fluctuations for larger transverse momentum which might be related to the lack of statistics in the EPOSHQ sample. From the comparison between the correlation distributions in p-Pb and pp collisions, one can deduce that the underlying events and near/away side peaks are similar features between the two collisional systems.

The difference lies in the magnitude and the baseline level as mentioned earlier in this section. The reason is not only due to the difference in multiplicity, but it may come from the small QGP droplet created in p-Pb collisions, although the impact looks minor it is not negligible as well. The away side peak, for example, is getting visible and clear only at higher D mesons p_T as it was noticed in pp collisions at 7 TeV.

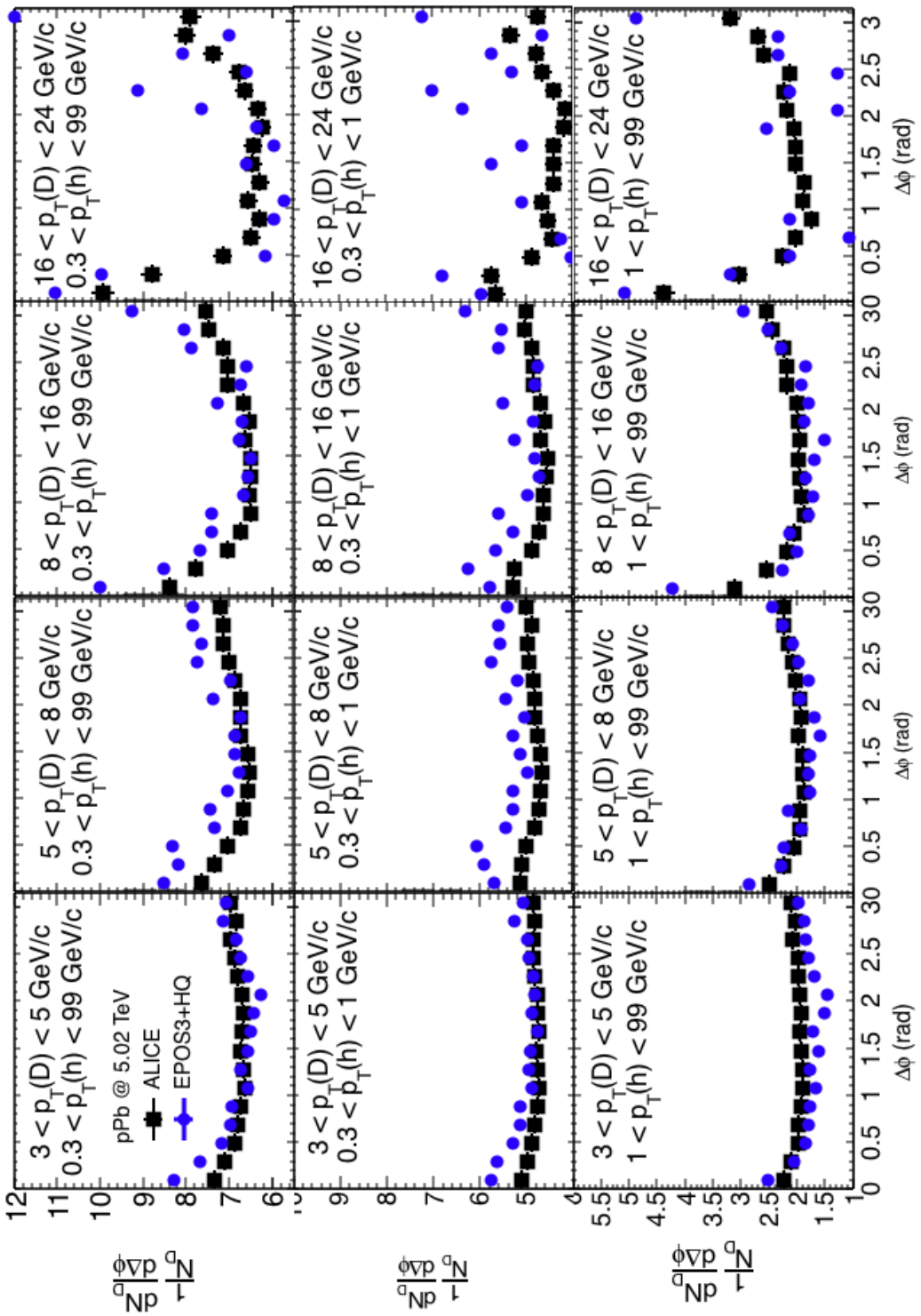

FIGURE 6.25: D-h correlations in p-Pb collisions at $\sqrt{s}$ = 5.02 TeV (2016 data) : ALICE (black squares) vs EPOSHQ (blue circles) with the standard thresholds of associated particles.

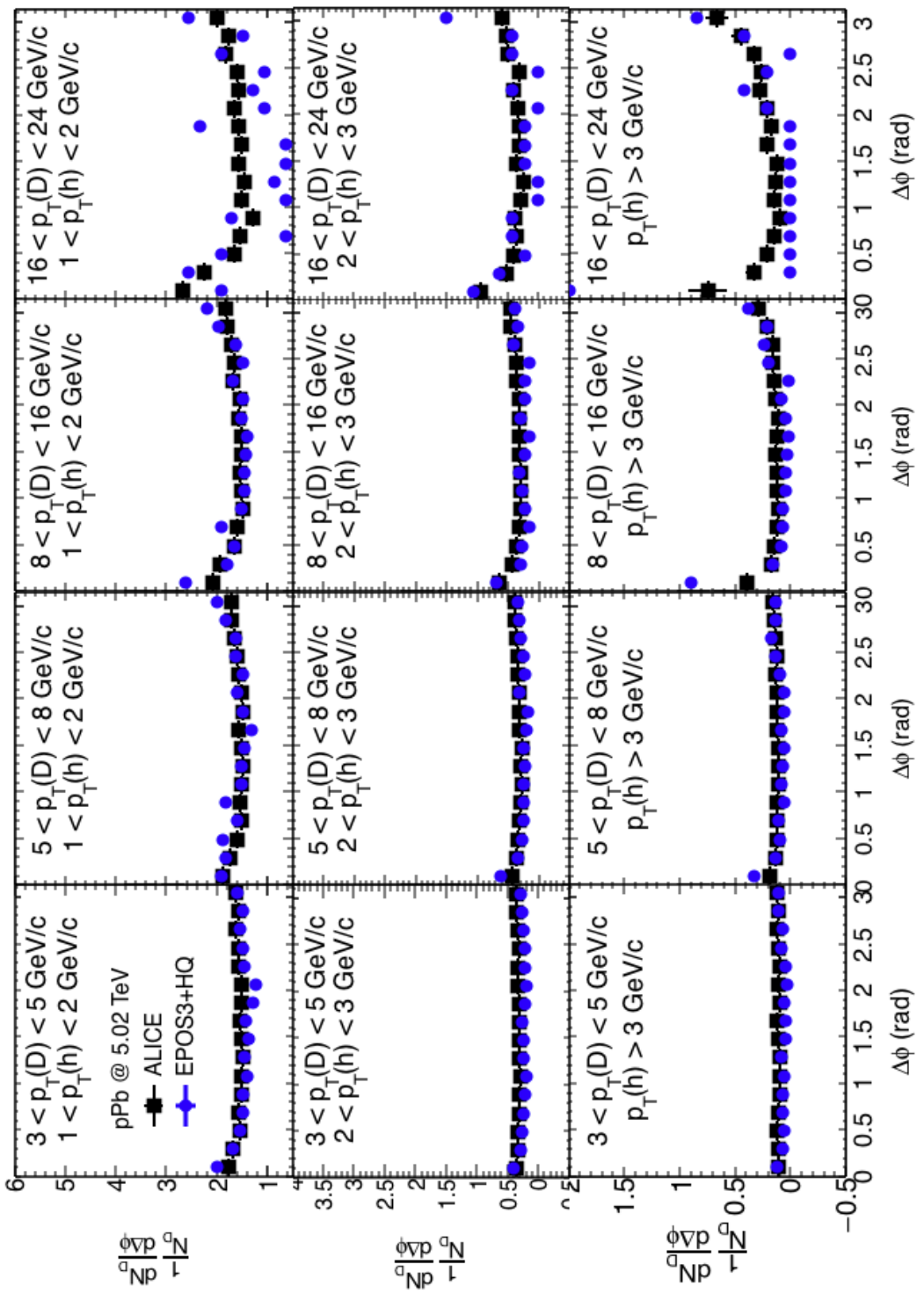

FIGURE 6.26: D-h correlations in p-Pb collisions at $\sqrt{s}$ = 5.02 TeV (2016 data) : ALICE (black squares) vs EPOSHQ (blue circles) with the new thresholds of associated particles.

6.5 Chapter conclusion

EPOS is a successful event generator thanks to the integrated "Parton-Based Gribov-Regge Theory" in addition to other implemented processes starting from the well defined initial conditions in addition to the principles of parton ladders, core-corona, hydrodynamic evolution and hadronisation. EPOS3 was also coupled with the package MC@sHQ to simulate heavy flavours which is the centre topic of this thesis. In this scope, several simulations for collisional systems (pp, $p-\bar{p}$, p-Pb) at different energies (500 GeV and 7, 13, 1.96, 5.02 TeV) were performed in order to extract comparable predictions to the measured distributions from experiments. Correlation distributions from predictions were found to be in reasonable qualitative agreement with the experimental output. Otherwise, no perfect quantitative match was established which dictates that more efforts are needed from both theory and experiments.

Chapter 7

Conclusions and Perspectives

In the first part of the manuscript, the experimental results on azimuthal correlations between D^{*+} mesons and charged hadrons are discussed. These correlations are obtained based on an event-by-event analysis in proton-proton collisions at $\sqrt{s} = 13$ TeV with the ALICE detector at the LHC. An improved analysis strategy compared to the one in pp at 7 TeV, is applied. The difference lies in performing a pool-by-pool correction instead of exploiting the integrated pool of events. The topological cut DCA_{XY} applied on associated charged particles was 1 cm instead of 0.25 cm. D^{*+} mesons were reconstructed via their hadronic channel in the range $3 < p_T < 16$ GeV/c. The associated tracks were reconstructed with a $p_T > 0.3$ GeV/c. The distributions are corrected for the efficiency, the contamination due to the presence of secondary charged particles, the B feed-down contribution and finally, they were normalised to the number of triggers. The final correlation distributions exhibited the expected behaviour already observed at 7 TeV. The distributions are characterised by a baseline, a near-side peak around $\Delta\phi = 0$ and an away-side peak around $\Delta\phi = \pi$. Both peaks are prominent at larger p_T. These observations suggest that a large number of particles (jet), strongly correlated at high p_T, are produced in the same direction as D mesons. In the opposite direction, particles are produced but weakly correlated with each other. The baseline of the distributions is a reflection of the underlying event. Since the correlations present the number of associated tracks to one D meson, it is reasonable that the baseline is dependent on the p_T of associated tracks. This is confirmed from the comparison between 7 and 13 TeV. The distributions at 13 TeV show a bit higher baseline compared to those at 7 TeV. This can be explained by the fact that larger multiplicities are reached at higher energies.

Concerning the theoretical part of this thesis, the event generators PYTHIA8 and EPOS3 are used to obtain correlations between D mesons and their anti-particles in p-p collisions at $\sqrt{s} = 200$ GeV, 7 TeV and between D mesons and charged particles in p-p collisions at $\sqrt{s} = 7$, 13 TeV and p-Pb collisions at $\sqrt{s_{NN}} = 5.02$ TeV. The adopted analysis strategy is similar to one applied in experimental measurements. Consequently, the same kinematical cuts and selection criteria are considered. From PYTHIA8 simulations, at centre of mass energies of the order of the TeV, heavy quarks are produced mostly via the gluon splitting mechanism and at energies of the order of the GeV, the dominant production mechanism

is pair creation. On the other side and according to the performed comparisons for different observables, heavy mesons at the hadron level reproduce the pattern of heavy quarks at the parton level. It was found also that the initial and final state radiation (ISR/FSR), as well as colour reconnection (CR), do not have a significant impact on the correlations. This was not the case for Multiple Parton Interaction (MPI) where its absence minimises the gluon splitting which is an important source of heavy flavours at higher energies. For the EPOS3/EPOSHQ event generator, the comparisons were performed between the predictions and the experimental data. The predictions describe the data qualitatively well. In p-p collisions at 7 TeV, a better agreement was established with distributions of a subtracted baseline. This indicates that the difference between data and predictions is due to a different treatment of the underlying events. For what concerns the comparison between distributions in p-p collisions at 7 and 13 TeV, it is clear that the underlying events (the baseline) were a bit higher at 13 TeV where the multiplicity is expected to be larger. Predictions from EPOS describe reasonably well the D^0-$\bar{D}^0$ / D^+-D^- correlations in p-p collisions at $\sqrt{s} =$ 7 TeV measured at LHCb collaboration. EPOS predictions describe also well the correlations D^{*+}-D^{*-} in p-p collisions at $\sqrt{s} = 500$ GeV measured at STAR collaborations but it fails to describe the correlations between D* mesons and charged particles in the same energy. Concerning the comparison between data and EPOSHQ predictions in p-Pb collisions at 5.02 TeV, only a qualitative agreement is established.

The lesson learned from the studies presented in this manuscript suggests the need of some improvements to the modelling side, such as a correct implementation of the D* meson in EPOSHQ. In addition, it seems mandatory to carry out a detailed study of the multiplicity and underlying events difference for various energy scales. For the experimental side, the consideration of different analysis techniques is advised. For instance, it is crucial to do the analysis for more than one dimension. The D* invariant mass needs to be processed differently at least by considering the left side band. In addition, D-hadron correlations are an extremely important measurement but not sufficient, $D - \bar{D}$ correlations are needed to get complementary information to do a correct estimation of charm production mechanisms. Finally, the upgrade of the ALICE detector with the inclusion of the new state-of-the-art performance silicon tracker (ITS2) and the new TPC capable of continuous readout will take the measurements several steps ahead enabling the experiment to perform the direct investigation of $D - \bar{D}$ azimuthal correlations and high precision studies on the D-h sector.

Appendix A

Run list for p-p collisions at 13 TeV

Period	Number of selected events (Millions)	Run list
LHC16d_pass1	12.15	252330, 252326, 252325, 252322, 252319, 252317, 252310, 252271, 252248, 252235
LHC16e_pass1	50.37	253591, 253589, 253563, 253530, 253529, 253517, 253488, 253482, 253481, 253478, 253437
LHC16g_pass1	27.92	254332, 254331, 254330, 254304, 254303, 254302, 254293, 254205, 254204, 254199, 254193, 254178, 254175, 254174, 254149, 254147, 254128
LHC16h_pass1	69.52	255467, 255466, 255465, 255463, 255447, 255442, 255440, 255421, 255420, 255419, 255418, 255415, 255407, 255402, 255398, 255352, 255351, 255350, 255283, 255280, 255276, 255275, 255256, 255255, 255253, 255252, 255251, 255249, 255248, 255247, 255242, 255240, 255182, 255181, 255180, 255177, 255176, 255174, 255173, 255171, 255167, 255162, 255159, 255154, 255111, 255091, 255086, 255085, 255082, 255079, 254984, 254983, 254654, 254653, 254652, 254651, 254649, 254648, 254646, 254644, 254640, 254632, 254630, 254629, 254621, 254606, 254604
LHC16j_pass1	45.06	256418, 256417, 256415, 256373, 256372, 256371, 256368, 256366, 256365, 256364, 256363, 256362, 256361, 256356, 256311, 256309, 256307, 256302, 256299, 256297, 256295, 256292, 256290, 256289, 256287, 256284, 256283, 256282, 256281, 256231, 256228, 256227, 256223, 256219

LHC16k_pass1	133.49	258537, 258499, 258477, 258456, 258454, 258452, 258426, 258393, 258391, 258387, 258359, 258336, 258332, 258307, 258306, 258303, 258302, 258301, 258299, 258278, 258274, 258273, 258271, 258270, 258258, 258257, 258256, 258204, 258203, 258202, 258198, 258197, 258178, 258117, 258114, 258113, 258109, 258108, 258107, 258063, 258062, 258060, 258059, 258053, 258049, 258045, 258042, 258041, 258039, 258019, 258017, 258014, 258012, 258008, 258003, 257992, 257989, 257986, 257979, 257963, 257960, 257957, 257939, 257937, 257936, 257892, 257855, 257853, 257851, 257850, 257804, 257803, 257800, 257799, 257798, 257797, 257773, 257765, 257757, 257754, 257737, 257735, 257734, 257733, 257727, 257725, 257724, 257697, 257694, 257692, 257691, 257689, 257688, 257687, 257685, 257684, 257682, 257644, 257642, 257636, 257635, 257632, 257630, 257606, 257605, 257604, 257601, 257595, 257594, 257592, 257590, 257588, 257587, 257566, 257562, 257561, 257560, 257541, 257540, 257539, 257537, 257531, 257530, 257492, 257491, 257490, 257488, 257487, 257474, 257468, 257457, 257433, 257364, 257358, 257330, 257322, 257320, 257318, 257260, 257224, 257209, 257206, 257204, 257144, 257141, 257139, 257138, 257137, 257136, 257100, 257095, 257092, 257086, 257084, 257082, 257080, 257077, 257028, 257026, 257021, 257012, 257011, 256944, 256942, 256941, 256697, 256695, 256694, 256692, 256691, 256684, 256681, 256677, 256676, 256658, 256620, 256619, 256592, 256591, 256589, 256567, 256565, 256564, 256562, 256560, 256557, 256556, 256554, 256552, 256514, 256512, 256510, 256506, 256504
LHC16l_pass1	40.66	259888, 259868, 259867, 259866, 259860, 259842, 259841, 259822, 259789, 259788, 259781, 259756, 259752, 259751, 259750, 259748, 259747, 259713, 259711, 259705, 259704, 259703, 259700, 259697, 259668, 259650, 259649, 259477, 259473, 259396, 259395, 259394, 259389, 259388, 259382, 259378, 259342, 259341, 259340, 259339, 259336, 259334, 259307, 259305, 259303, 259302, 259274, 259273, 259272, 259271, 259270, 259269, 259264, 259263, 259261, 259257, 259204, 259164, 259162, 259118, 259117, 259099, 259096, 259091, 259090, 259088, 258964, 258962, 258923, 258919

LHC16o_pass1	33.34	264035, 264033, 263985, 263984, 263981, 263978, 263977, 263923, 263920, 263917, 263916, 263905, 263866, 263863, 263810, 263803, 263793, 263792, 263790, 263787, 263786, 263785, 263784, 263744, 263743, 263741, 263739, 263738, 263737, 263691, 263690, 263682, 263663, 263662, 263657, 263654, 263652, 263647, 263529, 263497, 263496, 263490, 263487, 263332, 263331, 262858, 262855, 262853, 262849, 262847, 262844, 262842, 262841, 262778, 262777, 262776, 262768, 262760, 262727, 262725, 262723, 262719, 262717, 262713, 262708, 262706, 262705, 262428, 262426, 262425, 262424
LHC16p_pass1	21.03	264347, 264346, 264345, 264341, 264336, 264312, 264306, 264305, 264281, 264279, 264277, 264273, 264267, 264266, 264265, 264264, 264262, 264261, 264260, 264259, 264238, 264235, 264233, 264232, 264198, 264197, 264194, 264190, 264188, 264168, 264164, 264139, 264138, 264137, 264129, 264110, 264109, 264086, 264085, 264082, 264078, 264076

TABLE A.1: Run lists and the associated number of events in pp collisions at 13 TeV.

Appendix B

Topological cuts

Trigger mask	kINT7
Trigger class	CINT7
Use of physics selection	kTRUE
Use of centrality	kFALSE
Require sigma to vertex (esd tracks)	kFALSE
Require TPC refit (esd tracks)	kTRUE
Require ITS refit (esd tracks)	kTRUE
Cluster requirement ITS (esd tracks)	kSPD (kAny)
Min DCA to vertexXY (esd tracks)	0.
p_T range (esd tracks)	[0.3 - 1e10] GeV/c
Require sigma to vertex (soft pion)	kFALSE
Require TPC refit (soft pion)	kFALSE
Require ITS refit (soft pion)	kTRUE
Cluster requirement ITS (soft pion)	kSPD (kAny)
p_T range (soft pion)	[0-1e10] GeV/c
Use PID	kTRUE
Sigma TPC (PID)	3
Sigma TOF (PID)	3
Pile up rejection	kTRUE

TABLE B.1: Additional selection cuts applied on D^{*+} candidates measured in minimum bias pp collisions at 13 TeV.

	3-4	4-5	5-6	6-7	7-8	8-10	10-12	12-16	16-20	20-24	24-36
inv. mass [GeV]	0.032	0.032	0.18	0.18	0.18	0.058	0.058	0.074	0.37	0.37	0.37
dca [cm]	0.04	0.07	0.1	0.1	0.1	0.2	0.2	0.6	0.8	0.8	0.6
$cos\theta^*$	0.8	0.9	1.	1.	1.	1.	1.	1.0	1.0	1.0	1.0
$p_T(K)$ [GeV/c]	1.	1.	1.	1.	1.1	0.3	0.3	0.3	0.3	0.3	0.4
$p_T(\pi)$ [GeV/c]	1.	1.	1.	1.	1.1	0.3	0.3	0.3	0.3	0.3	0.4
d0(K) [cm]	0.06	0.07	0.1	0.1	0.12	0.15	0.15	0.15	0.35	0.6	0.5
d0(π) [cm]	0.06	0.07	0.1	0.1	0.12	0.15	0.15	0.15	0.35	0.6	0.5
d0xd0 [cm^2]	-0.000065	0.0001	0.0005	0.001	0.001	0.01	0.01	0.06	0.06	0.01	0.1
$cos\theta_{Point}$	0.9	0.9	0.9	0.7	0.6	0.5	0.7	0.5	0.1	0.1	0.7
inv. mass half width of D^{*+} [GeV]	0.3	0.3	0.3	0.3	0.3	0.3	0.3	0.3	0.3	0.3	0.1
half width of $M(K\pi\pi) - M(D0)$ [GeV]	0.1	0.1	0.1	0.1	0.1	0.1	0.1	0.1	0.1	0.1	0.1
Pt_{Min} of π_s [GeV/c]	0.05	0.05	0.05	0.05	0.05	0.05	0.05	0.05	0.05	0.05	0.05
Pt_{Max} of π_s [GeV/c]	100	100	100000	100	100	100	100	100	100	100	100
theta [rad]	0.5	0.5	0.5	0.5	0.5	0.5	0.5	1.	1	1.	1.
$\lvert cos\theta_{Point}XY\rvert$	0.	0.	0.	0.	0.	0.	0.	0.	0.	0.	0.
NormDecayLenghtXY	0.	0.	0.	0.	0.	0.	0.	0.	0.	0.	0.

TABLE B.2: Topological cut values for D^{*+} in the considered p_T bins in pp collisions at 13 TeV.

η	0.8
Require Sigma To Vertex (esd track cuts)	kFALSE
RequireTPCRefit (esd track cuts)	kTRUE
RequireITSRefit (esd track cuts)	kFALSE
MinNClustersTPC (esd track cuts)	70
MinNClustersITS (esd track cuts)	3
MaxChi2PerClusterTPC (esd track cuts)	4
MaxDCAToVertexZ (esd track cuts)	1 [cm]
MaxDCAToVertexXY (esd track cuts)	1 [cm]
p_T Range (esd track cuts)	[0.3-1e10] GeV/c
η range (esd track cuts)	[-0.8,0.8]
Maximum number of events in pool (event mixing)	200
Minimum number of tracks in pool (event mixing)	10000
Minimum number of events to mix (event mixing)	1
Target Frac tracks (event mixing)	0.0025
Number of pool bins (event mixing)	3×3
Multiplicity bin limits (event mixing)	0, 20, 35, 200
Z_{vtx} bin limits (event mixing)	-10, -2.5, 2.5, 10
min p_T (AOD tracks)	0.3 GeV/c
max p_T (AOD tracks)	10000 GeV/c
min impact parameter (AOD tracks)	-1000000000. GeV/c
max impact parameter (AOD tracks)	10000. GeV/c
FilterBit (AOD tracks)	kTrkTPCOnly
max dca between two daugters (cm) (AOD v0)	0.2
max chi square (AOD v0)	2
min decay length (cm) (AOD v0)	2
max decay length (cm) (AOD v0)	1000
min opening angle between two daugters (AOD v0)	1000
min p_T of k0 (GeV/c) (AOD v0)	0.
eta acceptance (AOD v0)	0.9
Sigma for TPC compat (PID)	3
Sigma for TOF compat (PID)	3

TABLE B.3: The cut values applied on the associated charged tracks measured in minimum bias pp collisions at 13 TeV

Appendix C

The partonic profile function

The partonic profile function is related to the Fourier transform of the elastic scattering amplitude through the equation,

$$G(s,b) = \frac{1}{2s} 2Im\tilde{T}(s,b) \tag{C.1}$$

As it was mentioned in Chapter.6, there are 3 contributions to the elastic amplitude of scattering because of the existence of different processes in play in parton-parton interaction (see figure.C.1):

- **Soft contribution** : or in other words the pure non-perturbative contribution where the virtualities should satisfy the cutoff $Q^2 < Q_0^2$ where $Q_0^2 \sim 1$ GeV^2. This contribution dominates the interaction of hadrons at not too high energies. It is presented by a blob in the top left diagram of figure.C.1.
- **Hard contribution** : this is the symbol of perturbative contribution and it is mainly due to the interaction valence-valence of partons, consequently the virtualities characterizing the internal intermediate partons are larger ($Q^2 > Q_0^2$) where perturbative QCD techniques are applicable. This contribution is presented by the top right diagram of figure.C.1. The horizontal lungs correspond to the final partons. The virtualities of t-channel increase from the end of the ladder to the blob where the momentum transfer of parton-parton interaction is the largest.
- **Semi-hard contribution** : it is the consequence of sea-sea partons interactions where the momentum transfer satisfies $Q^2 < Q_0^2$. In this case, the momentum fraction x is very small ($x << 1$) so the mass will be larger $\sim Q_0^2/x$ and the parton will be slow. The consequence is a non-perturbative parton cascade. A representative example is displayed in the bottom diagram of figure.C.1. The main idea is that dynamics are similar to those taking place in the soft parton-parton scattering where the external legs are connected with parton ladder through a soft pomeron and a hard scattering in the centre as introduced earlier.

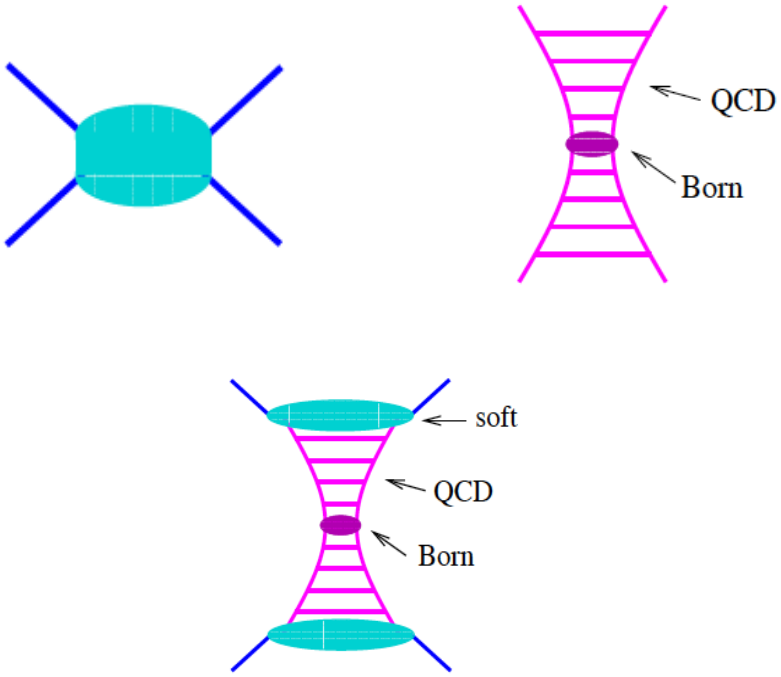

FIGURE C.1: Elastic amplitude : Soft contribution (top left diagram), hard contribution (top right diagram), semi-hard contribution (bottom diagram) [117].

Appendix D

Hadronization and pomerons

The "hidden complicated structure" of the pomeron, precisely the soft one, can be symbolized by a cylinder to take into account all possible QCD diagrams with the cylindrical topology as it is shown in the left diagram of figure.D.1. The external legs present the "nucleon components". In this case where the (soft) pomeron is a cylinder, the full line presents a quark and the dashed line an anti-quark. The two dotted vertical lines present the cut plane.

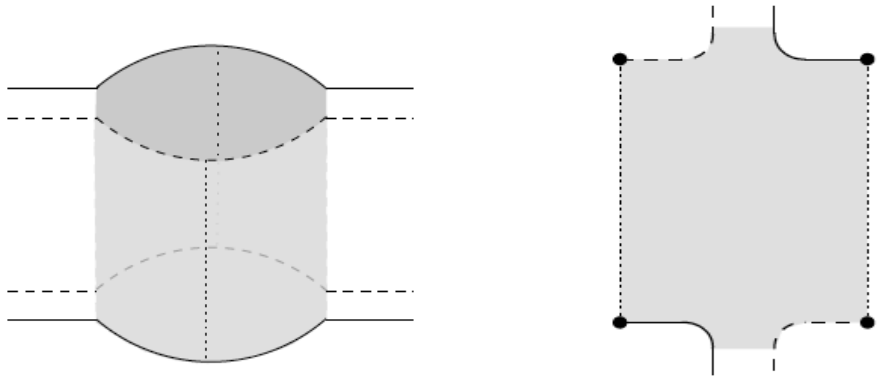

Figure D.1: Left: Representation of soft cut pomeron (cut cylinder). Right: Planar representation of a half cut pomeron [117].

After cutting, the right half cylinder is considered and the result is a planar presentation as displayed in the right diagram of figure.D.1 where the dotted lines refer to the cut plane and at this step, hadrons can show up. According to this approach and by simplifying the phenomenological procedure, this will lead to the string model where each cut line symbolizes a classical relativistic string which is a Lorentz invariant. The successive procedure of string breaking will create the hadronic final state. A different picture can be visualised at the microscopic level as a colour field connecting the string end-point and the partons resulted from the interaction. When the partons fly apart, the string stretches and becomes a colour tube that neutralises once it fragments into final state hadrons as presented in figure.D.2.

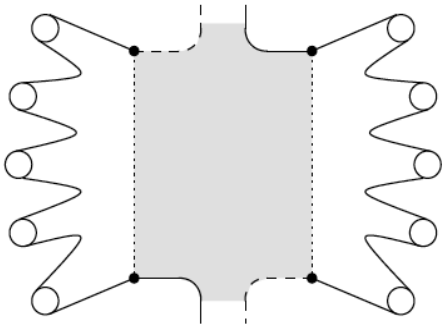

FIGURE D.2: String model : representation of the string (dotted vertical lines) + final state hadrons (circles) [117].

Concerning the semi-hard pomeron (or "sea-sea" interaction type), in the middle, a hard pQCD process takes place while the soft evolution occurs in the end. In this case, the pomeron can be presented by the left diagram in figure.D.3 which is still structured as a cylinder but with shaded areas representing the soft pomerons in addition to the strings along the cylinder surface. After cutting the diagram as it was done previously and by considering only the right half, the planar representation can be obtained and it is shown in the right diagram of figure.D.3. The difference with respect to the case of soft pomeron is the existence of one additional parton (dot) on each cut line (dotted vertical line) with internal gluons (kinks) in the middle and that is why the cut line, in this case, is called a "kinky string".

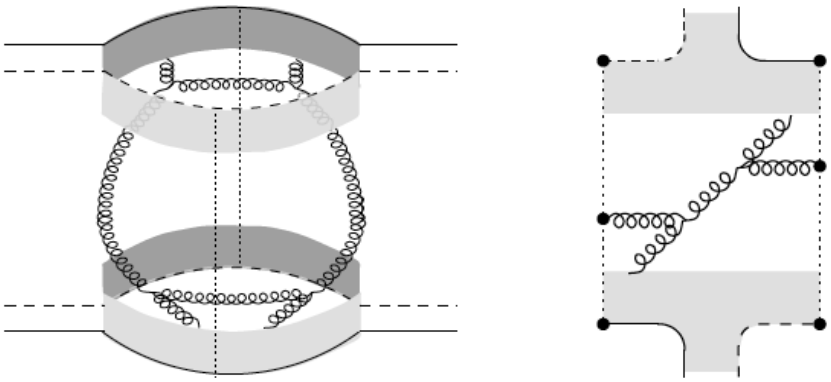

FIGURE D.3: Left: representation of a semi-hard pomeron (sea-sea type). Right: Planar representation of a semi-hard pomeron [117].

The kinky string can be visualised at the microscopic level by a three colour-connected partons since the gluon is connected by a colour field to the quark and the antiquark. For hadronisation, as it was stated in the case of soft pomerons, the procedure can be generalised even for more complicated parton ladders to create final state hadrons as presented in figure.D.4

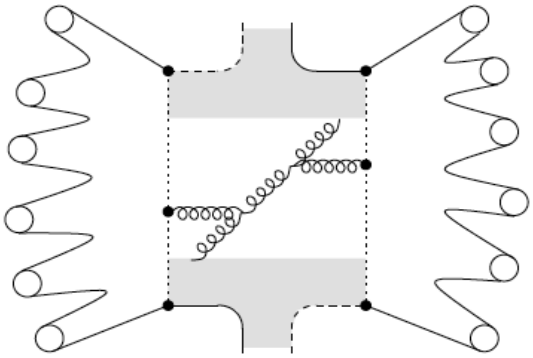

FIGURE D.4: Kinky string model : representation of a kinky string (dotted vertical lines) and final state hadrons (circles) [117].

The other type of pomerons is the hard or val-val where there is no sign of soft pomerons. In this interaction, only valence quarks are considered and they are the first partons in the parton ladder. The simplest representation for this kind of pomerons is displayed in the left diagram of figure.D.5 where two gluons are exchanged and coupled directly to the external partons. Following the same procedure of cylinder cutting and considering the right half will give the planar representation shown in the right diagram of figure.D.6 which includes one internal gluon only. The cut line is similar to the one presented for the case of soft pomeron, in addition to that, it incorporates external partons.

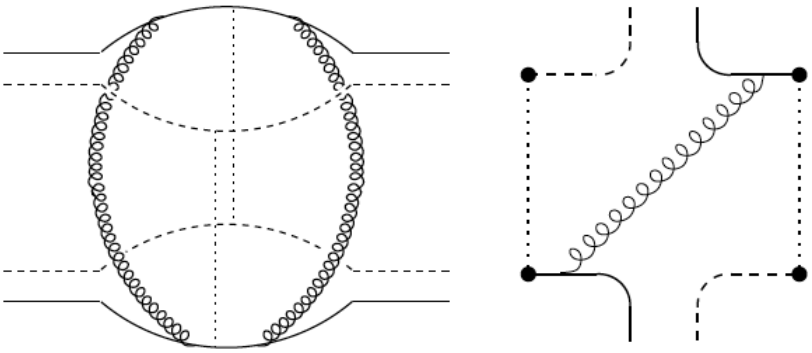

FIGURE D.5: Left: representation of a hard pomeron (val-val type). Right: Planar representation of a hard pomeron [117].

The usual procedure is applied for hadronisation where the string, connecting the quark and the anti-quark, will break to produce the final state hadrons as it is displayed in figure.D.6.

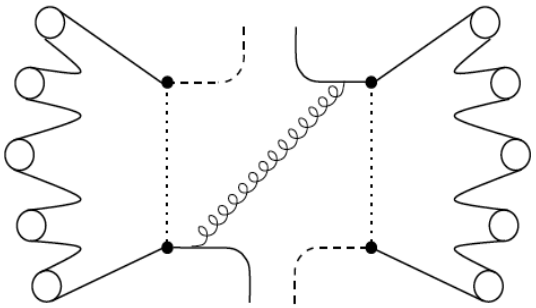

FIGURE D.6: String model : representation of a string (dotted vertical lines) and final state hadrons (circles) [117].

Bibliography

[1] Lyndon Evans and Philip Bryant, *LHC Machine, JINST 3 S08001, 2008.*

[2] P.B. Gossiaux, J. Aichelin, T. Gousset, V, Guiho, *Competition of Heavy Quark Radiative and Collisional Energy Loss in Deconfined Matter, arXiv:1001.4166v2 [hep-ph].*

[3] M. Nahrgang, J. Aichelin, P. Gossiaux, K. Werner. *Azimuthal correlations of heavy quarks in Pb+Pb collisions at $\sqrt{s} = 2.76$ TeV at the CERN Large Hadron Collider , Physical Review C 90 , 024907 (2014).*

[4] Mark Thomson, *Modern particle physics, CAMBRIDGE University Press, 2013.*

[5] Michael E. Peskin and Daniel V. Schroeder, *An introduction to Quantum Field Theory, PERSEUS BOOKS Reading, Massachusetts.*

[6] Francis Halzen and Alan D. Martin, *Quarks and Leptons : An introductory Course in Modern Particle Physics, Library of Congress Cataloging in Publication Data, John Wiley & Son, Inc, 1984.*

[7] A. Deur, S J Brodsky, G F. de Tramond, *The QCD Running Coupling, arXiv:1604.08082v4 [hep-ph] (2020).*

[8] The CMS Collaboration, *Measurement of the inclusive 3-jet production differential cross-section in proton-proton collisions at 7 TeV and determination of the strong coupling constant in the TeV range, arXiv:1412.1633v2 [hep-ex], CMS-SMP-12-027, CERN-PH-EP/2013-037.*

[9] Committee on the Physics of the Universe, National Research Council, *Connecting Quarks with the Cosmos: Eleven Science Questions for the New Century, The national Academy Press .*

[10] Donald Perkins , *Particle Astrophysics, Oxford Master Series in particle Physics, Astrophysics, and cosmology, Second Edition, 2009.*

[11] Johann Rafelski, *Connecting QGP-Heavy Ion Physics to the Early Universe, arXiv:1306.2471v1 [astro-ph.CO], Nuclear Physics B Proceedings Supplement 00 (2018) 1-8.*

[12] R. Averbeck, *Heavy-flavour production in heavy-ion collisions and implications for the properties of hot QCD matter, arXiv:1505.03828v1 [nucl-ex].*

[13] Panagiota Foka, Malgorzata Anna Janik, *An overview of experimental results from ultra-relativistic heavy-ion collisions at the CERN LHC: Bulk properties and dynamical evolution*, *Reviews in Physics 1 (2016) 154-171, 2016.*

[14] Bogdan Povh, Klaus Rith, Christoph Scholz, Frank Zetsche, *Particles and Nuclei: An Introduction to the Physical Concepts*, *Springer, 6th Edition, 2008.*

[15] Samuel S. M. Wong, *Introductory Nuclear Physics*, *Wiley-VCH Verlag GmbH & Co. KGaA, Second Edition, 2004.*

[16] Cheuk-Yin Wong, *Signatures of Quark-Gluon Plasma Transition in High-Energy Nuclear Collisions*, *arXiv:nucl-th/0007046v1, 2000.*

[17] Sarah Campbell, *Photon production from gluon mediated quark-anti-quark annihilation at confinement*, *arXiv:1504.01654 [nucl-ex], 2015.*

[18] Jean-Francois Paquet, *Probing the spacetime evolution of heavy ion collisions with photons and dileptons*, *Nuclear Physics A 00 (2018) 1-9, arXiv:1704.07842v1 [nucl-th], 2017.*

[19] D. Almaalol et all, *Anisotropic hydrodynamic modeling of 200 GeV Au-Au collisions*, *arXiv:1807.04337v1 [nucl-th].*

[20] H. Song et all, *200 A GeV Au+Au collisions serve a nearly perfect quark-gluon liquid*, *arXiv:1011.2783v2 [nucl-th].*

[21] Tapan K. Nayak, *Heavy Ions: Results from the Large Hadron Collider*, *arXiv:1201.4264v1 [nucl-ex], 2012.*

[22] Wit Busza, Krishna Rajagopal, and Wilke van der Schee, *Heavy Ion Collisions: The Big Picture, and the Big Questions*, *arXiv:1802.04801v2 [hep-ph], 2018.*

[23] Charles Gale, Sangyong Jeon, *Hydrodynamic modeling of heavy-ion collisions*, *arXiv:1301.5893v1 [nucl-th], 2013.*

[24] A. Banfi, G. Salam and G. Zanderighi, *Accurate QCD predictions for heavy-quark jets at the Tevatron and LHC*, *arXiv:0704.2999v1 [hep-ph].*

[25] D. Souza and N. H. Brook, *Analysis of Charm Pair Production at the LHC*, *arXiv:1511.06226v1 [hep-ph].*

[26] Matteo Cacciari, Stefano Frixione, Nicolas Houdeaua, Michelangelo L. Manganoc, Paolo Nason, and Giovanni Ridolfi, *Theoretical predictions for charm and bottom production at the LHC*, *arXiv:1205.6344v1 [hep-ph].*

[27] S. Frixione et all, *The MC@NLO 4.0 Event Generator*, *arXiv:1010.0819v1 [hep-ph].*

[28] C. Oleari, *The POWHEG BOX*, *arXiv:1007.3893v1 [hep-ph].*

[29] Torbjörn Sjöstrand, Stefan Ask, Jesper R. Christiansen, Richard Corke, Nishita Desai, Philip Ilten, Stephen Prestel, Christine O. Rasmussen, Peter Z. Skands. *A brief introduction to PYTHIA 8.2*, *arXiv:1410.3012.*

[30] M. Bär et all, *Herwig++ Physics and Manual*, *arXiv:0803.0883v3 [hep-ph]*.

[31] L. Gladilin, *Fragmentation fractions of c and b quarks into charmed hadrons at LEP*, *arXiv:1404.3888v2 [hep-ex]*.

[32] Bernd A. Kniehl and Gustav Kramer, *Charmed-Hadron Fragmentation Functions from CERN LEP1*, *DESY 06-102, ISSN 0418-9833, arXiv:hep-ph/0607306v1*.

[33] ZEUS Collaboration, *Measurement of the charm fragmentation function in D^* photoproduction at HERA*, *arXiv:0901.1210v2 [hep-ex]*.

[34] Mykhailo Lisovyi, Andrii Verbytskyi, Oleksandr Zenaiev, *Combined analysis of charm-quark fragmentation-fraction measurements*, *Eur. Phys. J. C (2016) 76:397, DOI 10.1140/epjc/s10052-016-4246-y*.

[35] T. Gershon, M. Needham, *Heavy Flavour Physics at the LHC*, *arXiv:1408.0403v2 [hep-ex]*.

[36] Jonathan Lewis, Rick Van Kooten, *Review of Physics Results from the TEVATRON : Heavy Flavour Physics*, *arXiv:1412.5211v2 [hep-ex], Fermilab-PUB-14-480-E*.

[37] R. Vogt, *Open and Hidden Charm Production at RHIC and LHC*, *arXiv:hep-ph/0412303v1*.

[38] Kai Schweda, *Experimental Overview of Open Heavy Flavour*, *arXiv:1610.04111v1 [nucl-ex]*.

[39] Michael Winn, *Heavy flavour production in proton-lead and lead-lead collisions with LHCb*, *Nuclear Physics A 00 (2017), arXiv:1704.04217v1 [nucl-ex]*.

[40] Li Yi (for the STAR Collaboration), *STAR Overview of Hard Probe Observables*, *Nuclear Physics B Proceedings Supplement 00 (2018), arXiv:1509.07746v1 [nucl-ex]*.

[41] A. Beraudo, A. De Pace, M. Monteno, M. Nardi, F.Prino, *Heavy flavors in heavy-ion collisions: quenching, flow and correlations*, *Eur. Phys. J. C (2015) 75:121, DOI 10.1140/epjc/s10052-015-3336-6*.

[42] G. Aarts et all, *Heavy-flavor production and medium properties in high-energy nuclear collisions - What next?*, *arXiv:1612.08032v2 [nucl-th]*.

[43] The LHCb Collaboration, *Measurement of the $B^{\pm}$ production cross-section in pp collisions at $\sqrt{s}$ =7 TeV*, *arXiv:1202.4812v1 [hep-ex] (2012)*.

[44] The LHCb Collaboration, *Measurements of prompt charm production cross-sections in pp collisions at $\sqrt{s}$ = 5 TeV*, *arXiv:1610.02230v2 [hep-ex]*.

[45] The LHCb Collaboration, *Prompt charm production in pp collisions at $\sqrt{s}$ = 7 TeV*, *arXiv:1302.2864v1 [hep-ex]*.

[46] The LHCb Collaboration, *Measurements of prompt charm production cross-sections in pp collisions at $\sqrt{s}$ = 13 TeV*, *arXiv:1510.01707v6 [hep-ex]*.

[47] The LHCb Collaboration, *Measurement of J/Ψ production in pp collisions at $\sqrt{s} = 7$ TeV, arXiv:1103.0423v2 [hep-ex].*

[48] The ALICE Collaboration, *Beauty production in pp collisions at $\sqrt{s} = 2.76$ TeV measured via semi-electronic decays, arXiv:1405.4144v2 [nucl-ex].*

[49] The ALICE Collaboration, *Measurement of charm production at central rapidity in proton-proton collisions at $\sqrt{s} = 2.76$ TeV, arXiv:1205.4007v3 [hep-ex].*

[50] Matteo Cacciari, Mario Greco, Paolo Nason, *The p_{T} spectrum in heavy-flavour hadroproduction, arXiv:hep-ph/9803400v1.*

[51] I. Helenius and H. Paukkunen, *Revisiting the D-meson hadroproduction in general-mass variable flavour number scheme, arXiv:1804.03557v2 [hep-ph].*

[52] The ALICE Collaboration, *Measurement of charm production at central rapidity in proton-proton collisions at $\sqrt{s} = 7$ TeV, arXiv:1111.1553v3 [hep-ex].*

[53] B. A. Kniehl, G. Kramer, I. Schienbein and H. Spiesberger, *Inclusive Charmed-Meson Production at the CERN LHC, arXiv:1202.0439v1 [hep-ph].*

[54] The ALICE Collaboration, *Measurement of D-meson production at mid-rapidity in pp collisions at $\sqrt{s} = 7$ TeV, arXiv:1702.00766v2 [hep-ex].*

[55] The ALICE Collaboration, *Measurement of D^0, D^+, D^{*+} and D_s^+ production in pp collisions at $\sqrt{s}$ =5.02 TeV with ALICE, arXiv:1901.07979v2 [nucl-ex].*

[56] The ATLAS Collaboration, *Measurement of $D^{*\pm}$, $D^{\pm}$ and $D_s^{\pm}$ meson production cross sections in pp collisions at $\sqrt{s} = 7$ TeV with the ATLAS detector, Nuclear Physics B 907 (2016) 717-763.*

[57] PHENIX Collaboration, *Measurement of Bottom versus Charm as a Function of Transverse Momentum with Electron-Hadron Correlations in p+p Collisions at $\sqrt{s} = 200$ GeV, arXiv:0903.4851v1 [hep-ex].*

[58] The STAR Collaboration, *Measurement of D^0 and D^* Production in p+p Collisions at $\sqrt{s} = 200$ GeV, arXiv:1204.4244v3 [nucl-ex].*

[59] Matteo Cacciari and Paolo Nason, *Charm Cross Sections for the Tevatron Run II, arXiv:hep-ph/0306212v1.*

[60] B.A. Kniehl, G. Kramer, I. Schienbein and H. Spiesberger, *Reconciling open charm production at the Fermilab Tevatron with QCD, arXiv:hep-ph/0508129v1.*

[61] The ALICE Collaboration, *D-meson production in p-Pb collisions at $\sqrt{s_{NN}} = 5.02$ TeV and in pp collisions at $\sqrt{s} = 7$ TeV, arXiv:1605.07569v2 [nucl-ex].*

[62] Néstor Armesto, *Nuclear shadowing, arXiv:hep-ph/0604108v2 (2016).*

[63] The LHCb Collaboration, *Study of J/Ψ production and cold nuclear matter effects in pPb collisions at $\sqrt{s_{NN}} = 5$ TeV, arXiv:1308.6729v4 [nucl-ex].*

[64] The CMS Collaboration, *Study of B meson production in pPb collisions at $\sqrt{s_{NN}} = 5.02$ TeV using exclusive hadronic decays, arXiv:1508.06678v2 [nucl-ex].*

[65] The CMS Collaboration, *Suppression of non-prompt J/Ψ, prompt J/Ψ, and Γ(1S) in PbPb collisions at $\sqrt{s_{NN}} = 2.76$ TeV, arXiv:1201.5069v2 [nucl-ex].*

[66] The CMS Collaboration, *Nuclear modification factor of D^0 mesons in PbPb collisions at $\sqrt{s_{NN}} = 5.02$ TeV, arXiv:1708.04962v2 [nucl-ex].*

[67] The ALICE Collaboration, *Measurement of D_s^+ production and nuclear modification factor in Pb-Pb collisions at $\sqrt{s_{NN}} = 2.76$ TeV, arXiv:1509.07287v2 [nucl-ex].*

[68] Giuseppe Eugenio Bruno, *Heavy Flavour Production at LHC: an overview, EPJ Web of Conferences 70, 00058 (2014).*

[69] E. L. Bratkovskaya, T. Song, H. Berrehrah, D. Cabrera, J. M. Torres-Rincon, L. Tolos, W. Cassing, *Heavy flavor in relativistic heavy-ion collisions, arXiv:1508.03887v1 [nucl-th].*

[70] B. A. Kniehl, G. Kramer, I. Schienbein, H. Spiesberger, *Inclusive $D^{*\pm}$ Production in $p\bar{p}$ Collisions with Massive Charm Quarks, arXiv:hep-ph/0410289v1.*

[71] A. Beraudo, A. De Pace, M. Monteno, M. Nardi, F. Prino, *Heavy flavours in heavy-ion collisions : quenching, flow and correlations, Eur. Phys. J C (2015) 75:121, DOI 10.1140/epjc/s10052-015-3336-6.*

[72] G. Aarts et al, *Heavy-flavour production and medium properties in high-energy nuclear collisions - What next ?, arXiv:1612.08032v2 [nucl-th].*

[73] X. Zhu, M. Bleicher, S .L . Huang, K. Schweda, H. Stcker, N. Xu, P. Zhuang, *$D\bar{D}$ Correlations as a Sensitive Probe for Thermalization in High Energy Nuclear Collisions, arXiv : hep-ph/0604178v2.*

[74] X. Zhu, N. Xu and P. Zhuang, *The effect of partonic wind on charm quark correlations in high-energy nuclear collisions, arXiv:0709.0157v1 [nucl-th].*

[75] Shanshan Cao, Guang-You Qin, and Steffen A. Bass, *Modeling of heavy-flavour pair correlations in Au-Au collisions at 200A GeV at the BNL Relativistic Heavy Ion Collider, arXiv:1505.01869v2 [nucl-th].*

[76] Shanshan Cao, Guang-You Qin, Steffen A Bass, *Suppression and Two-Particle Correlations of Heavy Mesons in Heavy-Ion Collisions, Nuclear Physics A 956 (2016) 505-508.*

[77] Shanshan Cao, Tan Luoc, Yayun He, Guang-You Qin, Xin-Nian Wang, *Heavy and light hadron production and D-hadron correlation in relativistic heavy-ion collisions, Nuclear Physics A 967 (2017) 628-631.*

[78] The CMS Collaboration, *Transverse momentum balance of b-jet pairs in pp and PbPb collisions at $\sqrt{S_{NN}} = 5.02$ TeV, CMS Physics Analysis Summary, CMS PAS HIN-16-005 (2016) .*

[79] The LHCb Collaboration, *Observation of double charm production involving open charm in pp collisions at $\sqrt{s} = 7$ TeV, arXiv:1205.0975v3 [hep-ex] (2014).*

[80] LHCb Collaboration, *Study of $b\bar{b}$ correlations in high energy proton-proton collisions, arXiv:1708.05994v1 [hep-ex] (2017).*

[81] CMS Collaboration, *Measurement of $B\bar{B}$ Angular Correlations based on Secondary Vertex Reconstruction at $\sqrt{s} = 7$ TeV , arXiv:1102.3194v2 [hep-ex].*

[82] B. Reisert on behalf of the CDF Collaboration, *Charm Production Studies at CDF, Nuclear Physics B (Proc. Suppl.) 170 (2007) 243-247.*

[83] Long Ma for the STAR Collaboration, *Measurement of D^*-meson triggered correlations in p+p collisions at RHIC, arXiv:1704.07098v1 [nucl-ex] (2017) 1-4.*

[84] The ALICE Collaboration, *Multiplicity dependence of two-particle azimuthal correlations in pp collisions at the LHC, arXiv:1307.1249v2 [nucl-ex].*

[85] The ATLAS Collaboration, *Observation of long-range elliptic azimuthal anisotropies in $\sqrt{s}$ =13 and 2.76 TeV pp collisions with the ATLAS detector, arXiv:1509.04776v2 [hep-ex], Phys. Rev. Lett. 116, 172301, CERN-PH-EP-2015-251.*

[86] The ALICE Collaboration, *Evolution of the longitudinal and azimuthal structure of the near-side jet peak in Pb-Pb collisions at $\sqrt{s_{NN}}$ = 2.76TeV, arXiv:1609.06667v2 [nucl-ex] CERN-EP-2016-228.*

[87] The ALICE Collaboration, *Particle-yield modification in jet-like azimuthal di-hadron correlations in Pb-Pb collisions at $\sqrt{s_{NN}}$ = 2.76TeV, arXiv:1110.0121v3 [nucl-ex] CERN-PH-EP-2011-161.*

[88] Pettersson, Thomas Sven; Lefèvre,P, CERN, Geneva *The Large Hadron Collider : conceptual design, CERN-AC-95-05-LHC*, 1995.

[89] O.Bruning, P.Collier, P.Lebrun, S.Myers, R.Ostojic, J.Poole, P.Proutdlock, *LHC Design Report, Volume I, The LHC main ring,* CERN-2004-003-V1, 2004.

[90] R. Bailey, *An Application for Research - the Large Hadron Collider - CERN, Geneva, Switzerland, arXiv:1404.0966 [physics.acc-ph]*, 2014.

[91] Benjamin Todd, Brunel U, *A Beam Interlock System for CERN High Energy Accelerators, CERN-THESIS-2007-019*, 2006.

[92] The CERN accelerator complex Complexe des accélérateurs du CERN, *http://cds.cern.ch/record/1260465/?ln=fr, CERN-DI-0812015*, 2008.

[93] ALICE Collaboration, *Performance of the ALICE Experiment at the CERN LHC, arXiv:1402.4476v4 [nucl-ex]*, 12 August 2015.

[94] ALICE Collaboration, *The ALICE experiment at the CERN LHC, JINST 3 S08002, 2008.*

[95] Fatiha Lehas (for the ALICE Collaboration), *Azimuthal angular correlations of D mesons with charged particles in pp collisions at $\sqrt{s} = 7$ TeV and p-Pb collisions at $\sqrt{s_{NN}} = 5.02$ TeV with the ALICE experiment at the LHC*, *EPJ Web of Conferences 164, 07004 (2017), ICNFP 2016.*

[96] ALICE Collaboration, *Measurement of azimuthal correlations of D mesons with charged particles in pp collisions at $\sqrt{s} = 7$ TeV and p-Pb collisions at $\sqrt{s_{NN}} = 5.02$ TeV*, *arXiv: 1605.06963v2 [nucl-ex].*

[97] Sandro Bjelogrlic, *Azimuthal angular correlations of D mesons and charged particles with the ALICE detector at the LHC*, *PhD thesis*, Utrecht University, 2016.

[98] Fabio Fillipo Colamaria, *Measurements of D-hadron azimuthal correlations with ALICE at the LHC*, *PhD thesis, Bari Aldo Moro University, 2014.*

[99] ALICE collaboration, *D-hadron correlations in p-p collisions at $\sqrt{s} = 13$ TeV*, *Internal notes, 2018.*

[100] P. Skands, S. Carrazza, J. Rojo. *Tuning PYTHIA 8.1: the Monash 2013 Tune*, *arXiv:1404.5630v1 [hep-ph], CERN-PH-TH-2014-069.*

[101] Torbjörn Sjöstrand, *Monte Carlo Tools*, *arXiv:0911.5286v1 [hep-ph].*

[102] V. V. Sudakov, *Vertex Parts at Very High Energies in Quantum Electrodynamics*, *Sov. Phys. J.E.T.P. 30 (1956) 65.*

[103] R. Corke, *Multiple Interactions in PYTHIA 8*, *arXiv : 0901.2852v1 [hep-ph].*

[104] Andreas Morsch (on behalf of the ALICE Collaboration), *Multiple Parton Interactions with ALICE from pp to p-Pb*, *Journal of Physics : Conference Series 535 (2014) 012012, 30th Winter Workshop on Nuclear Dynamics (WWND2014).*

[105] ALICE Collaboration, *Measurement of charm and beauty production at central rapidity versus charged-particle multiplicity in proton-proton collisions at $\sqrt{s} = 7$ TeV*, *arXiv:1505.00664v2 [nucl-ex] (2015).*

[106] Torbjörn Sjöstrand, *Color reconnection and its effects on precise measurements at the LHC*, *arXiv : 1310.8073 [hep-ph].*

[107] Spyros Argyropoulos and Torbjörn Sjöstrand, *Effects of color reconnection on $t\bar{t}$ final states at the LHC*, *JHEP11 (2014) 043.*

[108] A. Ortiz Velasquez and P. Christiansen, *Color reconnection and flow-like patterns in pp collisions*, *arXiv : 1303.6326v2 [hep-ph].*

[109] Arturo Rodriguez, *Sensitivity studies of colour reconnection in top UE measurements*, *DESY, summer student program, 2015.*

[110] B. Andersson, G. Gustafson, G. Ingelman, T. Sjöstrand, *Parton fragmentation and string dynamics*, *Phys. Rep. 97 (2?3): 31?145 (1983).*

[111] E. Norrbin and T. Sjöstrand, *Production and Hadronization of Heavy Quarks, arXiv : hep-ph/0005110v1.*

[112] Torbjörn Sjöstrand, Stephen Mrenna, Peter Skands. *A brief introduction to PYTHIA 8.1, arXiv:0710.3820.*

[113] Torbjörn Sjöstrand, *Monte Carlo Generators, arXiv:hep-ph/0611247v1.*

[114] Andrzej Siódomok, *LHC event generation with general-purpose Monte Carlo tools, ACTA PHYSICA POLONICA B, Vol. 44 (2013), No 7.*

[115] O, Nachtmann, *Pomeron Physics and QCD. Contribution to the Ringberg Workshop on HERA physics 2003, arXiv:hep-ph/0312279v1.*

[116] F. M. Lui, J. Aichelin, M, Bleicher, H. J. Drescher, S. Ostapchenko, T. Pierog and K. Werner, *Constraints on models for proton-proton scattering from multistrange baryon data. Physical Review D 67, 034011 (2003).*

[117] H.J. Drescher, M. Hladik, S. Ostapchenko, T. Pierog, K. Werner, *Parton-based Gribov-Regge Theory. Physics Reports, Volume 350, Issues 2?4, September 2001, Pages 93-289.*

[118] T. Pierog, K. Werner, *How to relate particle physics and air shower development : The EPOS model, PROCEEDINGS of the 31st ICRC, LODZ 2009.*

[119] T. Pierog, Iu. Karpenko, J. M. Katzy, E. Yatsenko, K. Werner, *EPOS LHC: Test of collective hadronization with data measured at the CERN Large Hadron Collider, PHYSICAL REVIEW C 92, 034906 (2015).*

[120] B. Guiot et al, *Charm and prompt photon production with EPOS, J. Phys.: Conf. Ser. 805 (2017) 012002.*

[121] S. Porteboeuf, T. Pierog, K. Werner, *Producing hard processes regarding the complete event : the EPOS event generator, Moriond 2010 proceedings, arXiv : 1006.2967v1 [hep-ph].*

[122] K. Werner, B. Guiot, Iu. Karpenko, T. Pierog, *Analysing radial flow features in p-Pb and p-p collisions at several TeV by studying identified particle production in EPOS3, arXiv : 1312.1233v1 [nucl-th].*

[123] B. Guiot and K. Werner, *Hard probes and the event generator EPOS, arXiv: 1411.1336v1 [hep-ph] .*

[124] K. Werner, T. Pierog, S. Porteboeuf, *EPOS 1 User's Guide Reference journal ou conference ... .*

[125] Klaus WERNER, *The hadronic interaction model EPOS, Nuclear Physics B (Proc. Suppl.) 175-176 (2008) 81-87.*

[126] Klaus WERNER, Fu-Ming LIU, Tanguy PIEROG, *Parton Ladders Splitting and the Rapidity Dependence of Transverse Momentum Spectra in Deuteron-Gold Collisions at RHIC, arXiv: hep-ph/0506232v1.*

[127] Klaus Werner, Fu-Ming Liu, Tanguy Pierog, *Parton ladders splitting and the rapidity dependence of transverse momentum spectra in deuteron-gold collisions at the BNL Relativistic Heavy Ion Collider, PHYSICAL REVIEW C 74, 044902 (2006).*

[128] Klaus Werner, *Core-Corona Separation in Ultra-Relativistic Heavy Ion Collisions, arXiv:0704.1270v1 [nucl-th].*

[129] M. Gemard and J. Aichelin, *Core-Corona Model analysis of the Low Energy Beam Scan at RHIC, arXiv:1402.0234v1 [hep-ph].*

[130] K. Werner, B. Guiot, Iu. Karpenko, T. Pierog, *A unified description of the reaction dynamics from pp to pA to AA collisions, Nuclear Physics A 00 (2014) 1-8, arXiv:1411.1048v1 [nucl-th].*

[131] J. Aichelin and K. Werner, *Core-Corona Model describes the Centrality Dependence of v_2/ϵ, arXiv:1008.5351v1 [nucl-th].*

[132] K. Werner, Iu. Karpenko, T. Pierog, *The "Ridge" in Proton-Proton Scattering at 7 TeV, arXiv:1011.0375v2 [hep-ph].*

[133] K. Werner, M. Bleicher, B. Guiot, Iu. Karpenko, T. Pierog, *Evidence for flow in pPb collisions at 5 TeV from v_2 mass splitting, arXiv:1307.4379v1 [nucl-th].*

[134] K. Werner, Iu. Karpenko, T. Pierog, M. Bleicher, K. Mikhailov, *Evidence for Hydrodynamic Evolution in Proton-Proton Scattering at LHC Energies, arXiv : 1010.0400v1 [nucl-th].*

[135] K. Werner, Iu. Karpenko, T. Pierog, M. Bleicher, K. Mikhailov, *Event-by-Event Simulation of the Three-Dimensional Hydrodynamic Evolution from Flux Tube Initial Conditions in Ultra Relativistic Heavy Ion Collisions, arXiv : 1004.0805v1 [nucl-th].*

[136] M. Bleicher, E. Zabrodin, C. Spieles, S. A. Bass, C. Ernst, S. Soff, L. Bravina, M. Belkacem, H. Weber, H. Stocker, W. Greiner, *Relativistic Hadron-Hadron Collisions in the Ultra-Relativistic Quantum Molecular Dynamics Model (UrQMD), arXiv:hep-ph/9909407v1.*

[137] K. Werner, Iu. Karpenko, M. Bleicher, T. Pierog, S. Porteboeuf-Houssais, *Jets, Bulk Matter, and their Interaction in Heavy Ion Collisions at Several TeV, arXiv : 1203.5704v2 [nucl-th].*

[138] K. Werner, B. Guiot, Iu. Karpenko, T. Pierog, *Hydrodynamic flow in proton-nucleus collisions at the LHC, 30th Winter Workshop on Nuclear Dynamics (WWND2014), Journal of Physics : Conference Series 535 (2014) 012028.*

[139] F. Cooper and G. Frye, *Single-particle distribution in the hydrodynamic and statistical thermodynamic models of multiparticle production, Physical Review D Volume 10 Number 1, 186-189 (1974).*

[140] Zack Wolff and Denes Molnar, *Self-consistent Cooper-Frye freeze-out of a viscous fluid to particles, arXiv : 1407.6413v1 [nucl-th].*

[141] Hannah Petersen, Jan Steiheimer, Gerhard Burau, Marcus Bleicher and Horst Stocker, *Fully integrated transport approach to heavy ion reactions with an intermediate hydrodynamic stage, Physical Review C 78, 044901 (2008).*

[142] Marlene Nahrgang, *Open heavy-flavour production and suppression in heavy-ion collisions, arXiv: 1510.03627v1 [nucl-th], CHARM 2015.*

[143] Marlene Nahrgang, Jörg Aichelin, *Open heavy-flavour observables at the LHC and the importance of higher-order flow harmonics, Journal of Physics: Conference Series 668 (2016) 012024, 15th International Conference on Strangeness in Quark matter (SQM2015).*

[144] Pol Bernard Gossiaux et al, *First results of EPOS-HQ model for open heavy flavour production in A-A collision at RHIC and LHC, arXiv: 1901.03856v1 [hep-ph].*

[145] Benjamin Guiot, *Production de charms et de photons prompts avec le generateur d evenement EPOS, PhD thesis,Universite de Nantes Angers Le Mans, 2014.*

[146] M. Nahrgang, J. Aichelin, P. Gossiaux, K. Werner, *Heavy-flavour azimuthal correlations of D mesons , Journal of Physics : Conference Series 509 (2014) 012047.*

[147] J. Aichelin, B. Guiot, V. Ozvenschuck, M. Nahrgang, P.B. Gossiaux and K. Werner, *EPOSHQ - a new approach to describe charmed mesons in pp, pA and AA collisions, Nuclear Physics A 956 (2016) 485-488.*

[148] M. Nahrgang, J. Aichelin, P. Gossiaux, K. Werner, *D mesons in non-central heavy-ion collisions : fluctuating vs. averaged initial conditions, arXiv:1405.0938v1, Nuclear Physics A 00 (2014) 1-5.*

[149] V. Ozvenchuk et al, *D-meson observables in Pb-Pb and p-Pb collisions at LHC with EPOSHQ model, J. Phys.: Conf. Ser. 779 (2017) 012033.*

[150] Marlene Nahrgang, Jörg Aichelin, Pol Bernard Gossiaux, Klaus Werner, *Heavy-flavour azimuthal correlations of D mesons, arXiv:1310.2218v2.*

[151] Vitalii Ozvenchuk, Jörg Aichelin, Pol-Bernard Gossiaux, Benjamin Guiot, Marlene Nahrgang, Klaus Werner, *D-meson observables in heavy-ion collisions at LHC with EPOSHQ model, EPJ Web of Conferences 130, 07018 (2016) MESON 2016.*

[152] Marlene Nahrgang, Jörg Aichelin, Pol Bernard Gossiaux, Klaus Werner, *Toward a consistent evolution of the quark-gluon plasma and heavy quarks, arXiv: 1602.03544v1 [nucl-th].*

Samenvatting in het Nederlands

In dit proefschrift worden de gemeten azimutale correlaties tussen D^{*+} mesonen en geladen deeltjes gepresenteerd. Deze correlaties zijn gemeten met de ALICE detector bij een botsingsenergie van $\sqrt{s} = 13$ TeV aan de Large Hadron Collider (LHC).

De gemeten azimutale correlatiefuncties laten, zoals reeds geobserveerd bij de lagere botsingsenergie van 7 TeV, een piek zien bij $\Delta\phi = 0$ en $\Delta\phi = \pi$, bovenop een onderliggende distributie. We zagen tevens dat de gemeten pieken meer prominent worden voor deeltjes met hogere transversale momenta. Dit laatste suggereert dat er tijdens de botsing een groot aantal geladen deeltjes geproduceerd wordt in dezelfde richting als het D-meson, een zogeheten jet. In de tegengestelde richting worden er ook meer deeltjes gevonden hoewel deze minder sterk met elkaar gecorreleerd zijn. De vergelijking tussen de 7 en 13 TeV botsingsenergieën laat ons zien dat de onderliggende distributie afhankelijk is van het totaal aantal deeltjes dat geproduceerd wordt omdat deze bijdrage toeneemt met het toenemende aantal deeltjes bij hogere botsingsenergieën.

Om deze metingen te vergelijken met de theoretische voorspellingen hebben we de botsingen gesimuleerd met de modellen PYTHIA8 en EPOS3. Middels deze modellen hebben we gekeken naar de correlaties tussen D-mesonen en hun antideeltjes in proton-proton botsingen bij $\sqrt{s} = 200$ GeV en 7 TeV en tussen D-mesonen en geladen deeltjes in proton-proton botsingen bij $\sqrt{s} = 7$ en 13 TeV. Daarnaast hebben we met deze modellen ook naar proton-lood botsingen gekeken bij $\sqrt{s_{NN}} = 5.02$ TeV. Voor deze vergelijking hebben we de gesimuleerde botsingen op dezelfde manier geanalyseerd als de ALICE metingen bij de LHC.

Voor PYTHIA8 observeerden we dat, voor botsingsenergieën van orde TeV, de zware quarks voornamelijk geproduceerd worden via gluonsplitsing. Bij lagere energieën, van orde GeV, vind de productie van zware quarks voornamelijk plaats door "paar-productie". We zagen ook dat de correlatie tussen de geproduceerde zware quarks zichtbaar blijft in de correlatie tussen de bijbehorende mesonen. Contributies van de zogeheten "initial" en "final state radiation (ISR/FSR)" en "color reconnection (CR)" veranderen deze correlatie niet noemenswaardig. Het zogenoemde "Multiple Parton Interaction (MPI)" mechanisme veranderd de distributie daarentegen wel omdat dit de gluonspitsing minimaliseert wat voor de hogere energieën een belangrijke bijdrage levert aan de azimutale correlaties.

Voor het model EPOS3/EPOSHQ zijn de voorspellingen vergeleken met de ALICE metingen en deze kwamen voor proton-proton botsingen bij 7 TeV kwalitatief overeen. De overeenkomst was beter als de onderliggende distributie niet werd meegenomen. Deze observaties laten zien dat de onderliggende deeltjes-multipliciteit niet goed beschreven wordt door dit model.

In proton-proton botsingen werden de correlatie tussen $D^0 - \bar{D}^0$ / $D^+ - D^-$, zoals gemeten door de LHCb-collaboratie bij 7 TeV en de D^{*+}-D^{*-} correlaties bij 500 GeV gemeten door de STAR-collaboratie, redelijk goed voorspeld. Daarentegen werden de metingen van de azimutale correlatie van de D^* met de geladen deeltjes door de STAR-collaboratie niet beschreven. Ook voor de proton-lood botsingen bij 5.02 TeV was er alleen een kwalitatieve beschrijving mogelijk van de gemeten azimutale correlatie.

Bij elkaar genomen laten de gemeten azimutale correlaties tussen D^{*+} mesonen en geladen deeltjes vergeleken met de model voorspellingen zien dat er voor de modellen nog een hoop te verbeteren valt. In de toekomst zullen we met een verder verbeterde ALICE detector met veel hogere precisie de correlaties tussen D mesonen en geladen deeltjes alsmede direct de correlatie tussen de D en $\bar{D}$ mesonen kunnen meten. Vooral deze laatste meting zal het mogelijk maken om de theorie en de modellen veel directer te toetsen en hopelijk daarmee de productie van zware quarks in de verschillende botsingen beter te kunnen begrijpen.

Acknowledgements

First of all, I would like to thank infinitely my supervisors for accepting me in this PhD program and giving me the chance to join such a scientific community to work on the cutting-edge topic of research, to be a part of this amazing journey and to have an experience in such a wonderful field of particle physics either the experimental part by working at CERN or the theoretical part by working with EPOS the state of the art event generator.

I am grateful to my principal supervisor Dr. André Mischke, who passed away at the end of my PhD, who assisted me and followed my advancement step by step from the beginning and I profit to express my condolence, and I wish for him the eternal rest in peace from his illness and pain. I am thankful to Prof. Paul Kuijer for his help in administrative procedure, and I appreciate all the support provided by Prof. Raimond Snellings at the beginning and the end of this PhD from all sides administrative or educational and for his contribution to the correction of the final manuscript. I am thankful to Prof. Jörg Aichelin and Prof. Pol-Bernard Gossiaux for their support and patience during my presence in Nantes for all the explanation and advice.

I am thankful to many other people I have met and worked with during my presence at CERN, Utrecht and Nantes and even those that I have never met, but they were always there supporting me whenever I needed them. I am grateful to Dr. Alessandro Grelli for the fruitful discussions and the contribution to correct the final manuscript. I would like to thank the PWG-HFCJ people Elena Bruna, Andrea Rossi for all the fruitful discussions, especially Dr. Fabio Colamaria for the discussions, for his patience, availability and understanding. I am thankful to Sara Porteboeuf for the interesting discussions on the technical details related to PYTHIA and Klaus Werner for the interesting discussions on EPOS/EPOSHQ simulations. I would like to thank as well Shyam, Sandro, Annelies, Redmer, Ed, Hamza, Syafudin and Benjamin.

I am so grateful to my friends: Turkistan, Jamila, Karima, Rosane, Ahlem and Shimaa, the nicest company I have ever had during these years, for the support and help during hard times and the advice in crucial moments.

Finally, I can't imagine what I would do without my family for which I am so grateful. I dedicate this work and effort to my precious and dear family, to my parents Zakia Benidir and Noureddine for encouraging me and believing in me, for their support and trust, for giving me the liberty to choose my way, for their advice and the patience that they taught me like they were passing the PhD in my place. I am so appreciative to the sweetest caring and supportive sister Imen and my two brothers Ilyes and Zaid who have always been by my side even from far and their words were always a relief and fuel no matter what situation I was in.

I appreciate the support of Mrs. Judith Jens, Mrs. Paulien Van Der Veer, the two paranymphs Mr. Syafudin, Mr. Rafik and the technicians during the PhD defence of Utrecht and the help of Mrs. Michelle Dauvé and Mrs. Delphine Turlier before the PhD defence of Nantes. I am thankful to all committee members who accepted to be part of these 2 events for the nice and interesting discussion we had : Prof. Stefan Vandoren and Prof. Philippe Crochet, Prof. Chris van Den Broeck, Prof. Allard Mosk, Prof. Eric Laenen, Prof. Auke Colijn, Prof. Elena Bratkovskaya, Prof. Marcel Merk, Prof. François Arleo.